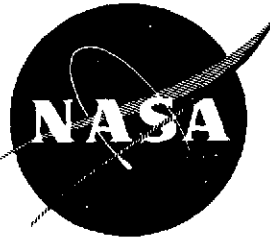NASA CR-134724

DYNAMIC CONVERSION OF SOLAR
GENERATED HEAT TO ELECTRICITY

by J. C. Powell, E. Fourakis, J. M. Hammer, G. A. Smith,
et al, Honeywell Inc., and J. C. Grosskreutz, E. McBride,
et al, Black & Veatch.

HONEYWELL INC.
Systems and Research Center
Minneapolis, Minnesota

BLACK & VEATCH
Consulting Engineers
Kansas City, Missouri

(NASA-CR-134724)   DYNAMIC CONVERSION OF   N75-16079
SOLAR GENERATED HEAT TO ELECTRICITY
(Honeywell, Inc.)   CSCL 10A
                                                      Unclas
                                          G3/44   08935

prepared for

NATIONAL AERONAUTICS AND SPACE ADMINISTRATION

NASA Lewis Research Center
Contract NAS 3-18014

1. Report No. NASA CR - 134724	2. Government Accession No.	3. Recipient's Catalog No. *N75-16079*
4. Title and Subtitle DYNAMIC CONVERSION OF SOLAR GENERATED HEAT TO ELECTRICITY		5. Report Date August 1974
		6. Performing Organization Code
7. Author(s) J. C. Powell, E. Fourakis, J. M. Hammer, G. A. Smith, et al, Honeywell Inc., and J. C. Grosskreutz, E. McBride, et al, Black & Veatch		8. Performing Organization Report No. 2852-41429
		10. Work Unit No.
9. Performing Organization Name and Address Honeywell Inc. Systems and Research Center Minneapolis, Minnesota Black & Veatch Consulting Engineers Kansas City, Missouri		11. Contract or Grant No. NAS 3-18014
		13. Type of Report and Period Covered Contractor Report
12. Sponsoring Agency Name and Address National Aeronautics and Space Administration Washington D. C., 20546		14. Sponsoring Agency Code

15. Supplementary Notes

Project Manager, Harvey Bloomfield, Power Systems Division, NASA-Lewis Research Center, Cleveland, Ohio

16. Abstract

The effort undertaken during this program led to the selection of the water-superheated steam (850 psig/900°F) crescent central receiver as the preferred concept from among 11 candidate systems across the technological spectrum of the dynamic conversion of solar generated heat to electricity.

This result was attained after a systematic technical and economic evaluation of distributed and central receiver solar thermal power systems, including flat plates, parabolic troughs at three different orientations, paraboloid-of-revolution dishes and four central receiver concepts. The polar mounted trough and the dish concepts were evaluated for saturated steam and pressurized water as the thermal transport fluids.

To perform the analytical specification of the components of these systems and to carry out the required systems studies, an extensive software capability was needed. The most versatile and significant software development is a Monte-Carlo simulation code which has been used to simulate the performance of the focusing collector systems. For the central receiver, the code has the unique capability of time-dependent flux mapping and yearly power integration.

The solar power plant designs were investigated in the range of plant capacities from 100 to 1000 Mw(e). The investigations considered the impacts of plant size, collector design, feed-water temperature ratio, heat rejection equipment, ground cover, and location on solar power technical and economic feasibility. For the distributed receiver systems, the optimization studies showed that plant capacities less than 100 Mw(e) may be best. Although the size of central receiver concepts was not parametrically investigated, all indications are that the optimal plant capacity for central receiver systems will be in the range from 50 to 200 Mw(e).

Solar thermal power plant site selection criteria and methodology were also established and used to evaluate potentially suitable sites. The result of this effort was to identify a site south of Inyokern, California, as typically suitable for a solar thermal power plant. The criteria used in the selection process included insolation and climatological characteristics, topography, and seismic history as well as water availability.

17. Key Words (Suggested by Author(s)) Solar central electric power, central receiver, heliostat, trough, dish	18. Distribution Statement Unclassified - unlimited PRICES SUBJECT TO CHANGE
19. Security Classif. (of this report) Unclassified	20. Security Classif. (of this page) Unclassified

FOREWORD

This is the final report describing the work performed by Honeywell/Black & Veatch for the NASA/Lewis Research Center, Cleveland, Ohio, under Contract Number NAS3-18014. Several systems for the dynamic conversion of solar generated heat to electricity were investigated and the water-superheated steam crescent central receiver emerged as the preferred reference system. The contract technical monitors were Mr. G. Kaplan, presently with the National Science Foundation, and Mr. H. Bloomfield.

This report consists of two volumes. Volume I presents the detailed analysis, simulation, and design results. Volume II is an Executive Summary of the contents of Volume I.

The authors express their appreciation for the data and methodology on margin analysis provided by Mr. P. Bos and his staff of Aerospace Corporation, El Segundo, California. The assistance offered by Mr. Bos was given freely and in the true spirit of scientific cooperation.

The authors' appreciation is also extended to Professor E. Sparrow, of the University of Minnesota, for his advice on heat transfer issues; and Dr. C. Austin, of China Lake Naval Weapons Center, for his assistance in the site selection survey.

The authors wish to thank Mr. R. Schmidt of Honeywell, Urban and Environmental Systems, Mr. D. Spencer, previously of the National Science Foundation and now with the Electric Power Research Institute, and Mr. H. Spuhler of the National Science Foundation for the constructive criticism and advance they offered throughout the program.

Finally, the technical assistants, Ms. Barbara Bender and Ms. Mary Jo Frisvold, and the secretaries, Ms. Linda Dyrus and Ms. Peggy Plack have the authors' sincere gratitude for the patience and cooperation.

The following personnel from Honeywell Systems and Research Center and Black & Veatch Consulting Engineers participated in the program effort:

Senior Personnel

Honeywell

- J. C. Powell, Program Manager
- E. Fourakis
- J. M. Hammer
- R. W. Palm
- A. M. Severson
- G. A. Smith

Black & Veatch

- J. C. Grosskreutz, Project Engineer
- R. Athey
- J. Kintigh
- E. McBride
- R. Wood

Contributing Personnel

M. Barrett	P. Myers
M. Bazakos	F. Ohnsorg
M. Borrow	R. Rich
R. Curran	R. Sampson
J. Gross	M. Stewart
T. Holland	W. Sun
S. Johnson	C. Tettemer
C. Knapp	D. Turck
A. Krause	

iii

TABLE OF CONTENTS

TABLE OF CONTENTS (CONTINUED)

TABLE OF CONTENTS (CONCLUDED)

LIST OF ILLUSTRATIONS

LIST OF ILLUSTRATIONS (CONTINUED)

LIST OF ILLUSTRATIONS (CONTINUED)

LIST OF ILLUSTRATIONS (CONCLUDED)

LIST OF TABLES

SECTION I

SUMMARY

This is the final report describing the work performed by Honeywell/Black & Veatch for the NASA/Lewis Research Center, Cleveland, Ohio, under Contract Number NAS3-18014 on the "Dynamic Conversion of Solar Generated Heat to Electricity".

The effort undertaken during this program led to the selection of the water-superheated steam (850 psig/900°F) crescent central receiver as the preferred concept from among 11 candidate systems across the technological spectrum of the dynamic conversion of solar generated heat to electricity.

This result was attained after a systematic technical and economic evaluation of distributed and central receiver solar thermal power systems, including flat plates, parabolic troughs at three different orientations, paraboloid-of-revolution dishes and four central receiver concepts. The polar mounted trough and the dish concepts were evaluated for saturated steam and pressurized water as the thermal transport fluids.

To perform the analytical specification of the components of these systems and to carry out the required systems studies, an extensive software capability was needed. The most versatile and significant software development is a Monte-Carlo simulation code which has been used to simulate the performance of the focusing collector systems. For the central receiver, the code has the unique capability of time-dependent, flux mapping and yearly power integration.

This capability, coupled with a time-independent aim strategy, enabled the selection of the water-superheated steam crescent central receiver as the preferred concept. Furthermore, a careful development of cost data was undertaken to ensure an objective comparative analysis, since the evaluation had to be made primarily on economic grounds.

System characteristics were parametrically investigated to determine the optimal design. To the fullest extent possible, individual system optimizations were carried out for the parameters judged to be most important in determining the total systems cost.

The systems comparisons excluded storage cost considerations, although conceptual storage studies were conducted. A margin analysis exercise showed the storage charge/discharge strategy to be an important issue in determining overall energy costs.

The solar power plant designs were investigated in the range of plant capacities from 100 to 1000 Mw(e). The investigations considered the impacts of plant size, collector design, feedwater temperature ratio, heat rejection equipment, ground cover, and location on solar power technical and economic feasibility. For the distributed receiver systems, the optimization studies showed that plant capacities less than 100 Mw(e) may be best. Although the size of central receiver concepts was not parametrically investigated, all indications are that the optimal plant capacity for central receiver systems will be in the range from 50 to 200 Mw(e).

Overall, the water-superheated steam central receiver was the preferred concept. In this design, pressurized water flows to a receiver located atop a tower at the center of a circular field of heliostats. The water is heated to boiling and then superheated by the redirected solar energy impinging on once-through boiler tubes which exit 850 psig, 900°F steam to drive the turbine-generator.

An estimate of direct capital investment resulted in busbar energy costs of approximately 35 mills/kwh (1974 dollars). A fixed-charge rate of 15 percent was used in this study. The cost estimates do not reflect any indirect charges and, therefore, the energy cost computation is based on the installed equipment costs plus operating and maintenance expenses.

Solar thermal power plant site selection criteria and methodology were also established and used to evaluate potentially suitable sites. The result of this effort was to identify a site south of Inyokern, California, as typically suitable for a solar thermal power plant. The criteria used in the selection process included insolation and climatological characteristics, topography, and seismic history as well as water availability.

2

SECTION II

INTRODUCTION

This is the final report describing the work performed by Honeywell/Black & Veatch for the NASA/Lewis Research Center, Cleveland, Ohio, under Contract Number NAS3-18014 on the "Dynamic Conversion of Solar Generated Heat to Electricity". The objectives of this study program were to:

- Establish criteria and methods for the selection of sites for central solar thermal power plants and use the criteria to evaluate potentially suitable sites within the continental United States.

- Develop a set of candidate systems configurations which typify the large number of possible design approaches for the collection and conversion of solar energy to electricity.

- Specify analytically the performance of all solar power plant subsystems such as the mirrors, receivers, energy transport, turbine-generator, heat rejection, steam generator, and storage.

- Conduct systems studies for the candidate design configurations and provide a technical and economic comparison from which the most promising concepts for large-scale conversion of solar generated heat to electricity can be identified.

All these objectives were successfully met. Furthermore, the summary conclusion is that the dynamic conversion of solar generated heat to electricity is a technologically feasible and potentially competitive energy source. No technical barriers to its implementation exist; the prerequisite for economic viability is the design and production of low cost hardware.

SECTION III

SITE SELECTION

The principal objective of this task was to provide general procedures and siting criteria for the dynamic conversion of solar heat to electricity, not the direct photovoltaic conversion of solar radiation to electricity. The procedures and criteria were then employed in an illustrative exercise to select a specific, potential site in the Southwestern United States.

GENERAL SITE SELECTION PROCEDURES

Site selection is a process of evaluation of alternatives. At the outset a siting region must be identified. Within the region, potential sites are selected and screened against certain general criteria to identify candidate sites. A relative evaluation of the technical, environmental, and economic considerations for each candidate permits final site selection. Many of the criteria used in site evaluation depend on the requirements of the specific solar-electric plant which is to be built. Therefore, a detailed description of the plant and its requirements is the starting point of the site selection procedure.

Plant Description

This description should begin with a general statement which specifies the proposed electric generating capacity of the plant and the basis for this rating. For example, the plant may be rated in terms of peak generating power in kilowatts, or in terms of the total electrical energy generated over a year's time in kilowatt-hours. The operating philosophy for the plant, whether base load, intermediate, or peaking, should be specified and the energy storage requirement in hours should be stated.

The major systems of the plant should be identified and described. The block diagram shown in Figure 1 illustrates the major systems which are to be included. For example, the collector/concentrator system may be either the distributed type in which solar heat is collected and transferred to a heat transport medium at each individual collector/concentrator in the field, or the central receiver type in which solar radiation is redirected by individual heliostats in the field and collected at one central receiver where heat transfer occurs. Special topography and foundation requirements for the collectors should be specified.

For the other major systems, the description should be detailed enough to aid in establishing the site selection criteria. For example, the proposed layout of the heat transport system from distributed collectors should be provided so that site topography may be properly selected. Another important consideration is the proposed method of heat rejection, e.g., wet or dry cooling towers, cooling lake, or river cooling. If wet towers are utilized, both peak and average makeup water requirements must be specified. A more detailed account of plant description requirements is given in Reference 1.
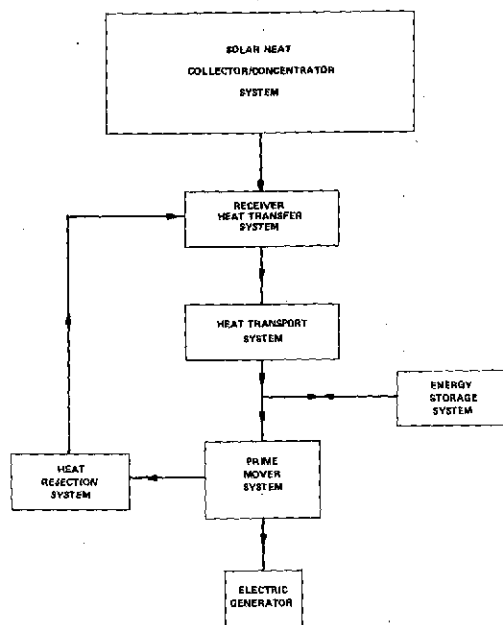
Figure 1. Generic Block Diagram of Major
Plant Systems

The most important plant requirements which must be specified are land area and water volume. Water requirements of the plant, both peak and average for a 24-hour period, should be enumerated and totaled.

Once the plant description is completed, site selection may proceed by exercising each of the following procedural steps.

Identification of General Siting Region

Selection criteria are established to meet the requirements of the plant owner, e.g., utility service area, consistent with maximum insolation. The general siting region is then identified.

Selection of Candidate Sites within the Region

General selection/screening criteria are established consistent with the plant requirements. Several candidate sites are then selected which meet the criteria.

Evaluation and Comparison of Candidate Sites

Specific evaluation criteria are derived from the general selection/screening criteria and then broken down into engineering, environmental, and economic categories. Candidate sites are compared and rated on this basis.

Final Site Selection

The top rated candidate sites (2 or 3) are selected for on-site inspection and further data gathering activity. Intangible considerations are identified, e.g., public attitudes. The final site is selected on the basis of these further data and the judgment of the power plant owner and his consultants.

SITING CRITERIA

The preceding site selection procedure requires that criteria be established for each step in the procedure. The purpose of this subsection is to define these criteria in detail. They are divided into Major Siting Criteria for identifying siting regions, General Selection/Screening Criteria for choosing candidate sites, and Evaluation Criteria for final site selection.

Major Siting Criteria

The two major site selection criteria are (1) high insolation and (2) favorable meteorological conditions, e.g., minimum sky cover. These criteria are unique to solar/electric power plants and control the selection of a general siting region, consistent with the requirement of the utility service area and proximity to load centers. Reference 2 presents a detailed analysis of these two major criteria.

Solar energy striking the surface of the earth consists of direct and diffuse (scattered) radiation. Solar collectors which employ focusing to achieve energy concentration and heliostats which redirect sunlight utilize only direct radiation. Nonfocusing collectors such as the flat plate, utilize both direct and diffuse radiation. Therefore, the collector system specified in the plant description determines which radiation component is of interest. Having determined this, the insolation criterion is:

- Maximum total annual insolation consistent with other siting requirements

The major meteorological criterion is:

- Meteorological records should demonstrate minimum interruption of insolation by clouds, fog, rain, or blowing dust and sand.

General Selection/Screening Criteria

Candidate sites within the siting region are selected and screened against a set of six categories of criteria which are:

(1) **Land Area and Topography** -- The land area criterion is straightforward.

- Candidate sites must satisfy the land area requirements for the proposed plant.

- Avoid shading by ridges adjacent to site.

- Seek relatively flat areas with good drainage. Slopes which face south are acceptable, especially for central receiver system configurations.

(2) **Land Use** -- A general land use criterion may be stated.

- Candidate site selection must satisfy existing local, state, and Federal land use statutes.

More specific land use criteria are:

- Avoid urban areas, agriculturally productive areas, and commercial and industrial activities including subsurface natural resources recovery.

- Avoid national, state, and local parks, American Indian land, wilderness areas, and wildlife reserves and sanctuaries.

- Avoid proximity to airports and flight corridors.

(3) Soils/Geology -- Two general soils/geology criteria may be stated:

- Avoid dry lake playas, depressions, and areas of uncompacted sand and sand dunes.

- Avoid areas containing active seismic faults.

(4) Water -- The general water criterion is straightforward:

- Water supply must meet the total plant requirements.

Recognizing that water is transportable, the water requirement criterion is not as rigid as, for example, the requirement for land area. Site selection must recognize the requirement for water supply and assure that a means for delivery of those water requirements is available for any candidate site. Such means may include pipelines, canals, or other water transport mechanisms.

(5) Transportation Access -- Construction of a solar/electric power plant will require the movement of men, materials, and equipment. Adequate highway and rail access is essential. The general criterion for transportation access can therefore be stated:

- Access to the candidate site by paved highway or railroad should be possible with a minimum of secondary road improvement or spur construction.

(6) Electric Transmission -- The site selection process should consider to some extent the availability of existing transmission facilities. However, the usefulness of existing transmission lines is largely dependent upon their capacity, and the size of the proposed solar/electric power plant may seriously limit their usefulness. In the absence of existing or adequate transmission lines, the site selection criteria must recognize the need to construct new transmission lines leading either to a transmission substation or to the load center.

The general criterion for electric transmission may be stated:

- The location of a candidate site should minimize construction of new transmission lines consistent with other siting constraints.

Evaluation Criteria

Final site selection requires evaluation of all candidate sites relative to detailed evaluation criteria. These criteria are derived from the General Selection/Screening Criteria, but they are more specific. The Evaluation Criteria are divided into three categories: Engineering Criteria, Environmental Criteria, and Economic Criteria.

(1) Engineering Criteria -- The major engineering factors to consider in evaluating each candidate site for a solar/electric power plant are local insolation/meteorology, topography, soils/geology, water supply, road and railroad access, and electric transmission. Each of these factors has already been discussed to some extent in previous paragraphs. For site evaluation they are applied in more detail.

Perhaps the most important engineering criterion is the adequacy of the water supply. Alternate water supply systems may be evaluated considering the following factors:

- Quantity of surface water available

- Quantity of ground water available

- The quality of the supply

- Present and projected uses of the proposed water supply

- Stability of a sustained yield based on a statistical analysis of historical or simulated low flows and/or pump tests for ground water aquifer evaluation

- Cost to import water as a function of transmission distance

- Pumping requirements

- Storage capability

- The effects of ground water pumpage on aquifer drawdown or surface water withdrawal on low flows

Sites which can satisfy the plant water requirements with water of adequate quality are strongly preferred.

(2) Environmental Criteria -- The major siting criteria (high insolation and favorable meteorological conditions) constrain the location of candidate sites for central solar/ electric plants to areas of relatively low population in the Southwestern United States. These same siting constraints favor regions of desert biome where generally uniform ecological characteristics might be anticipated. These conditions are to be contrasted with those associated with siting of conventional fossil or nuclear fuel power plants where high population densities and diverse ecological aspects can raise difficult environmental problems. For these reasons, environmental considerations are not expected to establish significant siting limitations for solar power plants. Nevertheless, the site evaluation analysis must recognize various environmental criteria. Some of the more important criteria are listed below. Considerably more detail is given in Reference 1.

Population -- Two general criteria can be stated as follows:

- Minimize the number of persons that would be displaced as a consequence of site selection

- Minimize the total population within 10 miles from the plant site.

Land Use -- In addition to the specific land use criteria given previously for Selection/Screening, evaluation of candidate sites should recognize current land ownership and compatibility with projected land use.

In the favored siting region (Southwestern United States), the majority of the land is owned by the Federal government. This land is usually under the control of the Bureau of Indian Affairs, and the National Park Service. The balance of the land is either privately owned or under state control. Recognizing this ownership pattern, the following criteria are suggested for site evaluation:

- Private land and Bureau of Land Management land offer the best potential for candidate sites.

- Military Reservations should be avoided unless specific communication with the commanding officer reveals a willingness on the part of the Department of Defense to cooperate.

Evaluation criteria regarding projected land use are as follows:

- Avoid location in areas of logical urban expansion

- Avoid areas suited to future agricultural development

- Avoid areas which overlie significant natural resources such as oil and minerals.

Water Use -- Water rights in the regions favored for solar/electric power plants are carefully regulated. The potential for adverse effects resulting from plant water use should be eliminated through the regulatory process necessary to obtain water rights for the plant.

In the absence of regulatory requirements, the following criteria are suggested:

- Avoid adverse effects upon surface water supplies

- Avoid adverse effects upon ground water supplies

Cultural and Aesthetic Features -- Cultural and aesthetic features include historical and archaeological sites as well as scenic resources. Aesthetic impacts are principally visual in character. A distinction is made between voluntary and involuntary visual contact. A solar plant will be of both scientific and general interest to the public, and such interest may prompt voluntary observation of the plant facilities. Involuntary visual impact is viewed as undesirable, and the following general criterion should be followed.

- Select site locations that will minimize significant casual involuntary visual contact with the plant facilities.

In addition to the general avoidance of visual contact, truly scenic locations should be avoided. The general criterion is as follows:

- Avoid site locations in areas of exceptional scenic value. Application of this criterion requires site investigation.

The suggested criterion for historical and archaeological locations is:

- Avoid significant known historical and archaeological sites. General application of this criterion is possible; however, specific site analysis is necessary to confirm application of the criterion.

Ecology -- Impacts upon rare, endangered, and important species have become an important siting consideration. In general, the location of such species must be determined by specific site investigations. The suggested criteria are:

- Avoid areas of habitat known to support rare, endangered, or important species.

- Avoid destruction of significant wildlife habitat.

(3) Economic Considerations -- The techniques for economic evaluation of solar/electric power plant sites are no different than those normally used for evaluation of conventional fossil or nuclear sites. In all cases, minimizing costs consistent with the technical requirements is the controlling criterion. Those items which contribute most significantly to the capital, operating, and maintenance costs of a site are described here. Costs should be developed for each candidate site so that differential costs may be calculated for final comparison.

Land -- Land costs should be minimized consistent with satisfying the technical and environmental criteria.

Site Preparation -- Site preparation costs include on-site inspection, surveying, soil boring and testing, excavation, preconstruction, and construction access costs.

Access Roads -- Costs should be determined for development of new roads and/or improvement of existing roads required for construction, operation, and maintenance.

Water Supply -- Determination of the total water supply costs requires information on pumping, pipeline, intake, storage, treatment, and water rights costs.

Transmission Lines -- The cost of transmission lines of adequate capacity, assuming one line out of service, should be determined for delivery of power to the nearest load center or distribution substation.

SELECTION OF A SPECIFIC SITE

This subsection describes an exercise in the application of the foregoing procedures which resulted in the recommendation of a specific site for a 1000 MW(e) solar/electric power plant.

Plant Requirements

A hypothetical plant with flexible requirements was assumed for this study.

Plant Capacity -- Capacity was specified to be in the range 100 to 1000 MW(e). However, for purposes of land area, water, and other size-specific requirements, the upper figure of 1000 MW(e) was assumed.

Collector/Concentrator System Configuration -- Both the distributed system and the central receiver system were considered in order to explore the problems of siting each concept. However, special site topography for the central receiver system was not specified.

Heat Transfer and Transport System -- The heat transfer media were specified to be water/steam. Piping from distributed collectors was specified to be above ground.

Prime Mover -- Steam turbines in the size range 100 to 1000 MW(e) were specified. For the distributed collector system, a saturated steam cycle operating at 925 psia/585°F throttle inlet conditions was specified. For the central receiver a steam cycle operating at 850 psia/900°F was chosen for this study.

Heat Rejection System -- Wet (evaporative) cooling towers were specified. Make-up water requirements were estimated at 7000 gallons per minute for a 1000 MW(e) plant.

Energy Storage Requirements -- No specific energy storage system was specified.

Land Area Requirements -- Land area of 15 to 20 acres per megawatt (average) of electric power generation was specified. For a base load plant which generates a daily average of 1000 MW(e) over a year, approximately 25 square miles is required. This figure was used to define the area requirement for site selection.

Total Water Requirements -- Typical water requirements for a 1000 MW(e) generating plant operating at 0.5 capacity factor are:

	Peak gpm	Average gpm
Evaporative Cooling Make-up	13,700	7,000
Feed Water Make-up	200	100
General Service	200	100
Totals	14,100	7,200

Identification of General Siting Region

No particular utility service area was specified. The general siting region was therefore chosen to be that area of the United States having the highest, direct solar radiation. Figure 2 shows isopleths of direct solar radiation superimposed on a map of the continental United States (Reference 2). The area enclosed by the 250 Langley per day isopleth was chosen as the General Siting Region.

Selection of Candidate Sites

A map of Arizona, Nevada, and California with scale 1 inch = 8 miles was used to make an initial selection of acceptable siting areas within the General Siting Region. The applicable General Selection/Screening Criteria were land area/topography and land use. These initial selections were then screened against the same two criteria by means of a closer inspection on U.S.G.S. 15 minute maps. Nine potential candidate sites satisfied the land area/topography and land use criteria after inspection of the 15 minute maps. They were:

- Blythe (two alternate sites)

- Danby Lake [topography marginal for 1000 MW(e) distributed system]
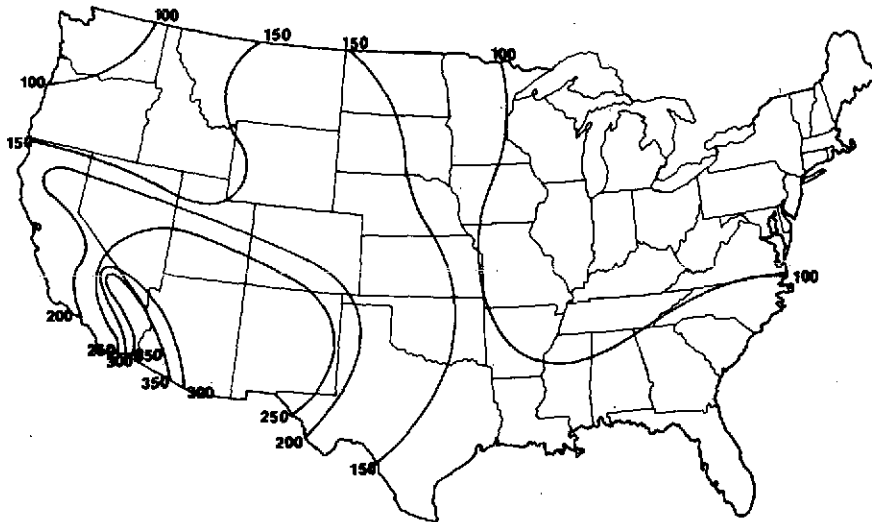
Figure 2. Isopleths of Mean Daily Direct Solar
Radiation (Langleys)

- Inyokern

- Inyokern South

- Manix

- Searles

- Soda Lake

- Superior Lake

The location of these areas is shown in Figure 3.

Of these nine, five were found to meet all of the General Selection/Screening Criteria in varying degrees. The candidate sites were:

- Blythe (two alternate sites) - located approximately 15 miles and 25 miles west of Blythe, California

- Inyokern South - located approximately 6 miles southwest of Inyokern, California

- Manix - located approximately 10 miles northwest of Manix, California

- Searles - located approximately 20 miles due east of China Lake, California
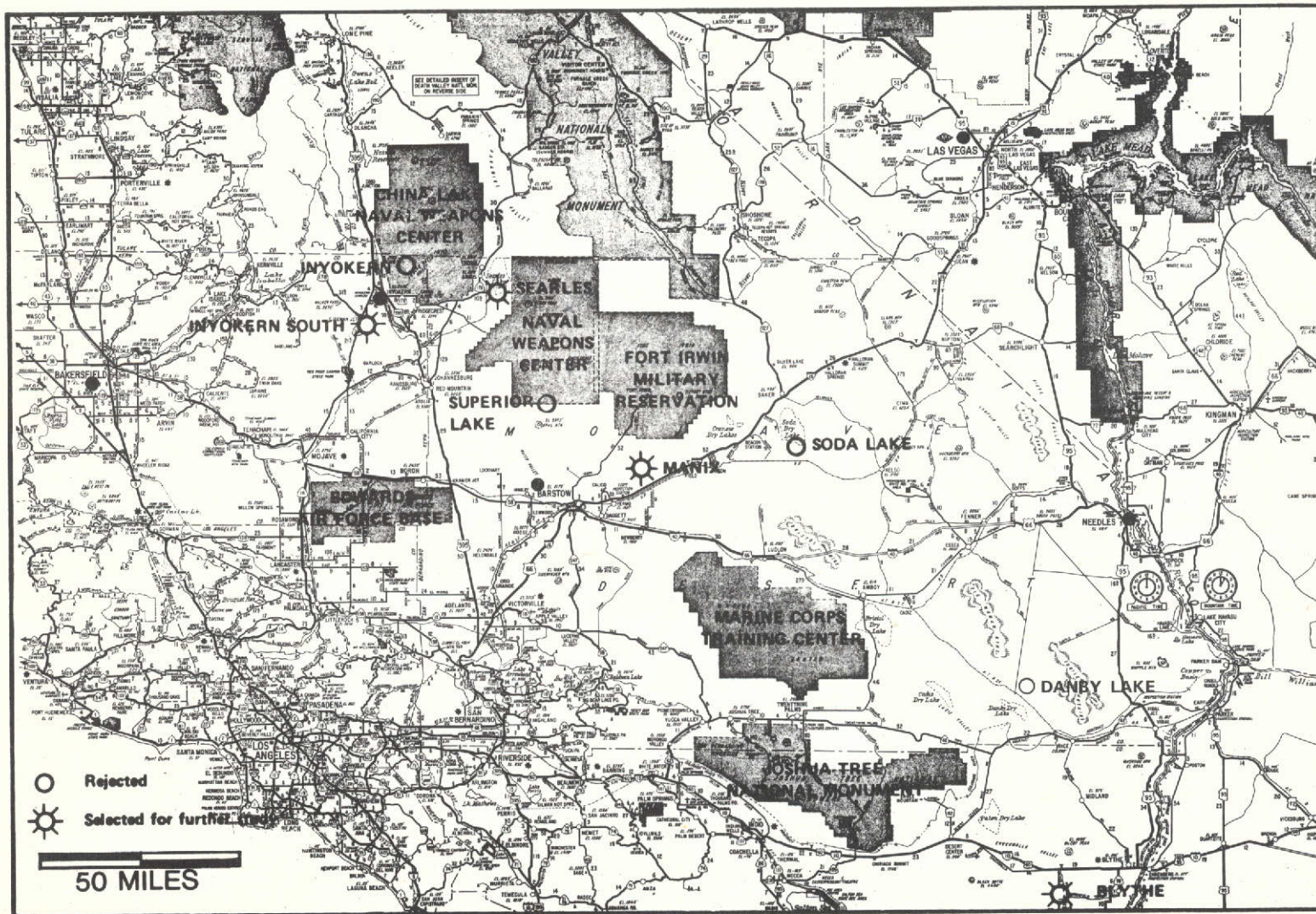
Figure 3. General Siting Area

Evaluation and Comparison of Candidate Sites

To evaluate and compare the candidate sites against the Evaluation Criteria listed previously, available data were compiled and a description of each site was written. Because of the importance of make-up cooling water sources in the arid regions of eastern California, an intensive effort was made to identify these sources for each candidate site. In the course of these efforts, several general conclusions were reached:

- For the near term, cooling water for large thermal power plants located in the desert regions will be obtained by negotiated diversions from existing aqueducts. Irrigation water may be useful for smaller plants provided water treatment is available to reduce the high salinity.

- For the long term, dry or dry/wet cooling tower technology must be developed to mitigate anticipated cooling water demands. Alternatively, plant designs which do not require cooling towers should be developed, e. g. , open-cycle gas turbines.

- California has implemented long-range plans for siting power plants and for the allocation of scarce water resources. If a solar power plant is to be built in the next decade, steps should be taken immediately to include it in the planning.

Engineering and Environmental Evaluation -- A summary of the data gathered for evaluation and comparison of the candidate sites is given in Table I. The amount of data and the degree of detail shown in Table I were limited by the scope and the time allotted to this particular exercise in site selection.

Current land usage at each site was left blank in Table I, but was determined by later on-site inspection.

Inspection of Table I shows that Inyokern South is the highest ranked site.

Economic Evaluation -- Economic evaluation and comparison of the candidate sites were made on a differential cost basis. The costs of land and site preparation were assumed equal for all sites. The cost of construction of plant access roads and railroad spurs were made on the basis of $74,000 per mile for roads and $200,000 per mile for railroad.

The cost of transporting water was based on piping and pump costs of $264,000 per mile.

The cost of constructing additional transmission lines for various size plants was based on the figures given in Reference 1. A substation which would be required at Searles was estimated to cost $380,000.

Table I. Engineering and Environmental Comparison of Sites

	Inyokern South	Searles	Manix	Blythe North / Blythe South (BN/BS)
1. Peak Insolation (Direct and Diffuse) Langleys	819	819	750	700
2. Mean Sky Cover	0.35	0.35	0.35	0.20
3. Topography (Ft/Mile - Direction of Rise)	150 -NW -SE	15-S	9-S	27-S (BS) 105-N (BN)
4. Transmission Distance to Nearest Major Load Center (Miles)	100	120	150	150 (BN) 160 (BS)
5. Water Supply (For Cooling Tower)				
A. Ground Water	Inadequate	Inadequate	Inadequate	Inadequate
B. Surface Water	Potentially Adequate	Potentially Adequate	Inadequate	Potentially Adequate
C. Distance to Surface Water (Miles)	5	45	72	25 (BN) 15 (BS)
6. Plant Access				
A. Distance to Nearest Railroad (Miles)	4	0	6	20
B. Distance to Paved Road (Miles)	0	0	3	4(BN) 1 (BS)
7. Land Use*	-	-	-	-
8. Land Ownership	BLM+	BLM	BLM	BLM
9. Population Density				
0-5 Miles	0	0	0	0
5-10 Miles	0	10,000	50	12,000
10-50 Miles	35,000	30,000	55,000	27,000

* Current Land Usage is Presently Undetermined for Specific Site Areas

+ BLM = Bureau of Land Management. Specific Site Areas May Contain Some Private Land

The economic comparison of the four candidate sites is given in Table II. Inyokern South is the most economic site.

Final Site Selection -- In the particular exercise under discussion, the top three candidate sites were selected by a rating scheme which gave the heaviest weight to insolation, sky cover, and water supply. All other factors were given equal weight. The ratings of each site for each of nine different criteria are shown in Table III, as determined from the previous engineering, environmental, and economic evaluation. Inyokern South is the top rated site. A topographic map of the site is shown in Figure 4.

Table II. Economic Comparison of Sites

Differential Costs	Inyokern South	Searles	Manix	Blythe
1. Transmission				
250 MW(e)	Base	$2,225,000	$ 3,415,000	$ 1,470,000
500 MW(e)	Base	Base	9,300,000	9,300,000
1,000 MW(e)	Base	Base	14,400,000	14,400,000
2. Water Supply				
[1,000 MW(e)]	Base	10,500,000	17,700,000	5,300,000
3. Plant Access	$148,000	Base	1,400,000	296,000
4. Cooling Cost	Base	Base	Base	Base
5. Site Preparation	Base	Base	Base	Base

Table III. Rating of Alternate Sites

Item	Inyokern South	Seales	Manix	Blythe	Weight Factor
1. Insolation	1	1	2	3	0.25
2. Sky Cover	2	2	2	1	0.25
3. Topography	4	3	1	2	0.05
4. Transmission	1	2	4	3	0.05
5. Water Supply	1	3	4	2	0.25
6. Plant Access	2	1	4	3	0.05
7. Land Use	3	2	1	4	0.05
8. Land Ownership	-	-	-	-	-
9. Population Density	1	3	2	4	0.05
Weighted Average	1.55	2.05	2.60	2.30	
Rating	1	2	4	3	
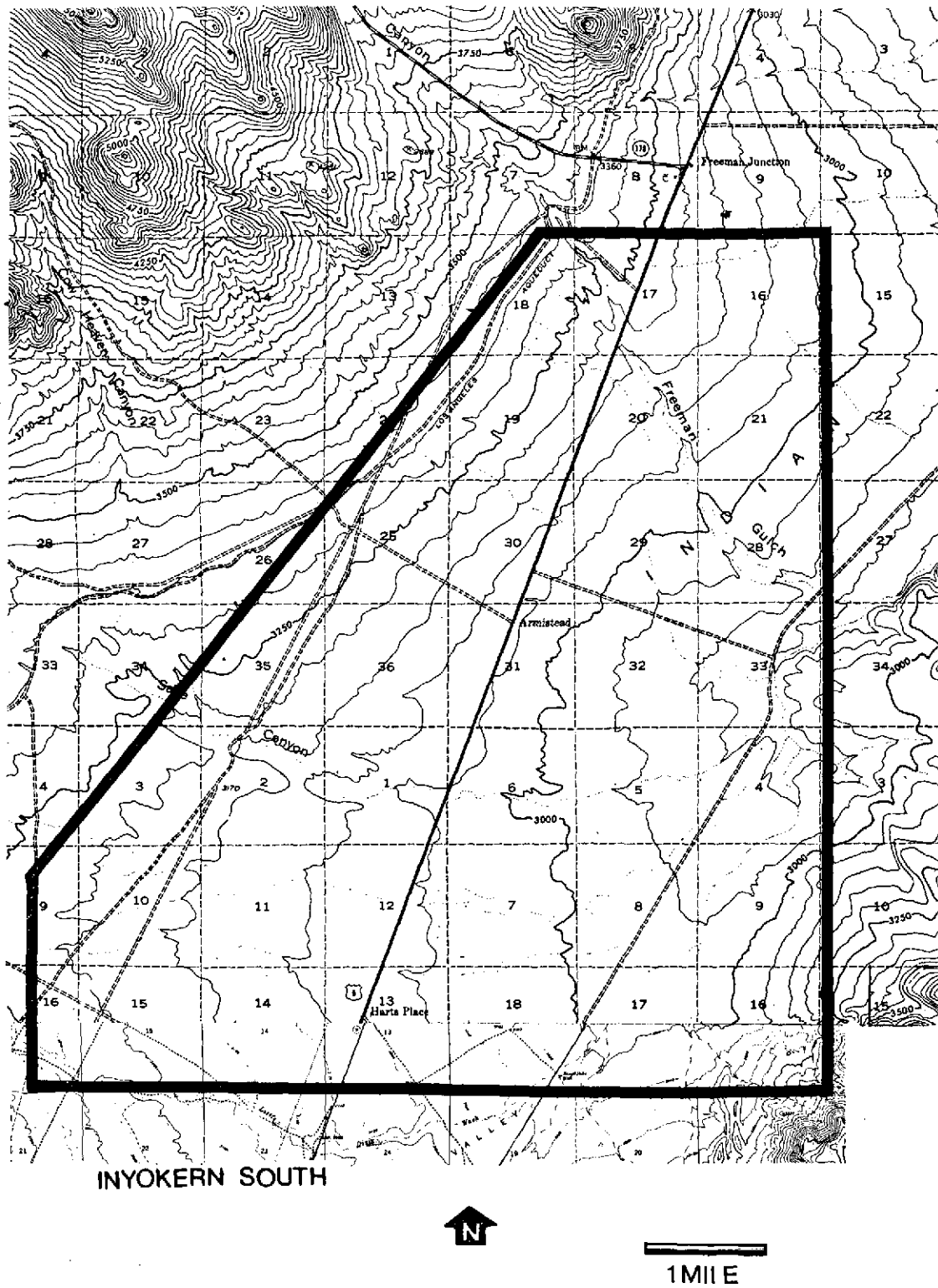
Figure 4. Topographic Map of Inyokern South Site

A special site inspection trip was made for the purpose of aerial and ground inspection of the Inyokern South site and the Blythe sites (Reference 3). Aerial reconnaissance of Searles Lake and of the Manix site was also accomplished.

The primary observations and conclusions were as follows:

- Inyokern South was confirmed as the prime site.

- Searles Lake was rejected as a candidate site because of industrial development, stack plumes, occurrence of inversion layers, and blowing alkali dust.

- The Blythe North site was rejected as a candidate because of loose, unconsolidated fine sand which occurs on a portion of the area, and severe drainage washes on the slope which comprises the northern half of the site.

- The Blythe South site was judged adequate. It would require less site development than Inyokern South, but soil conditions were not as good. Blowing sand could be a potential problem.

- The Manix site was judged adequate from aerial reconnaissance. However, water supply is inadequate for wet cooling towers at this site.

Selection of Prime Site -- Inyokern South is the prime site, based on office engineering analysis and on-site inspection. Figure 5 shows two aerial views of the site. Blythe South is the second ranked site.

a) State Highway 14 cuts across site in above view

b) View shows two lines of Los Angeles Aqueduct

Figure 5. Aerial Views of Inyokern South Site

SECTION IV

CANDIDATE SYSTEM SELECTION AND EVALUATION

This section describes the selection and evaluation of candidate systems in terms of various performance parameters and under a variety of conditions.

SYSTEM SELECTION AND EVALUATION METHODOLOGY

This program was to consider the complete spectrum of system possibilities (in contrast to other current studies of a "point" design within that spectrum) and to do so with finite effort and within a 10-month time span. Figure 6 presents some of the possibilities of this spectrum. The approach decided upon involved (1) selecting a "representative" set of systems (ultimately eleven), (2) analyzing these to determine the best existing system, and (3) theorizing from these results how an improved system could be synthesized. Figure 7 illustrates a partial basis for the selection methodology. These curves represent the performance of different kinds of collectors and, furthermore, they represent, to a high degree of approximation, the best practically achievable performance for the three basic types of collectors, i.e., no concentration, a single axis of concentration, and two axes of concentration. Thus, these curves divide the collector possibilities into distinct output temperature categories. Different design details of the various types of collectors may be handled as a perturbation of these curves.

The operational regime of conventional turbomachinery is shown in Figure 8. An attempt was made to match the fluid outlet temperature of the collectors with compatible prime movers to make maximum use of the available turbomachinery. Thus, flat plate collectors are matched with the organic Rankine cycle turbines. The single-axis collectors may be matched with saturated steam turbines. The two-axis collector appears consistent with superheated steam. Not shown on the efficiency versus temperature curves is the temperature available for the central receiver concept. Initial synthesis work matched the central receiver with its intrinsic high temperature with a gas turbine cycle.

The interplant energy transport considerations are also important. Various organic fluids, both saturated steam and pressurized hot water, sodium and/or other fluids suitable for high-temperature operation, and the various gases such as helium were studied as candidates. These elements were all considered in the initial synthesis work.

Heat rejection methods reviewed included both wet and dry cooling towers. Early system considerations were performed without storage considerations with the belief that storage could be folded into a system design down stream from the initial effort. This has proved satisfactory.

The following subsections describe 11 different systems which were defined and analyzed.

CANDIDATE SYSTEMS

The major systems of a solar power concept are identified in the block diagram of Figure 9. Each candidate system is covered independently of the others, and each system is accompanied by a schematic drawing.

20

Figure 6. Solar Thermal Power Concepts
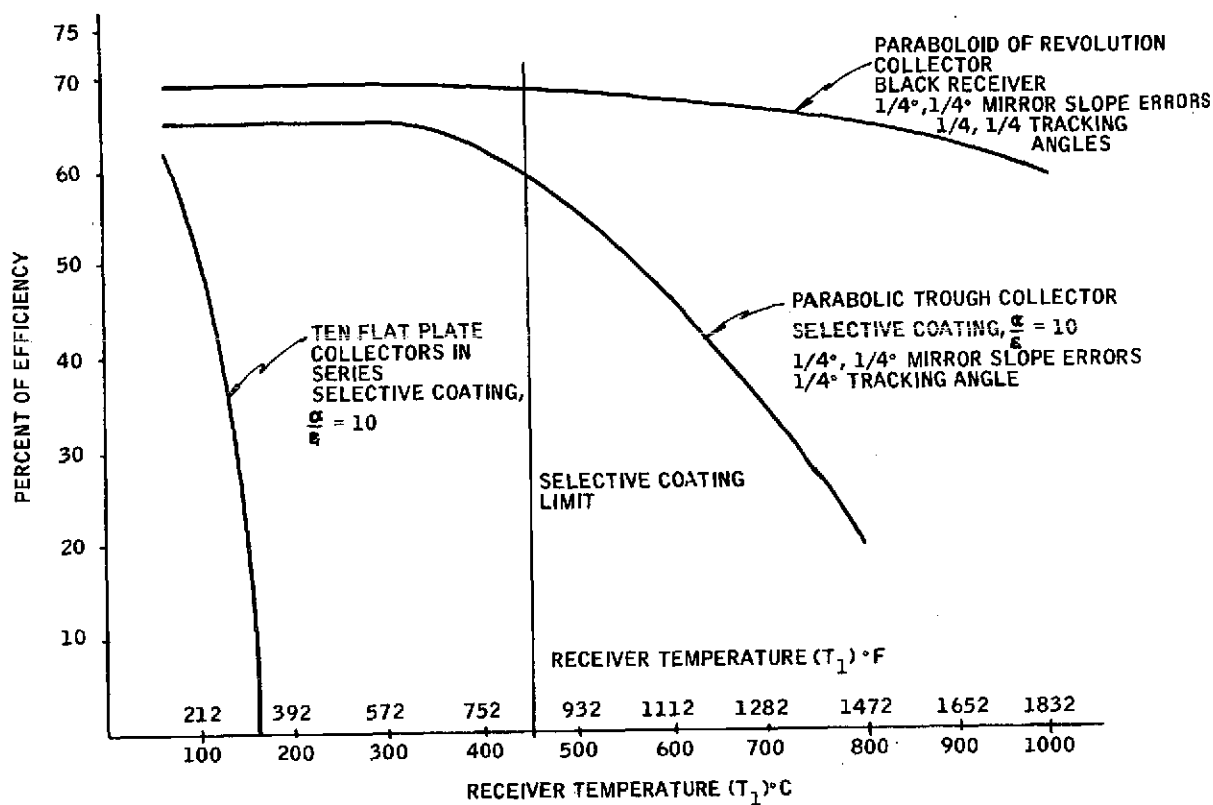
Figure 7. A Comparison of Collector Performance Curves

Energy storage is not included in the discussion because it is common to all the concepts. In addition, all of the heat rejection systems are wet cooling towers. Dry cooling towers are an option; however, for purposes of evaluation and comparison, wet towers are assumed for each candidate system.

Flat Plate Collector

The relatively low temperature available at the collector ($\sim300°F$ maximum) restricts the choice of a working fluid in the turbine. At the low temperature available, water is not a good choice. The prime mover fluid should have a relatively low vapor pressure, a large enthalpy change in expansion into a dry region, and a low cost. Following an extensive search, R-11 was chosen as the working fluid in the turbine (prime mover).

In the candidate system, pressurized water is heated from $210°F$ to $260°F$ by a series of 10 flat plate collectors (Figure 10). The hot water is used to generate saturated R-11 vapor at a temperature of $208°F$ (113 psia). Exhaust R-11 from the condenser returns to the vapor generator at a temperature of $100°F$. Condenser cooling is provided by a mechanical draft, wet cooling tower.

22
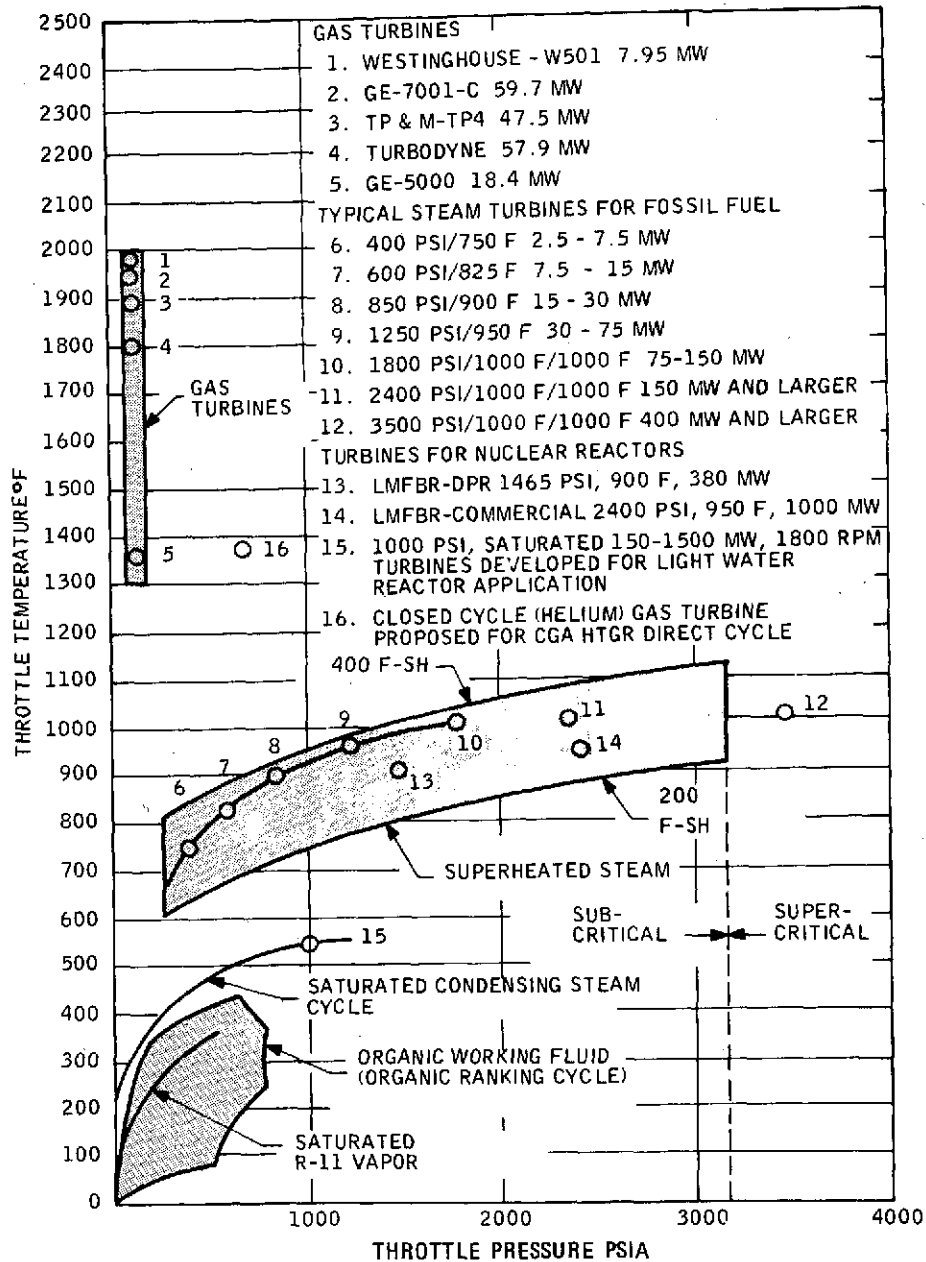
Figure 8. Temperature and Pressure Regime of
Conventional Turbomachinery
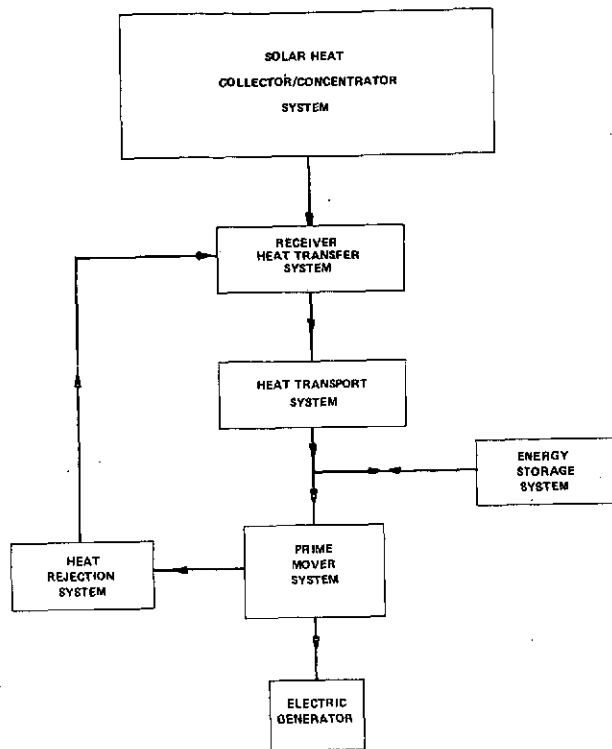
Figure 9. Generic Block Diagram of Major
Plant Systems
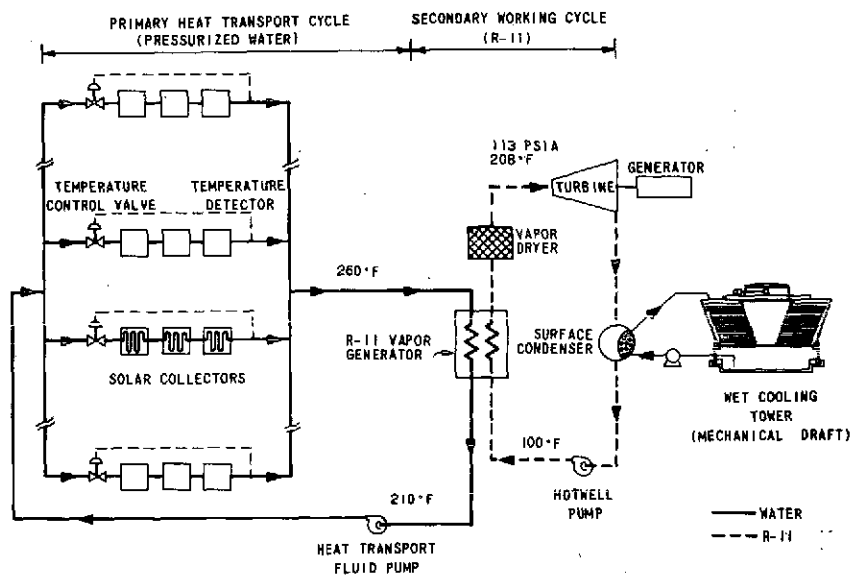
Figure 10. Candidate System Concept Flat Plate
Collector

Parabolic Trough Collector

Parabolic Trough Collector With Heat Pipe and Steam Generator -- In this candidate system, saturated steam is generated at each individual collector at a temperature of 550°F (1045 psia), as shown in Figure 11. The steam is transported in a distributed piping network to a moisture separator before entering the turbine. Dry, saturated steam enters the high-pressure turbine at a temperature of 543°F (985 psia). This turbine is typical of the 1800 rpm saturated steam turbines used with boiling water reactors and is commercially available. Water is exhausted from the condenser at a temperature of 120°F (dependent on ambient conditions). Condenser cooling is provided by a mechanical draft, wet cooling tower.

Regenerative heaters are used to raise the temperature of the water returning to the collector field to 420°F. Water is supplied to the individual steam generators by the distributed piping system.

Parabolic Trough Collector With Flow-Through Absorber -- The parabolic trough collector system with flow-through absorber has both a primary heat transport loop and a secondary steam generation loop (Figure 12). Pressurized water at 2100 psia is pumped through one or more collectors to raise the temperature from 547°F to 626°F. Pressure losses through the distributed piping network are approximately 100 psi.

The hot water is used to generate steam in a secondary loop. Steam from the steam generator is slightly superheated (50°F) with a temperature of 585°F and a pressure of 925 psia. Expansion through the turbine leaves the condensed water at a temperature of 120°F (dependent on ambient conditions). The turbine used in this system is typical of the 1800 rpm turbines used with the pressurized water reactors and is commercially available. Condenser cooling is provided by a mechanical draft, wet cooling tower.

Regenerative heaters are used to raise the temperature of the water returning to the steam generator to 453°F at a pressure of 975 psia.

Paraboloid of Revolution (Dish) Collector

Dish Collector - Liquid Metal Coolant -- This system utilizes a liquid metal as the primary loop coolant (Figure 13). The molten metal is circulated through the dish collectors, raising its temperature from 600°F to 1000°F. Pressure losses through the distributed piping network are approximately 100 psi. An analysis of the heat transport properties coupled with economic considerations led to the choice of sodium as the heat transport fluid.

After the molten sodium has passed through the collector field, it is sent to a "hockey-stick" steam generator. This steam generator is a single-tube, modular design sodium/steam generator which has been proposed for the LMFBR demonstration plant. In the steam generator, superheated steam is produced at a temperature of 950°F and a pressure of 1465 psia. A 1450/950 turbine is commercially available for use in this cycle. Water from the condenser at 120°F (dependent on ambient conditions) is returned to the steam generator.

Regenerative heaters are used to raise the temperature of the water returning to the steam generator to 475°F, and a boiler feed pump raises the pressure to 1480 psia. Condenser cooling is provided by a mechanical draft, wet cooling tower.

Dish Collector - Saturated Steam -- This candidate system is equivalent to the parabolic trough collector with heat pipe. The only significant change is in the use of a dish collector in place of the trough collector. However, due to the physical arrangement of the dish collector, the heat pipe must be replaced with a circulating pump. Because of the added complexity and expense of the pumps, this system was not considered as a viable candidate.

Figure 11. Candidate System Concept Parabolic Trough
Collector with Heat Pipe and Steam Generator

Figure 12. Candidate System Concept Parabolic Trough
Collector with Flow-Through Absorber

Figure 13. Candidate System Concept Dish Collector with
Liquid Metal Coolant

Dish Collector - Pressurized Water -- This candidate system is equivalent to the parabolic
trough collector with flow-through absorber. The only significant change is in the use of
a dish collector in place of the trough collector. Figure 14 illustrates this candidate
system.

Dish Collector - Superheated Steam -- The generation of superheated steam in the field
using a dish collector is a difficult design problem. Because of the desirability of
isolating the collectors that boil the water from the collectors that superheat the steam,
a series of collectors is required. A preliminary analysis indicated that three "boiling
collectors" would be needed prior to one "superheating collector."

Superheated steam at a temperature of 1000°F and a pressure of 2400 psia enters the high-
pressure turbine. A 2400/1000 turbine is commercially available for use in this cycle.
Water from the condenser at 120°F (dependent on ambient conditions) is returned to the
collector field via the regenerative feedwater heater.

Regenerative heaters are used to raise the temperature of the water returning to the
collector field to 475°F, and a boiler feed pump raises the pressure to 2500 psia.
Condenser cooling is provided by a mechanical draft, wet cooling tower. Figure 15
shows a schematic of this candidate system.

PRIMARY HEAT TRANSPORT PRESSURIZED CYCLE
(WATER)   SECONDARY WORKING CYCLE
                                              (STEAM)

925 PSIA
585 F
(50° SUPERHEAT)   TURBINE   GENERATOR

2000 PSIA
626°F

STEAM
GENERATOR

975 PSIA
453°F

BOILER
FEED PUMP

SOLAR COLLECTORS

SURFACE
CONDENSER

120° F
3.5" Hg

WET COOLING
TOWER
(MECHANICAL
DRAFT)

REGENERATIVE
HEATER

HOTWELL
PUMP

—— WATER
--- STEAM

2100 PSIA
547° F   HEAT TRANSPORT
                FLUID PUMP

Figure 14. Candidate System Concept Dish Collector -
Pressurized Water

SUPERHEAT
BOILING REGION | REGION

2400 PSIA
1000°F   TURBINE   GENERATOR

TEMPERATURE
CONTROL VALVE   TEMPERATURE
                  DETECTOR

SURFACE
CONDENSER

120° F
3.5" Hg

WET COOLING
TOWER
(MECHANICAL
DRAFT)

SOLAR COLLECTORS

HOTWELL
PUMP

REGENERATIVE
HEATERS

—— WATER
--- STEAM

2500 PSIA
475°F   HEAT TRANSPORT
               FLUID PUMP

Figure 15. Candidate System Concept Dish Collector -
Superheated Steam

Central Receiver

The central receiver concept differs from the method of collecting heat with flat plate collectors or concentrating mirrors. In this concept, sunlight is redirected to an elevated central heat receiver where it is absorbed. The "redirecting mirrors," or heliostats, are capable of being aimed at a predetermined point on the surface of the central receiver.

Central Receiver - Closed Brayton Cycle -- Several gases were considered for use in the Brayton cycle. Because of its superior heat transport and thermodynamic properties, noncorrosiveness, and cost, helium was selected for this candidate system. Hot helium leaves the central receiver at a temperature of 1060°F and a pressure of 1000 psia and passes to a noncombustion gas turbine (Figure 16). The exhausted helium from the gas turbine (790°F, 575 psia) gives up a portion of its heat in a regenerative heater and is then further cooled by circulating water from a mechanical draft, wet cooling tower.

Helium enters the gas compressor at a temperature of 86°F and a pressure of 555 psia (dependent on ambient conditions). In the compressor the helium pressure is boosted to 1110 psia. It is then heated in the regenerative heater prior to being returned to the central receiver to continue the cycle.

	TEMP (°F)	PSIA
1	1060	1000
2	790	575
3	333	565
4	86	555
5	283	1110
6	740	1100
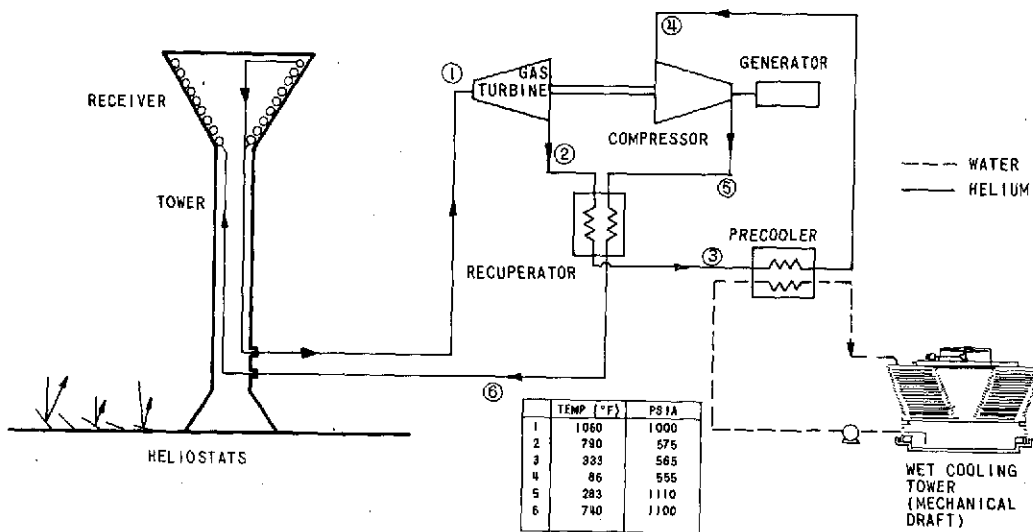
Figure 16. Candidate System Concept Central Receiver -
Closed Brayton Cycle

Central Receiver - Combined Brayton and Rankine Cycles -- One disadvantage to the simple, closed, Brayton cycle is the high temperature of the helium exhausted from the gas turbine. Even after giving up part of its heat in the regenerative heater, the helium temperature is nearly 350°F. This heat is rejected to the atmosphere via the cooling tower. However, if the high-temperature turbine exhaust heat can be utilized, the overall cycle efficiency can be improved.

A combined Brayton and Rankine cycle system meets the above requirements. In this candidate system helium from the turbine exhaust is used to generate superheated steam in a conventional steam generator (Figure 17). The helium then goes to a gas compressor where the pressure is increased to 1110 psia.

	TEMP. F	PSIA
1	1060	1000
2	790	575
3	468	550
4	800	1100
5	355	450
6	750	400
7	120	1.7
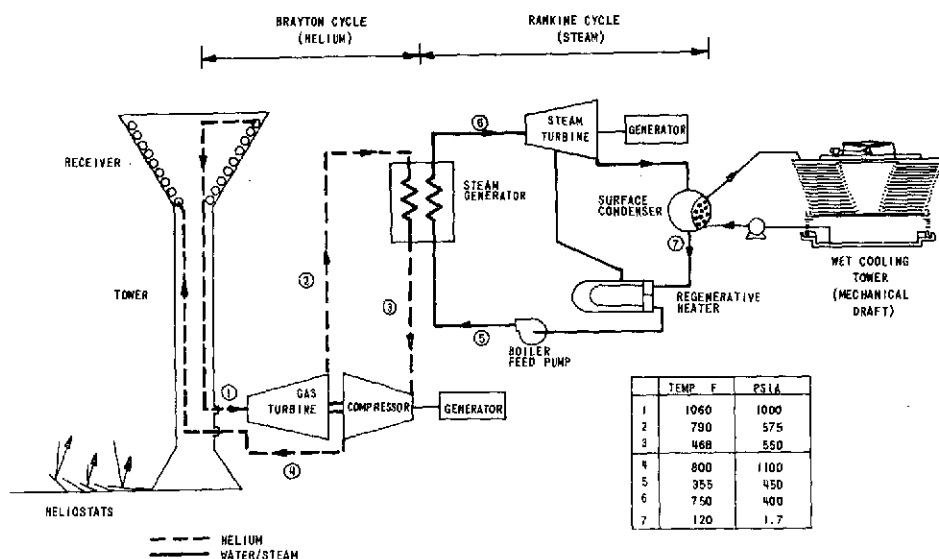
Figure 17. Candidate System Concept Central Receiver - Combined Brayton and Rankine Cycles

Superheated steam at a temperature of 750°F and a pressure of 400 psia enters the high-pressure turbine. A 400/750 turbine is commercially available for use in this cycle. Condensed water at 120°F (dependent on the ambient conditions) is returned to the steam generator. Regenerative heaters are used to raise the temperature of the water returning to the steam generator to 355°F, and a boiler feed pump raises the pressure to 450 psia. Condenser cooling is provided by a mechanical draft, wet cooling tower.

Central Receiver - Liquid Metal Coolant -- The central receiver system with a liquid metal coolant is similar to the dish collector, liquid metal coolant. A molten metal is circulated through the central receiver. Several metals were considered, but sodium

was selected based on its relative cost, heat transport and thermodynamic properties, and the experience gained on the Liquid-Metal-Fast-Breeder-Reactor Program (LMFBR). The design of the key components such as a "hockey-stick" steam generator and sodium pumps has been developed during the LMFBR program.

Superheated steam is generated in the steam generator at a temperature of 950°F and a pressure of 1465 psia (Figure 18). A 1450/950 turbine is commercially available for use in this cycle. Condenser cooling is accomplished using water sent through a mechanical draft, wet cooling tower.

Condensed water from the condenser hotwell is returned to the steam generator. Regenerative heaters are used to raise the temperature of the feedwater from 120°F (dependent on ambient conditions) to 475°F, and a boiler feed pump raises the pressure to 1480 psia.

Central Receiver - Water/Steam Cycle -- The final candidate system analyzed in this study is a central receiver with superheated steam generated directly in the receiver. Water at a temperature of 411°F is introduced into the central receiver, and steam at a temperature of 900°F and a pressure of 915 psia leaves the tower (Figure 19).

Generation of superheated steam directly in the central receiver is a more complicated procedure than generating saturated steam. The design of the receiver will include two separate heat transfer mechanisms, boiling and superheating. Approximately 75 percent of the energy will be used to boil the water and 25 percent for superheat.

Superheated steam enters the turbine, is condensed after expansion, and is preheated in the regenerative feedwater heaters prior to returning to the central receiver. Condenser cooling is provided by a mechanical draft wet cooling tower.

EVALUATION OF CANDIDATE SYSTEMS

Each of the 11 candidate systems presented in the previous subsection were evaluated and compared on the basis of performance and costs. This evaluation is presented in the following paragraphs. Two recommended candidates emerged for further detailed study and design analysis.

Flat Plate Collector System

Introduction -- The concept under consideration in this analysis uses simple flat plate collectors to absorb the solar heat and pressurized water to transport this heat from the solar collectors to a vapor generator. Vapor from the generator is expanded through a condensing turbine to generate electricity. Figure 10 is a schematic of the system concept.

The approach used in this analysis is to determine the number of solar collectors required to generate a given amount of electricity as a function of the temperature of the water both to and from the collector field. Based on these results, it can be shown that the flat plate collector concept is marginal.

With the low temperatures and corresponding low pressures available in the flat plate system (maximum temperature of 300°F), vapor cycles are relatively inefficient for generating power. Both steam and fluorocarbons were considered for use as the working fluid in the turbine. The most desirable fluorocarbon was R-11. The thermal cycle efficiency using R-11 as the working fluid was approximately the same as that for a steam cycle under the same temperature conditions. R-11 was selected for this analysis because of its low specific volume which should result in lower overall costs due to a reduction in the size of the turbine.
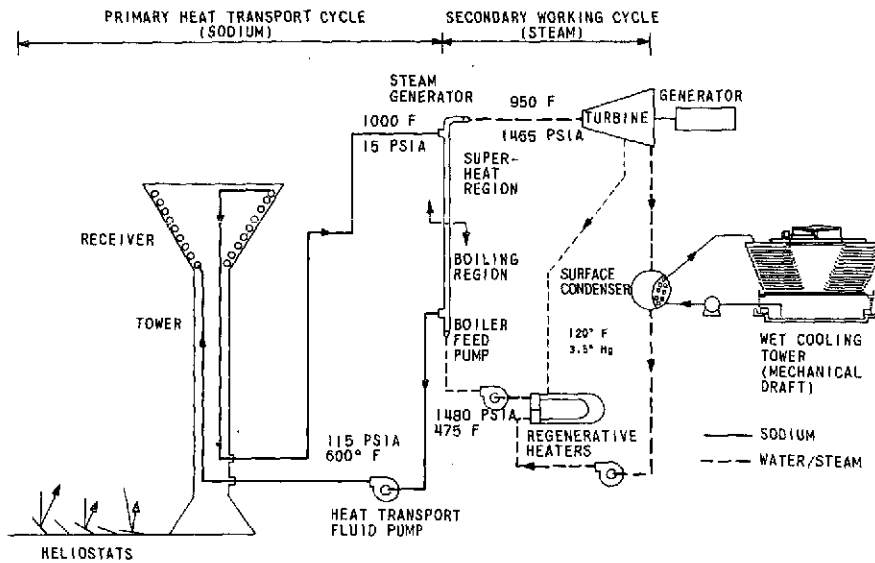
Figure 18. Candidate System Concept Central Receiver -
Liquid Metal Coolant
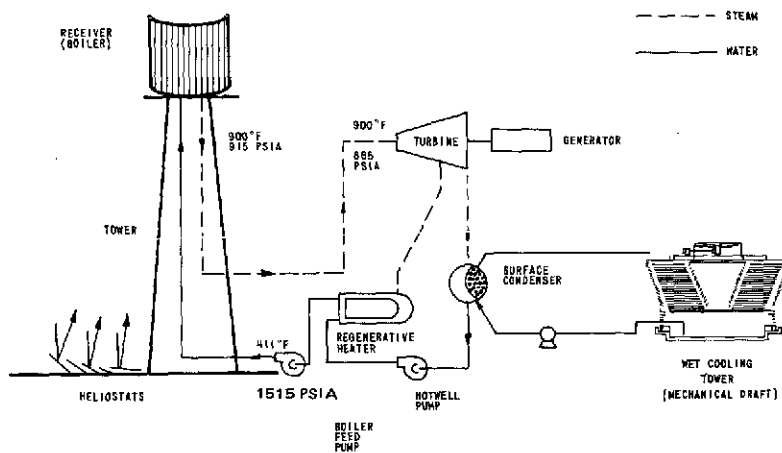
Figure 19. Candidate System Concept Central Receiver -
Water/Steam Cycle

Another advantage of using R-11 as the working fluid in the turbine is that it expands into a dry region, i.e., there is no wetness loss. The wetness loss in steam is generally taken as 1 percent loss of stage efficiency for every 1 percent of water present. Since the terminal wetness is about 12 percent, the average wetness and the associated reduction of output is 6 percent.

Both radial flow (centrifugal) and axial flow turbines can be used with R-11. The turbine design is simple (fewer stages) compared to a steam turbine. Also, higher turbine efficiencies are expected due to the simple design and absence of wetness loss.

System Efficiency -- Two separate efficiencies must be considered in order to determine the overall efficiency of the flat plate collector system. The first of these is the efficiency of the solar collectors. In order to determine the efficiency of the collectors, a thermal performance analysis was done by Honeywell. This computer analysis calculated the thermal performance of a series of 10 flat plate collectors. The collection fluid was assumed to flow in series through the collectors, each unit adding an incremental amount of energy to the fluid. The thermal efficiency was obtained as a function of the temperature of the fluid leaving the last collector, which was varied by altering the flow rate of the heat transport fluid. The pertinent geometrical and environmental conditions are listed in Table IV . Figure 20 shows the details of a typical flat plate solar collector.

An extension of the thermal performance analysis was made to include various values of the temperature of the fluid returning to the first collector. In all cases it was assumed that the incident radiation was 980 watts/meter^2. Results are shown in Figure 21 .

The second factor to be considered is the thermal efficiency of the R-11 turbine cycle. Assuming that there is no heat loss in the vapor generator, the inlet and outlet temperatures of the water are not completely independent. For any given values of T_1 and T_2, the use of a 15°F pinch-point determines the saturation temperature of the R-11 (Figure 22). The pinch-point temperature difference is the driving force for boiling. In all cases it is assumed that $T_4 = 100°F$, which specifies the inlet cooling water temperature to be 70°F or lower.

The thermal cycle efficiency is presented as a function of T_1 and T_2 in Figure 23 . A turbine efficiency of 90 percent, a pump efficiency of 80 percent, and a generator efficiency of 97 percent were used in calculating the cycle efficiency.

Number of Collectors Required -- The number of flat plate collectors required is a function of the combined efficiency of the collectors and the thermal cycle. The overall system efficiency of the flat plate collector system is shown in Figure 24 as a function of the temperature of the fluid both to and from the collector field. Using the overall system efficiencies, the number of collectors required to generate 100,000 kW(e) is shown as a function of T_1 and T_2 in Figure 25 . This set of curves was generated using the following equation:

$$N_c = \frac{100,000 \text{ kW(e)}}{[0.98 \text{ kW(t)}/M^2] (0.3048 \text{ M/ft})^2 (16 \text{ ft}^2/\text{collector}) [\eta \text{ overall kW(e)/kW(t)}]}$$

$$N_c = \frac{68,647}{\eta \text{ overall}}$$

One point that should be noted is that as T_1 decreases to 150°F, the number of required collectors increases.

Table IV . Geometrical and Environmental Conditions Used in the Evaluation of Collector Efficiency

Collector

Length	4 feet
Width	4 feet
Material	Aluminum
Thickness	0.060 inch
Tubes	12 on 4-inch centers
Coating	Selective, $\alpha = 0.90$, $\epsilon = 0.06$
Covers	One, glass, 0.150 inch
Insulation	Fiberglass, 3.0 inches
Fluid	Ethylene - glycol and water, 50/50
Inlet fluid temperature	120°F
Collector tilt angle with horizontal	33 degrees

Ambient

Temperature	70°F
Pressure	1 atmosphere
Wind velocity	10 miles per hour
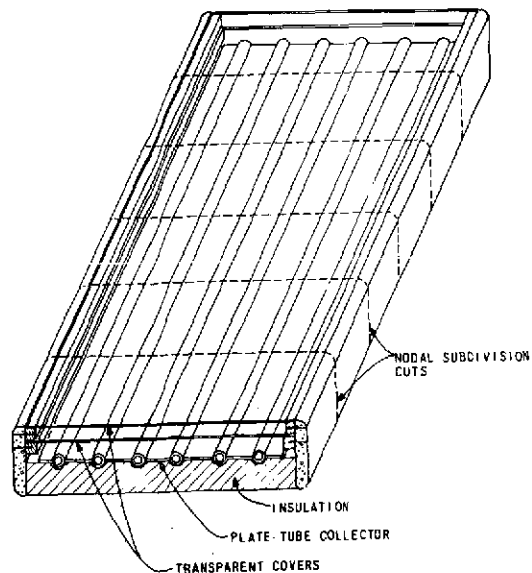
Figure 20. Flat Plate Solar Collector
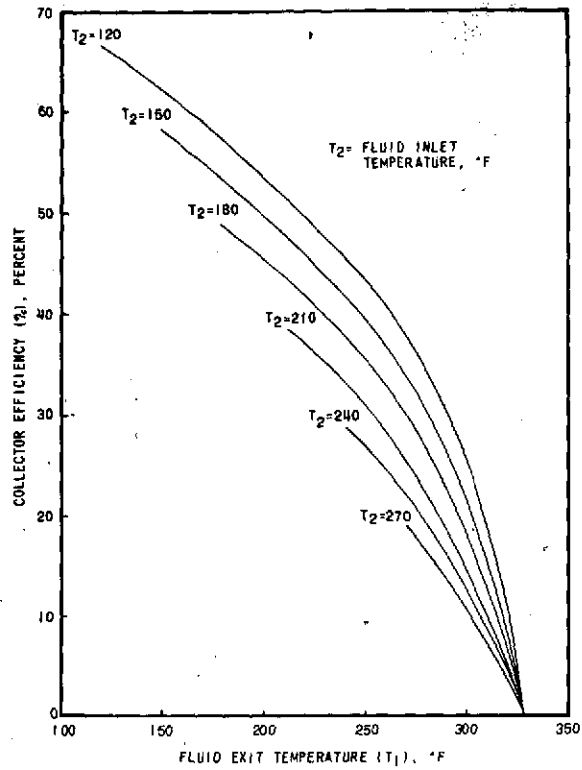
Figure 21. Thermal Efficiency of Flat Plate Collectors as a
Function of Inlet and Outlet Fluid Temperatures
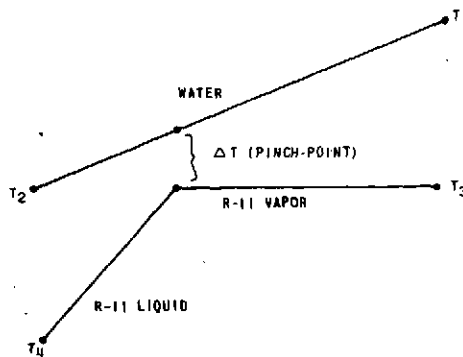
Figure 22. R-11 Vapor Generator Temperature Diagram
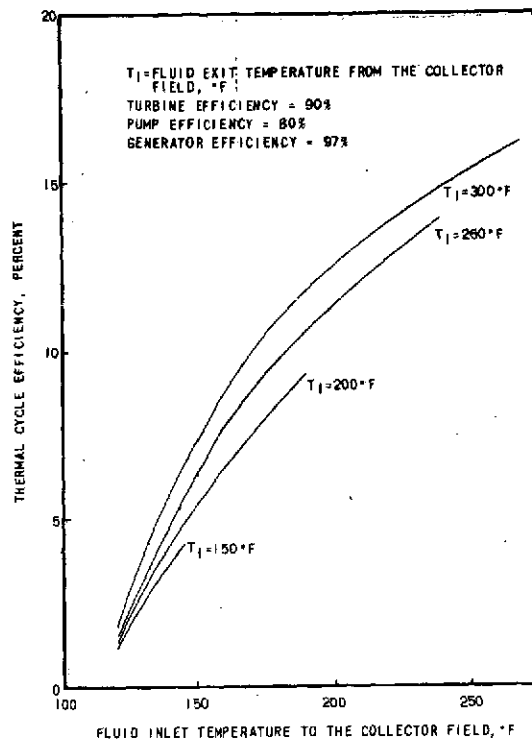
Figure 23. Thermal Cycle Efficiency Using R-11 as the
Working Fluid in the Turbine
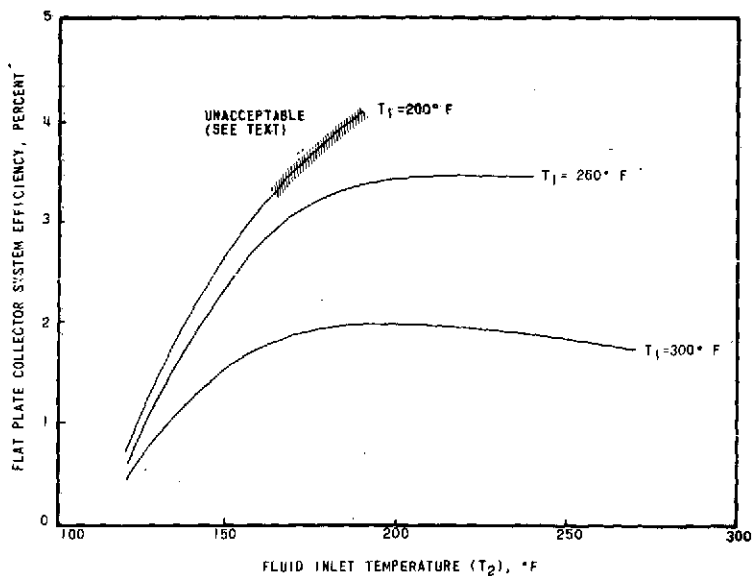
Figure 24. Efficiency of the Flat Plate Collector System as a
Function of Inlet and Outlet Fluid Temperatures

36
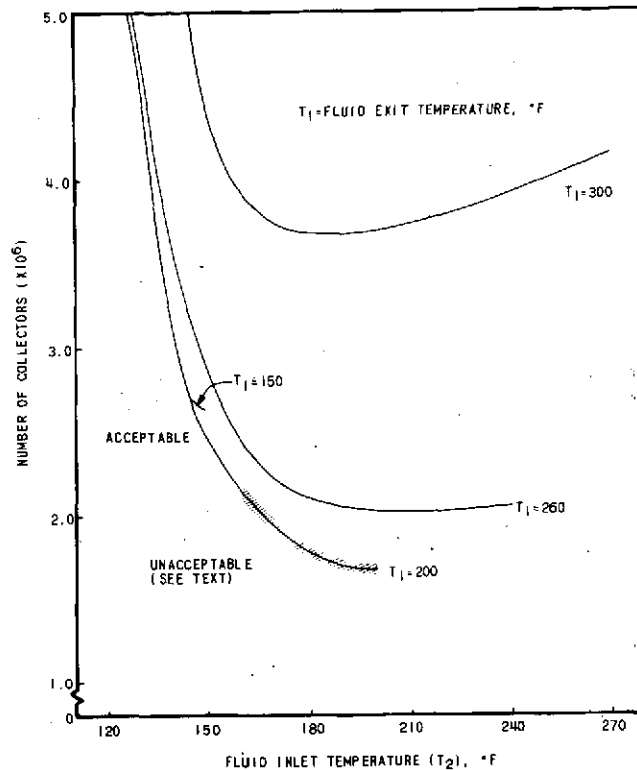
Figure 25. Number of Flat Plate Collectors Required to
Generate 100,000 kw of Electricity

Pressure Limitations -- One additional restraint must be applied to the previous set of
curves. A casual examination of the curves indicates that it would be desirable to set
T_2 = 190°F and let T_1 = 200°F. However, this small ΔT across the collector field would
require an extremely large mass flow rate and, thus, a large pressure drop. Due to the
design of the flat plate collectors, it is unrealistic to allow more than a 30 psi drop across
the collector string. This restriction limits the value of T_2 to 160°F for the case when
T_1 = 200°F. The cross-hatched areas in Figures 24 and 25 have a pressure drop greater
than 30 psi and are therefore unacceptable.

Based on the pressure limitation of 30 psi across the collector string, the minimum
number of flat plate collectors required to generate 100,000 kW(e) is 2.03 x 10^6. This
minimum number of collectors was achieved for the case of the exit fluid temperature
(T_1) at 260°F, and the inlet fluid temperature (T_2) at 210°F.

Conclusions -- The previous discussion has shown that the optimum efficiency of the flat
plate collector system is about 3.5 percent. It is important to note that the maximum
system efficiency did not occur with the maximum fluid exit temperature. This shows that
the decreasing efficiency of the flat plate collector overrides the increasing thermal cycle
efficiency as the fluid temperature increases. Therefore, increasing the surface

temperature of the collectors used in this study would not be beneficial to the overall system efficiency. An increase in the system efficiency can occur only if the collector efficiency can be increased at the higher surface temperature.

All of the results presented in this analysis were based on the following optimistic assumptions:

1. 980 watts/square meter incident radiation

2. 15°F pinch-point temperature

3. T_4 = 100°F (assumes 70°F cooling water)

4. No heat loss anywhere in the system

5. Fluorocarbon turbine efficiency of 90 percent (this is as yet an undesigned piece of equipment)

Whenever any of these assumptions cannot be met, the number of solar collectors required will be increased.

Parabolic Trough Collector Systems

The two types of parabolic collector systems previously selected for evaluation were:

- Heat pipe with pool boiling
- Flow-through receiver with pressurized water

For both systems the collector operating temperature was chosen to be approximately 600°F. Evaluating these system concepts was a part of the overall distributed system concepts evaluation and comparing the parabolic trough with the flat plate and parabolic dish collector fields was included.

As a part of the parabolic trough collector system evaluation, the trough collector was examined in three different orientations:

- East-West, with the tracking/rotating axis aligned East-West
- North-South, with this axis aligned North-South
- Equatorial or polar mount, with the axis aligned North-South but tipped up out of the horizontal by an angle equal to the local latitude. This orients the axis along the earth's spin axis, hence the usage of the term "polar mount"

For each of the trough orientations, the fabrication of the collector is the same. The support differs for the polar-mounted trough collector simply because of the added material required to install the collector at an angle equal to the latitude angle. In terms of cost, this additional support requirement should be negligible and the orientation choice can be made on the basis of performance alone. Sections V and VII contain the collector and collector field performance results which show that the polar trough orientation is best.

Using the polar mount trough collector orientation, the merits of the pool boiling system were compared to those of a pressurized water system. For corresponding temperatures, the pool boiling concept can operate at lower pressures, thus avoiding the heavier equip-

ment required for the pressurized water energy transport system. As discussed in Section VII, this advantage allows less expensive piping to be used so that, if all other things are equal, the energy costs are lower for the pool boiling system than for the pressurized water system. However, the pool boiling system must have a heat pipe and steam generator for every collector in the system. This is more expensive than the flow through receiver pipe and will increase the pool boiling system energy cost to a point where there is some uncertainty as to the best of the two trough systems.

The pool boiling steam generators produce steam at a temperature governed by the local pressure. To maintain an acceptable steam temperature at the turbine inlet, knowledge and control of the pressure at each collector is required. Because the collectors are distributed in a large array, the pressure at each collector differs; the further away the collector is from the pump, the lower the pressure is due to friction losses. In addition, the variable nature of the solar energy input causes different flow rates to be used at different times of operation. This will create variable friction losses and consequent pressure changes at each collector during the day. Control of this system thus involves a feedback control at individual or small groups of collectors everywhere in the field plus a liquid level control at the steam generator and a control at the pumping station.

In comparison, the pressurized water system requires that a temperature-regulated valve controls the flow at individual or small groups of collectors. The pressure may vary over the field as long as it is above the saturation pressure everywhere. The turbine inlet temperature can be controlled by adjusting the heat exchanger mass flow ratio.

For either the pool boiling or pressurized water systems, it is currently judged that thermal storage is desirable for system stability. The order of one-half hour of storage to avoid shutdown during temporary or scattered cloud cover is favored. As discussed in Section VII, thermal storage with the pressurized water system is less expensive than with the pool boiling system.

As a result of the cost of control and storage, a preference for the pressurized water system was developed. A comparison with the flat plate system showed that approximately 40 times more flat plate area than trough aperture area would be required; the flat plate system was eliminated from further consideration. The polar-mount parabolic trough system using pressurized water was then compared to the paraboloid of revolution dish collector system using pressurized water. The economic comparison results are shown in Section VII. If the fabrication and assembly costs of the dish and trough are equal, their respective economic optimums are approximately equal. In choosing a reference for the distribution systems, the dish collector was selected because of the subjective judgment for a potential cost reduction of this collector. Section VI presents the preliminary dish design and the reference system design.

Parabolic Dish Collector Systems

Each of the four candidate dish collector systems was evaluated on the basis of cost and performance. The evaluations are given in the following paragraphs.

Liquid Metal Coolant -- The dish collector with a liquid metal (Na) as the primary loop coolant was designed to generate steam at 900°F and 1465 psia. This necessitates that the heat transport fluid reach the steam generator at a temperature of 950°F (see Figure 13). Taking into account the heat losses as the fluid travels from the solar collectors to the steam generator, it is required that the operating temperature of the solar collector be 1000°F.

The first analysis of this concept led to the use of molten sodium as the heat transport fluid. Because of the corrosive nature of sodium, stainless steel type 316H (ASTM-376) is required for piping. This material is approximately 10 times as expensive as comparable carbon steel pipe. The total length of pipe required for a 100 Mw(e) peak electric generating station which uses sodium as a heat transfer medium is 306,000 feet, assuming a square array. This length is made up of approximately 31,000 feet of 10 inch (average) and 275,000 feet of 3 inch (average) lateral piping. The total, installed cost of this length of carbon steel pipe is approximately $16,000,000 less than for the stainless steel pipe. This appears to be too great a cost penalty to pay for the use of sodium. Yet, it seems desirable to retain the super heated steam cycle and its high efficiency.

One method of reducing the price of this system and making the concept more attractive is to use an alternate heat transport fluid which does not require stainless steel piping. Molten metals, molten salts, and gases are among the feasible alternates.

Alternate molten metals which were considered were NaK, K, Bi, Pb, and tin. NaK and K are just as corrosive as Na, so no advantage is realized. Bi, Pb, and tin all have melting points that are too high. In addition, Hg was considered but the expense and poisonous vapors of this metal eliminate it from serious consideration.

One other possibility in this area is a low melting alloy, probably of bismuth and lead. Cerrobase (55 percent Bi - 45 percent Pb) melts at 255°F. However, due to the high cost of bismuth ($7/lb), Cerrobase costs are in the range of $3-4/lb. This can be compared to $0.17/lb for sodium.

Molten salts which were studied included Therminol-88, OS-124, Dowtherm A, and Hi-tec. None of these except Hi-tec is capable of reaching the desired temperatures. Hi-tec undergoes a slow thermal decomposition according to the following reaction:

$$5 \text{ Na NO}_2 \rightarrow 3 \text{ Na NO}_3 + \text{Na}_2\text{O} + \text{N}_2$$
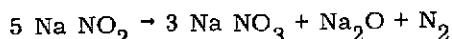
In the range of 850 - 1000°F this reaction is very slow, but at 1500°F the reaction is so rapid that the salt appears to boil. Some question remains as to the rate of reaction between 1000 - 1500°F.

In addition to the decomposition of Hi-tec, it appears that Hi-tec is not compatible with carbon steels. Corrosive attacks on low chromium steels are 0.010 inch per year in a quiescent pool of Hi-tec.

A preliminary search of the available phase diagrams indicates one additional possibility in the molten salt category. A eutectic of KCl (33 percent) and $AlCl_3$ (67 percent) has a melting point of 262°F. This is higher than desired, but still acceptable. A calculation of the equilibrium concentration indicates that the salt should be compatible with carbon steel pipe.

It is not certain that molten salt technology is sufficiently developed to provide large amounts of KCl-$AlCl_3$ salt. Also the corrosive effects of this material on carbon steel have not been experimentally determined. The technology of pumps, valves, etc., would have to be developed before this material could seriously be considered.

Several gases appear to be feasible alternates for use as a heat transport fluid. These include nitrogen, helium, and carbon dioxide, all of which are inert chemically with respect to carbon steel. The main disadvantage of using a vapor as a heat transport fluid is that transferring heat into a vapor requires large surface areas compared to that required for a liquid.

A good heat transport fluid should have a large value for the heat transfer coefficient.

40

In order to compare the heat transport characteristics of the fluids previously discussed, the heat transfer coefficients were calculated for Na, a molten salt, and several gases at varying pressures. The values for the heat transfer coefficients h are given in Table V. Also shown is the heat transfer surface area required to transfer a given amount of heat. Values of the area required are ratioed to the area required using sodium as the heat transport fluid.

Table V. Values for Heat Transfer Coefficients h

Fluid	h $(Btu/hr/ft^2 °F)$	A_s (ft^2)
Sodium	8344	1
$KCl-AlCl_3$*	~ 850	10
Nitrogen: 1000 psia-1000°F	136	61
1500 -1000	189	44
2000 -1000	242	34
Carbon Dioxide:		
1000-1000	188	44
1500-1000	264	32
2000-1000	339	25
Helium: 1000-1000	162	52
1500-1000	216	39
2000-1000	265	31

*Based on pseudo-values for the properties.

Of the gases, carbon dioxide and helium require the least heat transfer surface area.

The collector area available for receiving solar energy in the paraboloid collector system is 420 ft^2. Using a concentration ratio of 400, the surface area of the receiver is 420/400 = 1.05 ft^2.

To determine whether 1 ft^2 is sufficient to transfer the required heat to either carbon dioxide or helium requires some detailed design calculations for the receiver. In particular, the receiver configuration, (e.g., tube geometry), fluid flow rates, temperature rise in the fluid, and surface temperature must be known. Preliminary calculations indicate that about 5 ft^2 may be required for the gases in question.

In addition to the above problems of selecting a suitable heat transfer fluid the high-temperature receiver may not be practical because of the difficulties and cost associated with the energy transport and requisite heat exchanger. Cost estimates indicated that a lower temperature system would be more economically attractive even though the conversion efficiency would be reduced. At a receiver surface temperature of approximately 600°F the heat losses without a protective vacuum jacket are small; consequently, the cost of the jacket can be eliminated in a reduced temperature system. The use of stainless steel pipe and a high-cost steam generator is also eliminated with the lower temperature system.

The general conclusion reached was thus to abandon the dish system with molten metal,

molten salt or gases with a high-temperature receiver. In its place, systems with water or steam as the heat transport fluid and receiver temperatures of approximately 600°F were designed.

Saturated Steam -- This system is identical to the parabolic trough system with pool boiling, the trough collectors simply replaced by the dish collector. In the dish collector no heat pipe is present and a circulating pump must be used in its place. Because of the added complexity and expense of the pumps, the dish pool boiling system was not considered a practical candidate. Further, for the same reasons as discussed earlier in this section, the pressurized water system is preferred over the pool boiling system.

Pressurized Water -- The dish collector system using pressurized water as described in this section is evaluated in terms of performance in Sections V and VI and energy cost in Section VII. This concept was the most economically attractive of the distributed systems and was selected for a distributed system reference design as presented in Section X.

Superheated Steam -- The generation of superheated steam in the field, while technically feasible, is a difficult design problem. It appears less economically attractive than the pressurized water system because the increased cycle efficiency does not pay for the added cost of circulating pumps piping and insulation.

Central Receiver Heat Transfer/Prime Mover Cycle

Four different cycles were chosen for evaluation in a central receiver generating plant. They are:

1. Closed Helium Brayton Cycle (Figure 16)

2. Combined Helium Brayton/Steam Rankine Cycle (Figure 17)

3. Liquid Sodium/Steam Rankine Cycle (Figure 18)

4. Conventional Steam Rankine Cycle (Figure 19)

All four of these cycles are feasible in that electrical power could be generated in a central receiver plant utilizing any one of these cycles. A comparison of these cycles was, therefore, based on the cost of generating this electrical power. This comparison included calculations of both the plant efficiency and the plant capital cost.

As will be discussed subsequently, the tube-type receiver is the most advantageous. The analyses of these four cycles were all based on a central receiver in which the fluid flowed through a number of tubes in parallel.

Closed Helium Brayton Cycle -- For a central receiver plant, using a closed helium Brayton cycle, the cycle efficiency is strongly dependent on the helium turbine throttle temperature and the helium pressure drop in the riser, receiver, and downcomer. This is shown in Figure 26. This temperature and pressure drop depend on the incident flux, tube dimensions, and helium velocity. A computer program was written to analyze the heat transfer and fluid dynamics of helium in irradiated tubes. The variation of tube skin temperature with helium outlet temperature for various fluxes and velocities is shown in Figure 27. The pressure drop through the receiver for these fluxes and velocities is shown in Figure 28.

The most suitable tube material is Inconel 625, which can be operated with a skin temperature of about 1600°F at the required pressures. No tube material was found which would permit a higher operating temperature. The pressure drop in the tower includes the drops in the riser, the receiver, and the downcomer. An engineering decision was
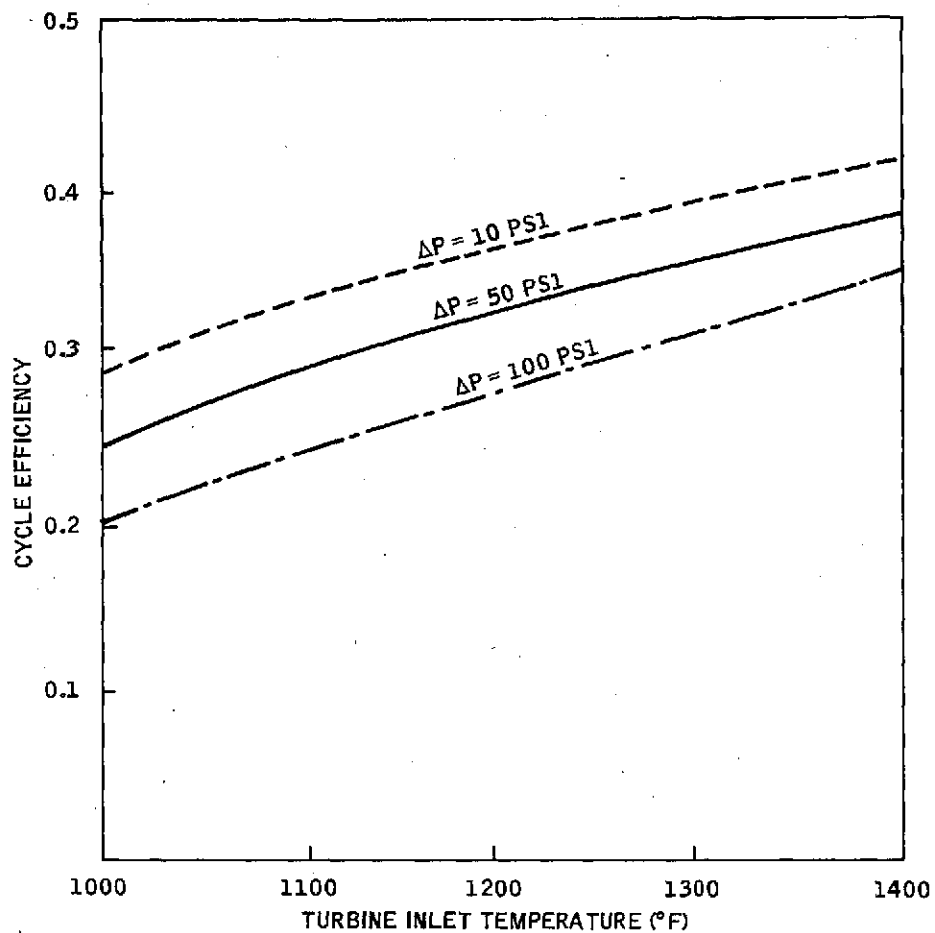
Figure 26. Optimum Brayton Cycle Efficiency as a Function of the Turbine Inlet Helium Temperature and the Pressure Drop across the Receiver with Wet Cooling Towers and 75°F Air
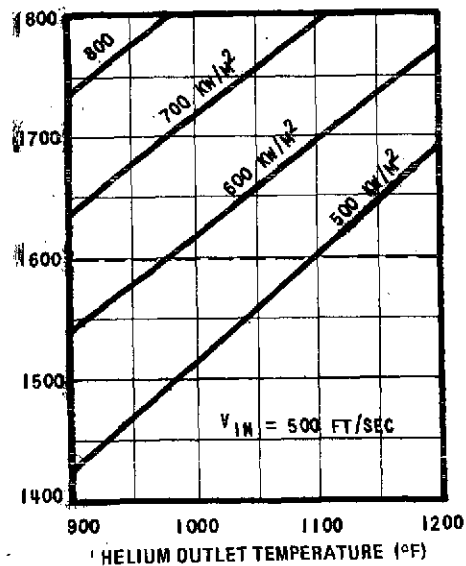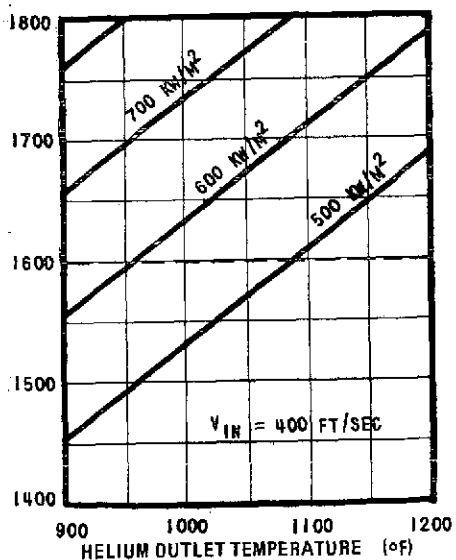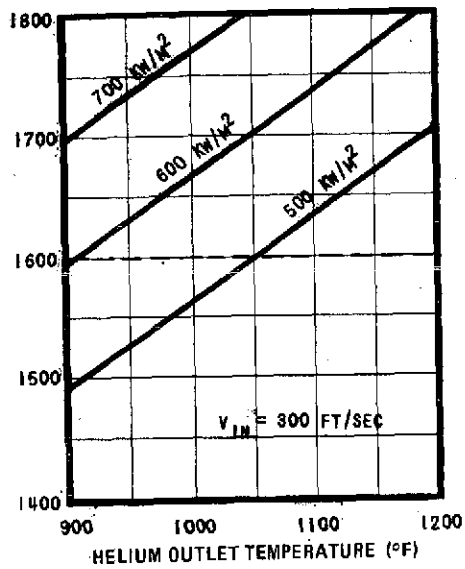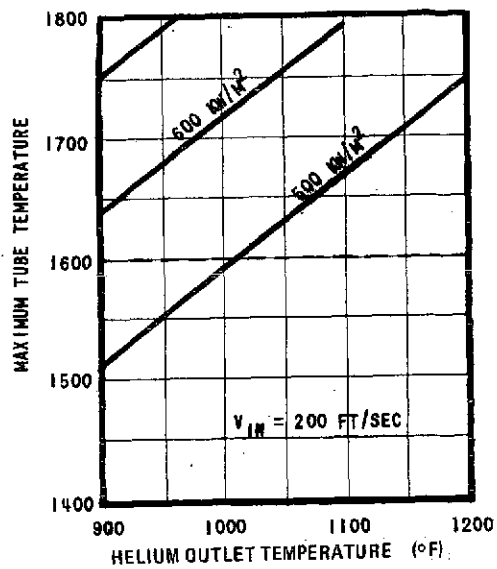
Figure 27. Variation of Skin Temperature with Helium Outlet
Temperature for Various Incident Radiation
Intensities and Fluid Velocities
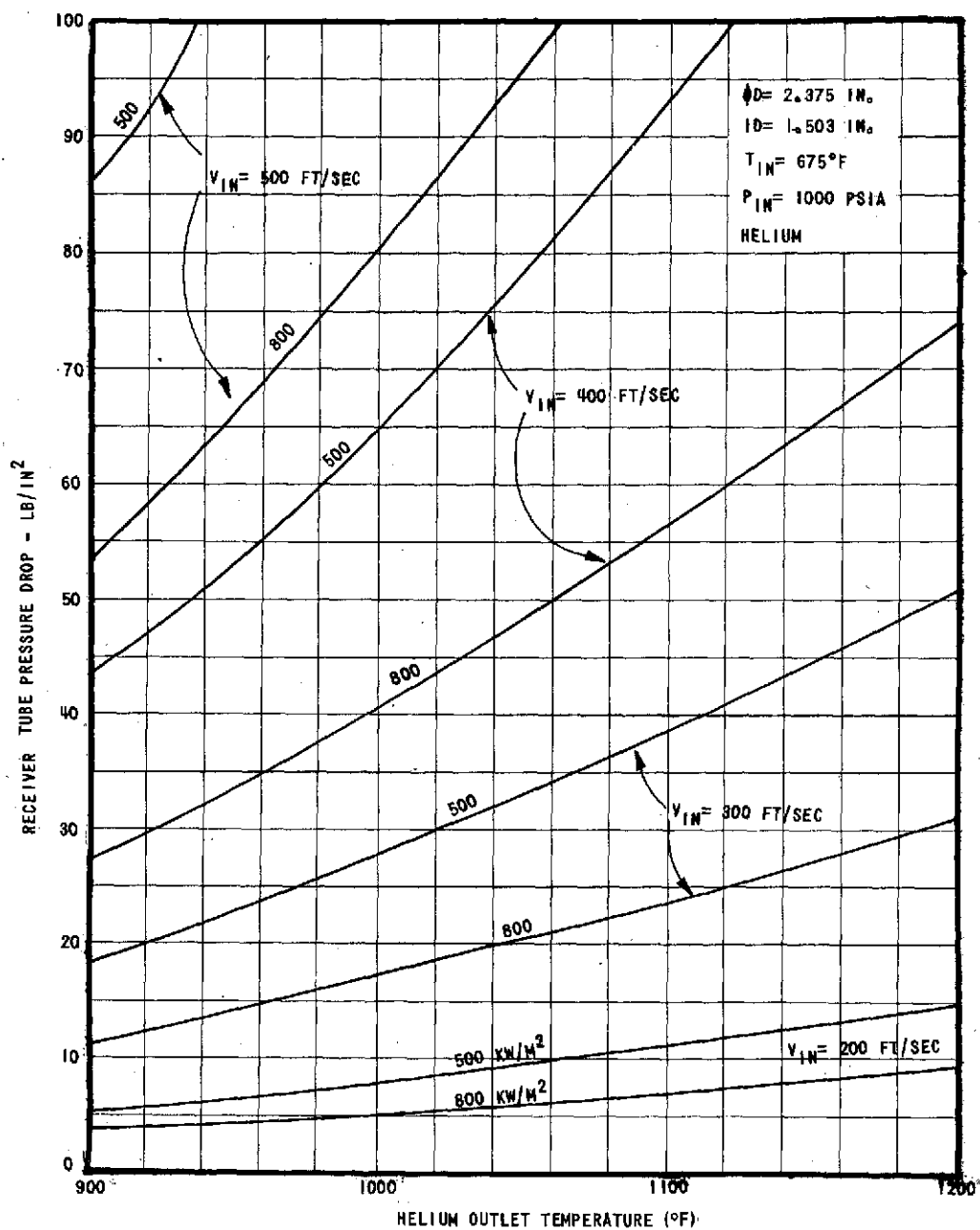
Figure 28. Receiver Tube Pressure Drop versus Helium Outlet
Temperature for Several Incident Radiation Intensities
and Fluid Velocities

made to limit the pressure drop in the riser, receiver, and downcomer to 100 psi and the pressure drop in the receiver to 50 psi. A detailed calculation of the pressure drops in the riser and downcomer is not possible because the design of the components must be based on plant economics which requires prior knowledge of cycle efficiency and the overall cost of power. The use of a 50 psi drop in the riser and downcomer is considered a good estimate.

With the above limitation in skin temperature and receiver pressure drop, an analysis of Figures 26, 27, and 28 shows that the highest obtainable cycle efficiency is about 23 percent with a helium temperature of 1060°F, a flux of 500 kw/m^2, and a velocity of about 300 feet/second. It should be noted that use of a dry cooling tower reduces the efficiency to 18 percent.

Two methods of obtaining higher helium outlet temperatures have been considered, the use of rifled tubes and the use of internally-finned tubes. Both of these tube types are commercially available in a wide range of materials and sizes.

The rifled tube has the advantage of creating a high degree of turbulence inside the tube. This leads to higher convective coefficients and smaller temperature drops between the tube wall and the bulk fluid. However, because of the high helium velocities being used, 200 to 300 feet per second, the flow is already highly turbulent. It is not anticipated that any significant advantage would result from the use of rifled tubes.

An internally-finned tube provides a larger surface area for heat transfer. This reduces the temperature drop across the fluid boundary layer and reduces the tube skin temperature. However, the added surface area also increases pressure drop per unit length of tubing. In the Brayton cycle this pressure drop has a far more significant effect on cycle efficiency than in conventional Rankine cycle boiler design. A preliminary analysis has indicated that the use of internally-finned tubes does not lead to a cycle efficiency which approaches that cycle efficiency which can be obtained from a conventional superheated steam cycle.

Since the capital costs associated with a helium Brayton cycle are greater than the costs for a conventional cycle, the helium Brayton cycle was rejected.

Combined Helium Brayton/Steam Rankine Cycle -- This combined cycle is superior to the Brayton cycle when the high helium exhaust temperature justifies the cost of a heat exchanger and of the Rankine cycle equipment. With maximum helium temperature of only 1060°F, as calculated previously, these costs are not justified. Therefore, this combined cycle was rejected.

Liquid Sodium/Steam Rankine Cycle -- Because liquid sodium has a corrosive effect on tube materials and because this effect is accelerated at elevated temperatures, a limiting design criterion is the sodium-tube interface temperature. With type 316 stainless steel as the tube material, this interface temperature can be about 1200°F. No tube material was found which permitted a higher interface temperature. A computer program was written to analyze the heat transfer and fluid dynamics of liquid sodium flowing in irradiated tubes. The variation of tube skin temperature with maximum sodium temperature for various fluxes and velocities is shown in Figure 29 . The pressure drop through the receiver for these fluxes and velocities is shown in Figure 30 . Examination of these two figures shows that the interface temperature is the limiting criterion.

Based on the heat exchanger technology developed in the LMFBR program, the highest temperature steam which can be economically generated from 1200°F sodium is about 950°F at 1450 psig. The capital cost associated with this sodium/steam cycle will be larger than that
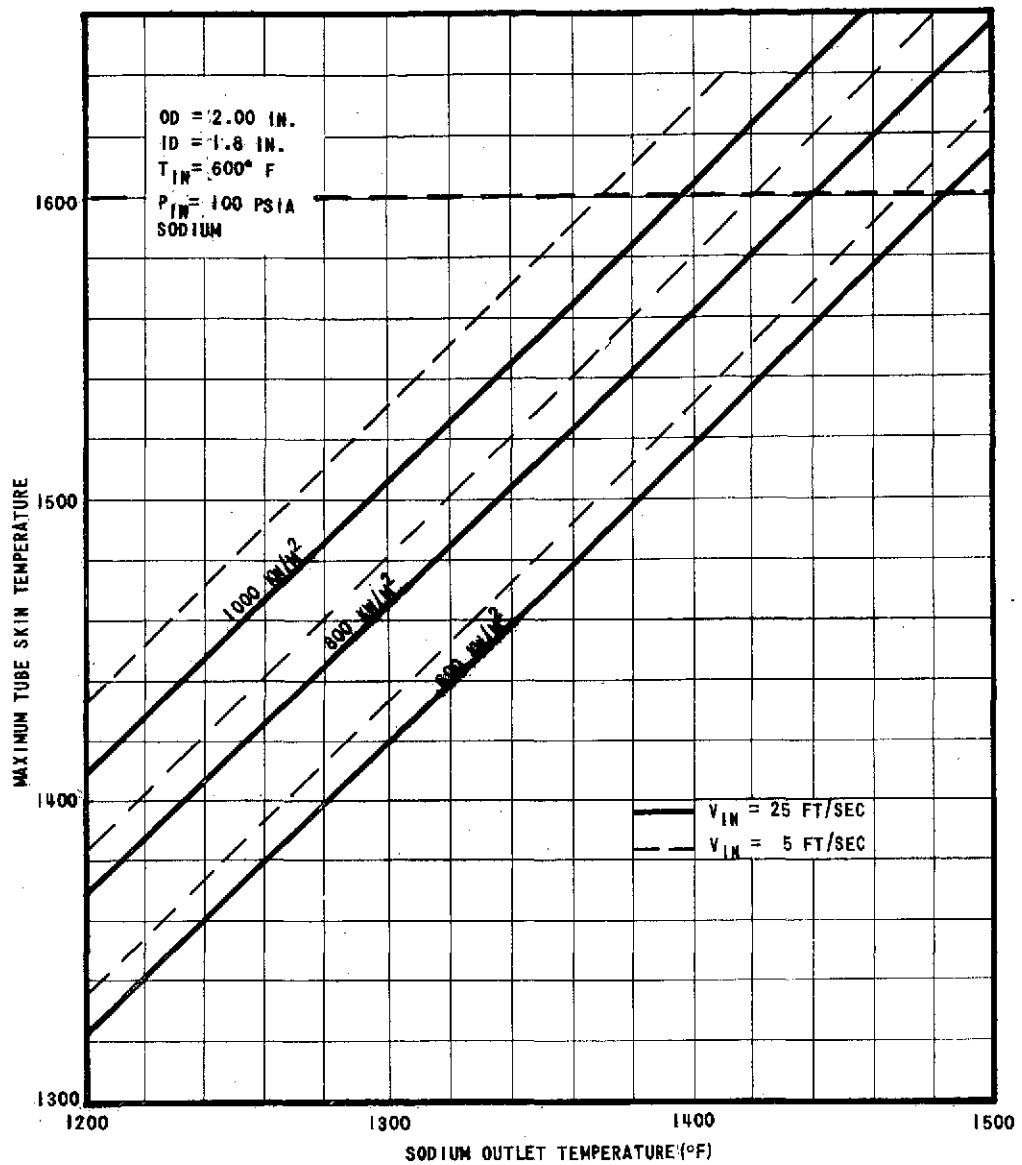
Figure 29. Variation of Skin Temperature with Sodium Outlet
Temperature for Various Incident Radiation
Intensities and Fluid Velocities
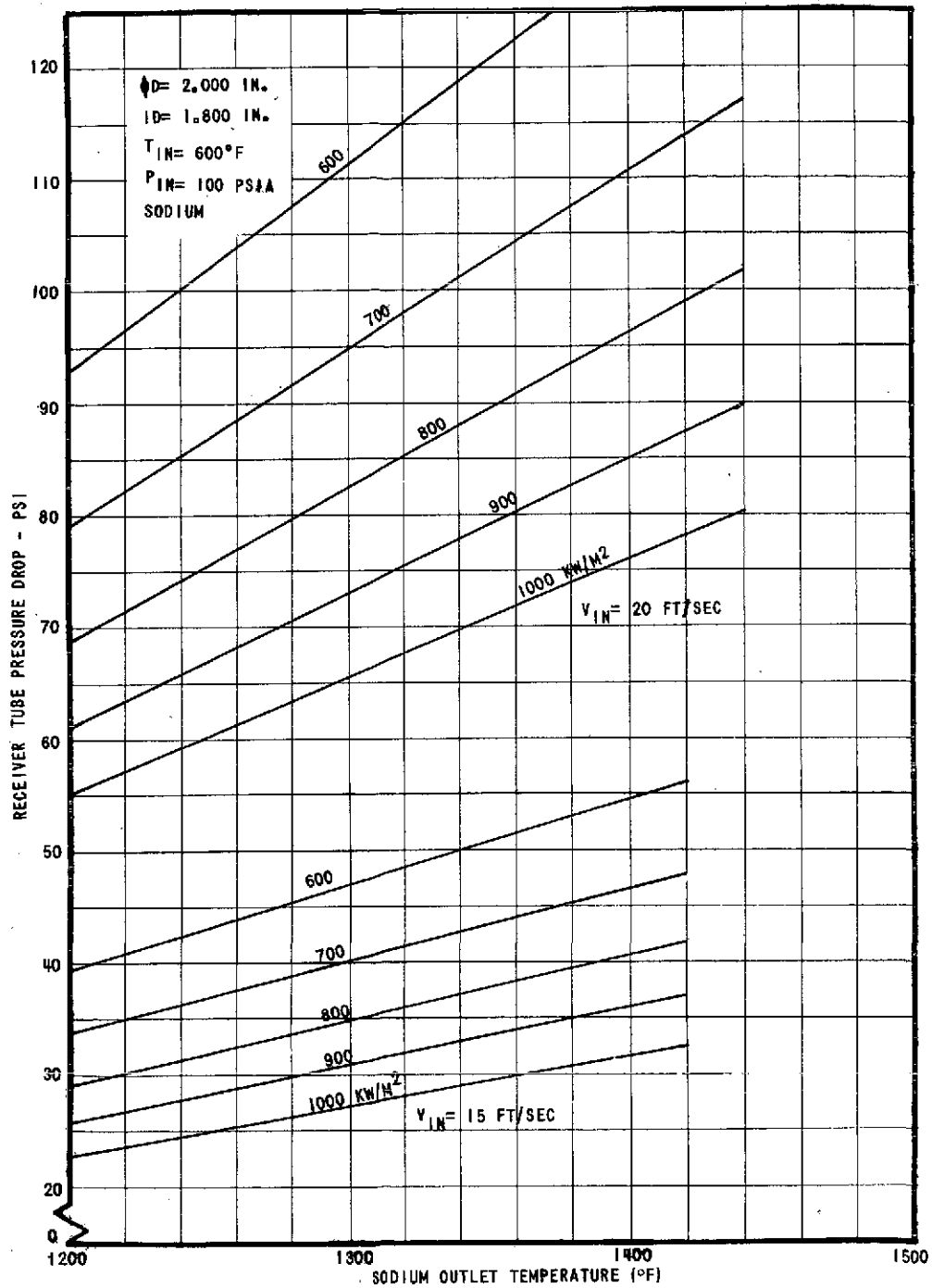
Figure 30. Receiver Tube Pressure Drop versus Sodium Outlet
Temperature for Various Incident Radiation Intensities
and Fluid Velocities

for a conventional steam cycle because of the high cost of the sodium/steam generator, sodium pump, and stainless steel riser and downcomer.* Therefore, the liquid metal/steam cycle was rejected.

Conventional Steam Rankine Cycle -- Four steam cycles were considered for use in a central receiver generating plant. They are:

1. 400 psig/750°F
2. 600/825
3. 850/900
4. 1250/950

The 1250/950 cycle was rejected because the higher pressure requires thicker receiver tubes which lead to a tube skin temperature in excess of design limitations.

The 400/750 cycle was rejected because of the lack of availability of prime movers in the 60 to 200 MW range.

The 850/900 cycle was selected over the 600/825 cycle because the cycle efficiency is greater.

As will be discussed in Section VI, the best design for a water/steam receiver is the tube type with a crescent geometry. A computer program was written to analyze the heat transfer and fluid dynamics of water-steam flow through this receiver. The Honeywell ray-trace code was used to obtain flux maps for this receiver geometry. By iterating the ray-trace code with this receiver design code, a suitable receiver was designed. The design parameters are presented in Section X.

Recommended Candidates for Design Studies

The evaluation of candidate system concepts described in the preceding paragraphs leads to the recommendation of two candidates for detailed design analysis and study:

1. Dish Collector with pressurized water in the primary heat transport loop and a secondary loop with steam Rankine cycle

2. Central Receiver with water-steam Rankine cycle

The design and cost analysis of the major systems required for each of these recommended solar/electric generating plant concepts is given in Sections V through IX.

---

*For a detailed account of the design and costs of the liquid sodium central receiver, see Monthly Technical Progress Narrative Nos. 6 and 7, dated 15 March and 15 April 1974. Contract No. NAS3-18014.

SECTION V

COLLECTOR/CONCENTRATOR PERFORMANCE STUDIES

There are two fundamental characteristics of solar energy collecting systems on or near the planetary surface: concentration of the solar flux; and tracking of the sun. Therefore, a number of design options are possible for mechanizing these two characteristics:

Concentration	Tracking
low	none
medium	one axis
high	two axes

Several combinations of these six elements have been investigated. Three of these combinations can represent typical collector performance families:

- Flat plate (low concentration and no tracking)

- Parabolic trough (medium concentration and single-axis tracking)

- Paraboloid of revolution dish and "power tower" (high concentration and two-axis tracking)

Designs different from the above three, such as Fresnel mirrors or lenses instead of the parabolic trough, have performance penalties.

The system constraint of the dynamic conversion of solar generated heat to electricity on the power-plant scale provides for further differentiation of the three families into two classes:

- Distributed systems (flat plate, parabolic trough and paraboloid of revolution dish collector)

- Central receiver systems (power tower)

DISTRIBUTED SYSTEMS

Methodology

The objective of the analytical work and the associated simulation effort in the study of all three distributive systems was the formulation of generalized optical-thermal performance statements.

The work was facilitated by the existing computer codes, which simulated both the flat-plate solar collectors and the parabolic trough systems. These codes have been extensively documented previously (References 4 and 5).

The parabolic trough code was evolutionary in this study because it had been developed to employ Monte Carlo ray trace simulation techniques, while the flat plate collector code had been written as a closed-form analytical tool. The experience gained in developing the parabolic trough code and the ease with which the exercise of this code produced meaningful physical insights led to the adaption of the ray trace technique for the paraboloid of revolution dish collector simulation code (HELIAKI III).

The system that is mathematically modeled in this code consists of a paraboloid of revolution circular mirror mounted on a two-axis, gimbaled tracking system and a fixed hemispherical receiver.

This receiver can be optionally contained within a "bell jar" glass envelope with vacuum between the receiver and the inner glass surface (Figure 31).

As required with the Monte Carlo technique, the optical performance of the system was formulated as an integration problem.

To examine the problem, first consider the perfect optics case, and then generalize the results for finite quality optics.

The amount of energy carried from any point on the sun's surface to any point on the heat receiver's surface depends on the exact path of the ray through the optical interfaces on the collector. The mirror reflectance and glass envelope transmittance are functions of both the wavelength of the light in the ray and the incident angle of the ray on the glass or mirror surface. The receiver surface can be given a flat 90-percent absorptance at all wavelength and incidence angles.

The angle any ray makes with respect to each optical interface is a function only of the angular position on the solar disk whence the ray came (two dimensional) and the impact point on the collector aperture plane (two dimensional). Thus, for any wavelength and perfect optics, the energy carried from the sun to the receiver surface can be found by specifying the four coordinates of the ray, no matter how many optical elements there are in the optics train.

If the angular position coordinate on the sun disk are δ_1 and δ_2 and the impact point coordinates on the test plane are X_1 and X_2, then the total thermal power absorbed at wavelength interval $d\lambda$ is

$$E_{d\lambda} = \int_{X_1} \int_{X_2} \int_{\delta_1} \int_{\delta_2} E(X_1, X_2, \delta_1, \delta_2,) \, dX_1 dX_2 \, d\delta_1 d\delta_2 \tag{1}$$

The function $E(X_1, X_2, \delta_1, \delta_2, \lambda)$ is a complex ray trace subroutine that performs all vector algebra necessary to trace the ray defined by $(X_1, X_2, \delta_1, \delta_2)$ through the optical surfaces up to the receiver. The units of E are thermal power absorbed per unit angular area on the sun's disk, per unit spacial area on the aperture disk, and per unit wavelength at the wavelength interval, $d\lambda$. This math model simulates the AIR MASS II spectrum, as published by Cambridge Research Institute. To get the energy from the entire spectrum we must integrate over all wavelengths to yield

$$E_p = \overbrace{\int_\lambda \underbrace{\int_{X_1} \int_{X_2}}_{\text{aperture}}}^{\text{Total spectrum}} \overbrace{\int_\delta \int_{\delta_2}}^{\text{sun disk}} E(X_1, X_2, \delta_1, \delta_2, \lambda) \, dX_1 \, dX_2 \, d\delta_1 \, d\delta_2 \, d \tag{2}$$

The wavelength integral is indefinite. That is, the limits are from 0 to positive infinity. In practice, this integral is performed by partitioning the spectrum into 20 equal energy bands.

Introducing finite quality optics into the model shows that the uncertainty in tracking accuracy and mirror quality will be known only statistically.

There are four such statistically uncertain optical parameters. The first two parameters are uncertainties in the angular position of the two-gimbaled tracking drives (θ_1, θ_2). The second two parameters are the angular uncertainties in the mirror surface normal at any point on the mirror surface (ϕ_1, ϕ_2). Each of these four parameters is statistically independent of each other, or any other design parameter. For example, a given error in the mirror normal is as likely anywhere on the mirror surface. The mirror is not modeled as a continuous surface with smooth waves or ripples, but rather as a probability distribution
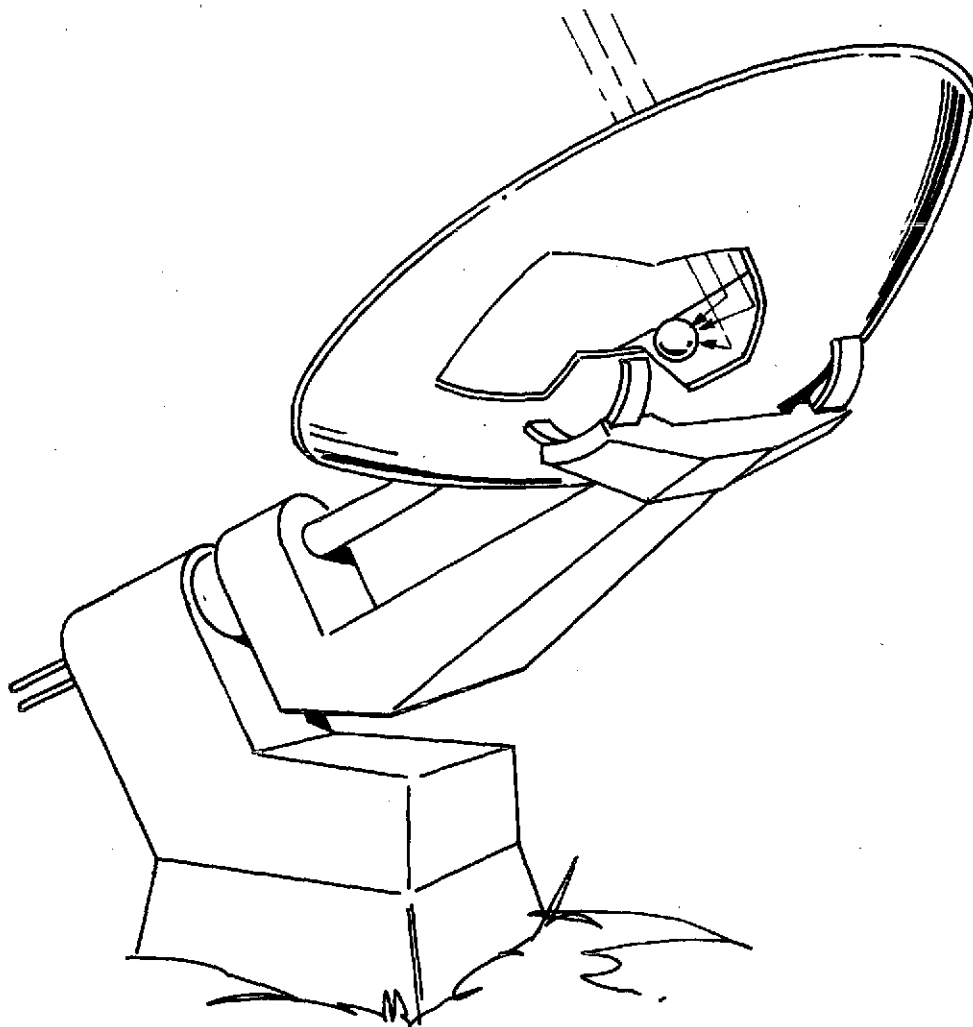
Figure 31. Dish Collector (Two-Axis Tracking
Paraboloid-of-Revolution)

of mirror normals perturbed from the mathematically correct shape by an assumed probability distribution. For each statistically known variable, the distribution is understood to be a "normal" or "standard error" distribution.

Now, consider a random variable, Z, defined by the normalized probability distribution P(Z). If we wished to calculate the mean value of $Z(=\bar{Z})$ or its expected value, we would form the integral of the product of P(Z) times Z over all allowed values of Z, e.e.,

$$Z = \int_{-\infty}^{\infty} P(Z) \, Z dZ. \tag{3}$$

To simulate a specific error set $(\theta_1, \theta_2, \phi_1, \phi_2)$, one would have to evaluate the integral:

$$\bar{E}_p(\theta_1, \theta_2, \phi_1, \phi_2) = \int_\lambda \int_{X_1} \int_{X_2} \int_{\delta_1} \int_{\delta_2} E(X_1, X_2, \delta_1, \delta_2, \lambda, \theta_1, \theta_2, \phi_1, \phi_2) dX_1 dX_2 d\delta_1 d\delta_2 d\lambda \tag{4}$$

If this is the thermal power absorbed for a given error set, then the expected value of the thermal power absorbed $(\bar{E}_p)$ is given by

$$\bar{E}_p = \int_{\theta_1} \int_{\theta_2} \int_{\phi_1} \int_{\phi_2} P_{\theta_1}(\theta_1) P_{\theta_2}(\theta_2) P_{\phi_1}(\phi_1) P_{\phi_2}(\phi_2) E_p(\theta_1, \theta_2, \phi_1, \phi_2) d\theta_1 d\theta_2 d\phi_1 d\phi_2 \tag{5}$$

because each distribution is statistically independent. Substituting E_p by the right-hand side of Equation (4) results in:

$$\bar{E}_p = \underbrace{\int_{\theta_1} \int_{\theta_2}}_{\substack{\text{tracking}\\\text{errors}}} \underbrace{\int_{\phi_1} \int_{\phi_2}}_{\substack{\text{mirror}\\\text{imperfections}}} P_{\theta_1} P_{\theta_2} P_{\phi_1} P_{\phi_2} \underbrace{\int_\lambda}_{\substack{\text{total}\\\text{spectrum}}} \overbrace{\int_{X_1} \int_{X_2}}^{\text{collector}}_{\text{aperture}} \underbrace{\int_{\delta_1} \int_{\delta_2}}_{\substack{\text{sun}\\\text{disk}}} E \, d\delta_2 \, d\delta_1 \, dX_2 \, dX_1 \, d\lambda d\phi_2 \, d\phi_1 \, d\theta_2 \, d\theta_1 \tag{6}$$

The Monte Carlo ray trace code evaluates this nine integral for the parabolic of revolution collector. The core of the analysis routine is a subroutine that evaluates the parameter E:

$$E = E(X_1, X_2, \delta_1, \delta_2, \lambda, \theta_1, \theta_2, \phi_1, \phi_2) \tag{7}$$

This subroutine performs the necessary vector algebra to find all the losses at each optical interface and to return the parameter E. (A detailed description of the vector algebra is given in Appendix B.)

COLLECTOR PERFORMANCE

Flat Plate Collectors

The thermal performance of a series of 10 flat plate collectors was calculated using the Honeywell Flat-Plate Collector Computer Program (Reference 4). The collection fluid was assumed to flow in series through the collectors, each unit adding an incremental amount of energy to the fluid. The thermal efficiency was obtained as a function of the temperature of the fluid leaving the last collector. The fluid exit temperature was varied by changing the flow rate of collection fluid. The pertinent geometrical and environmental conditions are listed in Table VI.

Table VI. Geometrical and Environmental Conditions

Collector

   Length: 4 feet

   Width: 4 feet

   Material: Aluminum

   Thickness: 0.060 inch

   Tubes: 12 on 4-inch centers

   Coating: Selective, $\alpha = 0.90$, $\epsilon = 0.06$

   Covers: One, glass, 0.150 inch

   Insulation: Fiberglass, 3.0 inches

   Fluid: Ethylene - glycol and water, 50/50

   Inlet fluid temperature: 120 degrees Fahrenheit

   Collector tilt angle with horizontal: 33 degrees

Ambient

   Temperature: 70 degrees Fahrenheit

   Pressure: 1.013 bar

   Wind velocity: 10 miles per hour

Results of the calculations are presented in Figure 32 . The thermal efficiency was defined as:

$$\eta = \frac{\text{rate of heat transport to storage}}{\text{solar flux incident on the collector}}$$

Efficiency varied from 66 percent at a fluid exit temperature of 125°F to zero at 325°F. The nonlinear behavior is due to the fact that the external heat loss by radiation is nonlinear.

Parabolic Trough Collectors

In previous work the optimal concentration ratio for a trough collector operating at 572°F (300°C) was found. To assess performance of this collector over a range of operating temperatures, recall that the absorbed thermal power is not a function of the receiver temperature. Therefore, one can use the absorbed thermal power at the optimal concentration ratio and assume a thermal power loss rate appropriate to any value of interest over a wide range of temperatures.

54
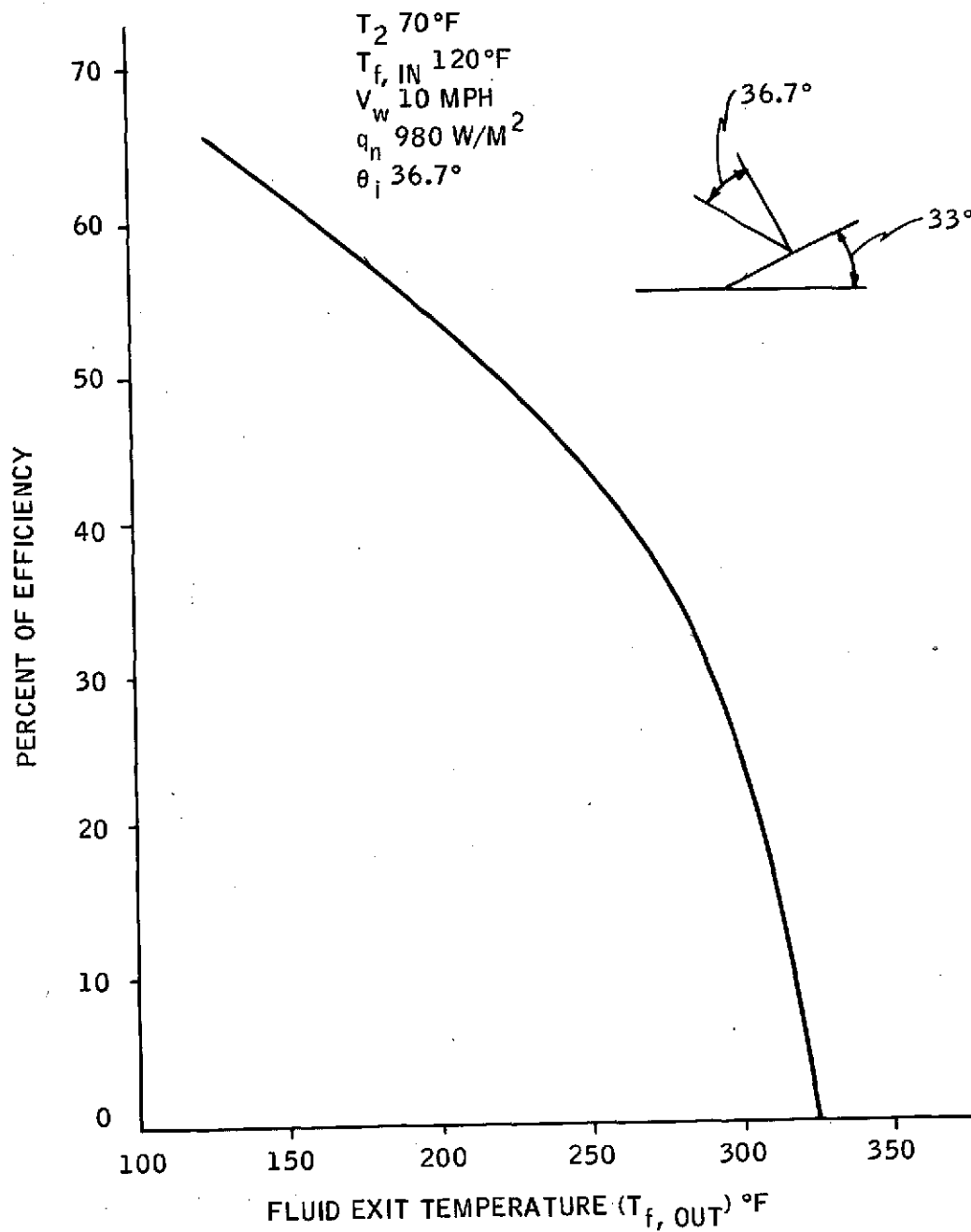
Figure 32. Thermal Efficiency of a Series of Ten Flat Plate Collectors

For the trough collector, the collection efficiency versus operating temperature is plotted in Figure 33. The numerator of the efficiency ratio is absorbed thermal power at the concentration ratio for 300°C minus lost thermal power appropriate to that concentration ratio and the receiver temperature on the ordinate. The denominator of the efficiency ratio is the direct normal power flux through the aperture plane.

The vertical line marked "selective coating limit" in Figure 33 indicates a current estimate of the upper temperature limit at which the AMA selective coating can be used for 20 years without degradation. If a flat black coating ($\varepsilon = 0.9$) were used with the low concentration ratios available with the trough, the collection efficiency would roll off drastically before the upper limit on the selective coating was reached. Obtainable concentration ratios are much higher for the dish collector system than for the trough collector (approximately the square of the trough collector concentration ratio).

If a selective coating material could be found to operate at high temperatures, it would not raise the performance of the trough system by more than 5 to 10 percent. Most losses that affect the efficiency are combined effects of the reflectance of the mirror (nominally 0.85), transmittance of the glass envelope (nominally 0.9), and absorptance of the receiver surface (0.90), which, combined, yield 0.69.

Further work resulted in calculating the optimal concentration ratio at each temperature (Figures 34 and 35). These curves were in turn used to calculate the truly optimal efficiency at each temperature. Results are shown in Figures 36 and 37. The denominator of the efficiency ratio is the direct normal flux of thermal power through the aperture plane. The optimal curve, Selective Coating, in Figure 36, is tangent to the curve in Figure 33 at the 300°C point because both plots represent the optimal design at 300°C. The new curve has somewhat higher efficiency at higher and lower temperatures.

The important point here is that the optimal curves show that a collector with a flat black receiver coating has much better efficiency at high temperatures than would have been concluded from the previous suboptimal results. Another important point is that the trough concept with a good mirror and a high-temperature selective coating (not now in existence) could be used with a 1000°F receiver temperature at 50 percent absorption efficiency.

The lower temperature end of the curve is also of interest. Note that even the 1/2° rms slope uncertainty with a flat black receiver has a collection efficiency of over 60 percent at 300°F. The 1/2° rms slope mirror is a very poor mirror.

In previous work (Reference 5) results were presented of a set of ray trace runs for the trough collector at one-hour intervals for one day (daylight hours) each month, around the year. These results were daily variations of collected thermal power (Figures 38 through 45) and daily total collected energy versus time of year (Figure 46). This time-varying presentation of the information has considerable appeal. However, the power industry uses another format which is quite useful, the load duration curves.

Examples of this type of curve are shown in Figures 47 and 48. The dashed line across the bottom of each figure represents the thermal power lost when the receiver is at its design point temperature. The total thermal energy collected in one year is the integral of the difference between the absorbed energy curve and the loss line. Also presented on each curve is the thermal power absorbed per unit aperture area and per unit mirror surface area.

The data presented in both figures are for unshadowed collectors with the solar energy flux from the Cambridge Research Center clear air (no clouds) model.

The total integrated thermal energy collected for each configuration is shown in Table VII. This is the area between the loss line and the absorbed power curve.
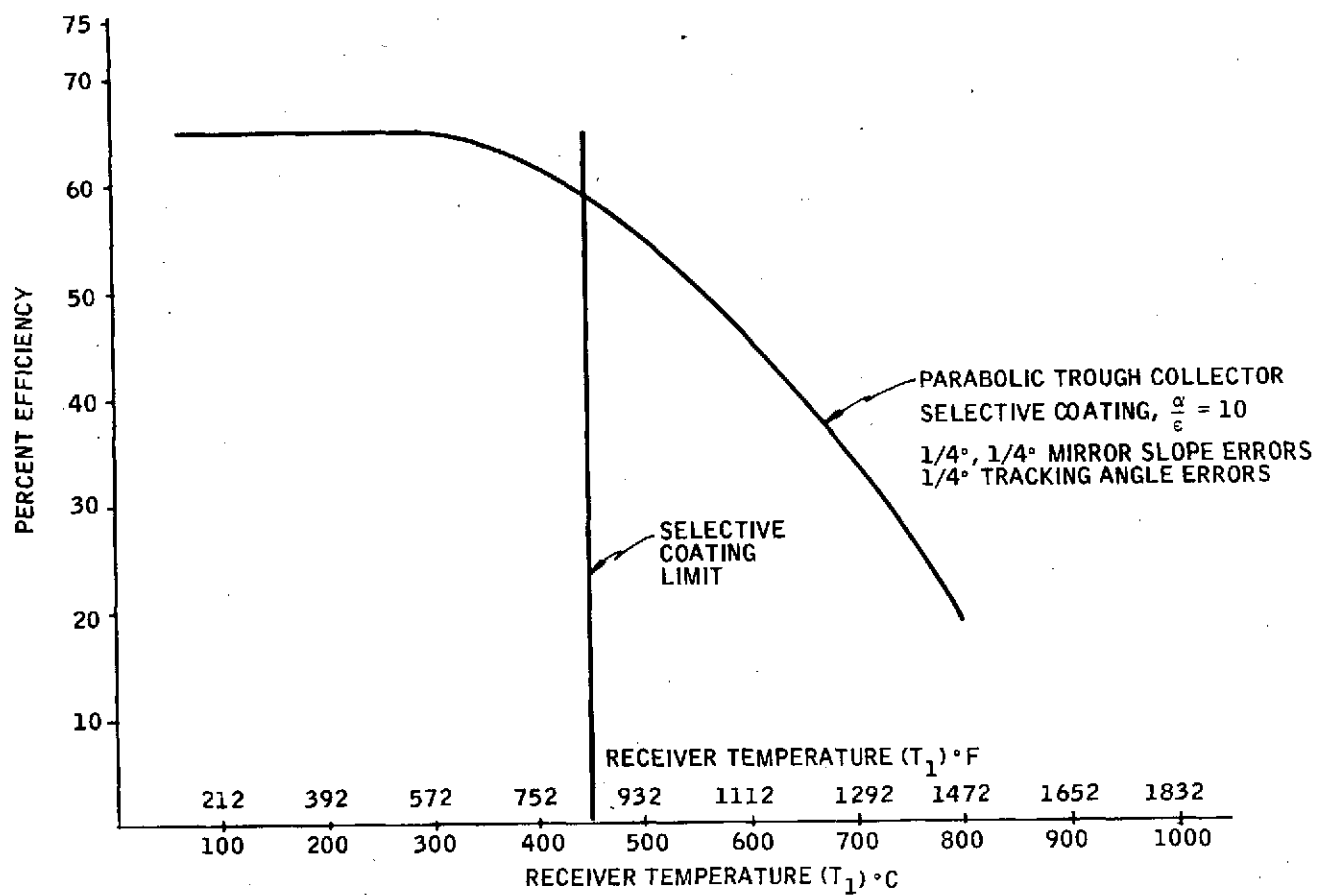
Figure 33. Trough Collector Efficiency versus Receiver Temperature
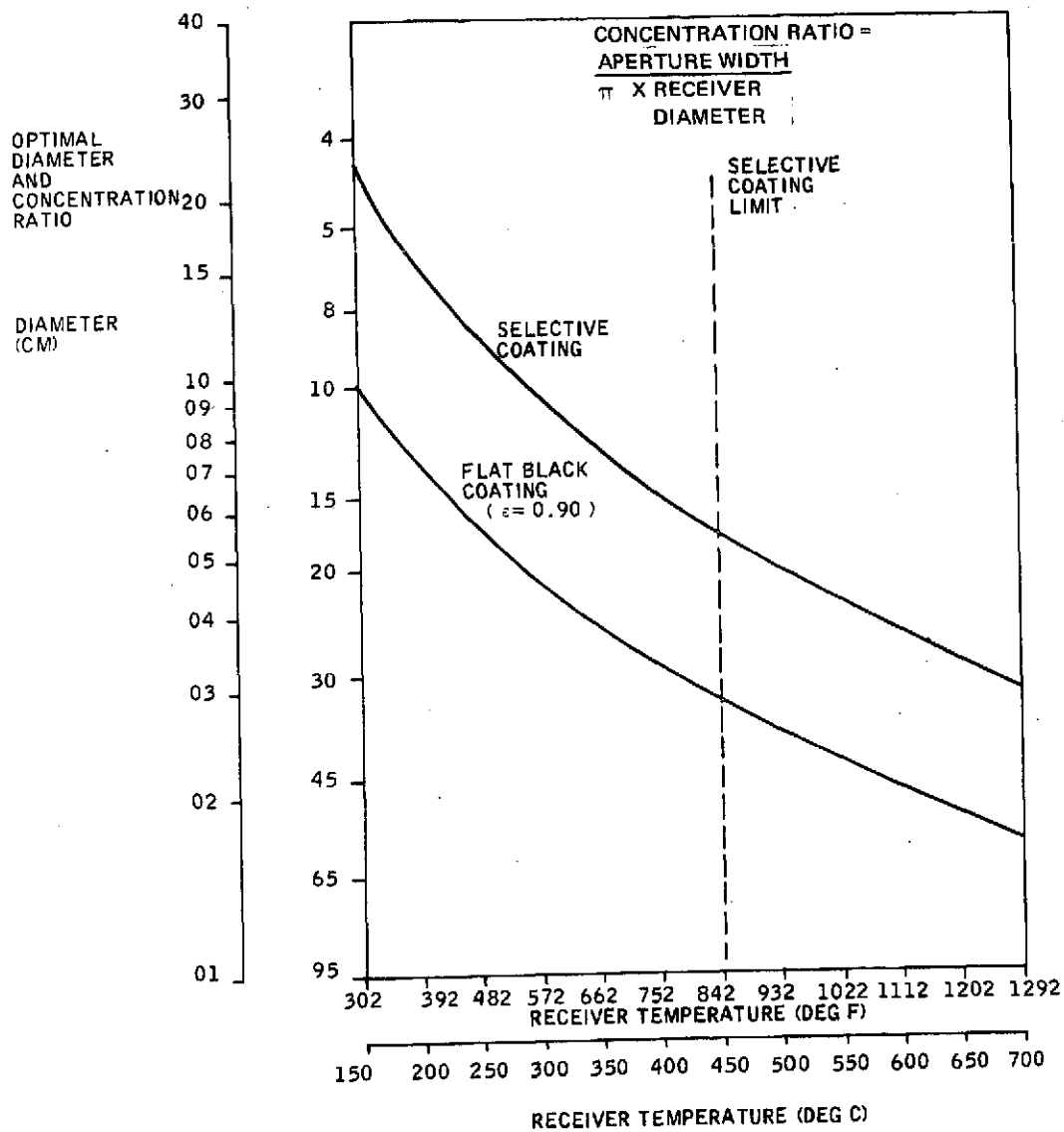
Figure 34. Optimal Concentration Ratio versus Receiver Temperature:
0.25 Degree Tracking Uncertainty; 0.25 Degree Mirror
Slope Uncertainty
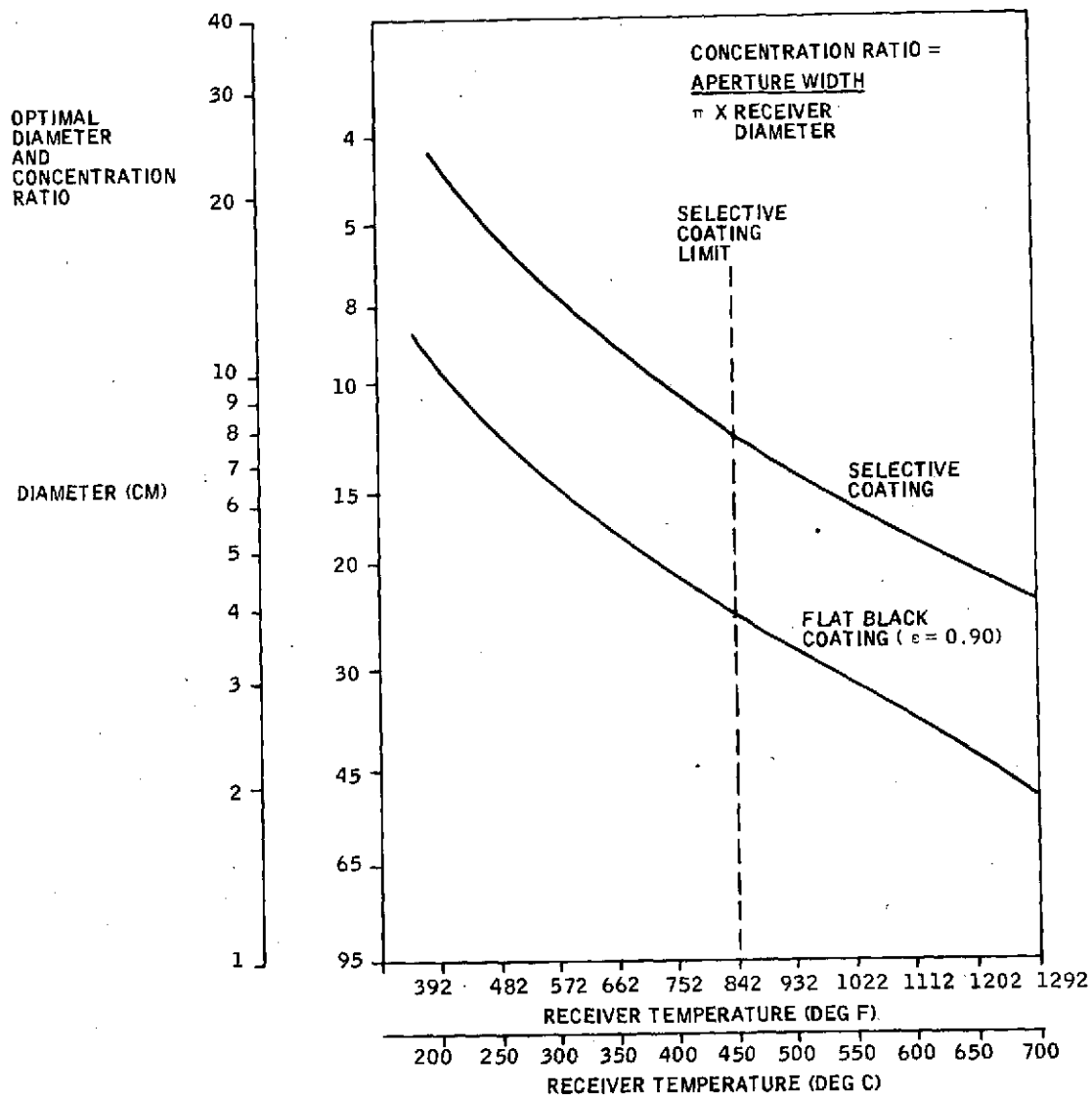
Figure 35. Optimal Concentration Ratio versus Receiver Temperature: 0.25 Degree Tracking Uncertainty; 0.50 Degree Mirror Slope Uncertainty
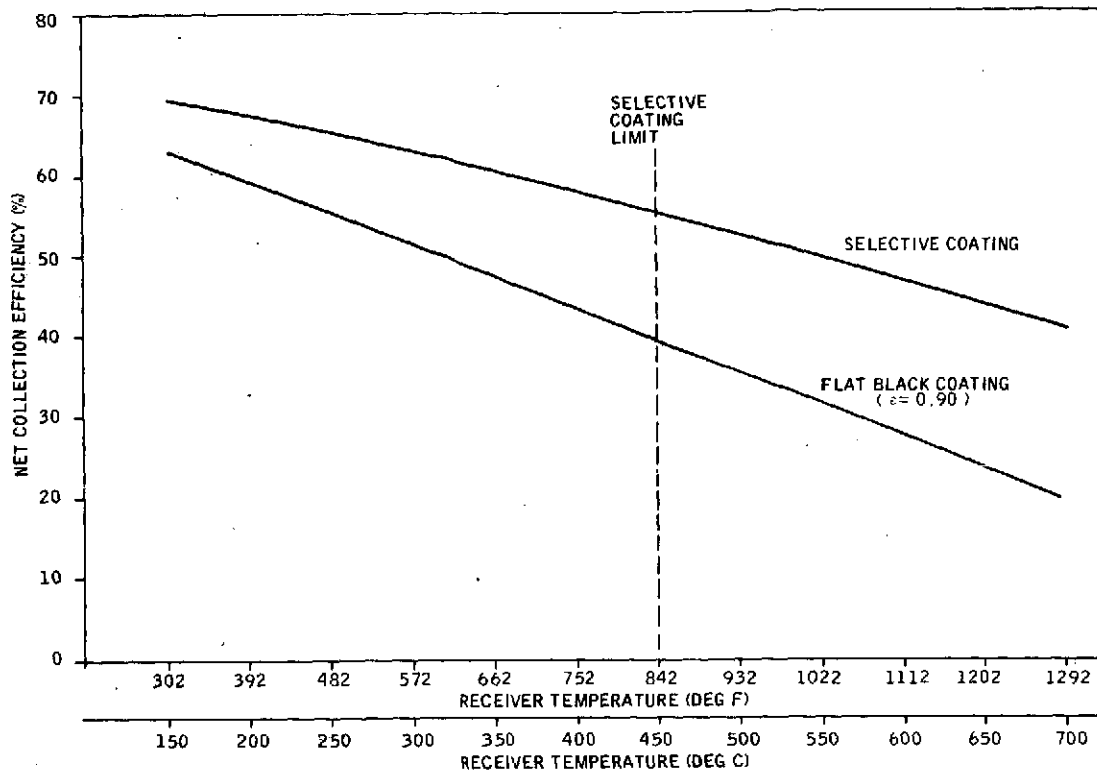
Figure 36. Optimal Efficiency versus Receiver Temperature: 0.25 Degree
Tracking Uncertainty; 0.25 Degree Mirror Quality
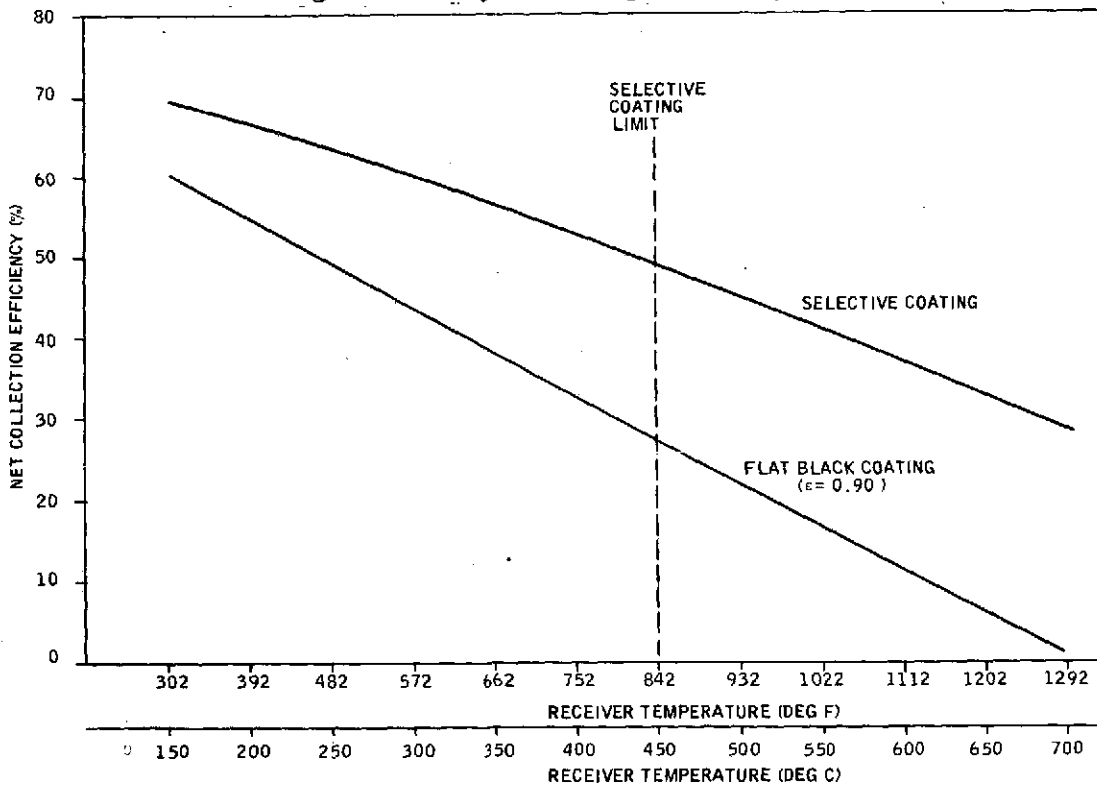
Figure 37. Optimal Efficiency versus Receiver Temperature: 0.25 Degree
Tracking Uncertainty; 0.50 Degree Mirror Uncertainty
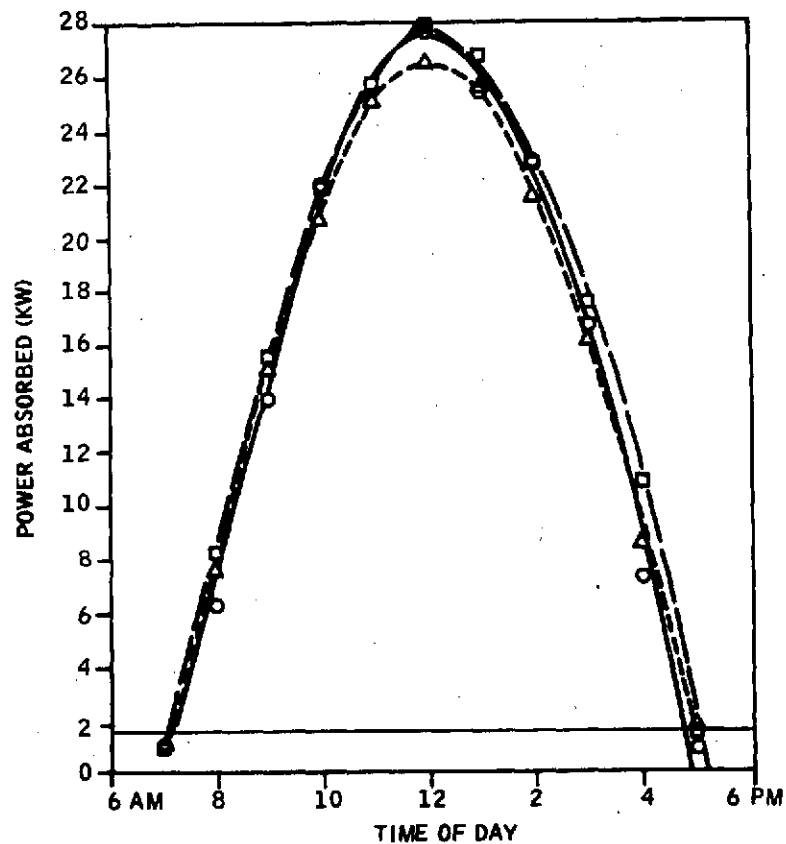
Figure 38. Power Absorbed versus Time of Day
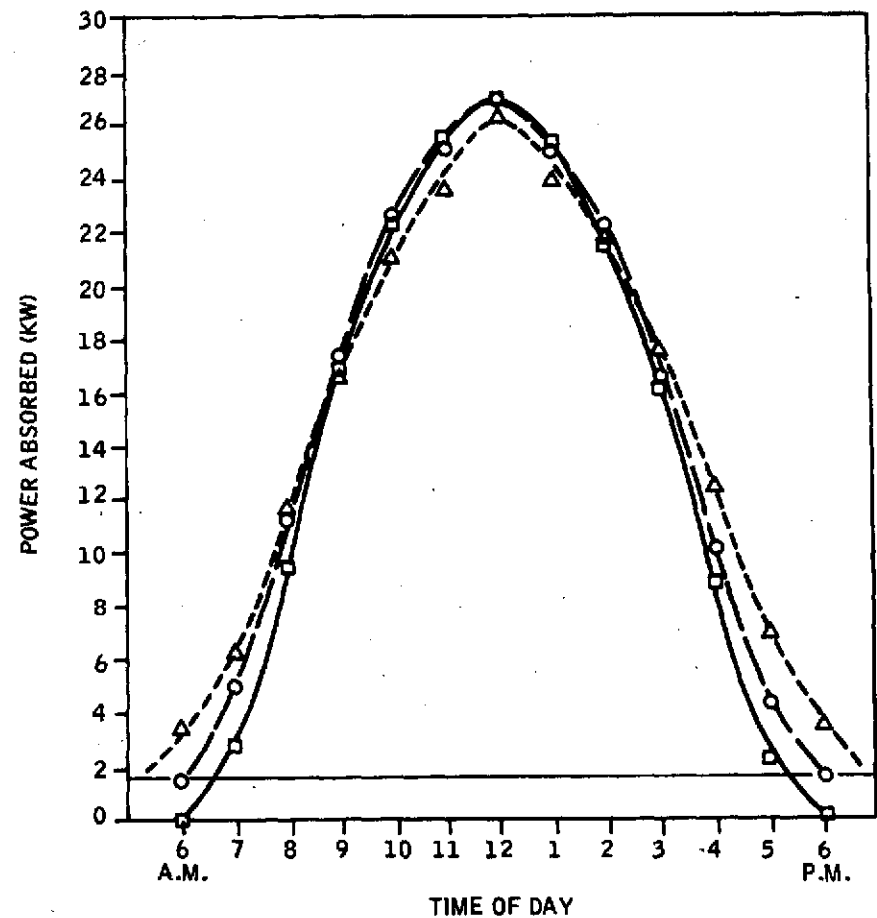
Figure 39. Power Absorbed versus Time of Day

CONCENTRATION RATIO = 13
EAST-WEST ORIENTATION
POINTING ACCURACY = 1/4°
SLOPE ERRORS = 1/4°

——————□——➤   7/15   164.7 KWH
————o————➤   8/15   151.6 KWH
———————△———➤   9/15   138.7 KWH

CONCENTRATION RATIO = 13
EAST-WEST ORIENTATION
POINTING ACCURACY = 1/4°
SLOPE ERRORS = 1/4°

——————o———➤   10/15   135.9 KWH
——————□———➤   11/15   141.5 KWH
————△———➤   12/15   148.7 KWH
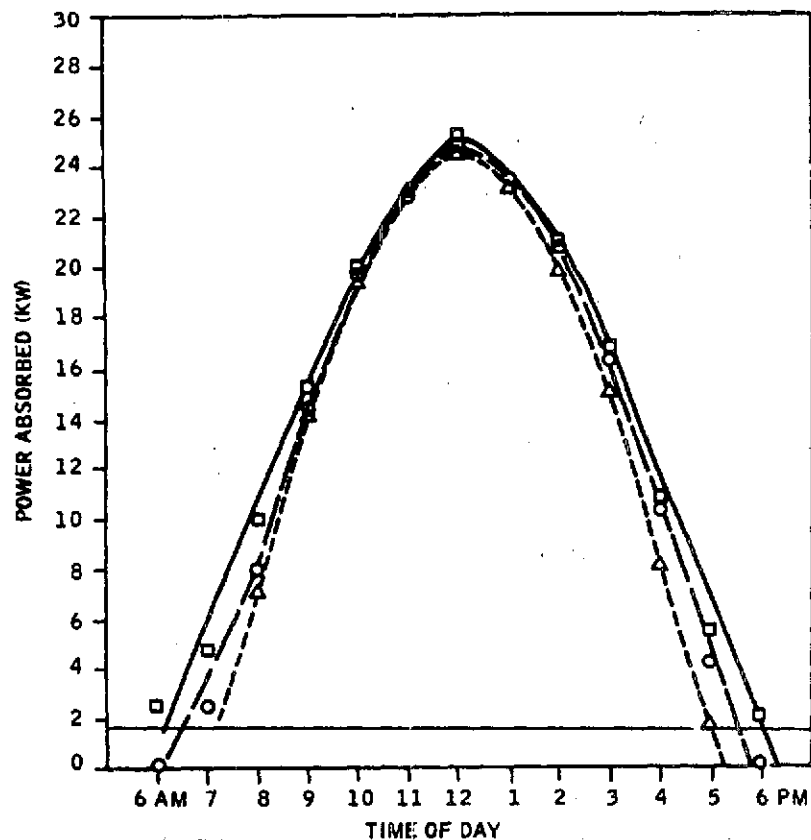
Figure 40.   Power Absorbed versus Time of Day
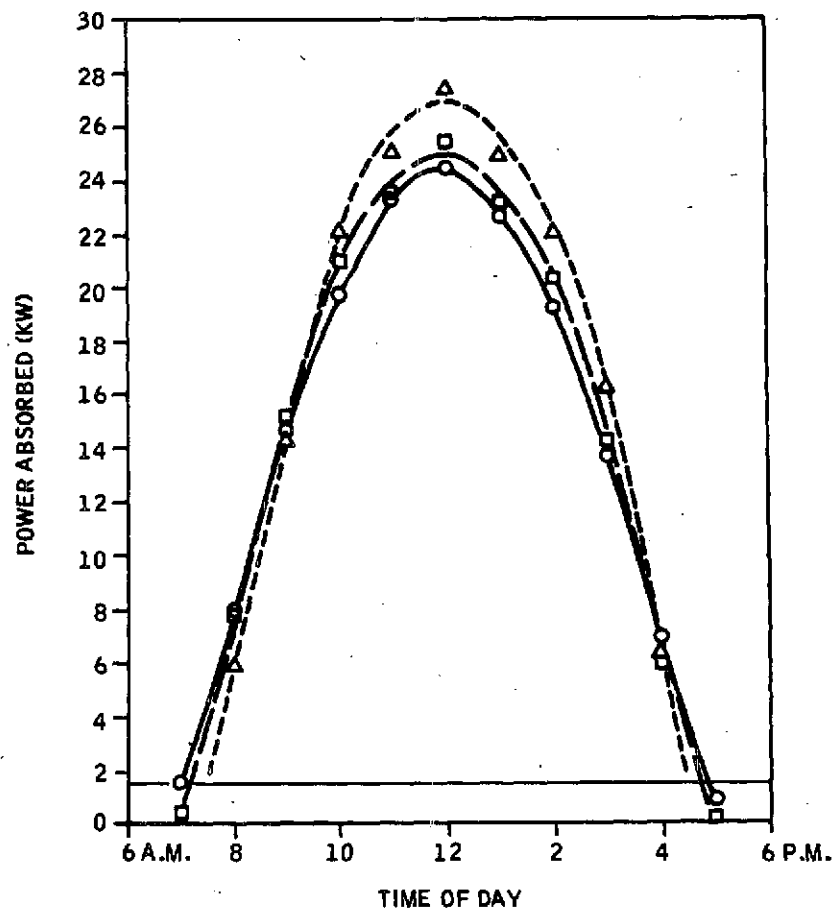
Figure 41.   Power Absorbed versus Time of Day

CONCENTRATION RATIO = 13
POLAR MOUNT
POINTING ACCURACY = 1/4°
SLOPE ERRORS = 1/4°

———□—➤ 1/15 185.5 KWH

———○—➤ 2/15 218.2 KWH

—————△—➤ 3/15 230.6 KWH

CONCENTRATION RATIO = 13
POLAR MOUNT
POINTING ACCURACY = 1/4°
SLOPE ERRORS = 1/4°

———□—➤ 4/15 253.9 KWH

———○—➤ 5/15 237.6 KWH

————△—➤ 6/15 225.7 KWH
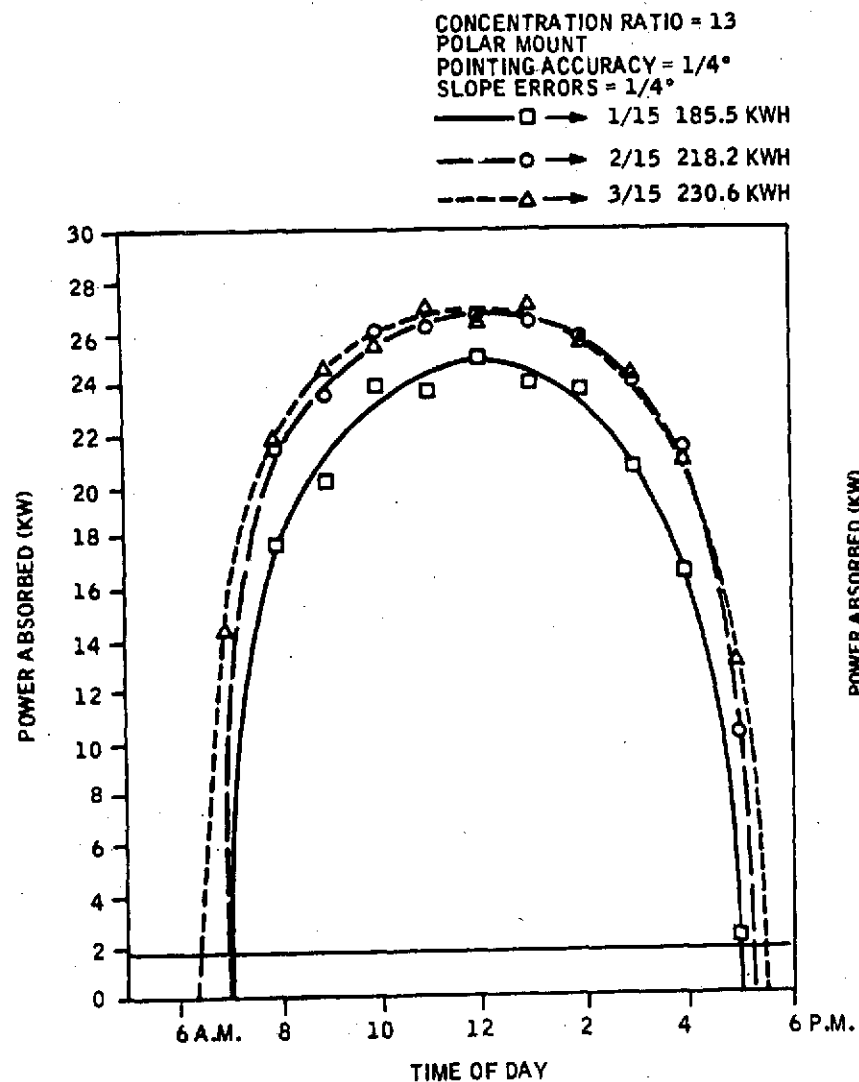
Figure 42. Power Absorbed versus Time of Day
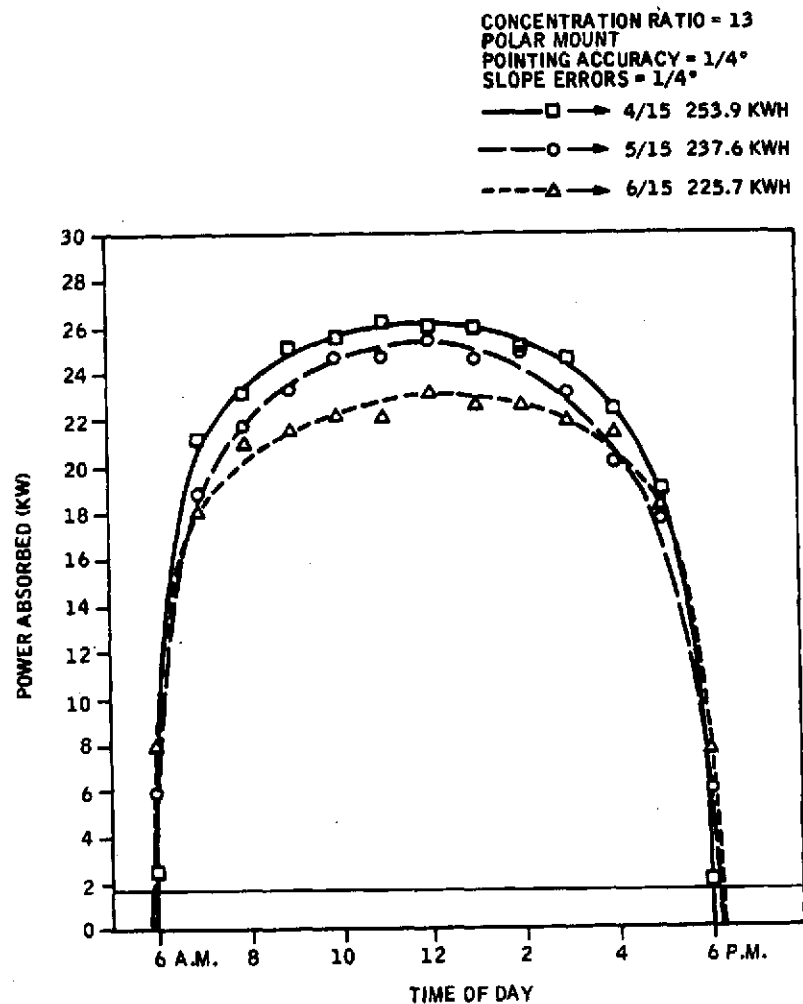
Figure 43. Power Absorbed versus Time of Day

CONCENTRATION RATIO = 13
POLAR MOUNT
POINTING ACCURACY = 1/4°
SLOPE ERRORS = 1/4°

———□——➤ 7/15 209.0 KWH

——·—○——➤ 8/15 220.3 KWH

——·—·—△——➤ 9/15 220.5 KWH

CONCENTRATION RATIO = 13
POLAR MOUNT
POINTING ACCURACY = 1/4°
SLOPE ERRORS = 1/4°

———□——➤ 10/15 193.6 KWH

——·—○——➤ 11/15 181.5 KWH
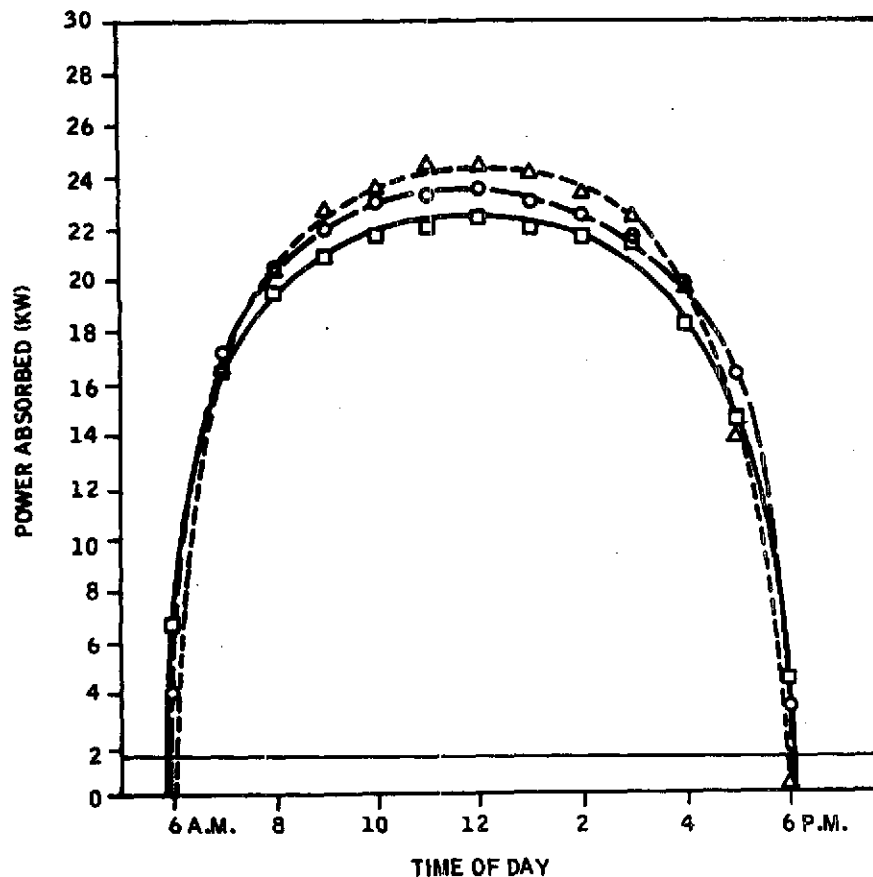
——·—·—△——➤ 12/15 175.5 KWH

Figure 44. Power Absorbed versus Time of Day
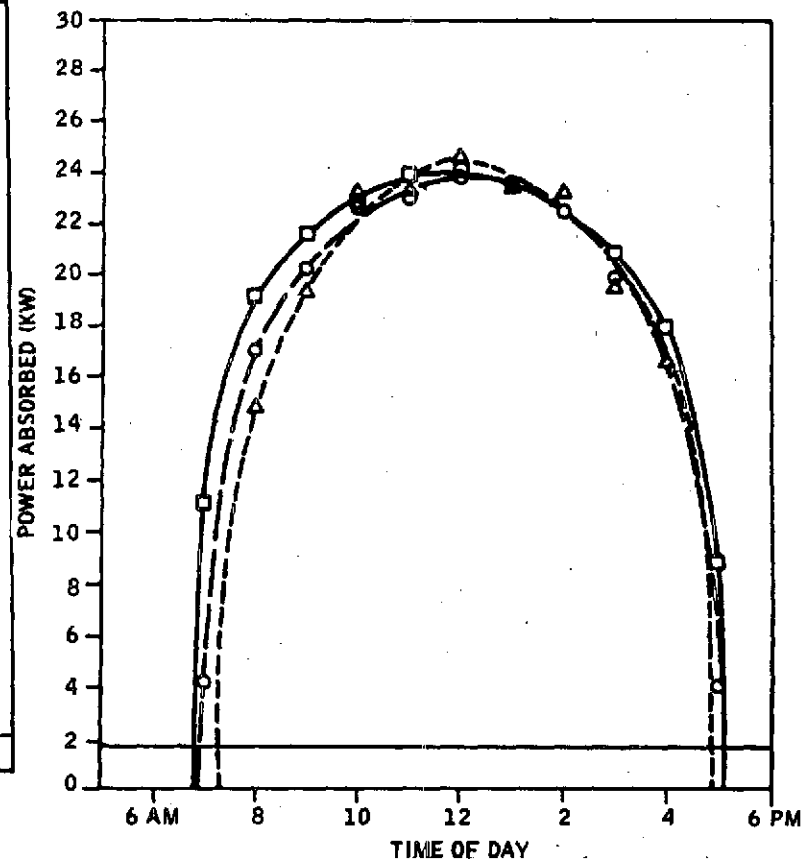
Figure 45. Power Absorbed versus Time of Day

ENERGY
ABSORBED (KWH)

CONCENTRATION RATIO = 13
POINTING ACCURACY = 1/4°
SLOPE ERRORS = 1/4°
LATITUDE = 33.0°

☐ EQUATORIAL
YEARLY TOTAL - 77587 KWH
MONTHLY AVERAGE - 6466 KWH

○ EAST - WEST
YEARLY TOTAL - 56118 KWH
MONTHLY AVERAGE - 4860 KWH
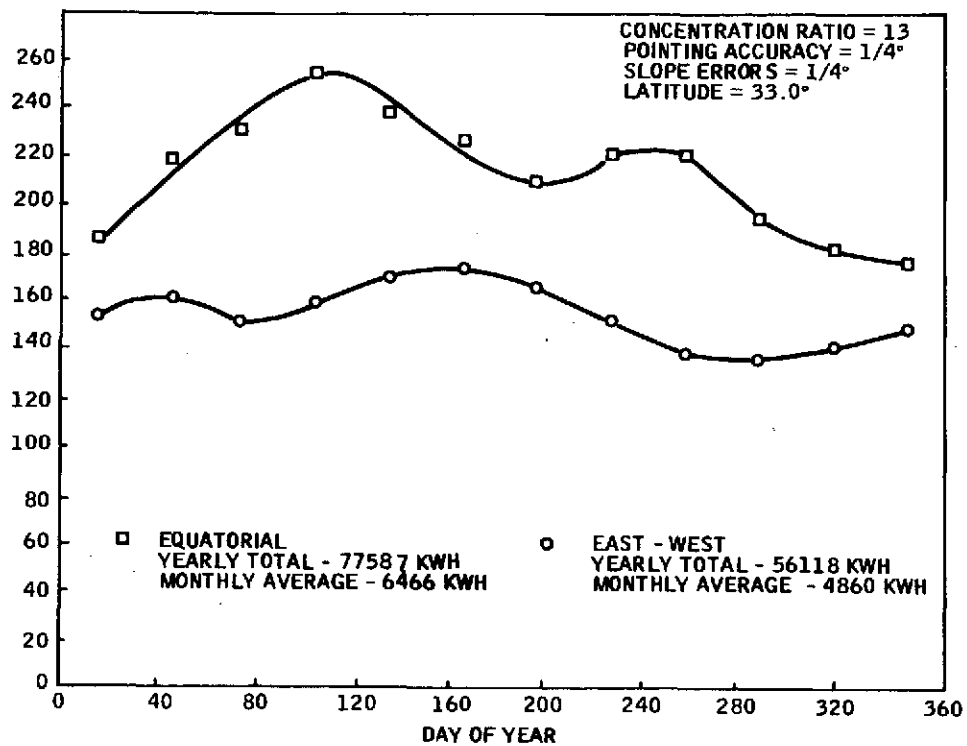
DAY OF YEAR

Figure 46. Daily Net Energy Absorbed versus Day of Year

Figure 47. Trough Collector Absorbed Thermal Power Versus Number of Hours in a Year for Which Collector Absorbed Power is at Least Equal to Indicated Value
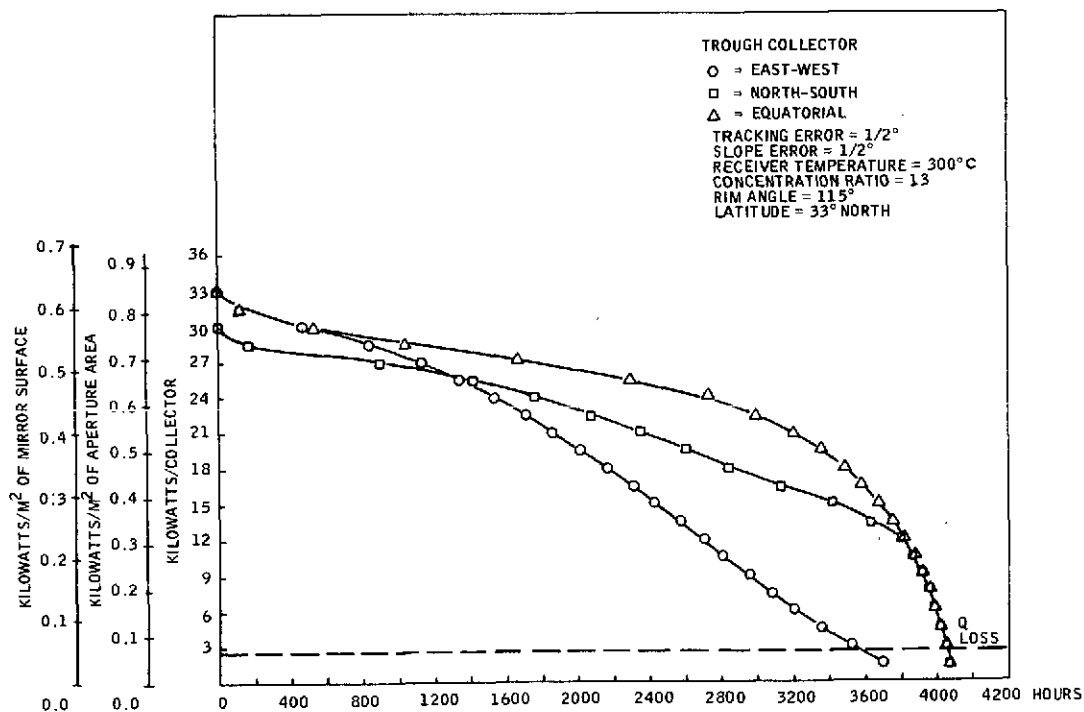
Figure 48. Trough Collector Absorbed Thermal Power Versus Number of Hours in a Year for Which Collector Absorbed Power is at Least Equal to Indicated Value

Table VII. Net Energy/Trough Collector for One Year

Temperature	Error (deg)	Orientation	Net Energy (kw hr)
300°C	0.25	E-W	70311
300°C	0.25	N-S	81456
300°C	0.25	Polar	94374
300°C	0.5	E-W	59583
300°C	0.5	N-S	74679
300°C	0.5	Polar	85284

These load duration curves were for a nominal collector field layout which gave no shadows from 8:00 a.m. to 4:00 p.m. on 12/15. The field layout is shown in Figures 49 and 50. These figures represent a ground cover ratio of 0.25 for the east-west and 0.097 for the north-south and equatorial (polar mount) configurations. The effect of spacing can be effectively studied by scaling the center-to-center spacing of these basic design layouts equally in all directions, and calculating the collector performance at each resultant ground cover ratio.

For each collector system, the control collector is the collector onto which the shadows from the adjacent collectors are projected. The adjacent collectors are shown in the field layouts, all others being ignored. In each case, the ray trace codes can accommodate any number and location of adjacent collectors (subject to time and memory limits). The program which plots out the output duration curves is not a ray trace code but only a curve fit of the ray trace data, and a simple back correction to the ray trace data for shadow losses. Figure 51 shows the thermal power output duration curve for a trough collector in an east-west orientation with 1/4 degree rms tracking and mirror slope uncertainty, a vacuum jacket, a selective coating with (α/ε) of nominally 10, which is operating at 300°C (572°F) receiver temperature. There are eight computer-drawn curves on these graphs at eight different ground cover ratios. These curves represent the thermal power collected per meter square of aperture area plotted versus hours of duration of the power level per year. The center-to-center spacings (ΔEW, ΔNS) associated with each of these ground cover ratios are shown in Table VIII.

The dashed line along the bottom of each curve (labeled Q LOSS) represents the magnitude of the thermal power lost (divided by the collector aperture area) by reradiation and convection from the receiver and glass vacuum envelope. The net thermal power collected over an entire year is the integral of the difference between the loss line and the absorbed power curve, the units of the integral being thermal-kilowatt-hour-per-meter squared of aperture.

Note that the loss line is higher and the absorbed power lower for the 0.50 degree mirror (Figure 52) case than for the 0.25 degree case (Figure 51). This is because an optimal design with a poorer optics quality always absorbs less power in the first place and also requires a larger receiver (which loses more power).

The results for the north-south orientation are shown in Figures 53 and 54 , while the load duration curves for the polar mount are plotted in Figures 55 and 56.

Paraboloid of Revolution Dish Collectors

The two-axis paraboloid of revolution collector simulation code was exercised for a dish collector mounted at 33 degrees north latitude, with an aperture area of 420 square feet (39 square meters). The chosen aperture area was the same as the aperture area of the trough collector, for which performance summaries have been published (Reference 6). All runs were made for 6/15 at 10 a.m. The direct normal solar flux at that time was taken to be 270 Btu/(hr/ft^2), or 33 thermal kilowatts of power. Adjacent collectors were sufficiently spaced to yield no shadows from 8 a.m. to 4 p.m. on 12/15.
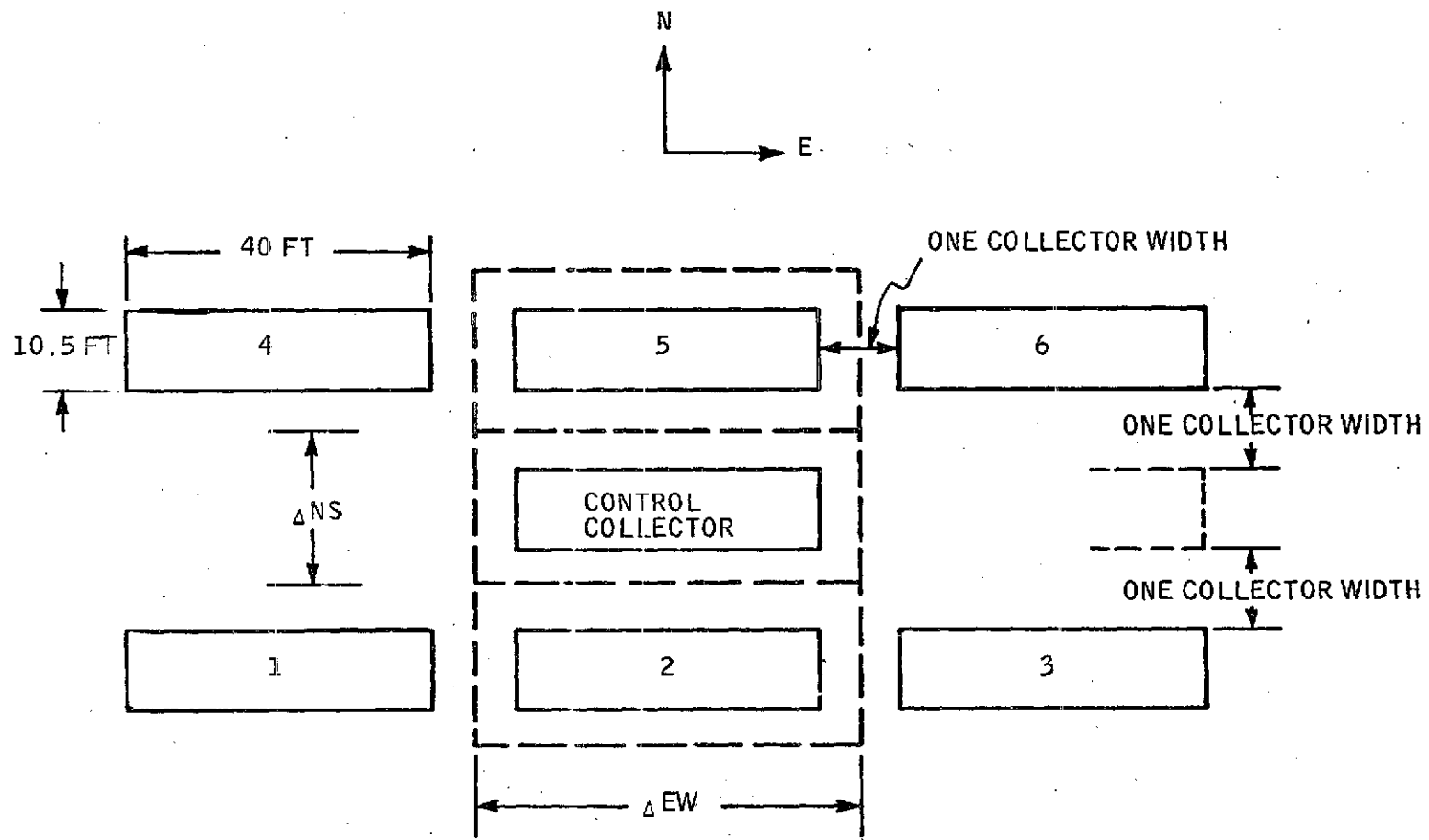
Figure 49. Trough Collectors in East-West Orientation

Figure 50. Trough Collectors in North-South and Polar Orientation
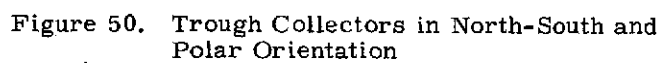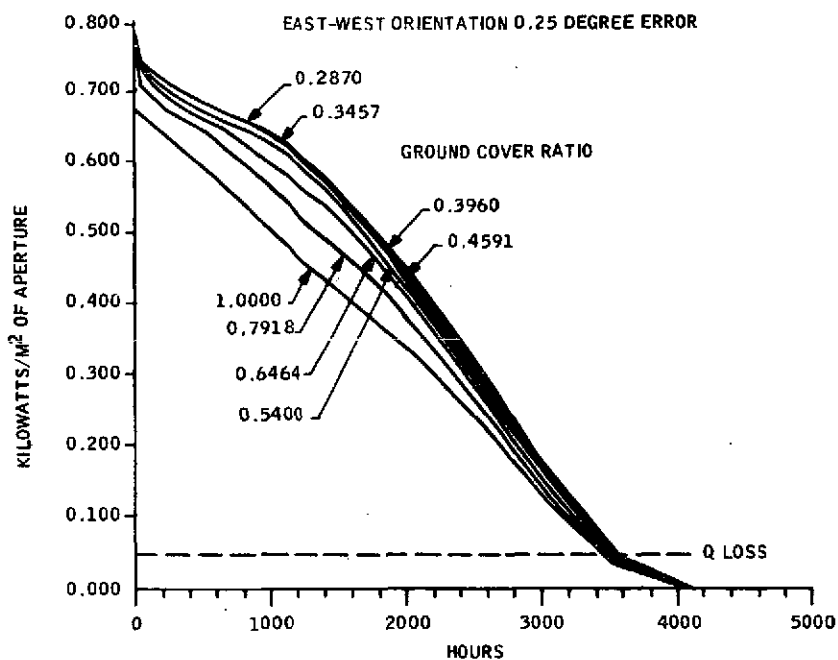
Figure 51   Trough-Absorbed Thermal Power versus Number
of Hours in a Year for Which Collector Absorbed
Power is at Least Equal to Indicated Value
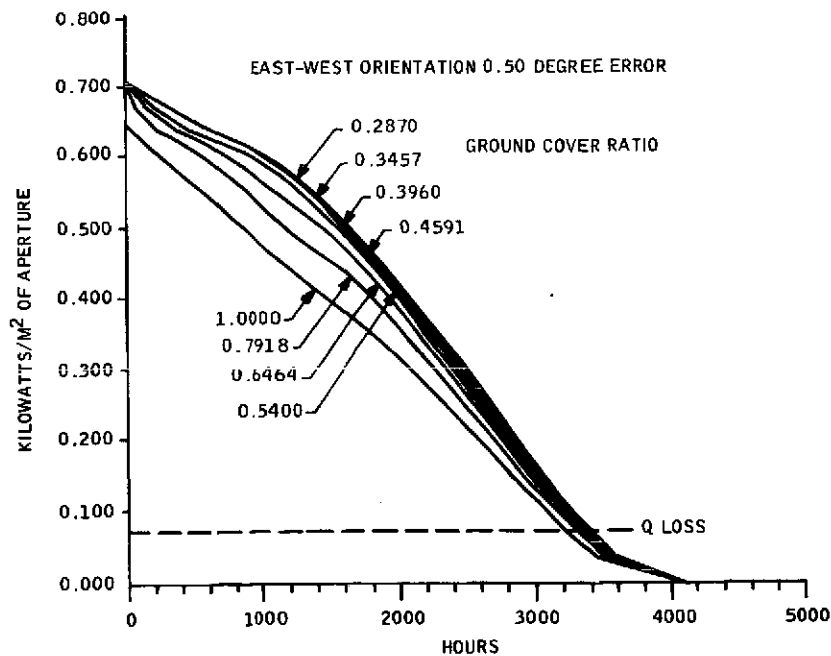
Figure 52.   Trough-Absorbed Thermal Power versus Number of
Hours in a Year for Which Collector Absorbed Power
is at Least Equal to Indicated Value
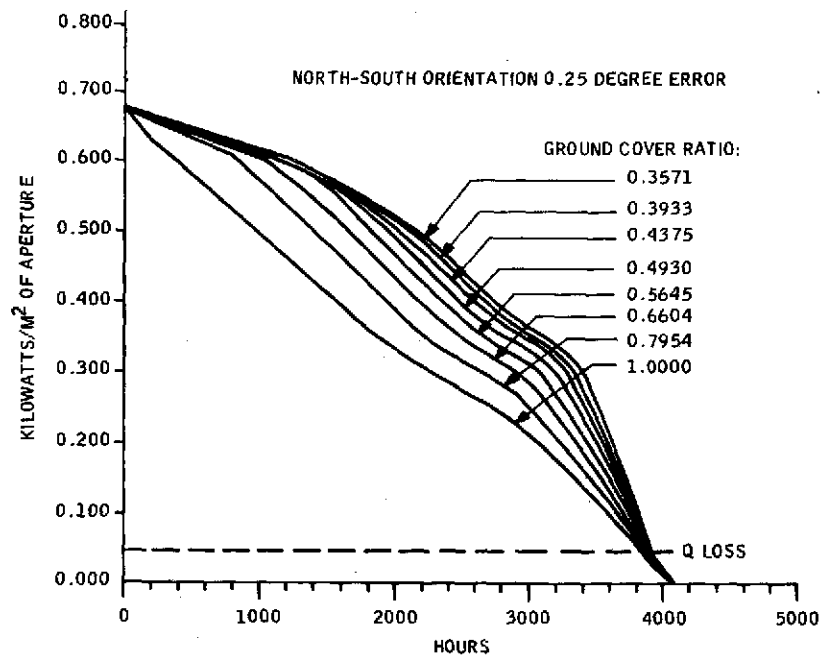
Figure 53. Trough-Absorbed Thermal Power versus Number of Hours in a Year for Which Collector Absorbed Power is at Least Equal to Indicated Value
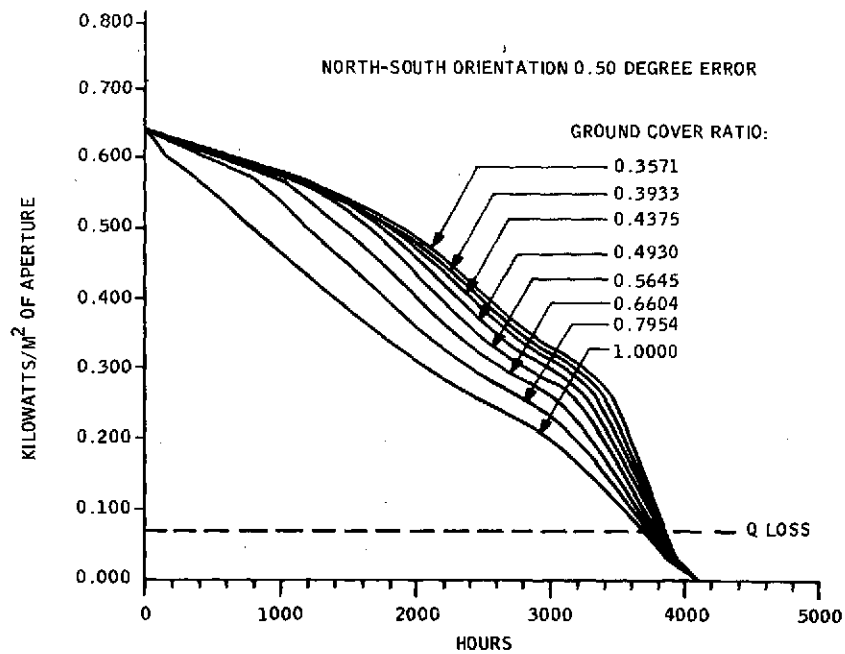
Figure 54. Trough-Absorbed Thermal Power versus Number of Hours in a Year for Which Collector Absorbed Power is at Least Equal to Indicated Value

71
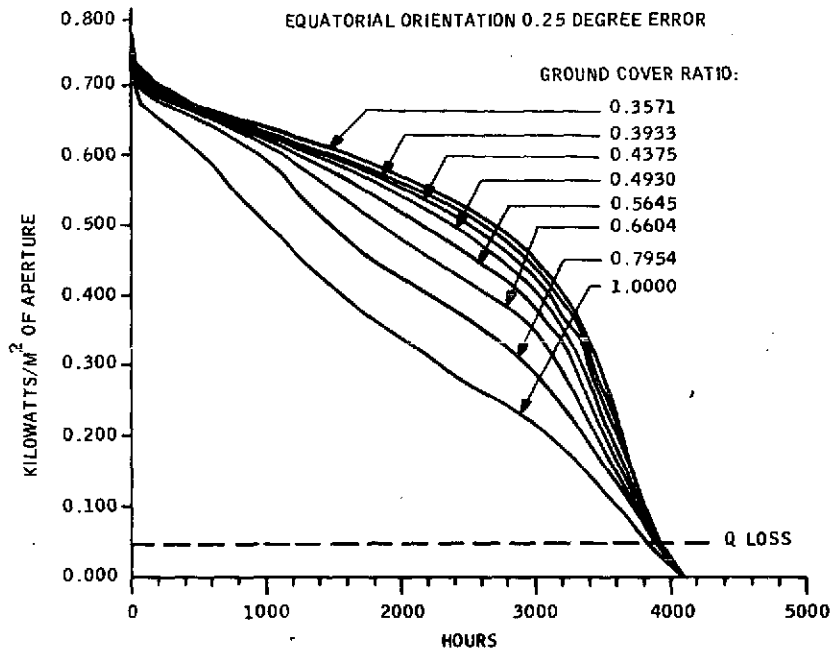
Figure 55. Trough-Absorbed Thermal Power versus Number of Hours in a Year for Which Collector Absorbed Power is at Least Equal to Indicated Value
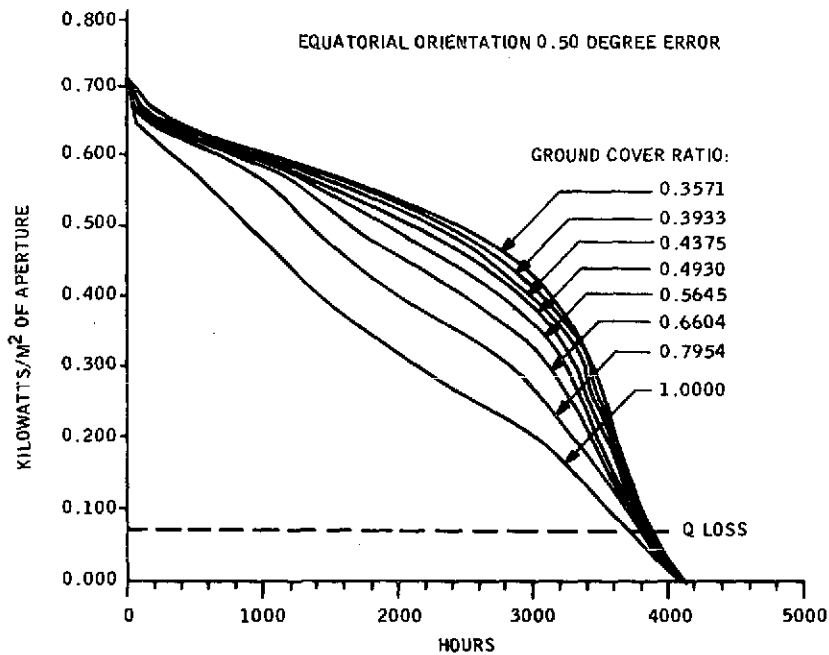
Figure 56. Trough-Absorbed Thermal Power versus Number of Hours in a Year for Which Collector Absorbed Power is at Least Equal to Indicated Value

72

Table VIII. Center-to-Center Trough Collector Spacings

Collector Type	Ground Ratio	Δ EW (feet)	Δ EW (meters)	ΔNS (feet)	ΔNS (meters)
Trough East-West	1.0000	40.0	12.192	10.5	3.200
	0.7918	42.1	12.832	12.6	3.840
	0.6464	44.2	13.472	14.7	4.481
	0.5400	46.3	14.112	16.8	5.121
	0.4591	48.4	14.752	18.9	5.761
	0.3960	50.5	15.392	21.0	6.401
	0.3457	52.6	16.032	23.1	7.041
	0.2870	55.75	16.993	26.25	8.001
Trough North-South and Equatorial	1.0000	10.50	3.200	40.0	12.192
	0.6667	15.75	4.801	40.0	12.192
	0.5000	21.00	6.401	40.0	12.192
	0.3683	25.20	7.681	45.25	13.792
	0.2829	29.40	8.961	50.5	15.392
	0.2242	33.6	10.241	55.75	16.993
	0.1822	37.8	11.521	61.0	18.593
	0.1509	42.0	12.802	66.25	20.193

The collector was assumed to have a 6-inch-wide slot from the rim to the center of the dish to accommodate the heat receiver mounting. This slot also accommodated the shadow of the receiver support structure. In all cases, the receiver surface was assumed to have a flat grey surface with an emittance of 0.90 at all wavelengths. The first gimbal-mounted axis was assumed to be vertical, which implies that the second gimbaled axis remained horizontal as it rotated above the first one. The receiver was earth-fixed and no rotating heat transfer joint was assumed or implied.

The offset of the receiver from the mirror focus was simulated as zero in all runs. The offset of the mirror focus from the crossing point of the tracking axis was also set at zero for all runs.

It has been shown that the optimal rim angle is the rim angle at which a weighted average factor is proportional to the aperture area as a function of the distance from the focus. The predicted value for the trough collector was 115 degrees and the ray trace results agreed to within 2 degrees. The predicted optimal value for the dish collector was 109 degrees.

The simulation code was exercised for a series of concentration ratios at a receiver temperature of 1000°F (537.8°C) with a 109-degree rim angle and a range of mirror and tracking accuracies. Results are shown in Figure 51 . The case labeled perfect optics has mathematically perfect tracking and mirror shape. The 1/4-degree curve is for a 1/4-degree rms uncertainty in the angular position of the mirror normal at any point. The curve labeled 1/2 degree represents a system with a 1/2-degree rms uncertainty in mirror normal angular position at each point, but the tracking uncertainty was left at 1/4-degree rms. In all cases, the distribution of angular errors had a mean of zero and a normal probability distribution. However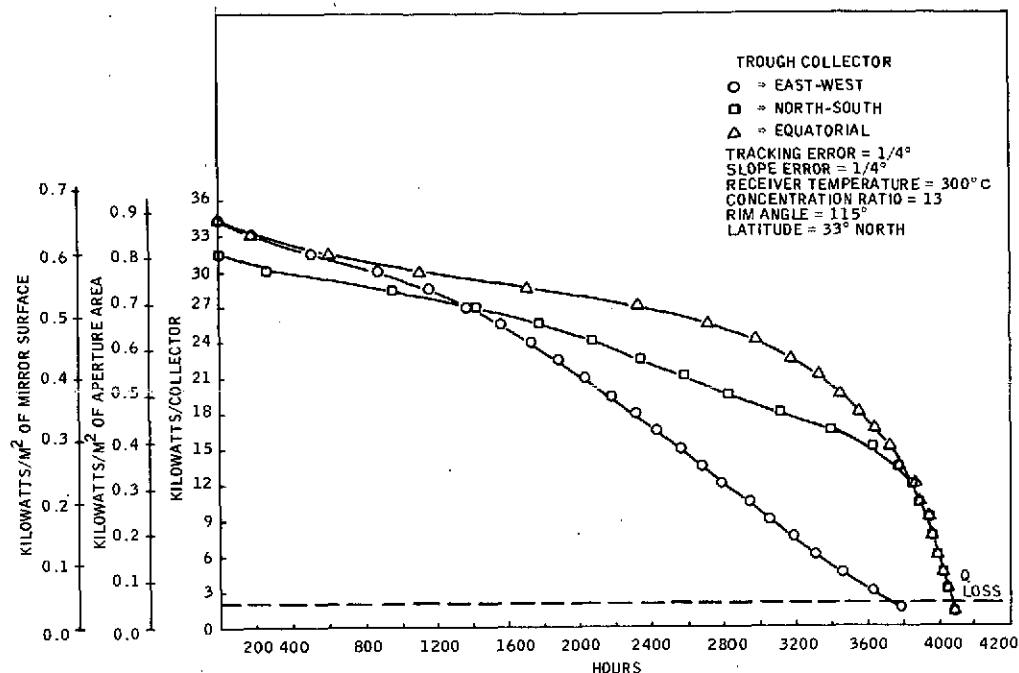, the 1/4 degree case represents a relatively high quality system that is also practical to expect from a mass-manufactured system.

The best concentration ratio is 400 for the 1/4-degree curve and 180 for the 1/2-degree curve. In either case, if more concentration than the optimal is attempted, heat losses reduced by a smaller receiver area are overcome by reducing absorbed energy received due to the smaller sized receiver target. The higher the quality of the optics, the higher

the optimal concentration ratio. Even the perfect-optics case appears to have a weak optimal at a concentration of 800. In the perfect optics case, the only limit to the concentration ratio is the finite angular extent of the sun, itself.

A dish collector with a receiver at 1500°F (815°C) was also simulated (Figure 58). In this case, the optimal concentration for each optics quality shifts to higher values. Optimal thermal power at higher temperatures is lower. The optimization can only minimize the extra heat losses at the higher temperatures, but does not eliminate them altogether. The optimal concentration is 1500 to 2000 for perfect optics, 500 for the 1/4-degree case and 300 for the 1/2-degree case.

To test the prediction, the optimal rim angle was 109 degrees. A set of runs was made at a concentration ratio of 400 for the 1/4-degree mirror, and 185 for the 1/2-degree mirror for a wide range of rim angles. The results are plotted as thermal power absorbed (kilowatts) versus rim angle in Figure 59 . This is absorbed power only and the thermal power losses have not been subtracted.

The prediction was based on results of the parabolic trough simulation code, which showed that the optimum rim angle was independent of the optimum concentration ratio and equal, within our uncertainty limits, to 110 degrees. This is also the rim angle at which the trough collector is mass-balanced at its focus. The discrepancy between the dish simulation results and the prediction of our hypothesis reinforces the intuitive statement that there is a fundamental generic difference between the trough and the paraboloid of revolution collectors.

Heat Losses--The heat receiver for the paraboloid of revolution collector was modeled as a coated heat pipe in a glass vacuum envelope. The geometry assumed for the heat balance equations is shown below.
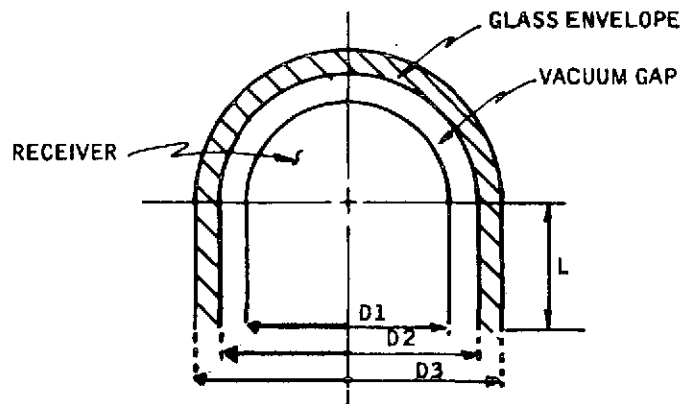
The cap was considered a hemisphere, such that surface areas are given by

$$A_i = 0.5 \, \pi D_i^2 + \pi D_i L .$$

The computer code used to determine heat losses from the cylindrical heat pipe (Reference 6) was modified for this configuration. The radiation from the glass envelope to ambient was included:

$$Qr_{3a} = \epsilon A_3 \, \sigma \, (T_3^4 - T_a^4),$$
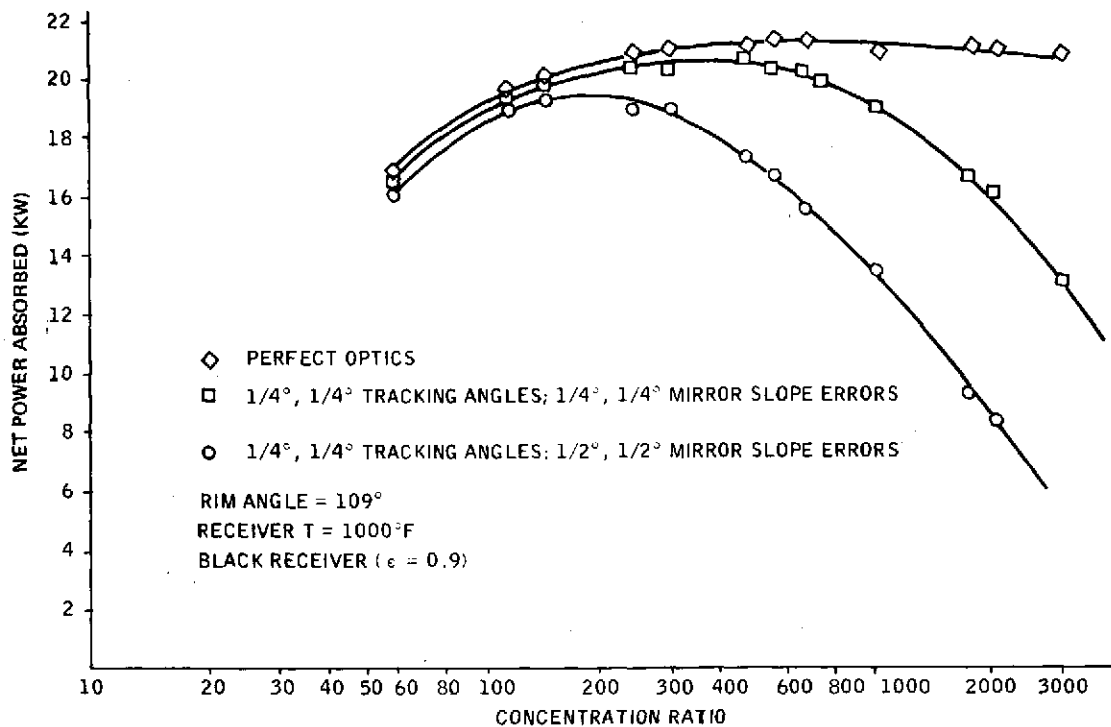
Figure 57. Dish Collector Net Power Absorbed versus Concentration Ratio at 1000°F Receiver Temperature
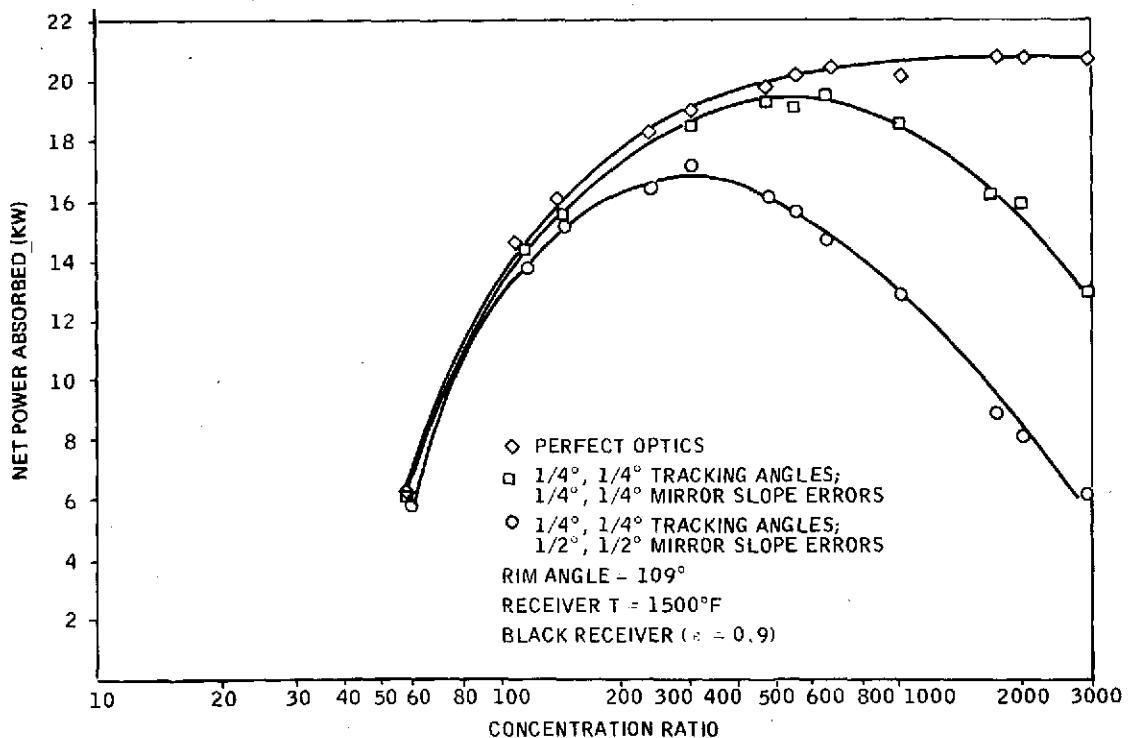
Figure 58. Dish Collector Net Power Absorbed versus Concentration Ratio at 1500°F Receiver Temperature
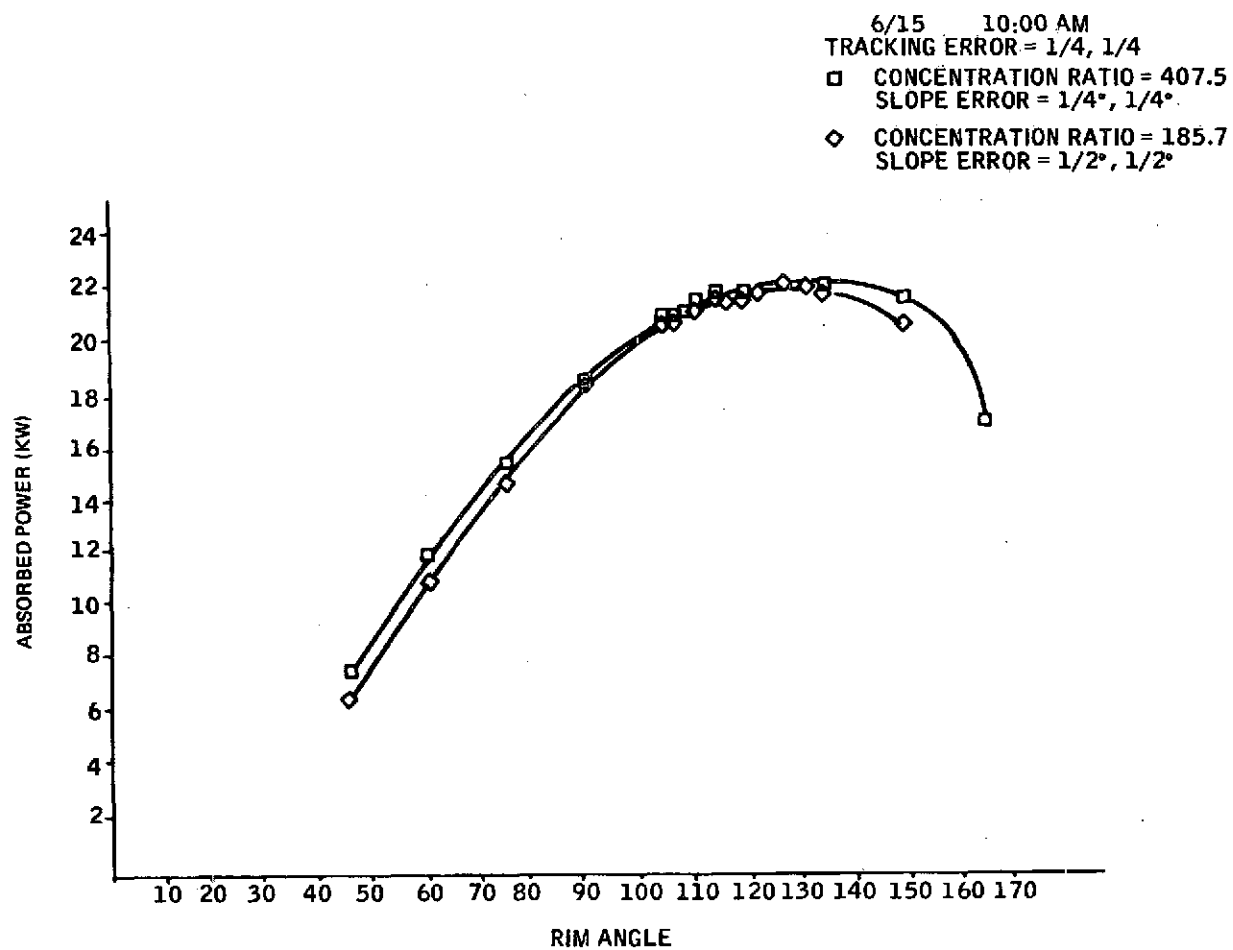
Figure 59.   Dish Collector Absorbed Power versus Rim Angle

where

$Q_{r_{3a}}$ = heat radiated to the sky

ϵ = emissivity of the glass surface

σ = Stefan-Boltzmann constant

T_a = air temperature

The code was exercised to determine sensitivity of the model to the variation of L and D at a fixed concentration ratio. It was found that the difference in the heat loss (Q_{loss}) for varying L/D was trivial.

The formula for Q_{12} is different for glass assumed specular as opposed to diffuse. The program was exercised under both conditions and little difference was noted.

The variation of heat lost to the environment as a function of the receiver area is shown in Figure 60 . The variation of heat lost to the environment as a function of receiver surface temperature is shown in Figure 61 .

The parabolic trough heat loss results suggested an equation of the form

$$Q_{loss} = C(A_1) (T_1) \alpha \qquad (8)$$

to fit the data. To establish this relation, the heat-loss-versus-receiver temperature was plotted on log-log paper in Figure 62 . By taking the slope of the curves (they appear parallel), we find $\alpha = 2.7$. Also note that for $T_1 \le 300°C$ the errors in the Q_{loss} equation may be high in percentage, but the losses are so small as to be insignificant.

For the range of concentration ratios 100 to 1000 and receiver temperatures 300°C to 1000°C, the following equation can be applied:

$$Q_{loss} = 3.5 \times 10^{-7} (A_1) (T_1)^{2.7} \qquad (9)$$

where T_1 has units of degrees centigrade, A_1 is in m^2 and Q_{loss} has units of KW.

The results of the exercise of the paraboloid of revolution simulation code were combined with those of the heat balance to provide a curve of efficiency versus receiver temperature (Figure 63).

Furthermore, the heat balance code was exercised to establish the optimal concentration ratio as a function of the receiver temperature. Results are shown in Figures 64 and 65 for the 1/4 and 1/2 mirror slope errors.

The optimal concentration ratio at 1500°F for the 1/4 degree error is about 595, and for the 1/4 degree error it is approximately 325. These values are far below a concentration value of 1000. Note that even though high temperatures can be produced, it is not practical to use these because of material breakdown and heat transfer problems.

Efficiency at the optimal-concentration-ratio-versus-receiver temperature was also calculated (Figures 66 and 67). At 1500°, the 1/2-degree error mirror has an efficiency of about 50 percent, while the 1/4 degree error mirror has an efficiency of over 55 percent.

Furthermore, a computer plotting program was written to take the ray trace code results and put them in a format which is apparently standard practice for the power industry. The format consists of a plot on the abscissa of the number of hours in a year for which power output is at, or above the value read from the ordinate. The industry name for these plots is "load duration curves."
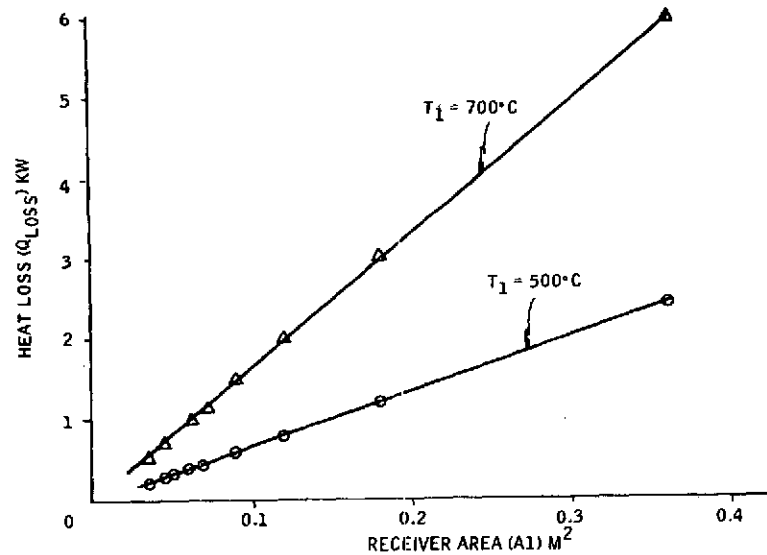
Figure 60. Dish Collector Receiver Heat Loss
versus Receiver Surface Area
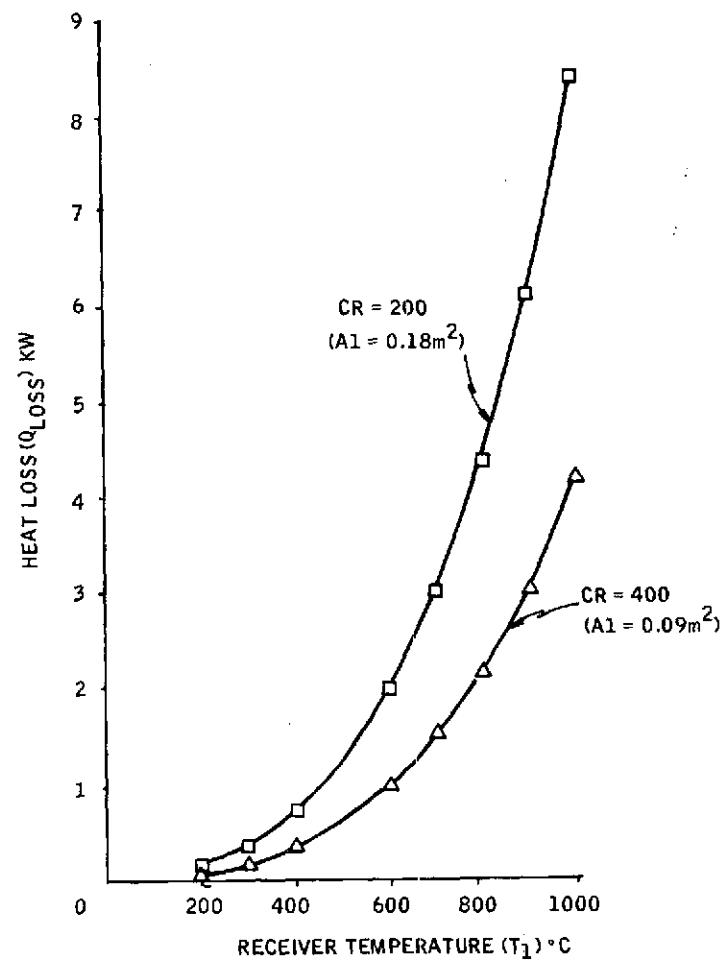
Figure 61. Variation of Dish Collector Receiver
Heat Loss versus Receiver
Temperature
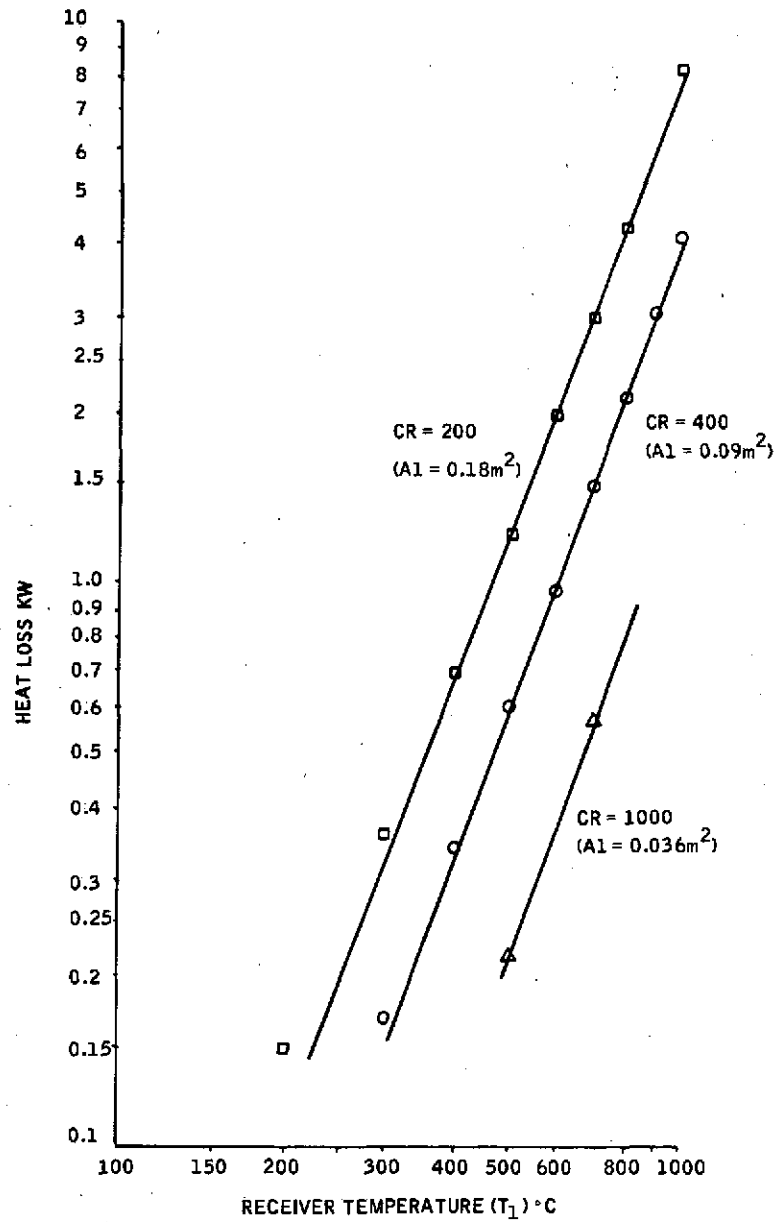
Figure 62. Dish Collector Receiver Heat Loss versus
Receiver Temperature
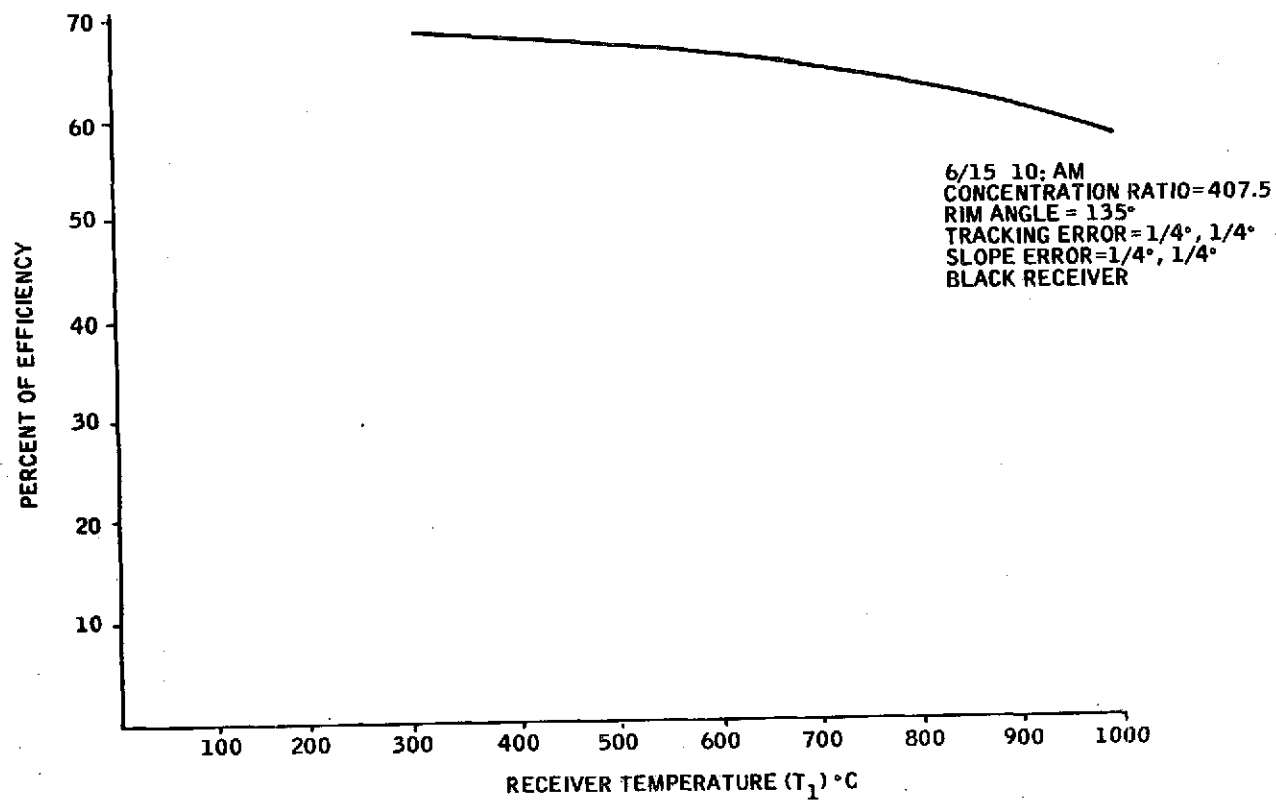
Figure 63. Dish Collector Efficiency versus Receiver Temperature (T_1)

RECEIVER   CONCENTRATION
AREA (M²)   RATIO

RECEIVER   CONCENTRATION
AREA (M²)   RATIO
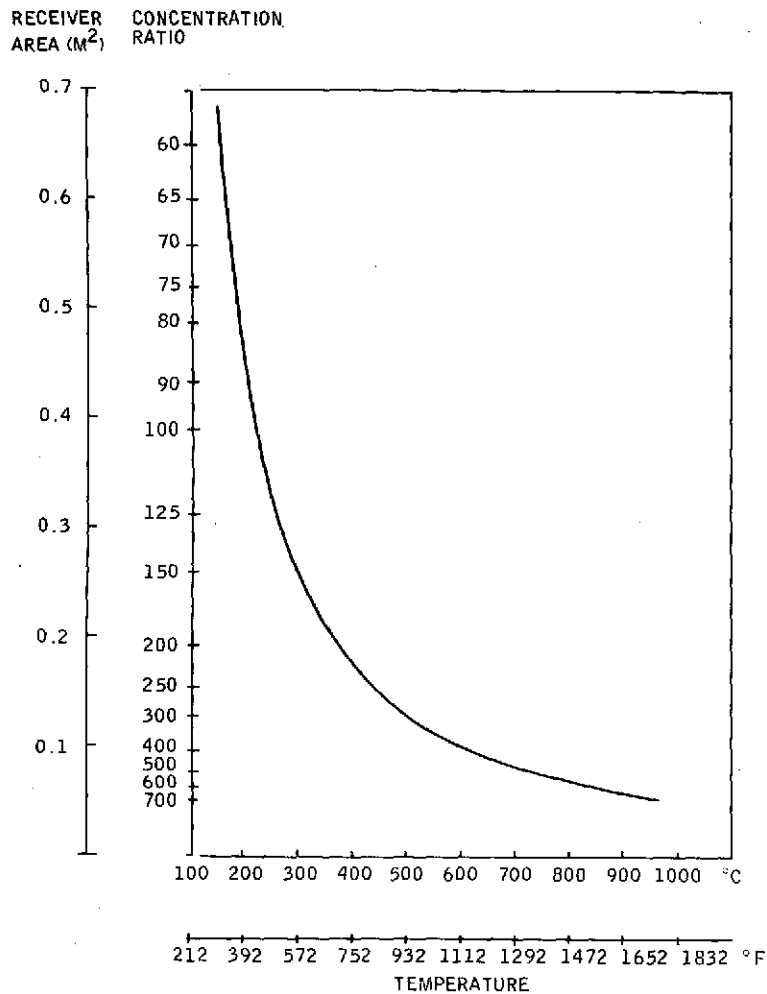
Figure 64. Dish Collector, 1/4° Mirror Errors
            Optimal Concentration Ratio
            versus Receiver Temperature
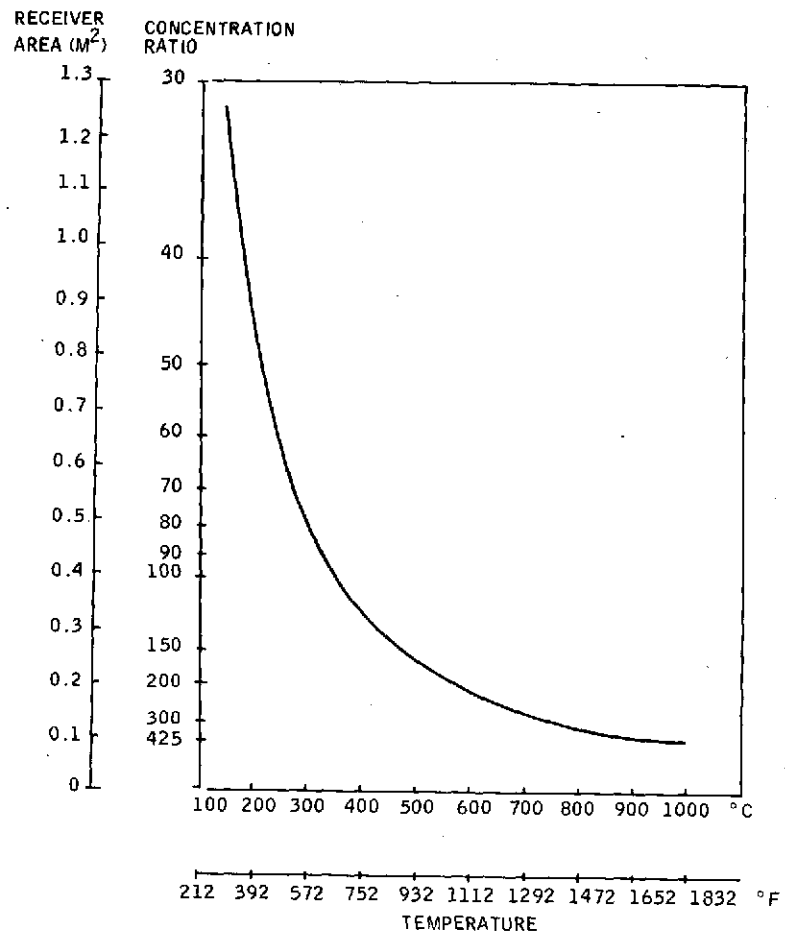
Figure 65. Dish Collector, 1/2° Mirror
            Errors Optimal Concentration
            Ratio versus Receiver Temperature
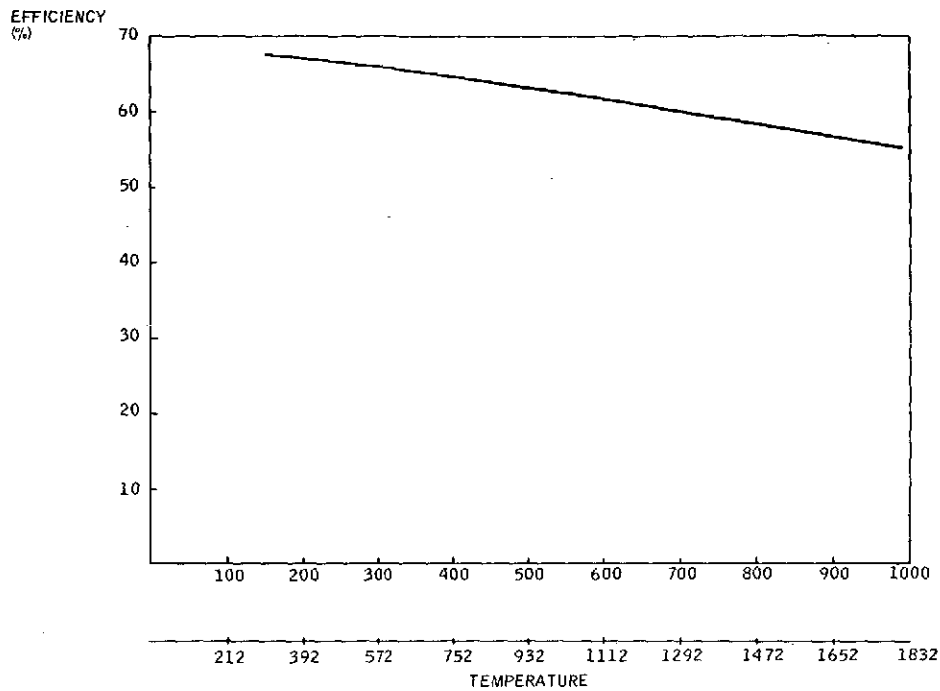
Figure 66. Dish Collector, 1/4° Mirror Errors Optimal
Efficiency versus Receiver Temperature
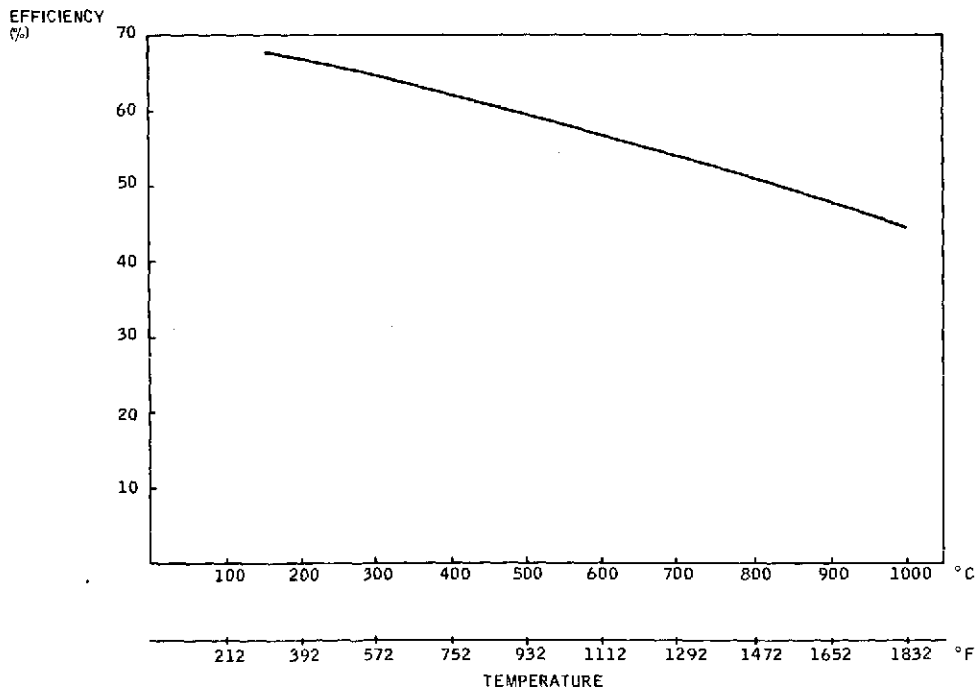
Figure 67. Dish Collector, 1/2° Mirror Errors Optimal
Efficiency versus Receiver Temperature

This plotting program was run for the dish collector on ray trace results, for which the collectors were so spaced so as to not shade each other. The output of these runs for the 1000°F and 1500°F dish collectors is shown in Figures 68 and 69.

The optimal concentration ratio for the 1/4 degree mirror slope uncertainty was 328 and the 1/2 degree mirror was 181 at 1000°F. The optimal concentration at 1500°F was 594 and 325 for the 1/4 and 1/2 degree mirror respectively.

The dashed line along the bottom of each curve (labeled Q LOSS) represents the magnitude of the thermal power lost (divided by the collector aperture area) by reradiation and convection from the receiver and glass vacuum envelope. The net thermal energy collected over an entire year is the integral of the difference between the loss line and the absorbed power curve. Also presented on the curves is the thermal power absorbed per unit aperture area and per unit mirror surface area. The integral for each dish collector configuration is shown in Table IX.

Table IX.   Net Energy/Dish Collector for One Year

Temperature	Error (Deg)	Orientation	Net Energy
1000°F	0.25	---	77232
1500°F	0.25	---	69299
1000°F	0.5	---	70767
1500°F	0.5	---	60208

The concurrent piping system design work indicated that, at temperatures above 600°F, the cost of piping would become prohibitive in the distributed systems. For this reason, the dish system was redesigned to operate at 630°F surface temperature to produce saturated steam or pressurized water at about 585°F (assuming a 45°F temperature drop from the receiver surface to the transport fluid). The preliminary study of the heat transfer for this system indicated that the heat flux should be limited to less than 300 kilowatts-per-meter squared of receiver surface. This limit resulted in a 20-centimeter diameter (spherical) receiver for a 40-meter square aperture area. This receiver also had no vacuum jacket and a "flat" 0.85 absorptance and a 0.85 emittance coating.

The absorption efficiency (not counting re-radiation) for such a design is plotted against receiver diameter in Figure 70.

Clearly, for all optics qualities from 0.05° rms slope and tracking uncertainty out to 0.50° rms, the 10-centimeter design attains the maximum efficiency possible consistent with the reflectivity of the mirror surface and the absorptance of the receiver surface. This design results in a relatively uniform flux distribution over the receiver surface because the energy is re-directed from a deep dish (110° rim angle) mirror which, in essence, "wraps around" the receiver. This "wrap around" tends to bring in the flux over a larger solid angle so that a simple spherical receiver can intercept it and better use its surface area.

The data of Figure 70 are presented in Figure 71 in dimensional form. This plot shows the net thermal power absorbed (including re-radiation and convection losses) versus receiver radius. If the heat flux were not an issue, the optimal design based on collection efficiency would have a receiver diameter of 8 or 9 centimeters. This design is said to be heat-flux-limited in concentration ratio, rather than optics-limited, as is the case of the trough collector.

The plotting program was run to give load-duration curves for the new dish design for several ground-cover ratios.
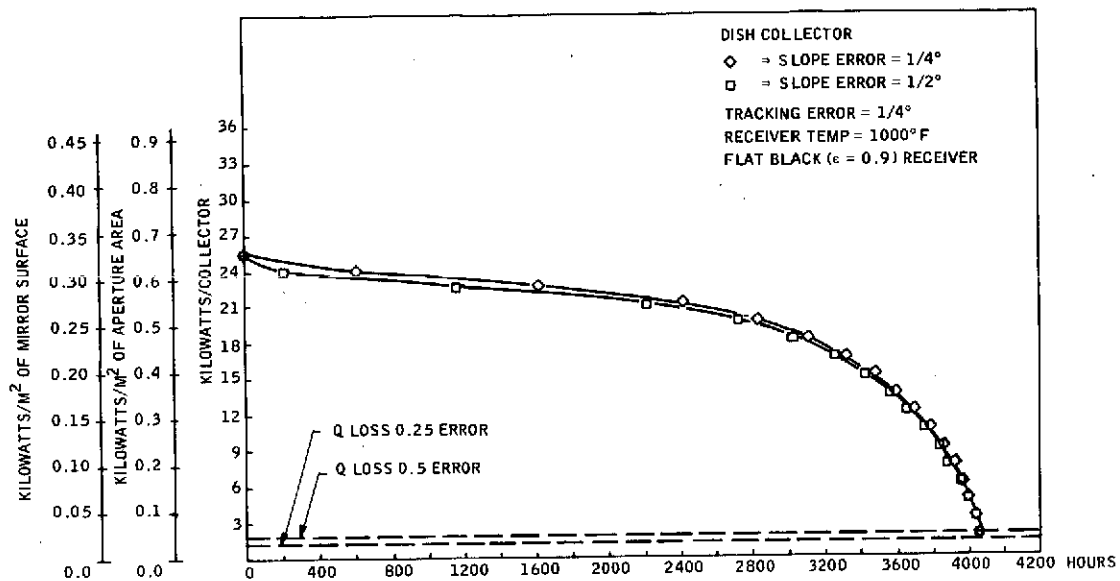
Figure 68. Dish Collector Absorbed Thermal Power versus Number of Hours for Which the Absorbed Power is at Least Equal to Indicated Value
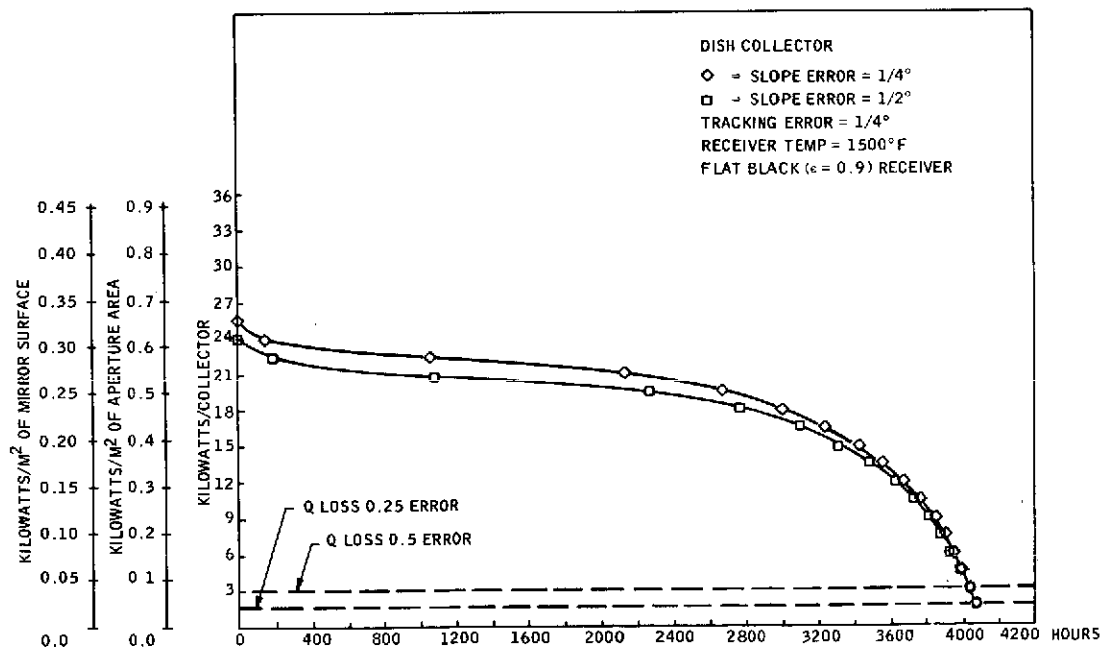
Figure 69. Dish Collector Absorbed Thermal Power versus Number of Hours in a Year for Which the Absorbed Power is at Least Equal to Indicated Value
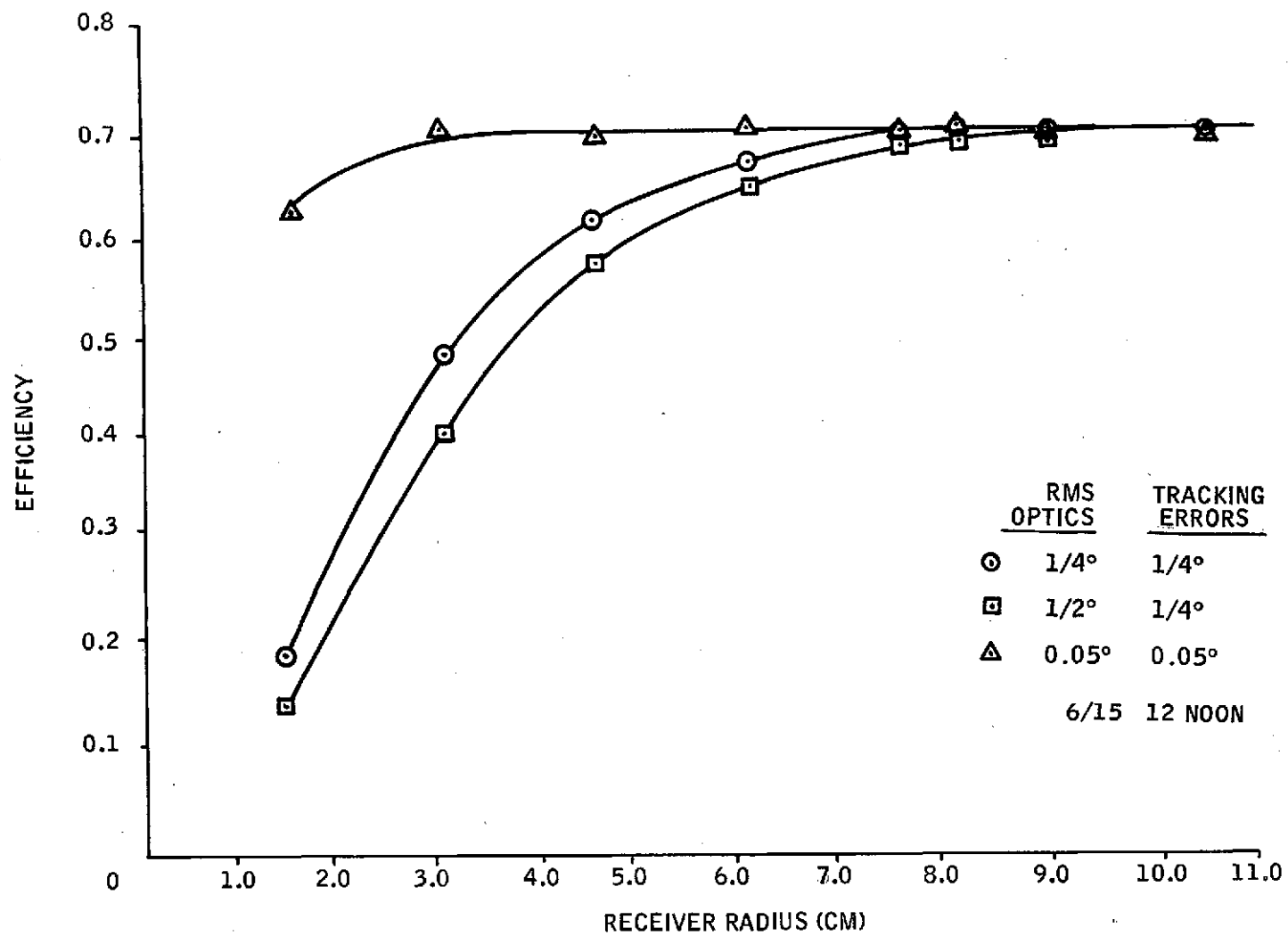
Figure 70.   Dish Efficiency versus Receiver Radius
Without Vacuum Jacket

C-2
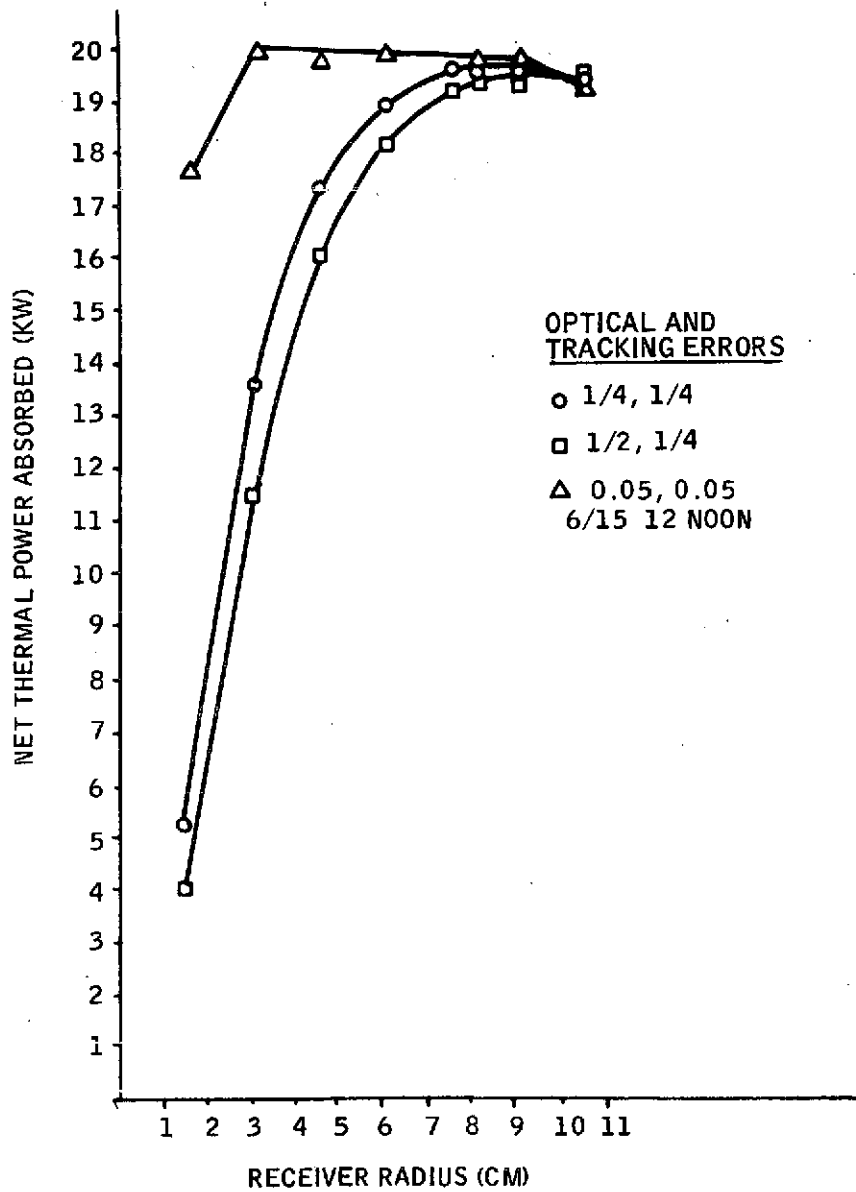
Figure 71. Dish Collector Without Vacuum Jacket
Net Thermal Power Absorbed versus
Receiver Radius

The general layout of the dish collectors on the field is shown in Figure 72 . This is a basic "hexagon, close-packed" array. The center-to-center distance (ΔEW, ΔNS) for the dish layout thermal power output duration curves (Table X) were run out for all eight-ground-cover ratios, with 1/4 and 1/2 degree optics at a receiver temperature of 630°F. Results are shown in Figure 73. The lowest curve shown has the control collector just touching all six of the adjacent collectors.

Table X. Center-to-Center Dish Collector Spacings

Ground Cover Ratio	ΔEW (feet)	ΔEW (meters)	ΔNS (feet)	ΔNS (meters)	1/2 ΔNS (feet)	1/2 ΔNS (meters)
0.9068	20.03	6.105	23.125	7.049	11.566	3.525
0.6297	24.04	7.327	27.750	8.458	13.88	4.231
0.4627	28.05	8.550	32.375	9.868	16.19	4.935
0.3542	32.05	9.769	37.000	11.278	18.51	5.642
0.2799	36.06	10.991	41.625	12.687	20.82	6.346
0.2267	40.07	12.231	46.250	14.097	23.13	7.05
0.1874	44.07	13.433	50.875	15.507	25.45	7.757
0.1451	50.08	15.264	57.812	17.621	28.92	8.815
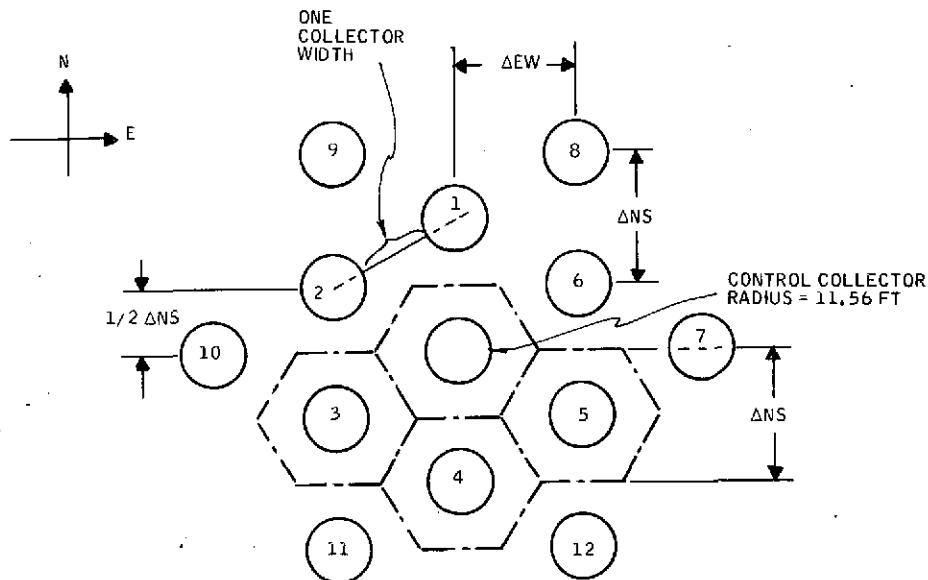
Figure 72. Dish Collector in Hexagonal Closed Pack Spacing on the Field
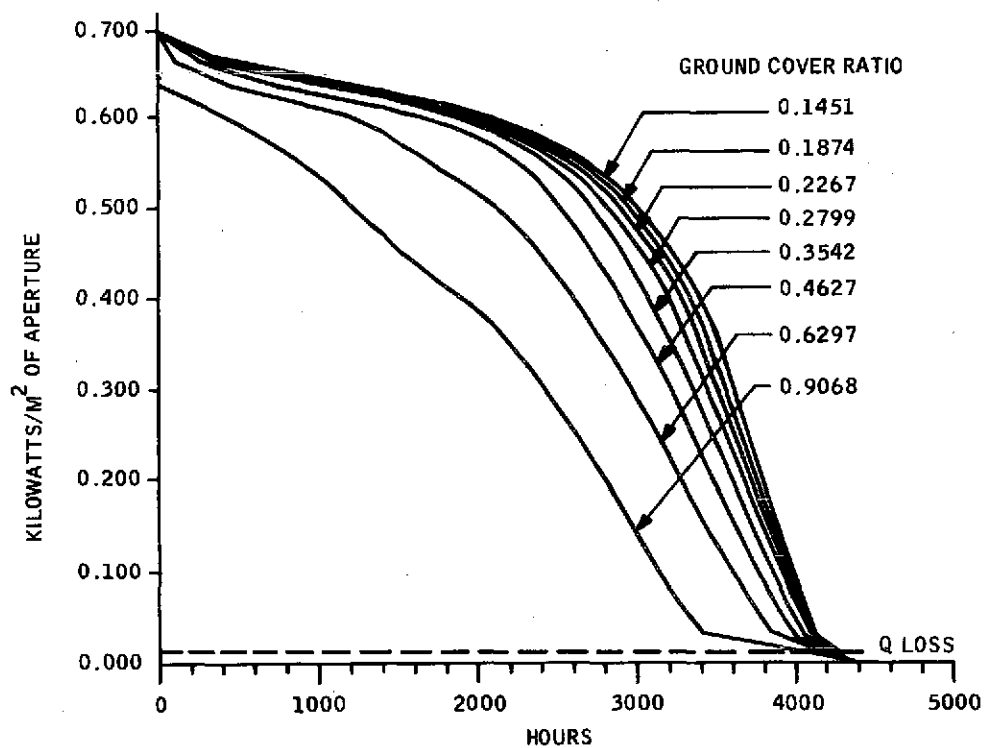
Figure 73. Dish Collector Without Vacuum Jacket Absorbed Thermal Power versus Number of Hours in a Year for Which Collector Absorbed Power is at Least Equal to Indicated Value

CENTRAL RECEIVER

The central receiver (power tower) was taken to be a tower with an absorbing top encircled by an array of flat mirrors which redirect the incident solar flux onto the absorbing top.

The following assumptions were made initially:

- The mirror array was rectangular, with a uniform spacing in each direction.

- The field and the mirrors were circular.

- The absorbing top (receiver) consisted of any combination of a sphere or part of a sphere, with or without cylindrical support. The configuration also involved the option of a vacuum gap around the receiver and contained by a glass envelope.

The assumptions were later modified to allow for square mirrors, square field, non-uniform spacing and three other receiver configurations: an inverted truncated cone, a cruciform and a crescent (see Section VI of this report). The coupling of the central receiver to a heat transfer and electrical power generation system is shown schematically in Figure 74.

Methodology

The Monte Carlo ray-trace technique was used to perform numerical experiments to define the integrated thermal performance of the system in the collection and net absorption of the solar flux. The formal definition of the problem can begin with the simplified case of a single mirror (heliostat) tracking the sun and redirecting the solar flux onto the receiver.

Given a position of the heliostat relative to the receiver, the amount of energy carried from any point on the sun's surface monochromatically at any given instant depends on the exact path of the ray through the optical interfaces of the system.

These interfaces are the mirror (heliostat), the optional glass envelope and the actual surface of the receiver. The mirror reflectance and the glass envelope transmittance are non-gray functions of the incident energy as well as of the incidence angle of the ray on the glass and mirror surface.

The receiver surface is held constant. An absorptance of 85 percent for all wavelengths and incidence angles can also be specified. The angle made by any ray with respect to each optical interface is a function only of the angular position on the solar disk whence the ray came and the impact point on the particular mirror.

Thus, for any wavelength and perfect optics, the energy carried from the sun to the receiver surface can be found by specifying the four coordinates of the ray, independent of the number of optical elements in the optics train.

If the sun's disk coordinates are δ_1 and δ_2 and the impact point coordinates are X_1 and X_2, then the total thermal power absorbed in a wavelength interval $d\lambda$ is

$$E_{d\lambda} = \int_{X_1} \int_{X_2} \int_{\delta_1} \int_{\delta_2} E(X_1, X_2, \delta_1, \delta_2, \lambda) \, dX_1 \, dX_2 \, d\delta_1 \, d\delta_2 \qquad (10)$$
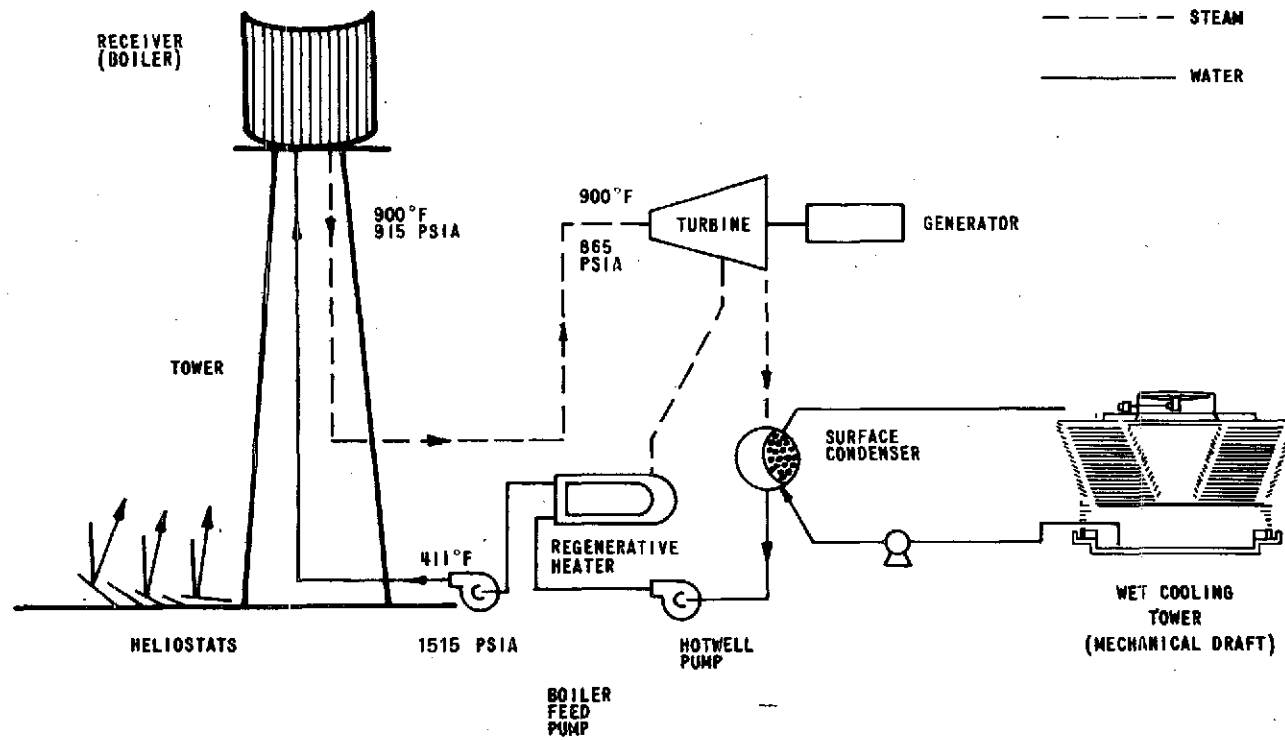
Figure 74. Coupling of Central Receiver to Heat Transfer and
Electrical Power Generation System

where X_1 and X_2 are bounded by the actual surface extent of the mirror. To obtain the energy from the entire solar spectrum, integration over all wavelengths is required. This yields

$$E_p = \underbrace{\int_\lambda \overbrace{\int_{X_1} \int_{X_2}}^{\text{mirror surface}} \overbrace{\int_{\delta_1} \int_{\delta_2}}^{\text{sun disk}} E(X_1, X_2, \delta_1, \delta_2, \lambda)\, dX_1\, dX_2\, d\delta_1\, d\delta_2\, d\lambda}_{\text{total spectrum}} \qquad (11)$$

Introducing finite quality optics into the model means that the uncertainty in tracking accuracy and mirror quality will be known only statistically.

There are four uncertain optical parameters that are known only statistically. The first two parameters are uncertainties in the angular position of the two gimbaled tracking drives (θ_1, θ_2). The second two parameters are the angular uncertainties in the mirror surface normal at any point on the mirror surface (ϕ_1, ϕ_2). We assume that each of these four parameters is statistically independent of each other, or any other design parameter. For example, a given error in the mirror normal is equally likely anywhere on the mirror surface. The mirror is not known as a continuous surface with smooth waves or ripples but rather as a probability distribution of mirror normals perturbed from the mathematically correct shape by an assumed probability distribution. For each statistically known variable, the distribution is understood to be a "normal" or "standard error" distribution.

Now consider a random variable, Z, defined by the normalized probability distribution, $P(Z)$. If we wished to calculate the mean value of $Z(=\bar{Z})$ or its expected value, we would form the integral of the product of $P(Z)$ times Z over all allowed values of Z, i.e.,

$$\bar{Z} = \int_{-\infty}^{\infty} P(Z)\, Z\, dZ \qquad (12)$$

To simulate a specific error set (θ_1, θ_2, ϕ_1, ϕ_2), one would have to evaluate the integral:

$$E_p(\theta_1, \theta_2, \phi_1, \phi_2) = \int_\lambda \int_{X_1} \int_{X_2} \int_{\delta_1} \int_{\delta_2} E(X_1, X_2, \delta_1, \delta_2, \lambda, \theta_1, \theta_2, \phi_1, \phi_2)\, dX_1\, dX_2\, d\delta_1\, d\delta_2\, d\lambda \quad (13)$$

Then the expected value of the thermal power absorbed ($\bar{E}_p$) is given by

$$E_p = \int_{\theta_1} \int_{\theta_2} \int_{\phi_1} \int_{\phi_2} P_{\theta_1}(\theta_1)\, P_{\theta_2}(\theta_2)\, P_{\phi_1}(\phi_1)\, P_{\phi_2}(\phi_2)\, E_p(\theta_1, \theta_2, \phi_1, \phi_2)\, d\theta_1\, d\theta_2\, d\phi_1\, d\phi_2 \quad (14)$$

because each distribution is statistically independent. The above expression is:

$$E_p = \int\limits_{\theta_1}\int\limits_{\theta_2} \underbrace{\int\limits_{\phi_1}\int\limits_{\phi_2}}_{} P_{\theta_1} P_{\theta_2} P_{\phi_1} P_{\phi_2} \int\limits_{\lambda} \underbrace{\int\limits_{X_1}\int\limits_{X_2}}_{} \int\limits_{\delta_1}\int\limits_{\delta_2} E d\delta_2 d\delta_1 dX_2 dX_1 d\lambda d\phi_2 d\phi_1 d\theta_2 d\theta_1 .$$

$$\underbrace{\qquad\qquad}_{\substack{\text{tracking}\\\text{errors}}} \underbrace{\qquad\qquad}_{\substack{\text{mirror}\\\text{imperfections}}} \underbrace{\qquad}_{\substack{\text{total}\\\text{spectrum}}} \Big| \underbrace{\qquad\qquad}_{\text{sun disk}}$$
$$\text{mirror}$$
$$\text{area}$$

(15)

To calculate the total thermal power redirected from the field of heliostats onto the receiver, one sums over the total number of heliostats

$$E_T = \sum_{i=1}^{\text{number of mirrors}} E_{p_i} .$$

(16)

Furthermore, integration over the total number of hours of sunlight during any given time period results in the expression

$$W_T = \int\limits_{\text{time period}} E_T \, dt .$$

(17)

The stochastic nature of four of the independent variables in the ten-integral of Equation (17) and the prime objective of performing a parametric study of the performance of the system indicated that the experimental Monte Carlo approach was more suitable.

A computer code was written to calculate experimentally the right-hand side of Equations (16) and (17). The basic premise was that the ratio of the thermal power incident on the receiver over the direct normal solar flux on the heliostat field can be obtained from the convergent ratio of randomly drawn rays which reached the receiver over the total number of rays drawn uniformly over the heliostat field, the value of each successful ray being scaled down approximately for reflectance and absorptance losses.

The ray trace followed the physics of each interaction of individual rays through the optics train. The execution flow is shown in Figure (75).

The user of the code has the option to vary at will any or all of the following input parameters:

- Option: integrate Equation (16) and/or (17)

- Time of day and/or date [if only equation (16)]

- Latitude

- Circular or square mirrors

- Circular or square field

- Uniform or non-uniform mirror spacing

92
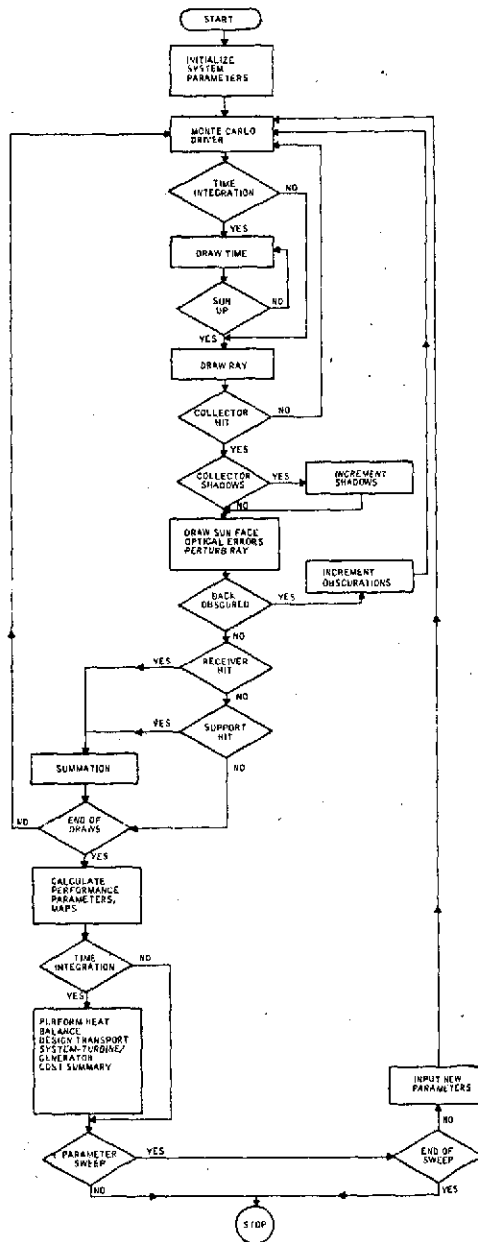
Figure 75. Central Receiver Simulation Code Execution Flow

93

- Field radius/side length

- Mirror optical quality

- Mirror tracking accuracy

- Single or multiple focusing points

- Tower height

- Receiver type

- Receiver dimensions

- Radius of the cylindrical support and extent of that support vertically below the center of the receiver

The output is a set of dimensional and non-dimensional performance parameters. If only the integral of Equation (16) is to be evaluated, then the nondimensional output is:

η_1 = Fraction of field flux that hits mirrors

η_2 = Fraction of field flux that was lost because of mirror shadows

η_3 = Fraction of field flux that was lost because of mirror obscuration

η_4 = Fraction of field flux that hits tower (receiver and support)

η_5 = Fraction of field area covered by mirrors

η_6 = Fraction of field area related to shadows on mirrors

η_7 = Fraction of field area related to back obscurations on mirrors

η_8 = Fraction of field flux that got to the receiver on the tower

η_9 = Fraction of field flux that got to the cylindrical support of the receiver on the tower

η_{10} = Ratio of obscuration flux losses over mirror flux

η_{11} = Ratio of shadow flux losses over mirror flux

η_{12} = Ratio of tower flux (receiver and support) over mirror flux

η_{13} = Ratio of receiver flux over mirror flux

η_{14} = Ratio of cylindrical support flux over mirror flux

The dimensional output is:

$Flux_1$ = Total flux on mirrors in Kw

$Flux_2$ = Flux losses due to shadows on mirrors in Kw

$Flux_3$ = Flux losses due to mirror back obscurations in Kw

$Flux_4$ = Total flux on tower (receiver and support) in Kw

$Flux_5$ = Flux on tower receiver in Kw

$Flux_6$ = Flux on cylindrical support of receiver in Kw

$Area_1$ = Total mirror area in ft sq

$Area_2$ = Shadowed mirror area in ft sq

$Area_3$ = Back obscured mirror area in ft sq

Map_i = Map(s) of the flux on the surface(s) of the receiver in Mw/m^2

Map_2 = Map of the flux on the surface of the cylindrical support of the receiver in Mw/m^2

Map_3 = Map of the field in terms of redirected flux that hits the receiver in Kw/m^2

If integration over time is performed [equation (17)], the code outputs a corresponding set of parameters except that the dimensional output is then in energy units, where appropriate.

In this case, the code can also design the whole system including the heat transport/ exchange and electric power generation subsystems and give a complete inventory and cost summary.

Details of the vector algebra involved in the mathematical modeling of the system are in Appendix C.

The first runs performed simulated a round field with uniform mirror spacing and round mirrors.

The field radius was defined as 0. 9 Km (2957 ft). The ground coverage factor was 0.456. The optical mirror quality and tracking accuracy were set as recommended by the University of Houston at 0.05 degree. The specification that the spherical receiver be seen by the most distant mirror on the field by 0.5 degree is equivalent to a receiver radius of 10. 56 m (34. 68 ft), given that the mirror radius was set to 3. 52 m (11. 56 ft). The tower itself was placed 243 m (797. 5 ft) due south of the center of the field.

A clear-day model and aluminum mirrors with a flat grey coating on the spherical receiver and the cylindrical support were used. The radius of the support was set at 1. 52 m (5 ft) and extended two spherical receiver radii vertically down from the junction.

A parametric sweep was performed of tower displacements and tower heights for 12/15, 3/15, and 6/15 from 8:00 p.m. to 12:00 noon for five different tower heights: 1800, 1500, 1200, 900, and 600 feet (450, 365.5 274.2, and 182.8 m). The results are shown in Figures 76 through 78. Integration over time showed that the tower height of 450 m (1500 feet) appeared close to optimal (Figure 79).

Flux Densities on the Central Receiver -- The ray trace code mapped the flux on the surface of a spherical receiver and its cylindrical support. The spherical receiver was zoned out in latitudes and each latitude was sectioned out in longitudes. (The maps consist of the flux on each one of these "geographical" sectors.) A similar geography was provided for the cylindrical support.

A typical flux density map is shown in Figure 80 for noon at June 15. The latitude is set to zero degrees at the top of the sphere and 180 degrees at the bottom, while longitude starts at 0 degree at due north and goes clockwise N-E-S-W-N. This map in isopleths of Mw/m^2 is also shown in Figure 81. The results indicate unacceptable power densities on the spherical receiver in the region of 2. 0 - 2. 5 Mw/m^2. This necessitated

THERMAL POWER
(10³ MW)

1.2

1.1

1.0

GROUND COVER = 0.456
FIELD LENGTH = 8,584.6 FT
NUMBER OF COLLECTORS = 45,396
TOWER: 797.5 FT SOUTH OF CENTER
    (TDISY = −797.5)
RMS OPTICS & TRACKING = 0.05°

TOWER HEIGHT

0.9
0.8
0.7
0.6
0.5
0.4
0.3
0.2
0.1
0

1800 FT
1500 FT
1200 FT
900 FT
600 FT
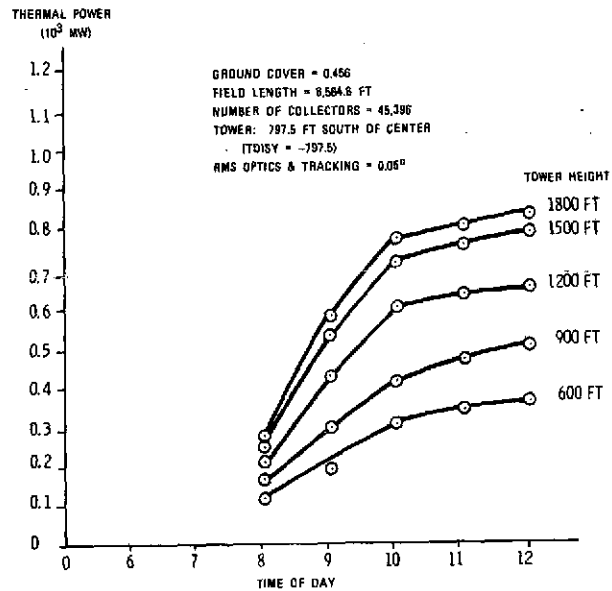
TIME OF DAY

Figure 76. Power Tower Total Absorbed
Thermal Power versus Time
of Day, 12/15

THERMAL POWER
(10³ MW)

1.2

1.1

1.0

GROUND COVER = 0.456
FIELD LENGTH = 8,584.6 FT
NUMBER OF COLLECTORS = 45,396
TOWER: 797.5 FT SOUTH OF CENTER
    (TDISY = −797.5)
RMS OPTICS & TRACKING = 0.05°

TOWER HEIGHT

.9
.8
.7
.6
.5
.4
.3
.2
.1
0

1800 FT
1500 FT
1200 FT
900 FT
600 FT
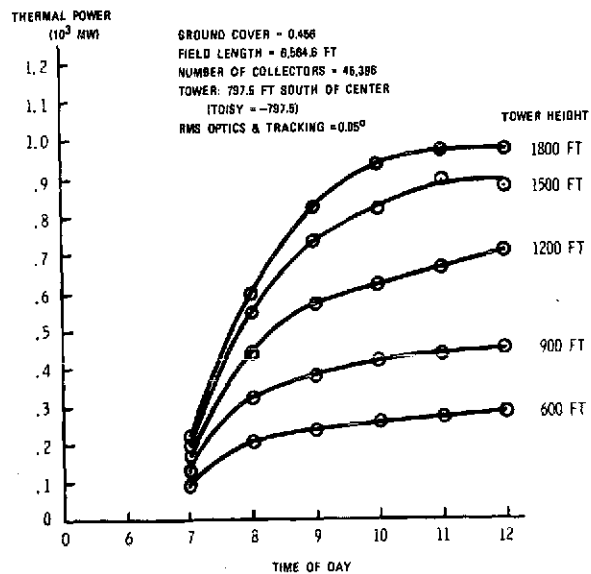
TIME OF DAY

Figure 77. Power Tower Total Absorbed
Thermal Power versus Time
of Day, 3/15

THERMAL POWER
(10³ MW)

GROUND COVER = 0.456
FIELD LENGTH – 6,564.6 FT
NUMBER OF COLLECTORS – 45,396
TOWER: 797.5 FT SOUTH OF CENTER
(TDISY = 797.5)
RMS OPTICS & TRACKING = 0.05°

TOWER HEIGHT

1800 FT
1500 FT
1200 FT
900 FT
600 FT
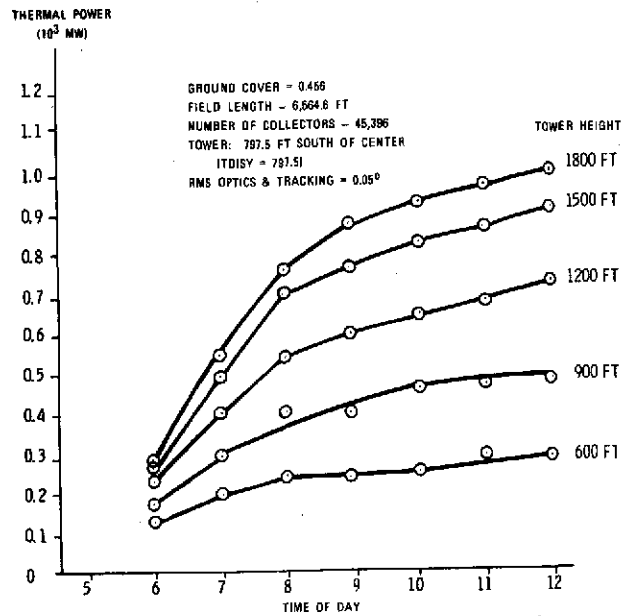
TIME OF DAY

Figure 78.   Power Tower Total Absorbed
Thermal Power versus Time
of Day, 6/15

THERMAL ENERGY
(10³ MWH)

GROUND COVER = 0.456
O =   12/15
□ =   3/15
△ =   6/15
FIELD LENGTH = 6,564.6 FT
NUMBER OF COLLECTORS = 45,936
TOWER: 797.5 FT SOUTH OF CENTER
(TDISY = =797.5)
RMS OPTICS & TRACKING = 0.05°
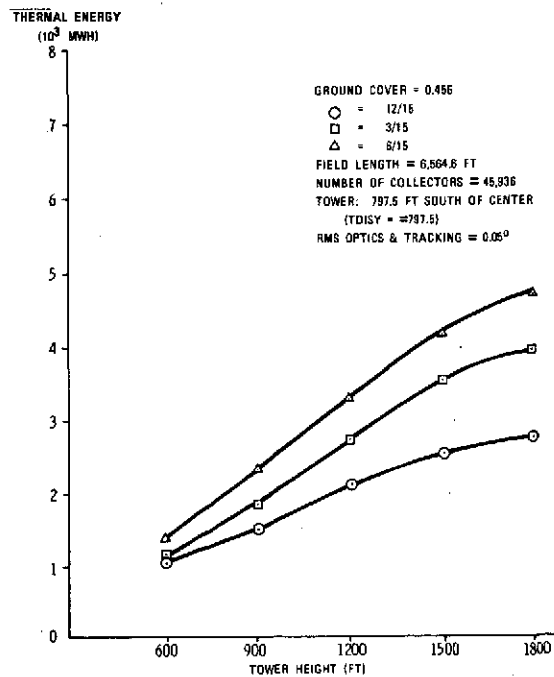
TOWER HEIGHT (FT)

Figure 79.   Power Tower--Energy
versus Tower Height

97

MW/SQ.M FLUX MAP OF POWER TOWER SPHERICAL RECEIVER DIVIDED
IN 15 LATITUDE ZONES(COLUMNS) AND 36 LONGITUDE SECTIONS(ROWS)

LAT LONG	12	24	36	48	60	72	84	96	108	120	132	144	156	168	180
10.00	0.000	.036	.027	.025	.042	.213	.516	1.281	1.882	2.035	2.462	1.623	1.065	.750	0.000
20.00	0.000	0.000	0.000	.023	.044	.274	.775	1.202	1.652	2.158	2.559	1.910	1.000	.547	0.000
30.00	0.000	0.000	0.000	.023	.020	.200	.627	1.322	1.797	1.967	2.003	1.758	.851	.377	0.000
40.00	.057	0.000	.027	0.000	.079	.134	.651	.977	1.824	2.200	2.392	1.484	1.292	.496	0.000
50.00	0.000	0.000	.060	0.000	.123	.175	.435	.870	1.557	2.300	2.210	1.252	.861	.564	0.000
60.00	0.000	0.000	0.000	.025	.103	.174	.490	1.104	1.638	1.987	1.752	1.408	.627	.542	0.000
70.00	0.000	0.000	0.000	0.000	.147	.210	.525	1.245	1.705	2.343	2.143	1.602	.980	.338	0.000
80.00	0.000	0.000	0.000	.022	.063	.210	.569	.950	1.675	2.240	2.178	1.746	1.379	.167	0.000
90.00	0.000	0.000	0.000	0.000	.022	.137	.405	.799	1.748	2.327	2.167	1.461	1.313	.190	0.000
100.00	0.000	0.000	0.000	.048	0.000	.151	.409	1.014	1.593	2.096	2.035	1.425	1.443	.505	0.000
110.00	0.000	0.000	0.000	0.000	.021	.218	.394	.956	1.529	2.179	2.010	1.566	.862	.530	0.000
120.00	0.000	0.000	0.000	0.000	.042	.208	.369	1.032	1.565	1.923	1.925	1.283	1.291	.331	0.000
130.00	0.000	0.000	0.000	.025	0.000	.230	.364	1.017	2.028	1.985	1.925	1.640	1.468	.165	0.000
140.00	0.000	0.000	0.000	0.000	.044	.079	.364	.921	1.643	2.206	1.640	1.646	1.468	.165	0.000
150.00	0.000	0.000	0.000	0.000	.043	.097	.327	.819	1.554	1.837	2.006	1.150	1.028	.356	0.000
160.00	0.000	0.000	0.000	0.000	.022	.018	.250	.557	1.094	1.760	1.777	1.815	1.170	.385	0.000
170.00	0.000	0.000	0.000	0.000	.039	.038	.174	.543	1.234	1.391	1.809	1.486	1.070	.355	0.000
180.00	0.000	0.000	0.000	0.000	.020	.037	.190	.566	.685	1.234	1.745	1.530	.438	.551	0.000
190.00	0.000	0.000	0.000	.025	.020	.062	.111	.298	.847	1.496	1.522	1.349	.739	.189	0.000
200.00	0.000	0.000	0.000	0.000	0.000	.042	.158	.341	1.149	1.538	1.703	1.453	.948	.704	0.000
210.00	0.000	0.000	0.000	.022	.019	.074	.207	.776	1.026	1.748	1.705	1.582	.811	0.000	0.000
220.00	0.000	0.000	0.000	0.000	.019	.096	.357	.702	1.359	1.635	2.121	1.547	.968	.358	0.000
230.00	0.000	0.000	0.000	0.000	.022	.125	.302	.794	1.604	1.864	1.823	1.283	1.137	.354	0.000
240.00	0.000	0.000	0.000	0.000	.148	.075	.325	.968	1.614	2.507	2.113	1.888	1.311	.361	0.000
250.00	0.000	0.000	0.000	.025	.042	.157	.398	.993	1.202	2.246	2.197	1.568	1.063	.542	0.000
260.00	0.000	0.000	0.000	.026	.087	.057	.422	.651	1.425	1.865	2.277	1.504	1.580	0.000	0.000
270.00	0.000	0.000	0.000	.022	.040	.039	.396	1.014	1.709	2.271	2.544	1.381	1.224	0.000	0.000
280.00	0.000	0.000	0.000	.050	.064	.181	.463	.912	1.467	2.064	1.741	1.655	.605	.548	0.000
290.00	0.000	0.000	0.000	0.000	.062	.175	.444	.819	1.684	2.502	2.168	1.592	1.217	.377	0.000
300.00	0.000	0.000	0.000	.048	.043	.217	.595	.891	1.792	2.271	2.268	1.410	1.055	.567	0.000
310.00	0.000	0.000	.029	.025	.086	.201	.520	1.098	1.939	2.176	1.661	1.065	.866	1.213	0.000
320.00	0.000	0.000	0.000	.067	.105	.561	.561	1.218	1.660	1.994	1.975	1.574	.930	.526	0.000
330.00	0.000	0.000	0.000	.050	.105	.276	.701	1.694	1.640	2.408	1.833	1.732	1.053	.518	0.000
340.00	0.000	0.000	0.000	0.000	.104	.134	.677	1.041	2.130	2.099	1.959	1.769	.767	.354	0.000
350.00	0.000	0.000	0.000	.025	.105	.212	.669	1.164	2.001	2.036	2.104	1.421	1.604	.361	0.000
360.00	0.000	0.000	0.000	.025	.059	.137	.521	1.240	1.534	1.913	1.838	1.281	1.240	.354	0.000

Figure 80. Flux Density Map on Spherical Receiver for
12:00 Noon on 15 June
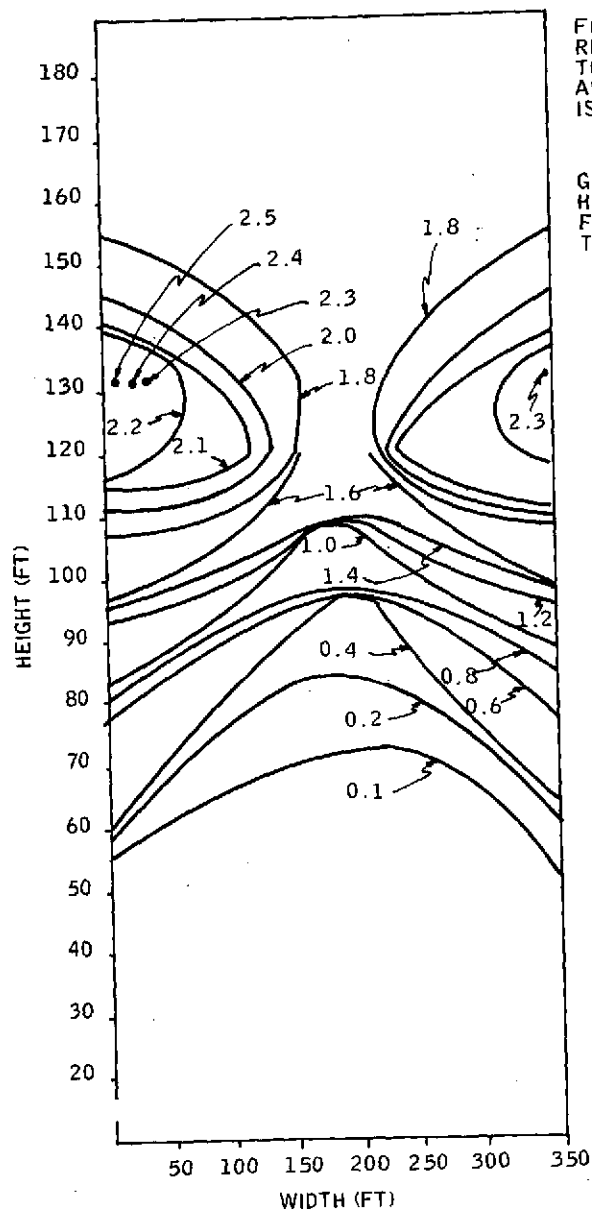
Figure 81. Flux Map in Isopleths of MW/m^2

modifying the code to include the simulation of other receiver configurations, the most promising being the cruciform and half-cylinder (cresent) receivers. Both of these concepts consisted of hung tubes acting as flow-through boilers which take in water at the bottom and deliver superheated steam out the top.

Further investigation of the power density distributions showed that even though the densities had been lowered to the range of 1.4-1.7 Mw/m^2, further refinement was necessary. The obvious candidate was the heliostat aiming strategy which, up to that time, involved a straight shooting for the center of the receiver. A new strategy was devised and proved successful.

The rationale assumed that the individual tube could be thought of as having three sections: the water heater, which takes the feedwater from nominally 425°F (218°C) up to the boiling point of water which is nominally 550°F (288°C) at typical working pressures, in the boiler and the superheater. The water heater and boiler sections can both withstand high-incident solar flux for different reasons. First, the water heater section has a relatively good heat transfer coefficient and the fluid temperature is low so that the high-temperature drops associated with high flux do not produce excessive tube skin temperatures (the tube skin temperature limit imposed by stress creep limits is nominally 1200°F (648°C). The boiler region can withstand high fluxes (1000 Kw/m^2) because of the excellent heat transfer associated with nucleate boiling. The superheater section cannot withstand such high fluxes (the limit is 400 Kw/m^2) because of the relatively lower heat transfer coefficient for a gas-metal interface. For the steam cycle under consideration, 75 percent of the energy absorbed is used in pre-heating and boiling the water, and the remaining 25 percent is needed to superheat the steam. At 1000 Kw/m^2 of flux on the boiler and water heater sections and 400 Kw/m^2 on the superheater, the preheating and boiling section is 55 percent of the tube length and the superheat section is 45 percent. With these numbers and the total power flux on the brightest day of the year, the length and width of the receiver can be calculated.

In the search for an aim point strategy which would achieve the desired flux distribution, the vertical location of the aim point on the tower's receiver was defined as a simple function of radial position of the aimed heliostat from the tower base. Ignoring for now the variation in the re-directed power from various locations in the field, the rate of increase in power from a narrow anulus of radius (R) from the tower base is proportional to R itself.

The integrated total power flux from the field area between two radial positions R_1 and R_2, therefore, goes as the difference of the squares of R_1 and R_2. To achieve a uniform flux over the receiver surface, the integrated power absorbed between vertical positions X_1 and X_2 on the receiver surface must be proportional to the difference X_1-X_2. This means that the vertical position of the aim point of a heliostat should be proportional to the square of the radial distance from the tower base out to that heliostat.

The other factor that influences the flux distribution on the receiver is the overlap of the light beams from the various heliostats in the field.

Clearly, the close-in heliostats must be aimed at the receiver center or the beam will miss the receiver off the top and bottom. Rays lost over the top would not be serious, but any significant flux on the tower near the receiver base could damage the tower itself.

This leads to an aim strategy whereby the nearest heliostats aim at the receiver center. The heliostats which aim at the boiler have aim points which move down from the receiver center with R^2. At the radial position where 75 percent of the redirected power is encircled, the aim point jumps up to the superheater. This boundary occurs at approximately 87 percent of the field radius. The superheat aim point moves up the receiver as the heliostat distance increases as shown in Figure 82.

100

R = RADIAL DISTANCE OF HELIOSTAT FROM CENTER OF FIELD
R_S = FIELD SIZE RADIUS REQUIRED TO PRODUCE SATURATED STEAM
$R_S^2 / R^2_{TOTAL} = 0.75$
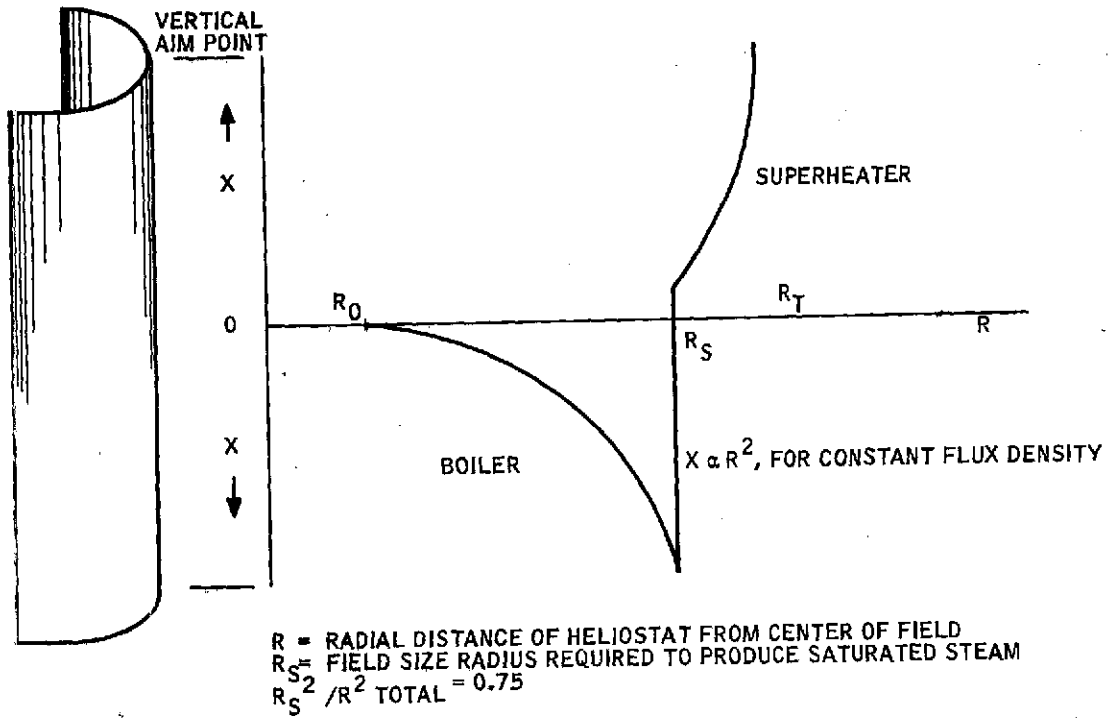
Figure 82. Heliostat Vertical Aim Point Strategy

After the incorporation of the aim strategy, the code was used to simulate the crescent receiver. The results for noon 6/15 are plotted in terms of isopleths of Mw/m^2 in Figures 83 and 84. The meaning of these results becomes more explicit when one examines the variation of the thermodynamic variables along the height of one tube, as shown in Figure 85. The design is within engineering limits, even for this one worst case of high flux.

The code was also exercised for the cruciform receiver option and the results for noon 6/15 are shown in Figures 86 through 89. Again, the design was shown to be within engineering limits.

It should be noted that in both the crescent and cruciform designs presented, the safety margin is minimal.

Another issue which affects aim strategy is the choice between once-through and drum type boilers. Our baseline design is once-through, but the drum design was a serious candidate. The mass flow into the drum is controlled by a liquid level sensor in the drum. As water is boiled off and passes into the superheater section of the receiver, the liquid level sensor activates a control valve to introduce water into the drum as needed. The rate of steam flow to the superheater is controlled entirely by the net heat flux on the boiler. The superheater raises the steam temperature by an amount proportional to the heat flux on the superheater and inversely proportional to the mass flow through it.

Clearly, any drum-type receiver will be designed to operate with the correct ratio of boiler heat flux to superheater flux so that the desired outlet superheater temperature will be maintained. Unfortunately, the daily and yearly variations of the sun's position will cause continuous deviations in solar flux on the receiver, which will result in imbalances between the boiler and superheater. Some kind of continuous feedback control system will be needed to monitor the output temperature and make appropriate corrections.

With the once-through boiler design, an over or under temperature condition is corrected by increasing or decreasing the mass flow. With the drum-type system, solar flux must be diverted to change the mass flow. For example, an over temperature would require a transfer of flux from the superheater to the boiler, and the reverse for under temperature. This requires that the aim point of at least some of the heliostats be a variable, subject to continuous feedback control. The simplicity of the once-through design and the ease of heat balance control were strong factors in the choice of the once-through, as opposed to drum-type receivers as the baseline design.

RECEIVER/TOWER DESIGN

Tower Configuration

The tower design parameters for a central receiver generating plant cannot be calculated independently of the heliostat field parameters. Sufficient calculations were performed though to ensure that the methodology was understood and to obtain a good estimate of the tower height as a function of plant generating capacity. The results for two plant sizes are shown below:

Plant Size	Tower Height
60 Mw	750 feet
215 Mw	1500 feet

102
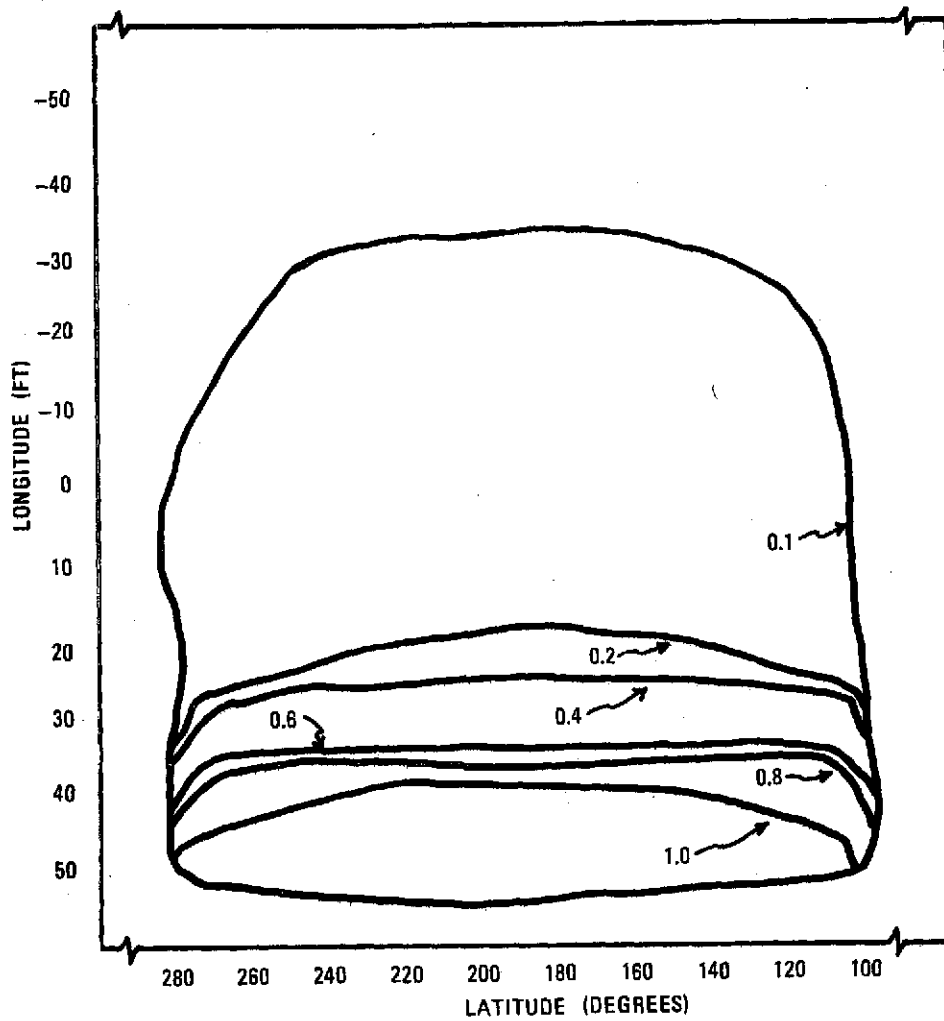
Figure 83. Flux Map of Crescent with Aim Strategy in Isopleths of Mw/m^2, Noon 6/15, South Side

NOON   6/15

GROUND COVER RATIO ➜ 0.456
HELIOSTATS ➜ 35,275
RADIUS OF HELIOSTATS ➜ 11.562 FT
RADIUS OF FIELD ➜ 3282.276 FT

103
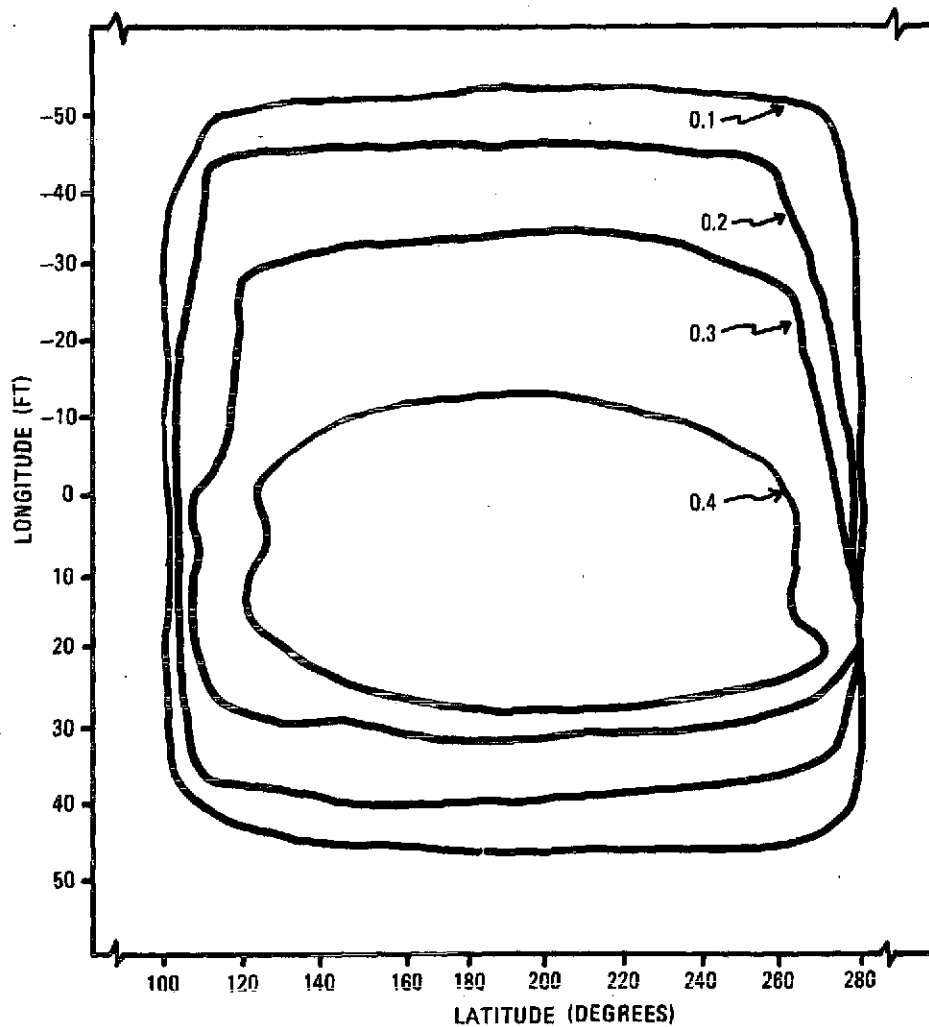
Figure 84.   Flux Map of Crescent with Aim Strategy in
Isopleths of Mw/m^2, North Side Noon 6/15

NOON   6/15

GROUND COVER ⇒ 0.456

HELIOSTATS ⇒ 35,275

RADIUS OF HELIOSTATS ⇒ 11.562 FT

RADIUS OF FIELD ⇒ 3282.276 FT
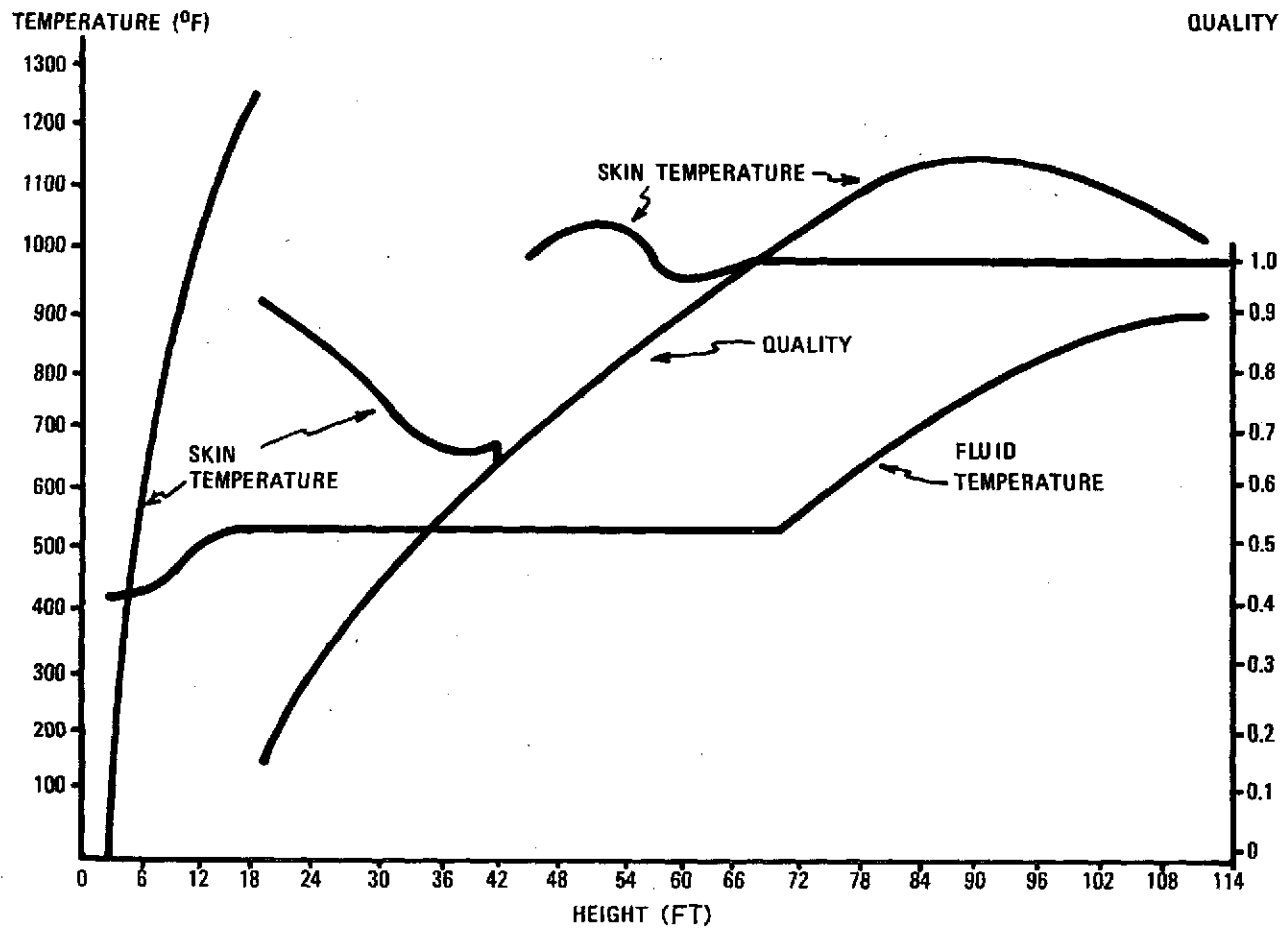
Figure 85. Variation of Thermodynamic Variables
Versus Crescent Height

NOON   6/15

GROUND COVER ⇒ 0.456
HELIOSTATS ⇒ 35,275
RADIUS OF HELIOSTATS ⇒ 11.562 FT
RADIUS OF FIELD ⇒ 3282.276 FT
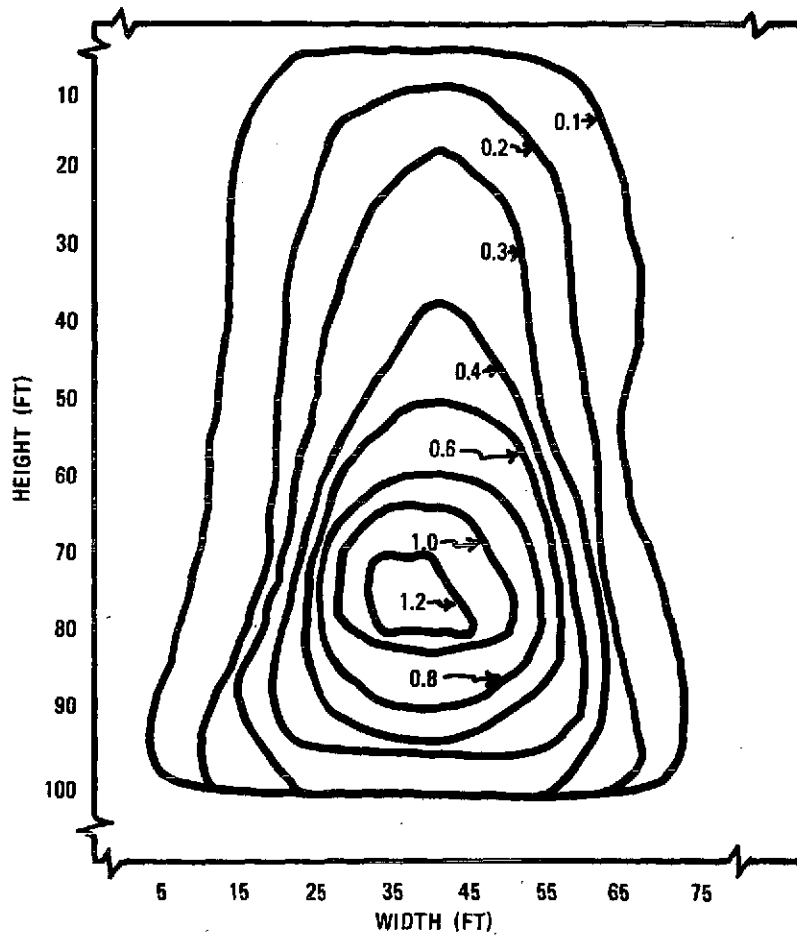
Figure 86. Flux Map of Cruciform Receiver on
Power Tower with Aim Strategy in
Isopleths of Mw/m^2 North-South Plane
East Surface.

NOON   6/15

GROUND COVER ⇒ 0.456
HELIOSTATS ⇒ 35,275
RADIUS OF HELIOSTATS ⇒ 11.562 FT
RADIUS OF FIELD ⇒ 3282.276 FT
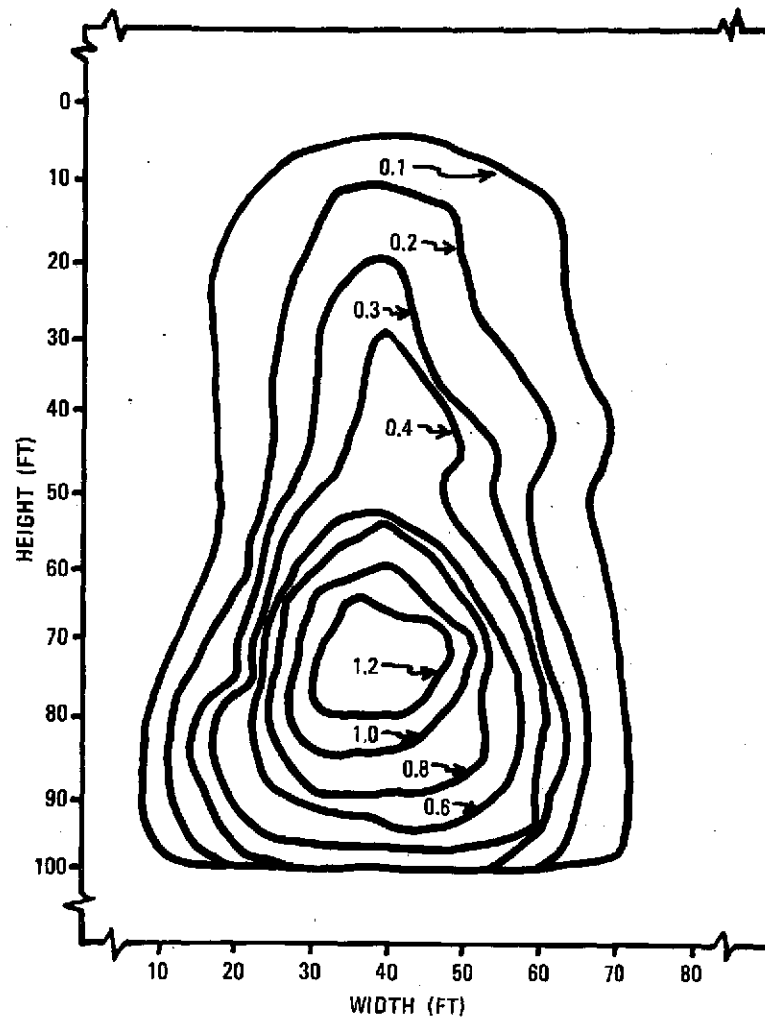
Figure 87.   Flux Map of Cruciform Receiver
on Power Tower with Aim Strategy
in Isopleths of Mw/m^2 North-South
Plane West Surface.

107
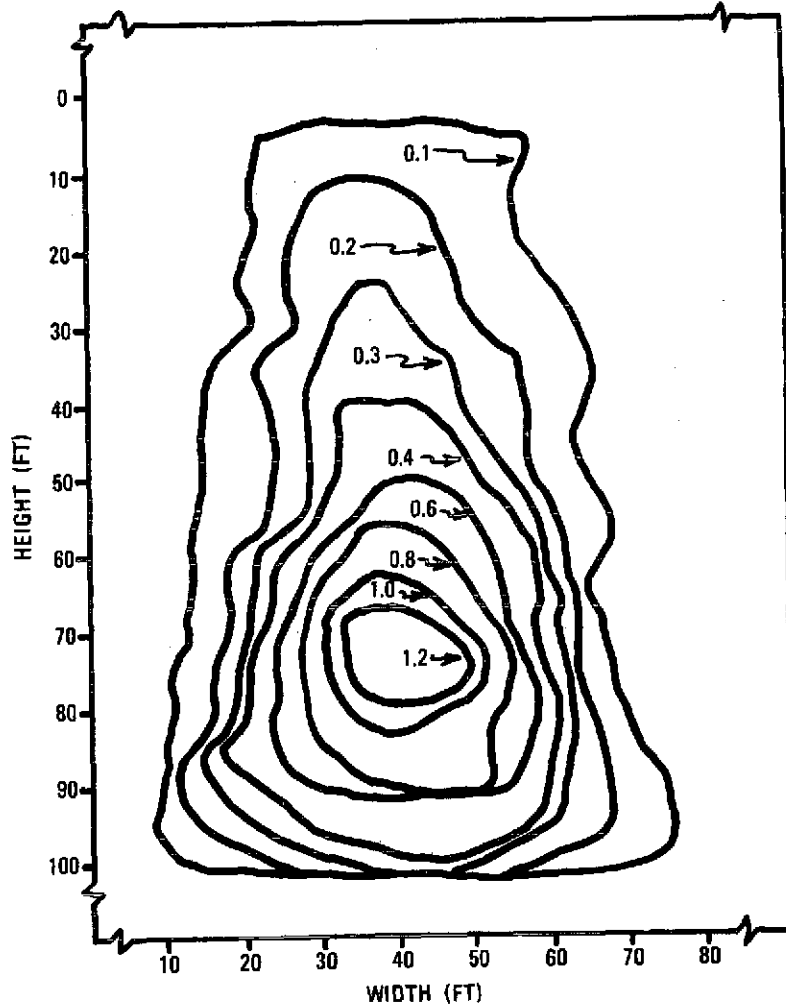
Figure 88. Flux Map of Cruciform Receiver
on Power Tower with Aim Strategy
in Isopleths of Mw/m^2 East-West
Plane South Surface.

NOON   6/15

GROUND COVER RATIO ⇒ 0.456
HELIOSTATS ⇒ 35,275
RADIUS OF HELIOSTATS ⇒ 11.562 FT
RADIUS OF FIELD ⇒ 3282.276 FT
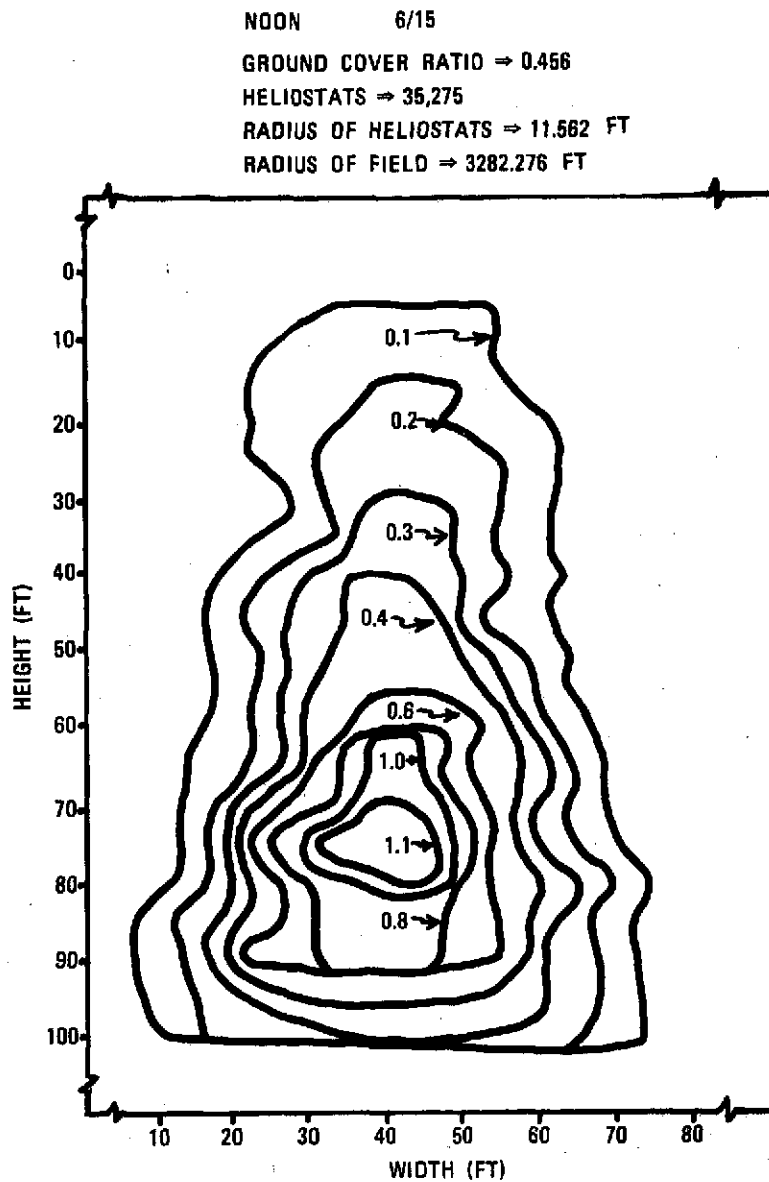
Figure 89.   Flux Map of Cruciform Receiver
on Power Tower with Aim Strategy
in Isopleths of Mw/m^2 East-West
Plane North Surface.

Preliminary design requirements for the tower are that it should:

- Be capable of supporting the mass of the receiver with maximum sway of 18 inches under steady wind velocities of 120 miles per hour at the top and 75 miles per hour at ground level

- Provide stability for the receiver in a Seismic Zone, I, II, or III

- Provide a supporting structure for the riser and downcomer piping which circulates the heat transfer fluid between the base and the top of the tower

- Provide personnel access to the top of the tower for receiver maintenance

- Provide a design lifetime of at least 30 years

Three structural concepts were considered for their ability to meet the above requirements: reinforced concrete (slip form construction), free standing welded steel construction, and guyed steel construction. Our experience indicates that the guyed tower would be unsatisfactory for this application. Although it is less expensive than the other two candidates, the drift (sway) and buckling problems caused by the combination of a heavy mass at the top and wind gust or seismic loading would require that extensive design studies be made to prove feasibility. Furthermore, the reliability of guyed towers is not as great as the other two candidates. Failure of these towers is not uncommon and recent episodes have been recorded in Texas, Iowa, and Florida. Therefore, the choice of design was limited to reinforced concrete and welded steel construction.

If aesthetics is not an issue, the costs of reinforced concrete and welded steel construction are about the same. There are, however, advantages to the reinforced concrete construction which have led us to select this concept. These advantages are:

- Simpler to design

- Costing experience immediately available from wide industry practice

- Enclosed tower acts as thermal insulation for downcomers and risers

- Provides enclosed space for maintenance of receiver, risers and downcomers

Reinforced concrete structures, using the slip form process, have been built up to heights of 1500 feet without difficulty. The CN tower in Toronto, Canada, which is nearing completion, is a good example of a tall (1500 feet) reinforced concrete tower.

The detailed design parameters for the reference central receiver system tower are listed in Section X.

The tower costs were calculated on the basis of a 40-foot outside diameter at the top and a load-carrying capacity of 500 tons. The M. W. Kellogg Company, which has extensive experience in the construction of tall chimneys, supplied the following costs for a tower height of 750 feet.

Seismic Zone	Cost - $
I	2,000,000
II	2,000,000
III	2,200,000

The costs for towers of different heights were calculated from these costs by applying the industry-wide relationship of cost being proportional to the square of the tower height. The results of these calculations are shown in Figure 90. These costs include the tower, base, access elevator, and aircraft warning light system.

Receiver Design

In the design of the receiver for the selected steam cycle, (850 psig/900°F) the following choices were made:

Tube Type versus Other -- Conventional steam generators are constructed of tube sheets. No other geometry was found which provided any advantages over a tube-type receiver. In addition, tube sheets are easily fabricated and commercially available in many sizes and materials.

Fully-Exposed versus Half-Exposed Tubes -- When a plane or curvilinear sheet of elastic material, such as a tube sheet, is irradiated on one side only, the differential thermal expansion across the panel causes it to alter shape. If this alteration of shape is structurally opposed, stresses will result; if there is no restraint, translations and rotations of portions of the sheet will result. In the present case, these motions would cause difficulties with the large number of connections between the individual tubes and any headers or drums. Therefore, only fully-irradiated tube designs were considered. This also has the advantage of reducing the required tube length and receiver weight by a factor of two.

Drum-Type versus Once-Through -- A tube-type receiver which produces superheated steam can be one of two types. In a drum-type receiver, the feedwater is heated until some boiling has occured. This water-steam mixture then enters a drum (steam separator) where the steam is removed and fed into a superheater. In a once-through receiver, the feedwater travels through a single tube (one of many) until it has reached the desired degree of superheat. A schematic of these two receiver types is shown in Figure 91.

The drum-type receiver has a higher capital cost. In addition to the cost of the large, heavy drum, there is the added cost of the supporting structure for the drum. Since only part of the boiler-region throughput is converted to steam, the excess water must be returned from the drum to the feedwater cycle. This involves additional pumps, piping, and controls.

Since the drum-type receiver has no advantages for a solar plant, the once-through receiver is superior.

Receiver Geometry Options -- The design geometries of a once-through, fully irradiated, tube-type receiver are limited. Standard boiler practice has demonstrated the superiority of tube-wall sheets, as shown in Figure 92 supported from above with freedom to expand downward. The two available alternatives are the crossed-sheet type, shown in Figure 93 and curvilinear-sheet type, shown in Figure 94.

The goal of receiver design is to determine a geometry which, when coupled with an optimized heliostat field and aiming philosophy, will have the following results:

- The flux will be the same on both sides of the tube sheet for any point on the sheet. The magnitude of the flux may, of course, vary from point to point on the sheet.

- The flux distribution along a single tube will be the same for all tubes for any specific time and day of the year.

The disadvantage of the crossed-sheet receiver is that these two goals cannot be satisfied without a heliostat aiming philosophy which is a function of both time of day and day of the year. This would add a new order of magnitude to both the cost and complexity of analysis of the heliostat control system.

111

POWER TOWER CONSTRUCTION SPECIFICATIONS

- CYLINDRICAL SHELL, REINFORCED CONCRETE CONSTRUCTION
- DESIGNED FOR WIND GUSTS OF 120 MPH MAXIMUM
- TAPER 4-5.5 FT/100 FT. DEPENDING ON HEIGHT
- APPROXIMATELY 30,000 CU. YDS. OF CONCRETE IN 1500 FT. TOWER
- TOWER CONTAINS A 3-MAN ELEVATOR AND STAIRS
- LIGHTING: STROBE-LIGHTING FOR AIRCRAFT WARNING
              INTERIOR LIGHTING FOR MAINTENANCE
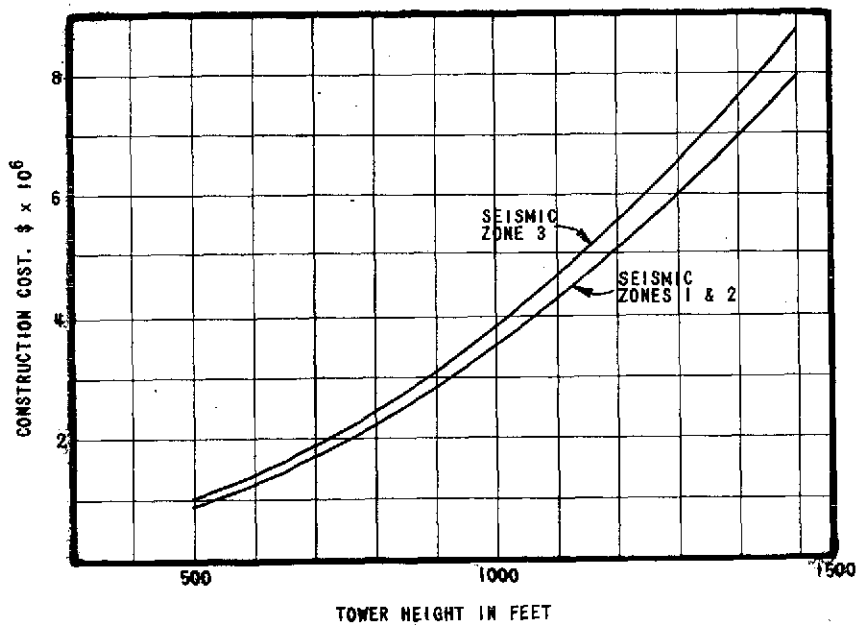
Figure 90. Tower Specifications and Construction Costs
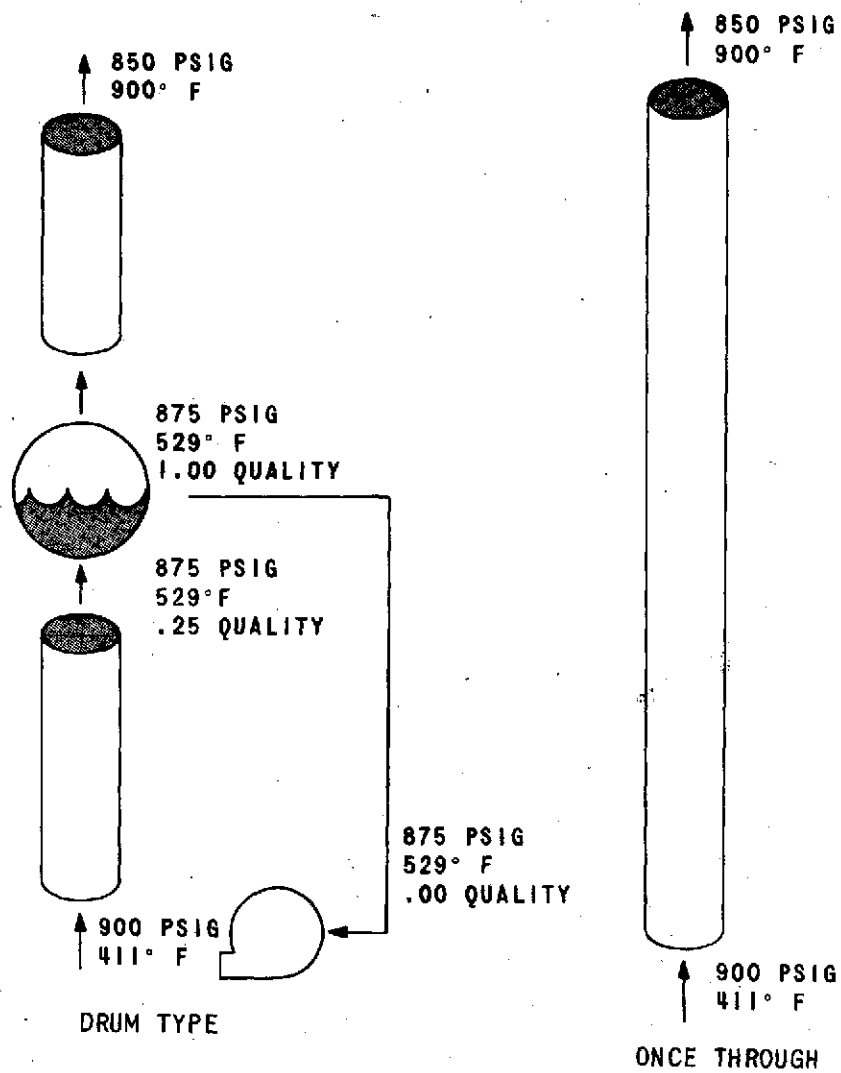
Figure 91.   Schematic of Drum and Once-Through Boilers
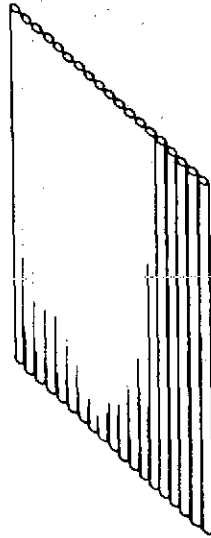
Figure 92. Single Tube Sheet Wall
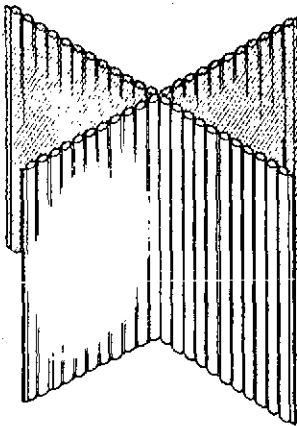
Figure 93. Crossed Tube
Panel Receiver
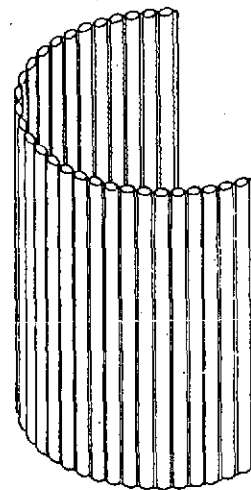
Figure 94. Curvilinear
Tube Sheet

114

The curvilinear-sheet receiver, however, will satisfy both of these requirements. Preliminary analysis indicated that a reasonable first choice of geometry was a right circular cylinder with an angle of enclosure of 180 degrees (Figure 95). This receiver geometry, the Crescent, was analyzed with the Honeywell Ray-trace Code and the results were as follows, for a tower located in the center of a circular field:

1) For any given time of day and day of the year, the flux variation among tubes was small, almost always less than 20 percent. This was true even though the heliostat aiming philosophy was not varied with time.

2) The total flux on the two sides of the sheet was closely balanced, as shown below.

Day	Time	Power (North)	Power (South)
6/15	9:00	239 Mw(th)	303 Mw(th)
6/15	10:30	266	331
6/15	12:00	273	319
12/15	12:00	258	259

3) The flux along a single tube was different for the north and south sides of that tube. This was caused by the aim point being the same for north and south heliostats.

The assumptions used to arrive at a point design were as follows:

• The heliostats were of constant size and spacing and were in a circular field

• The tower was in the center of the field

• All the heliostats were aimed at the same point in a horizontal plane. Different areas of the field were aimed at different vertical points in order to obtain vertical flux dispersion

The results of this point design are presented in Section X.

In calculating the receiver cost, the weights of the receiver tubes and structural supports were determined. From these weights, the costs of the individual tubes and supports were calculated. The cost of the receiver tubes was based on $2.50 per pound for stainless steel boiler tubes. The assembled selling costs were estimated as four times the material costs; the factor of four being a commonly used factor in the boiler construction industry. The erection costs were calculated at 10 percent of the assembled receiver cost. This factor of 10 percent was based on a detailed estimate of the time, manpower, and equipment required for erection.

STEAM
OUT

WATER
IN
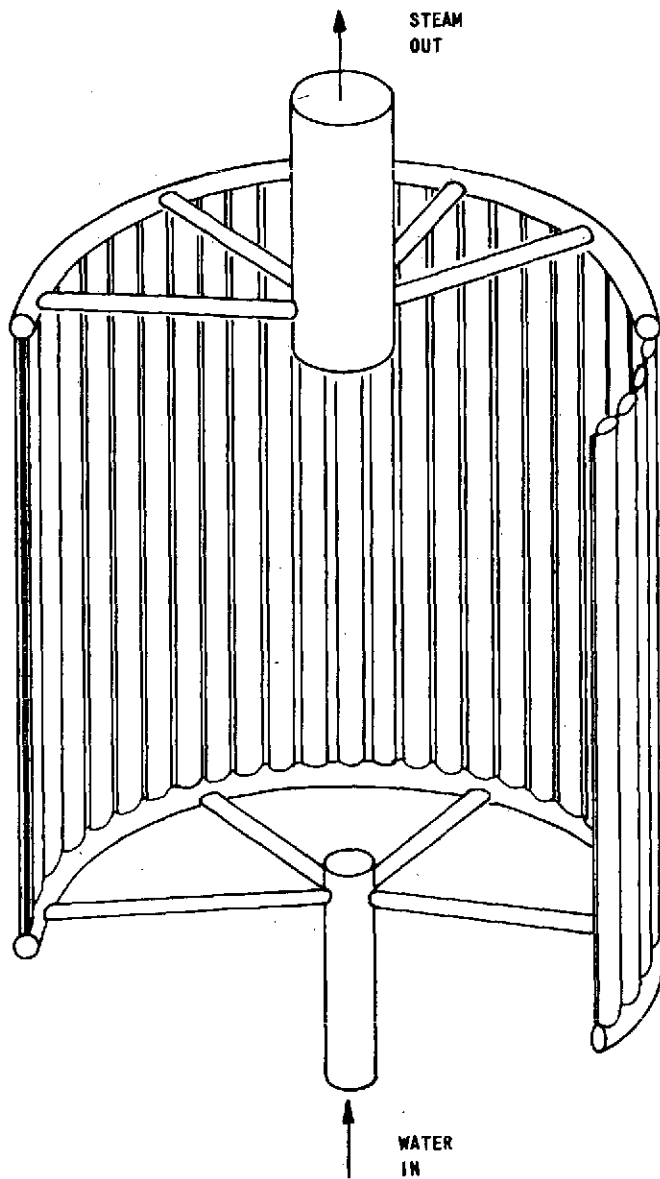
Figure 95. Crescent Receiver

ENERGY PERFORMANCE COMPARISON

The integrated yearly energy absorbed by the dish and trough collectors can be calculated from the load-duration curves. Results are plotted in Figures 96 and 97 in terms of thermal energy absorbed per square meter of aperture versus ground-cover ratio. For comparison, the corresponding curve has been plotted for a central receiver with a 450-meter tower, a square field with a uniform heliostat spacing, and a field length of 2000 meters. The receiver was a hemisphere and the heliostats circular.

In both figures, the 1/4 and 1/2 degree error labels apply only to the trough collector. The power tower was taken to have a 0.05 degree rms slope uncertainty in each tracking axis and on the mirror surface. The dish results apply to all optic qualities from 0.05 to 0.50 rms as these designs are heat-flux-limited rather than optics-limited. The ordinate, labeled kwh/m^2 aperture, is the integrated thermal energy divided by the aperture area for the dish and trough, and the mirror aperture area for the power tower. Note that all three mirrors had an aperture area equal to 420 square feet (the heliostat aperture area is equal to its surface area).

The trough system can be run at a ground-cover ratio of up to 1.0 for the east-west and north-south configuration, and higher than 1.0 for the polar mount. The polar mount collectors can overlap on the ends, as seen from above, because they are pitched up out of the ground plane. That is, the low end of the north adjacent collector can be under the high end of the control collector without becoming entangled if the end support structure is designed to allow it.

The yearly integrated thermal power absorbed per square meter of the collector field versus the ground-cover ratio is shown in Figures 98 and 99. This performance measure expresses the relative ability of the various systems to collect the maximum amount of energy possible with the suitable land available in the United States.

The final integrated performance measure is the net thermal energy collected per square meter of mirror surface plotted versus ground-cover ratio (Figures 100 and 101).

117
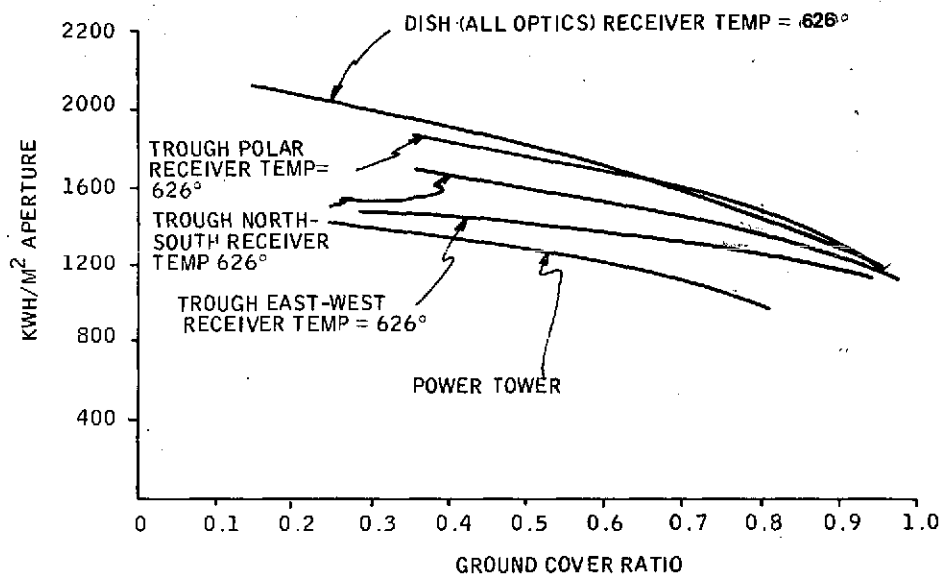
Figure 96. Integrated Thermal Energy versus Ground Cover
Trough Optics and Tracking Rms Error = 1/4°;
Latitude = 33°
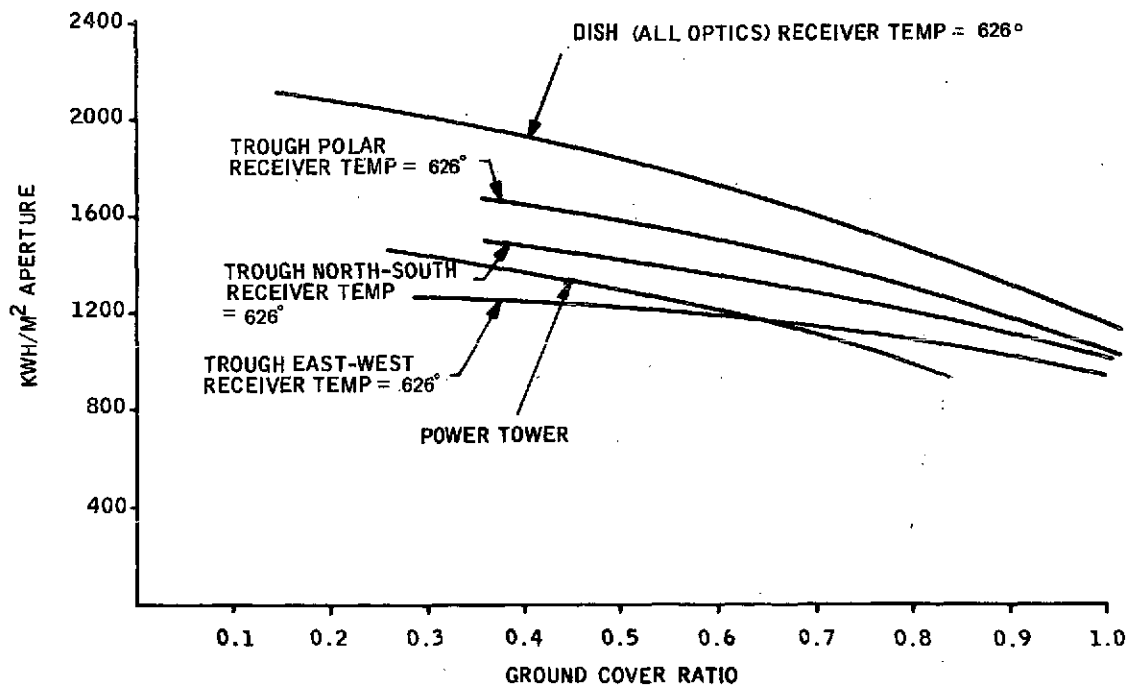
Figure 97. Integrated Thermal Energy versus Ground Cover,
Latitude = 33°, Trough Optics and Tracking Rms
Error = 1/2°

118
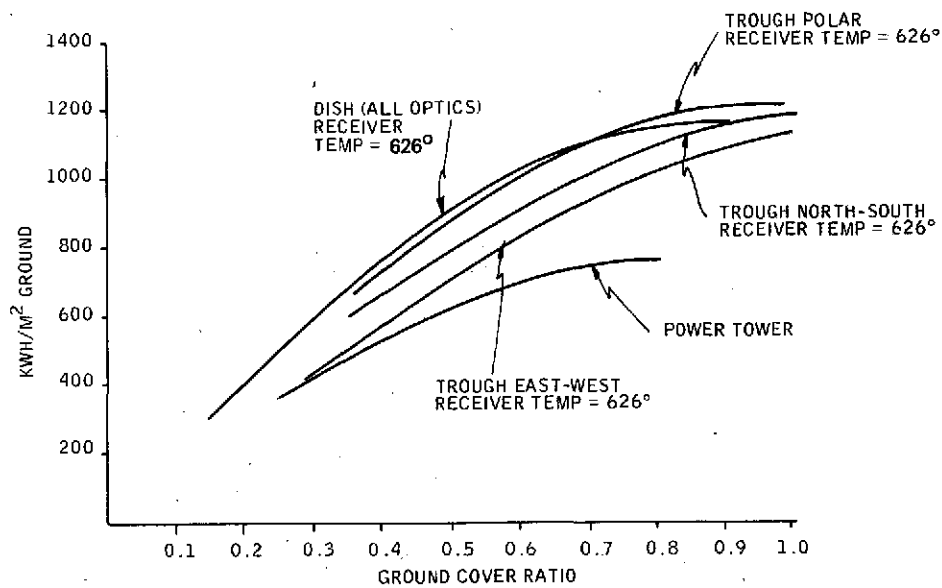
Figure 98.   Integrated Thermal Energy versus Ground Cover,
Latitude = 33°, Trough Optics and Tracking RMS
Error = 1/4°
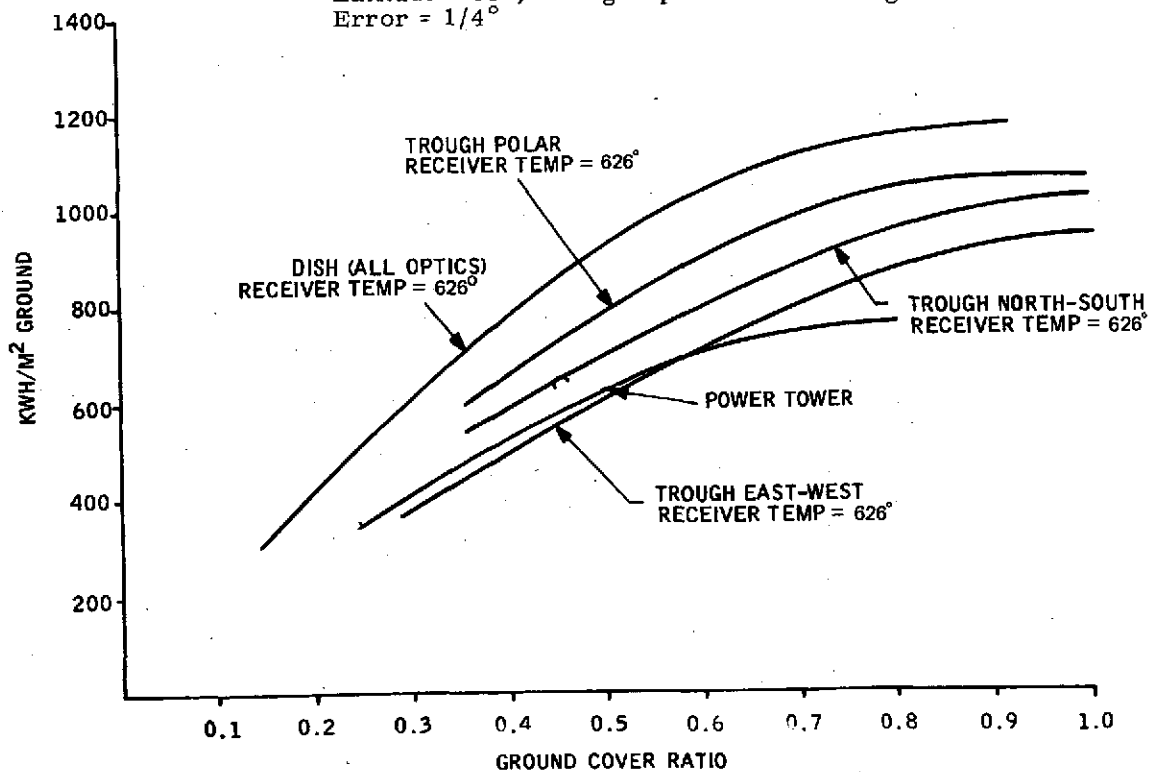
Figure 99.   Integrated Thermal Energy versus Ground Cover,
Latitude = 33°, Trough Optics and Tracking RMS
Error = 1/2°
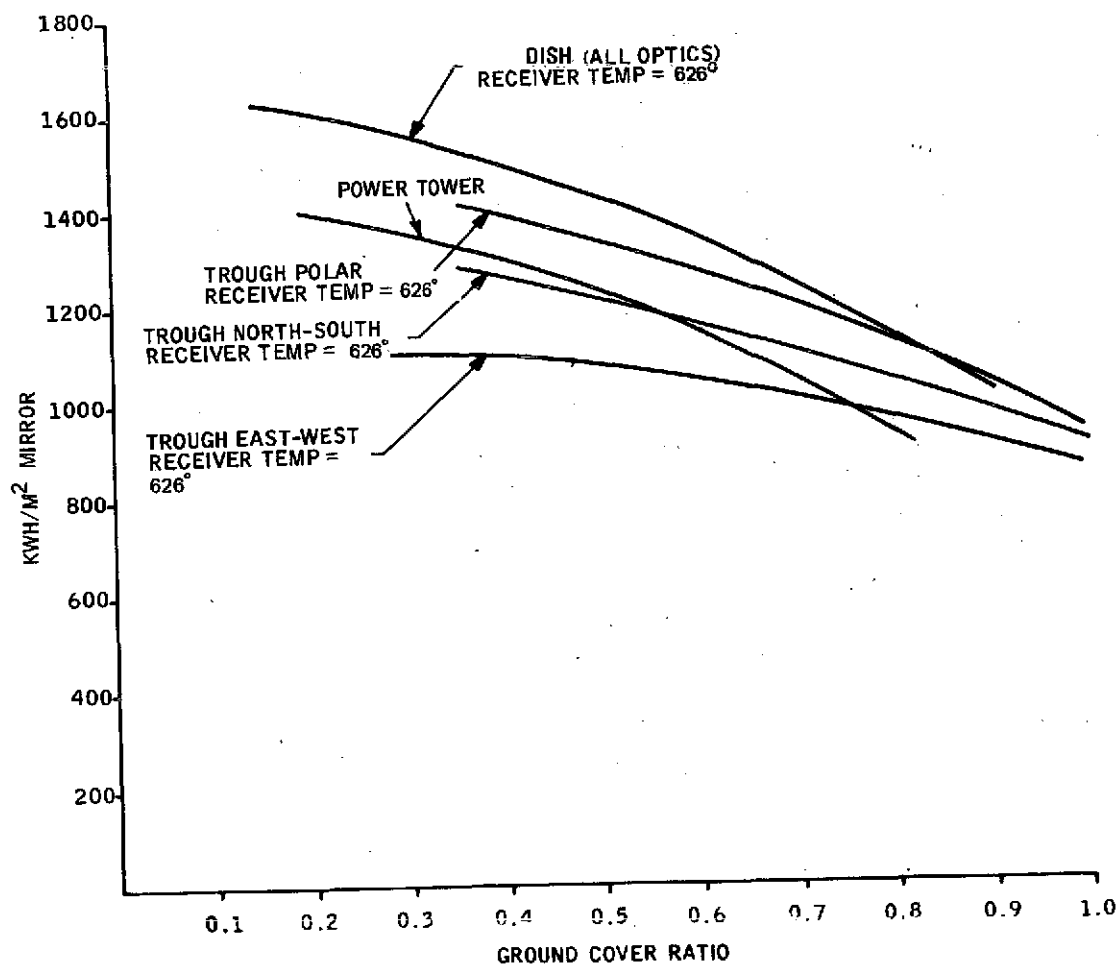
Figure 100. Integrated Thermal Energy versus Ground Cover,
Latitude = 33°, Trough Optics and Tracking RMS
Error = 1/4°
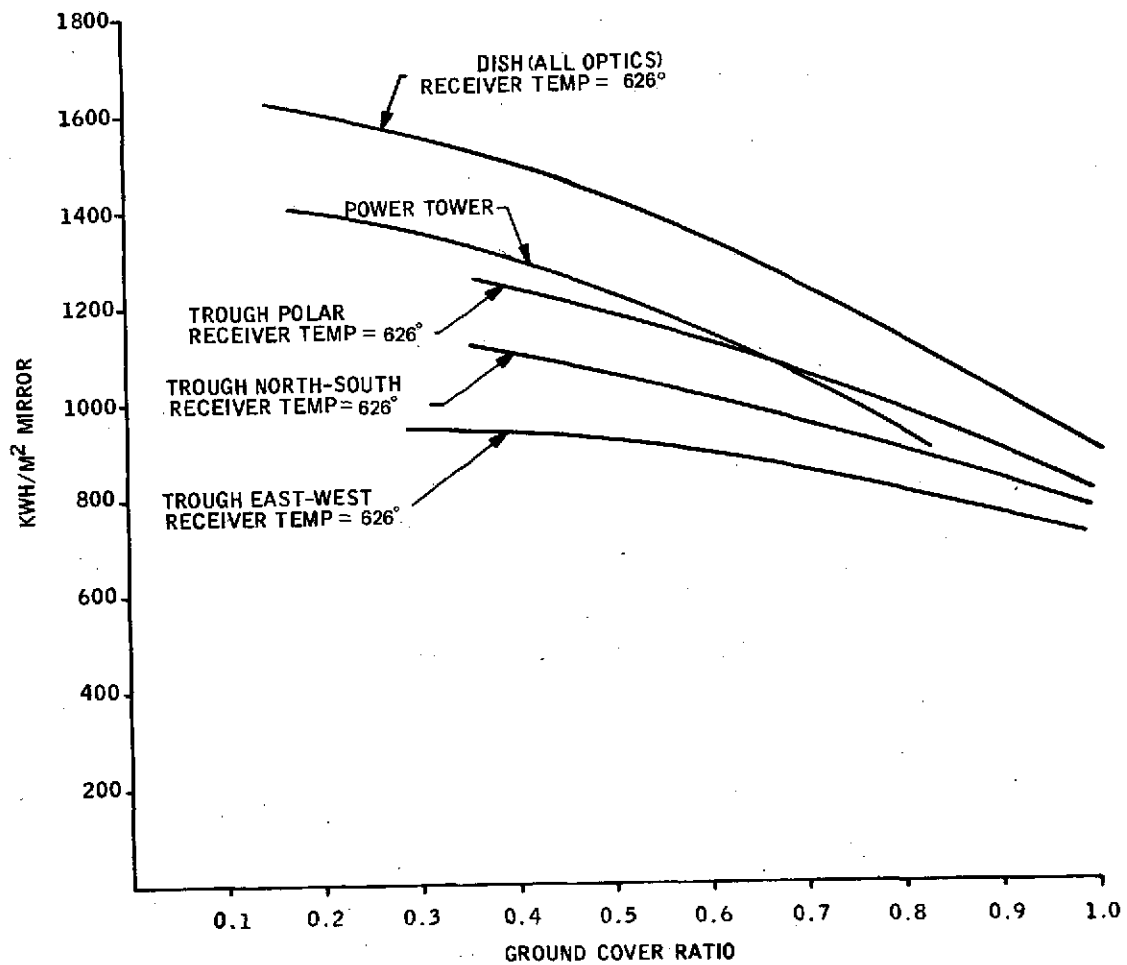
Figure 101. Integrated Thermal Energy versus Ground Cover,
Latitude = 33°, Trough Optics and Tracking RMS
Error = 1/2°

SECTION VI

COLLECTOR/CONCENTRATOR DESIGN STUDIES

Mechanical configuration design studies were carried out for the parabolic trough, paraboloid of revolution and heliostats.

PARABOLIC TROUGH

The parabolic trough collector consists of the four major subassemblies of the fixed support frame, the rotatable parabolic mirror, the vacuum envelope and coated steel heat tube, and the mechanical drive and tracking system. A drawing of the trough collector described is shown in Figure 102.

The results of the ray trace code exercise indicated that this collector is in the best attitude for energy collection when on an equatorial axis about the focus of the parabola (polar mount). The collector tracks the sun in a single axis mode. The mirror rotates about a fixed vacuum envelope surrounding a carbon steel pipe receiver and can turn a full 360 degrees, permitting it to protect the envelope and mirror surfaces at night and in inclement weather. . The collector is designed to use off-the-shelf equipment as far as practical, to be easily serviced and to withstand high wind loads (120 mph).

Support Frame

Each collector is supported by an "I" beam and channel-type steel frame. As shown in Figure 102 three poured concrete bases with appropriate mounting pads support angled support legs to steel rails which form cradles for the mirror structure. The side rails are mounted in a north-south direction at the equatorial angle. At each end of the cradle, the frame structure ties together the rails and also provides mountings for the mirror, the heat receiver, and the drive mechanism. The frame structures may be guyed with steel rods and turnbuckels to provide both stiffness and a small degree of adjustment. The structures are also equipped with locating points to permit attachment to their neighboring mirror frames for mutual support.

The frames are factory welded and assembled in position on the prepoured concrete bases. They are finished in a resistant paint. Table XI gives a detailed list of the required frame and foundation materials, their weight and cost.

Rotatable Parabolic Mirror

The mirror assembly consists of 11 ribs made of aluminum machined to form the required parabola. The ribs are welded to lightweight "T" sections and spaced 4 feet apart. A large aluminum tube forms a backbone and is also arranged to permit twisting the mirror for axis alignment. Special frames for each end support the mirror and also attach to cast steel rotation rings. These rings surround the heat absorber tube and ride on sealed ball bearings permitting rotation of the mirror about its focus. The reflecting surfaces of the mirror consist of 4-foot-wide pieces of 0.020 inch aluminum surfaced with Alzak. The reflectance of Alzak is approximately 0.85 and will permit collection of over 50 percent of the sun's energy.

The aluminum sheets are compressively end-loaded by adjustable beams mounted on the long edge of the mirror. The aluminum sheets are forced into contact with the parabolically shaped ribs and fastened at intervals to the ribs. The compression is maintained by spring loading to compensate for temperature variations, etc.

This scheme permits easy replacement of the mirror surface and requires only that the support ribs carry the accurate contours. These ribs may be batch machined by a numerically controlled milling machine to assure accurate shape. Table XII gives the material, weight, and cost estimates for the mirror assembly.

122
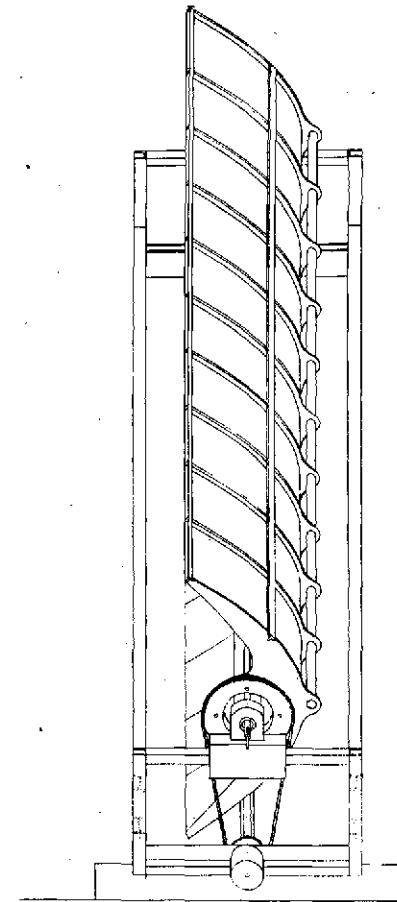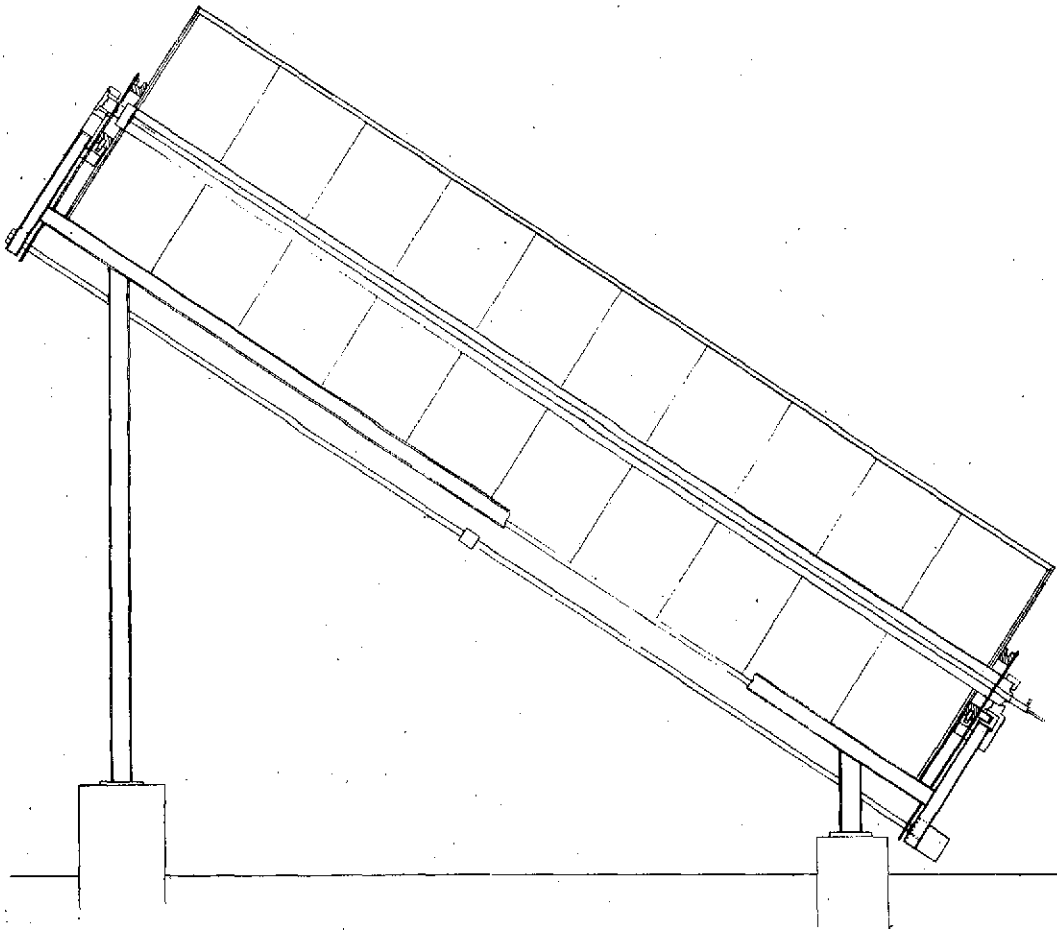
Figure 102. Parabolic Trough Solar Concentrator

Table XI.   Parabolic Trough Frame and Foundation

Quantity	Description	Weight (Lb.)	Material Cost ($)	Fabrication Cost ($)	Total Cost
2	Steel I Beam, 6 x 2-1/2 inches, 24 feet	504	101	50	151
2	Steel I Beam, 6 x 2-1/2 inches x 5/16 inches, 4 feet	84	17	8	25
2	Steel U Beam, 4 inches x 1-5/8 inches x 5/16 inches, 41 feet	594	119	59	178
4	Steel U Beam, 4 inches x 1-5/8 inches x 5/16 inches, 8 feet	232	46	23	69
2	Concrete Base, 4 x 4 x 3 feet	---	27	27	54
2	Concrete Base, 10 x 3 x 3 feet	---	50	50	100
4	Steel U Beam, 4 x 1-5/8 inches x 5/16 inches, 4 feet	116	23	13	36
	Total	1532	383	230	613

Notes:
1. Material cost of steel taken as $0.20/lb (May 1974).
2. Fabrication cost of $0.10/lb (includes assembly preparation).
3. Concrete costed at $15/yd. poured, assumed half material, half labor cost.

Table XII. Parabolic Trough Mirror Surface and Supports

Quantity	Description	Weight (Lb.)	Material Cost ($)	Fabrication Cost ($)	Total Cost
9	Aluminum Rib, 1/4 x 2 inches x 14 feet	108	81	135	216
2	Aluminum End Brace (w/mt. flange)	120	90	45	135
10	Aluminum (Alzak) reflecting sheets, 4 x 14 feet x 0.02 inches	400	300	400	700
1	Aluminum Torque Tube, 5 inches OD, 0.375 inches th, 40 feet	280	210	105	315
2	Aluminum T Beam, 1-1/2 x 1-1/2 x 1/4 inches, 40 feet	64	48	24	72
2	Aluminum L Beam, 1-1/2 x 1-1/2 x 1/4 inches, 40 feet	64	48	24	72
	Total	1036	777	733	1510

Notes:

1. Aluminum material costed at $0.75/lb. (May 1974)
2. Alzak costed at $1.25 ft^2
3. Ribs machined at $15 each
4. Torque tube, T&L beams fabricated at 0.5 material cost (includes assembly preparation).

Vacuum Envelope and Heat Receiver

The receiver temperature is expected to be 630°F. This requires a transparent vacuum jacket and a coated internal receiver. To avoid the necessity of field vacuum pumps, a large single glass envelope 40 feet long by 10 inches OD made of borosilicate glass is used. The upper end is sealed shut and it is supported on a flexible ring in an external support. The centrally located 2.5-inch OD steel heat receiver is supported inside the glass cylinder on several tripod type supports. They contact the glass wall through Teflon buttons to permit axial movement. The metal receiver is sealed to the lower end of the glass envelope with a special glass-to-metal seal of high vacuum capability. After installation of the heat receiver, the entire assembly is baked out at temperatures over 300°F, evacuated, and sealed. The unit is a complete component and does not require field servicing.

The heat receiver is a 2.5-inch OD steel pipe coated with an absorptive coating. The vacuum envelope permits application of the coating. The receiver has a concentric inner tube which has a 0.5 inch OD. Water is pumped through the inner tube to the upper end of the receiver and flows downward as it is heated. Appropriate insulation and connections are made to the main piping system at the lower end. A description of the heat receiver components, their weight and cost is given in Table XIII.

Mechanical Drive and Tracking System

The mirror is supported on each end by a 3-feet-diameter cast steel rotating ring. Each ring rides on two large sealed ball bearings. Two additional bearings at the lower end support the thrust load by being properly oriented with respect to the rings. For servicing of the mirrors and heat receivers, the rings are made in halves, fastened together above the mirror end frame supports. The mirror is fastened to the lower half of the rings only. Thus, the mirror can be removed without disturbing the heat receiver and envelope, and vice-versa.

A split chain sprocket is fastened to each rotating ring. A tracking drive, located on the main frame below the mirror, is connected to the rotating rings through tensioned chains. Both ends of the mirror are driven to reduce problems due to mirror torques.

The chain drive serves to keep the entire system held against the bearings and must also support the mirror against wind loads. The design permits complete rotation of the mirror. In bad weather and at night, the mirror may be turned face down for protection. The mechanical drive system components, their cost and weight, are given in Table XIV.

The total estimated cost of this parabolic trough design is $5140 in 1974 dollars. The design aperture area is 420 square feet. A cost summary for the design is given in Table XV. The design details for the parabolic dish and low profile heliostat are given in Section X.

Table XIII.　Parabolic Trough Heat Receiver

Quantity	Description	Weight (Lb.)	Material Cost ($)	Fabrication Cost ($)	Total Cost
1	Borosilicate Glass Housing, 10 inches OD, 9 inches ID, 42 feet	733	597	398	895
1	Heat Tube, 2-1/2 inches Outer and 1/2 inch inner SCH 80 Pipe	360	72	58	130
	Heat Tube Supports	10	2	18	20
	Steel End Supports	50	10	8	18
	Absorptive Coating	---	---	100	100
	Glass/Metal Vacuum Seal	21	---.	50	50
	Total	1165	681	532	1213

Notes:

1. Glass envelope costed at $1.22/lb. total, assumes fabrication cost 0.5 x material cost.

Table XIV. Parabolic Trough Mechanical Drive

Quantity	Description	Weight (Lb.)	Material Cost ($)	Fabrication Cost ($)	Total Cost
2	Boston Gear, 120A80 (1-1/2 inch pitch) pd 38.207 inches	100	---	---	480
2	Boston Gear, 120B13 (1-1/2 inch pitch) pd 6.268 inches	5	---	---	100
6	Norma Hoffman LS17 Sealed ball bearing, 2-1/2 inches bore	12	---	---	180
2	Counter Shaft Bearing	25	---	---	100
2	Chain and Take-up	50	---	---	100
1	Sensor (single axis tracking)	1	---	---	100
1	Drive Motor	50	---	---	100
2	Rotating Ring Assembly, 36 inches OD, 30 inches ID, Steel	880	176	88	264
1	Drive Shaft, 2 inches Diameter, 41 feet	441	---	---	137
	Total	1309	176	88	1561

Notes: 1. Material costed at $0.20/lb for steel

Table XV. Parabolic Collector Cost Summary *

	Parabolic Trough
Frame and Foundation	$1.53
Mirror Surface and Support	3.78
Mechanical Drive	3.90
Heat Receiver	3.03
Total Cost Per Ft^2	12.24
Total Cost Per Pound	0.97

*Shipping and Assembly Costs not included.

PARABOLOID OF REVOLUTION DISH COLLECTOR

The dish collector is a paraboloid of revolution mirror surface which tracks the solar image to maintain heat flux on a spherical receiver. The receiver will use pressurized water at approximately 2000 psi and, due to the available concentration ratio, it will not

require a protective vacuum envelope or special absorptive coating. The mirrors will be mounted on an equatorial mount suitable for the latitude of the power plant. The mirrors designed are approximately 16 feet in diameter and will be able to rotate a full 360 degrees.

This will permit the polished surface to face downward at night and in inclement weather. The frame structure will be designed as an integral unit to be fastened to concrete pads, will withstand 120-mph wind loads, and will be readily serviceable. Standard components will be used to the greatest extent possible.

The collector consists of four major subassemblies; the equatorially oriented support structure, the reflective parabolic mirrors, the spherically shaped heat receiver, and the mechanical drive and dual-axis tracking system. The total dish collector assembly is shown in Figure 103.

Support Structure

The main structure consists of "I" beam section steel beams. The horizontal base consists of three beams forming a triangle. The ends of the triangles are bolted to three concrete pads, previously poured. At the southern apex, a steel housing, welded to the beams, forms the support for the heat receiver and also for the lower main support gimbal bearing. The cylindrical receiver housing passes through the center of the bearing; both are bolted to a steel cradle. The outer bearing sleeve is bolted to the mirror frame flange and the drive sprocket. The bearing at the northern apex is mounted on a flange supported by two "I" beams bolted to the northern corners of the triangular horizontal frame. The bearings permit the cradle to turn 360° at the equatorial position.

The dual-axis tracking requirement means the mirror must be supported on the cradle on a tiltable mount. Bearings on a line through the focus of the mirror support the mirror on the cradle and since the center line of the north-south bearings is also on the focus of the mirror, dual-axis tracking about the central heat receiver is possible.

The entire assembly may be shop fabricated and installed as a unit. The mirror can be easily removed for servicing without disturbing the receiver by removing the yoke above the mirror slit and the bearing assemblies from the tiltable cradles.

Paraboloid of Revolution Mirror

The mirror is designed to rotate completely around the equatorially mounted spherical heat receiver. Since the annual angular solar excursion is 47.0 degrees, the mirror must be tiltable plus and minus 23.5 degrees from its normal equatorial position. With a fixed column supporting the spherical receiver, a notched or slotted mirror is necessary to provide the required geometric functions. The mirror consists of a large bowl-like structure with radial ribs terminating at a hub-like center and at the outer extremities in a circular ring.

The aluminum ribs are assembled and welded to the inner ring and outer ring. Second and third support rings are used to reinforce the ribs and also form attachment points for the two mirror supports. After assembly, a numerically controlled, single-point tool will be used to generate a very accurate parabola of revolution on the inside edges of the ribs. Special provisions will be made in the ribbing structure for the slot required for the heat receiver support.

The reflective surfaces will be made of 0.020 inch aluminum (Alzak). Pre-shaped pieces will be sheared and then stretch formed to produce the needed parabolic shape. These sections will be laid into the mirror on the ribs and forced into place by an adjustable outer rim. The reflective surfaces will be easily removed for servicing.

130

BACK OF MIRROR ASSEMBLY

SIDE VIEW
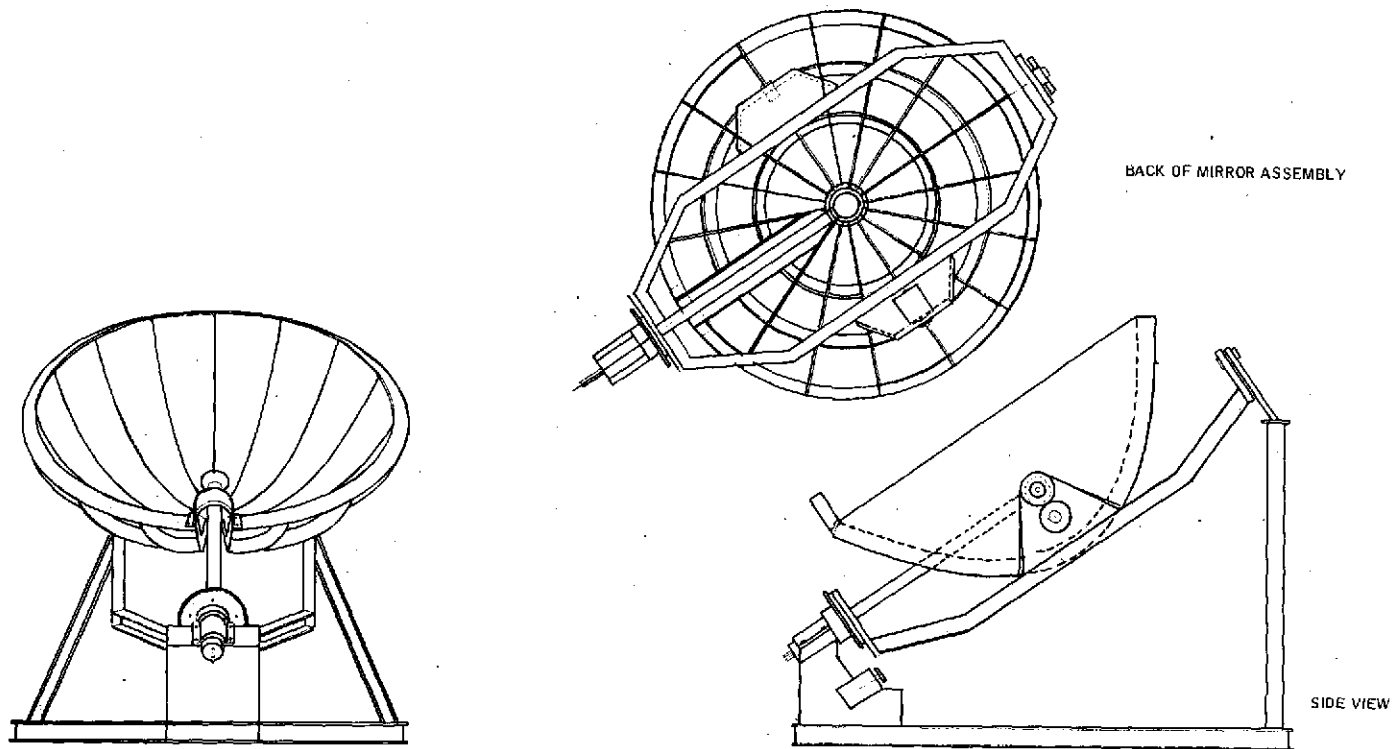
Figure 103. Paraboloid of Revolution Dish Solar Collector

Heat Receiver

The heat receiver will consist of a fixed, water-cooled steel sphere. Two insulated water lines from the field system are brought up through the cylindrical housing. The receiver is designed with proper interior baffling to provide uniform cooling. The system is designed to operate at approximately 2000 psi. The mounting system passes through the lower mirror support bearing. The heat receiver is basically supported on a cantilever from the lower support housing.

Mechanical Drive and Tracking System

The drive sprocket is driven by a chain from a geared down small sprocket on a counter shaft. The daily drive for solar tracking is accomplished by a sensor controlled motor drive of the main north-south axis. On the cross gimbal, a small motor and chain or toothed belt drive controls the seasonal angle. This drive need operate only to move specific intervals. This adjustment will be made only when the mirror is "parked" for the night.

Cost

A list of each of the subassembly components; their description and cost, is given in Tables XVI through XIX. The summary of total costs and the cost per unit aperature area are given in Table XX. Note that these prices do not represent a final installed price. Note also that this design is based on a 16-foot diameter aperture while the reference system dish has been selected to be a 23 foot diameter aperture. The 23-foot diameter dish was used to reduce the number of connections from the branch header piping to the collectors. Also, preliminary cost estimates show that the 23-foot dish may be fabricated for less dollars per square foot than a 16-foot dish.

An approximate price of $12 per square foot for an installed 23-foot aperture diameter dish was accepted for the initial cost estimates of the reference system design.

Table XVI. Paraboloid of Revolution Dish Frame and Foundation

Quantity	Description	Weight (Lbs.)	Material Cost ($)	Fabrication Cost ($)	Total Cost
1	Steel U Beam Frame, 4 inches x 1-5/8 inches x 0.247 inch, 61 feet	387	77	39	116
2	Steel I Beam, 5 inches x 1-3/4 inches x 0.325 inches, 11 feet	198	40	20	60
1	Steel Top Flange	75	15	8	23
1	Steel Housing	200	40	20	60
3	Concrete Base, 4 feet x 4 feet x 4 feet	---	107	107	214
	Total	860 lbs.	$279	$194	$473

Notes: 1. Material cost of steel $0.20/lb. (May 1974).

2. Concrete cost $15/yd. material labor.

Table XVII. Paraboloid of Revolution Dish Mechanical Drive

Quantity		Weight (Lbs.)	Total Cost
1	Top Bearings	10	50
1	Bottom Bearings	50	100
2	Mirror Bearings	20	50
2	Drive Motor	100	200
1	Sensor	1	100
2	Chain and Take-up	30	65
1	Boston Gear, sprocket 120A80 (1-1/2 inch pitch) pd 38.207 inches	50	65
2	Boston Gear, sprocket 120B13 (1-1/2 inch pitch) pd 6.268 inches	10	60
1	Boston Gear, sprocket 120A40 (1-1/2 inch pitch) pd 19.119 inches	25	100
	Total	296 lbs.	$965

Notes:

1. Costs are for purchased parts.

Table XVIII. Paraboloid of Revolution Dish Heat Receiver

Quantity	Description	Weight (Lbs.)	Material Cost ($)	Fabrication Cost ($)	Total Cost
1	Heat Receiver	72	36	36	72
1	Pipe 6 inch diameter, 5/16 wall 10 feet	200	40	20	60
2	Pipe 10 x 1.3 inch diameter	34	11	6	17
	Insulation	20	5	10	15
	Total	326 lbs.	$92	$72	$164

Table XIX. Paraboloid of Revolution Dish Mirror Surface and Frame

Quantity		Weight (Lbs.)	Material Cost ($)	Fabrication Cost ($)	Total Cost
15	Aluminum Rib, 9 inches x 3/8 inches x 10 feet	287	215	107	322
2	Aluminum Rib (Slot edge) 9 inches x 3/8 inch x 9 feet	35	25	13	38
1	Aluminum Edge Ring, 16 foot diameter x 9 inches x 1/8 inch	64	48	24	72
1	Aluminum Slot Support Bridge	10	8	4	12
1	Aluminum Frame Ring 8 foot diameter x 9 inches x 1/8 inch	32	24	12	36
1	Aluminum Frame Ring 12 foot diameter x 9 inches x 1/8 inch	48	36	18	54
1	Aluminum Frame Ring 1.5 foot diameter x 9 inches x 1/8 inch	6	4	2	6
1	Alzak Surface 0.020 inch	200	150	200	350
	Total	682 lbs.	$510	$350	$890

Notes:

1. Material cost of aluminum $0.75/ft. (May 1974).

Table XX. Paraboloid of Revolution Dish Costing Summary

Frame and foundation		$ 473
Mechanical drive		$ 965
Heat Receiver		$ 164
Mirror surface and frame		$ 890
Total		$2492
Aperture diameter	16 ft	(4.8 Meters)
Aperture area	201 (sq ft)	(19 Meter^2)
Cost per unit area	12.4 $/ft^2	(131 $/Meter^2)

HORIZONTAL ROTATING HELIOSTAT

A heliostat, which presents a low profile, was designed for the solar central receiver concept. The basic design involves a square or rectangular frame mounted on a turntable and arranged to be turned angularly to track the sun. The reflective surfaces are supported on axes which permit them to be turned in a vertical mode. The combination of the angular horizontal function and the vertical angle permits steering the reflected beam onto the power tower receiver. The heliostat is composed of four subassemblies: the main support frame, horizontal turntable, the reflector plates, and the tracking system. The total heliostat assembly is shown in Figure 104.

Main Support Frame

The heliostat frame consists of five steel bar joists welded into an open box structure. The structure consists of three parallel bar joists, with two additional joists welded across the ends. Flanged steel wheels are fastened to the frame to permit supporting the entire assembly on a round track. Pillow block bearings are mounted on the bar joists at each end and are able to turn between the joists 180°. The frame structure is opened internally to permit the reflector plates to be turned over through the frame.

Horizontal Turntable -- The main support for the heliostat consists of a 20 foot-diameter, poured-concrete ring surmounted by a circular section of light railroad-type rail. The main frame rides on four flanged, steel, ball-bearing wheels on the rail and also is guided by the circular track. Heavy lugs inside the wheels do not touch the rail but prevent the frame from being blown off during high winds. The rail is curved and welded into a single ring. The upper surface is ground to form a flat plane.

Reflector Plates -- The reflector plates will consist of a lightweight aluminum "egg crate"-type structure supported on a hollow 3-inch-diameter, keyed shaft through the structures. All cross webs will be keyed to the shaft to provide a tight coupling between shaft and reflector. The aluminum webs will be tack-welded together and the spaces filled with an expanded foam plastic. The reflecting surface will be silvered glass sheets cemented to the web and plastic surface. The reverse side of the reflector will consist of the foamed polyurethane filler. The present design will consist of six 10 foot x 7 foot panels mounted on three parallel shafts on the main frame. The ends of the shafts and centers will be supported on ball-bearing-type journals. Between the mirrors on each shaft will be a 36-inch diameter lightweight "vee"-belt type pulley. The pulleys will be connected to each other by aircraft cable which can be wrapped around the pulleys several times and which also can be tensioned to avoid slack. This will allow the reflectors to be driven in the vertical mode in a precise ganged fashion.

Tracking Drive -- This mirror concept requires a dual-axis drive and will use two separate motors, one for turntable rotation and one for vertical orientations. The turntable will be turned by a wire cable wrapped around the fixed circular rail and also around a small drum driven by a small gear motor controlled by a sensor or central computer. A separate motor mounted on the frame and coupled to the cable drive system through a chain, and a single sprocket will drive the centers of the three reflector shafts. The concept should minimize twisting and deformations due to wind loads.
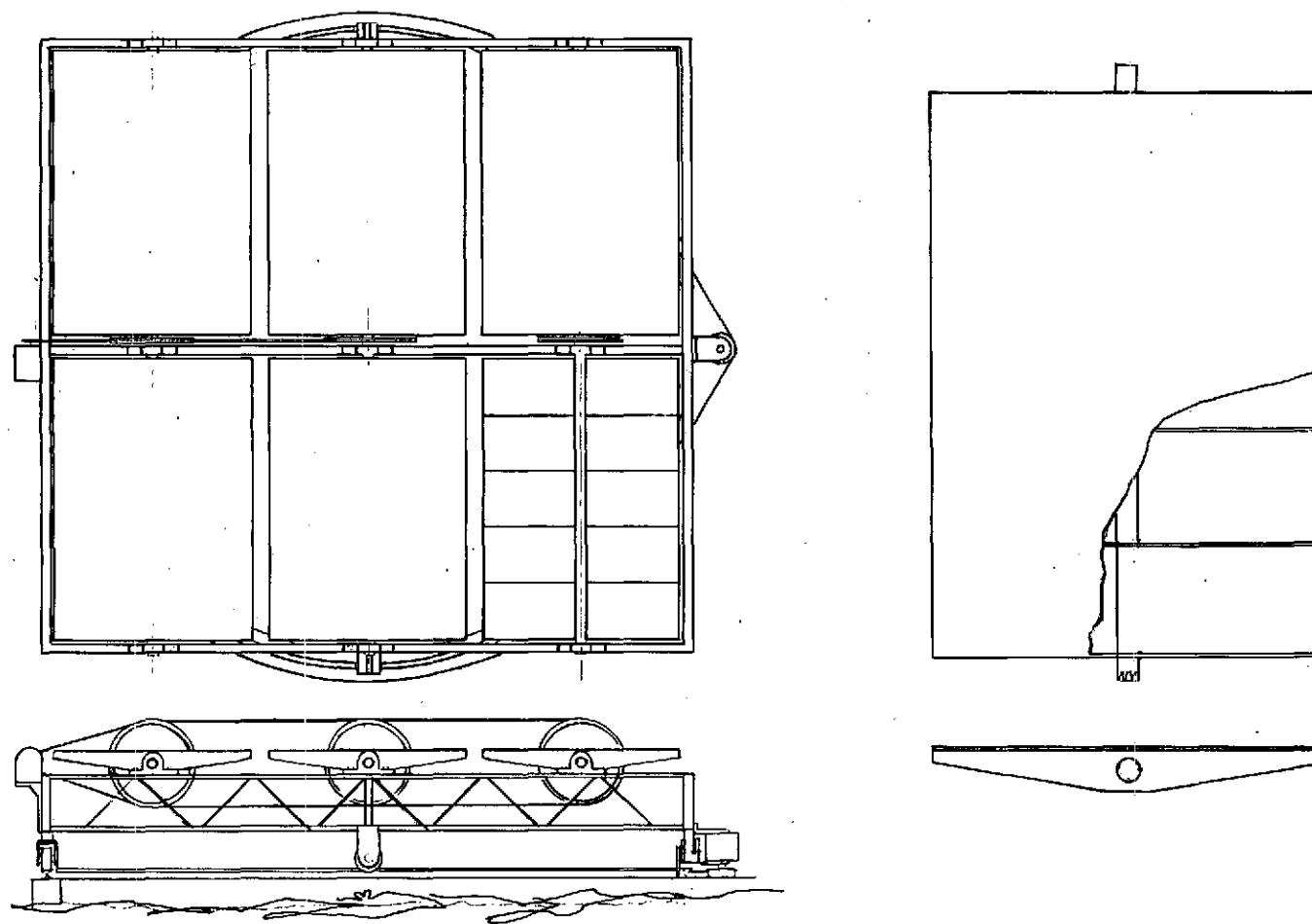
Figure 104.   Total Heliostat Assembly

The mirror may be stored in a horizontal position, with the mirrored side down for severe weather or at night. The low profile should minimize the 120-mph wind load condition and the mounting should simplify maintenance. The use of chain and tensioned cable drives should permit low cost and good performance. The system is specifically designed to avoid highly stressed components. This will reduce problems such as drifting and frequent servicing due to misalignment. Lubrication and care of drives should also be minimized.

The subassemblies component descriptions and costs are given in Tables XXI through XXIII. The total costs add to $2921 for the entire heliostat assembly. No shipping or field labor charges are included. This cost estimate should be regarded as preliminary as no structural analysis or cost optimization of the design has been completed.

A summary of these costs and the costs-per-unit mirror area are given in Table XXIV.

Table XXI. Low Profile Heliostat Frame and Foundation

Quantity	Description	Weight (Lbs.)	Material Cost ($)	Fabrication Cost ($)	Total Cost
3	Steel Bar Joist, 22.5 feet x 2 feet x 3-1/2 inches	843	168	34	202
2	Steel Bar Joist, 21.5 feet x 2 feet x 3-1/2 inches	537	107	22	129
1	Concrete Base, 22.75 feet diameter x 1 foot x 1 foot	---	58	58	116
1	Rail, 22.75 foot diameter	730	146	73	219
	Total	2110 lbs.	$479	$187	$666

Table XXII. Low Profile Heliostat Mechanical Drive

Quantity	Description	Weight (Lbs.)	Material Cost ($)	Fabrication Cost ($)	Total Cost
9	Pillow Block, Boston Gear 06894-12H 2-1/4 inches	113	---	---	270
3	Drive Tube, 2-1/4 inch diameter x 3/16 inch x 22 feet Steel	273	---	---	81
2	Drive Motor	50	---	---	200
2	Motor Mount	20	4	12	16
1	Chain, 18 feet	80	---	---	108
1	Pitch Motor Drive Sprocket, Boston Gear 120B13 (1-1/2 inch pitch), pd 6.268	5	---	---	30
1	Rotary Drive Cable, 81 feet	5	---	---	12
1	Pitch Drive Cable, 59 feet	4	---	---	9
1	Rotary Drive Pulley	5	---	---	5
3	Spoked Pitch Drive Pulley,	75	15	210	225
4	Wheel, 1 foot diameter x 4 inches and bearing	80	---	---	140
4	Wheel Mounting	140	28	14	42
4	Safety Bracket	20	4	4	8
	Total	870 lbs.	$51	$240	$1146

Table XXIII. Low Profile Heliostat Mirror Surface and Frame

Qty	Description	Weight (lb)	Material Cost ($)	Fabrication Cost ($)	Total Cost
36	Mirror Cross Brace (aluminum)	214	160	80	240
12	Mirror End Brace	51	38	19	57
6	Glass Mirror Surface 7 ft x 10 ft x 1/8 in.	730	357	90	447
150 ft^3	Polyurethane Foam	450	315	50	365
	Total	1445	870	239	1109

NOTES: 1. Glass mirror 0.85/ft^2

2. Polyurethane $0.70/lb.

Table XXIV. Low Profile Heliostat Costing Summary

Frame and foundation	666
Mechanical drive	1146
Mirror surface and frame	1109
Total	2921

Mirror area: 420 ft^2 (40 meter^2)

Cost per unit area: $6.95/ft^2 ($73/meter^2)

ENERGY TRANSPORT STUDIES

DISTRIBUTED SYSTEM

The energy transport system for a field of solar collectors (as defined in Section IV) consists of a network of insulated pipes necessary to carry the collected energy to a central station. The individual collectors generate steam by pool boiling or heating up a fluid which is later used to generate steam. As the fluid or steam is moved through the piping network, heat is lost by convection and radiation; friction on the pipe wall dissipates energy. It is clear that for a given power plant operating condition the size of the pipes and the thickness of the insulation selected will determine these losses as well as the cost of the energy transport system. The design of the system was thus approached as a problem of cost optimization, involving the cost of the piping network and the cost of the energy losses within the network.

Heat Loss

Figure 105 shows a cross section of a pipe of length L with constant pipe diameter and insulation thickness along its length.
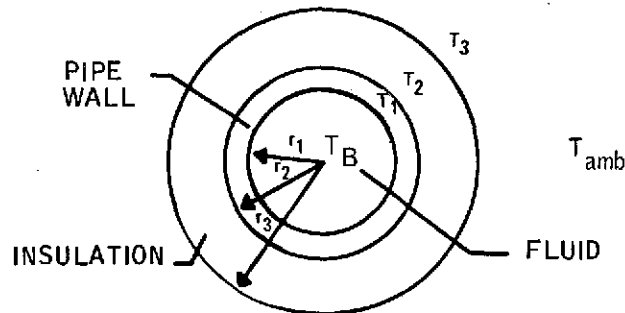
Figure 105. Cross Section of Pipe

The inner fluid bulk temperature is T_B and steady-state radial heat transfer can be assumed. The heat that is conducted to the outer surface is removed by convection and radiation, so that

$$Q_{conduction} = Q_{convection} + Q_{radiation} \qquad (18)$$

At the low surface temperatures of the insulated pipe, the radiation heat transfer may be ignored. It can also be assumed that no significant resistance to heat flow is offered from the fluid to the outer pipe wall. The heat transfer equations of concern are:

$$Q_{conduction} = \frac{2\pi \overline{K} L (T_B - T_3)}{\ln (r_3/r_2)} \qquad (19)$$

$$Q_{convection} = (2\pi r_3 L) h_a (T_3 - T_{amb}) \qquad (20)$$

where

$\overline{K}$ = mean thermal conductiveity of the insulation

h_a = convection heat transfer coefficient (the convection is assumed forced)

The thermal conductivity, K, of several types of insulation is shown graphically in Appendix B. The data can be curve fit by polynomials of the form:

$$K = A_0 + A_1 \overline{T} + A_2 \overline{T}^2 \qquad (21)$$

where $\overline{T}$ is the mean temperature of the insulation. To find the mean thermal conductivity, $\overline{K}$, the conduction equation

$$Q = -2\pi r L K \, dT/dr \qquad (22)$$

is integrated with K as a function of T and put into the commonly used form for $Q_{conduction}$ given previously (Equation 19). The mean thermal conductivity is then given by:

$$\overline{K} = A_0 + \frac{A_1}{2} (T_3 + T_2) + \frac{A_2}{3} \frac{(T_3^3 - T_2^3)}{T_3 - T_2} \qquad (23)$$

The forced convection heat transfer coefficient is found from

$$h_a = 1.1 \, C \, (Re)^n \, P_r^{.31} \, (\frac{K_{air}}{2 r_3}) \qquad (24)$$

where the constants C and n are given by Kreith and Hilpert (References 7 and 8) as a function of the Reynolds number of air (Re).

$$Re = \frac{2 r_3 V_{air} \rho_{air}}{\mu_{air}} \qquad (25)$$

and P_r is the Prandtl number for air.

The fluid temperature drop over a pipe length L can be calculated from the heat balance for a given pipe section. The piping network has tee-junctions at given intervals to feed cold fluid to the solar collectors or to receive hot fluid or steam from the collectors. For a section of length ΔX, as shown in Figure 106, the heat balance is:

$$\dot{m}_1 C_p T_1 = \dot{m}_2 C_p T_2 + \dot{m}_c C_p T_1 + Q_{loss} \qquad (26)$$
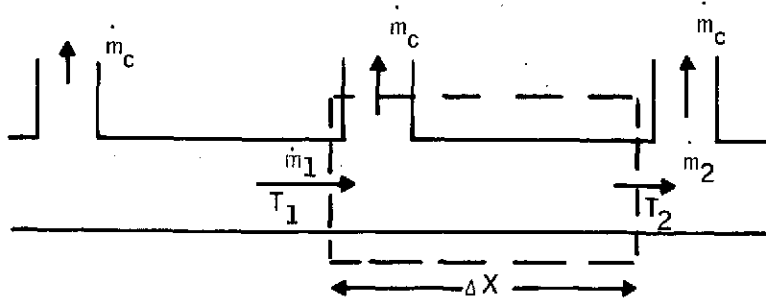
Figure 106. Pipe Section of Length ΔX

where the $\dot{m}$'s are the mass flow rates, C_p is the specific heat of the fluid and Q_{loss} is the heat lost by conduction.

The above equation can be solved for the temperature drop across the section. Using the continuity relation $\dot{m}_2 = \dot{m}_1 - \dot{m}_c$, the temperature drop is

$$\Delta T = T_1 - T_2 = \frac{Q_{loss}}{(\dot{m}_1 - \dot{m}_c) \, C_p} \qquad (27)$$

The temperature drop across a section where the fluid is added to the pipe can be formulated similarly, the only difference being that flow is entering the line at the collector ourput temperature, T_c.

For the purpose of evaluating the transport loop performance, the temperature of interest is the fluid bulk temperature at the entrance to the heat exchanger. To a first approximation, this temperature is

$$T = T_c - \frac{Q_{loop}}{\dot{m}_{total} C_p} \qquad (28)$$

where

Q_{loop} - sum of all return piping heat losses

$\dot{m}_{total}$ - total mass flow rate

Pressure Loss

Static pressure in the piping falls in the direction of the flow due to the effects of friction. The friction losses are given by

$$\frac{dp}{dx} = \frac{F}{D} \; 1/2 \; \rho v^2 \qquad (29)$$

where D is the pipe diameter, ρ is the transport fluid density, v is its velocity and F is the Moody friction factor found from

$$\frac{1}{\sqrt{F}} = -2\log_{10}\left(\frac{2.51}{Re\sqrt{F}} + \frac{2\epsilon}{3.7D}\right) \tag{30}$$

The surface roughness, ϵ, is taken to be that of commercial steel pipes.

The effect of the tee-junctions on the static pressure can be evaluated from momentum considerations. Figure 107 shows a typical tee-junction.
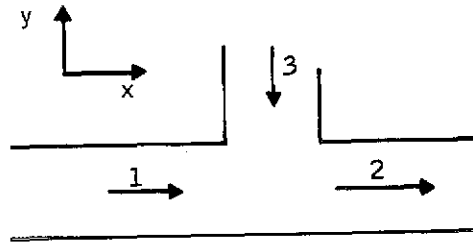
Figure 107. Typical Tee-Junction

Writing the momentum equation in the x-direction

$$P_1A_1 - P_2A_2 = \dot{m}_2U_2 - \dot{m}_1U_1 \tag{31}$$

where A_i is the cross-sectional area of the ith side of the tee.

The pressure difference across the tee is

$$\Delta P_{tee} = P_1 - P_2 = (\theta/A)(\dot{m}_2 U_2 - \dot{m}_1 U_1) \tag{32}$$

where θ is an empirically determined momentum coefficient and $A = A_1 = A_2$.

In the piping which feeds cold fluid to the collectors, the reduction in velocity due to the outflow of fluid at the tee is accompanied by a pressure rise in the flow direction. The momemtum coefficient is taken to be 0.3 as approximated by Benson (Reference 2). In the piping which collects the heated fluid, the tee junctions add fluid to the mainstream and the pressure must fall in the flow direction. The momentum coefficient is taken as 0.9 (Reference 2).

The equations for the friction and tee pressure losses can be combined for a section length L to give the total pressure loss, ΔP, in the pipe section.

The pump work due to the pressure loss is

$$PW = \text{Pump Work} = \frac{\dot{m} \Delta P}{\rho \eta_p \eta_m} \tag{33}$$

where

$\dot{m}$ = total mass flow rate

ρ = fluid density

η_p = efficiency of the pump

η_m = efficiency of the motor

For large pumps and electric motors, typical efficiency η_p is 0.80 and η_m is 0.95.

CONCEPTUAL SYSTEM DESIGN

Several design configurations are possible for the solar collector field and its associated piping network. Given the collector spacing basic patterns of Section V, the piping network is arrayed as shown in Figure 108 for a square collector field. This arrangement was chosen for its simplicity, although several other piping patterns were considered. None offered any overwhelming advantages over the simple network.

Each pipe shown running vertically between the collector columns either supplies or collects fluid from solar collectors on either side. These pipe lines are called branch headers. The piping, shown running horizontally in Figure 108 either supplies or collects fluid from branch headers on either side. These pipe lines are referred to as main headers.
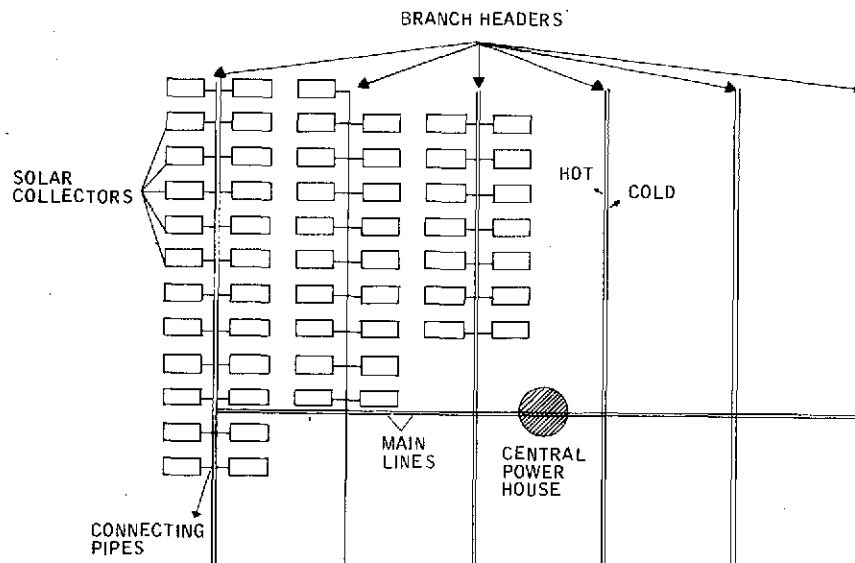
Figure 108. Collector Field Geometry

The piping network is divided into sections approximately 80 feet long so that an integer number of collectors is associated with each branch header section. A typical branch header section and the cost of its various components is detailed in Appendix A. Main header sections are also approximately 80 feet long so that an integer number of branch headers is associated with each main header section.

The depicted reverse-flow branch header design was chosen to keep the piping length required at a minimum. A parallel-flow branch header arrangement would require another length of pipe equal to the field width. Furthermore, the parallel-flow arrangement would provide pressure gradients in the same direction for both branch headers. This would be beneficial in promoting a uniform pressure differential between branch headers whereas the reverse-flow has opposing pressure gradients, but this advantage is negligible since either scheme would require flow restriction valves to regulate the flow through each solar collector.

By proper flow regulation, flow maldistribution problems can be controlled. The larger pressure drop incurred by reverse-flow branch headers is negated by the additional pressure loss in the added main line of the parallel-flow method.

Design Methodology

To determine the performance and flow characteristics of the energy transport system, the governing equations of the system must be solved. Normally, flow distribution problems are solved with a simultaneous equation set involving non-linear pressure loss equations and the continuity relations. For the energy transport system, the non-linear heat loss equations must be added. An iteration technique could be used to solve the equation set, but the simultaneous equations set would be nearly unmanageable because of the large number of pipes and loops needed in a solar collector field. Therefore, it is desirable to avoid this solution technique.

By assuming that the heat losses in the feed water branch header are small, the temperature at the solar collector inlet is set constant over the entire field. With a fixed collector outlet temperature and a known amount of power collected, the mass flow through each collector is

$$\dot{m}_c = \frac{Q_{coll}}{\Delta h} \tag{34}$$

where

Q_{coll} - power absorbed by the solar collector receiver

Δh - enthalpy change of fluid $(h_{out} - h_{in})$ as found by known temperatures.

Given a specific field design with known Q_{coll}, the mass flow rate at all points in the piping network can be determined. This information allows the heat and pressure loss equations to be solved directly.

The actual design of pipe size and insulation thickness to be installed in the field is based on a cost optimization of the individual pipe sections within the piping networks. To evaluate the cost of a section, the cost of the capital (for installed pipes and insulation, etc.) must be combined with weighted relative values of pumpwork and heat loss. The design of the individual sections is accomplished by varying pipe diameter and insulation thickness until a minimal summation of the three relative costs is achieved. The annual cost of capital, heat loss, and pumping power is the basis for the calculation of the weighted relative costs:

A) ACCC = Annual Cost of Capital Cost ($/yr)

$$ACCC = CC \times FCR$$

Where

    CC   = Capital cost ($)

    FCR = Fixed charge rate

The capital cost includes the cost of the following components:

    1)   Pipe material

    2)   Insulation material

    3)   Transportation of the materials

    4)   Installation of the materials

A fixed charge rate of 15 percent is used throughout the study, but the value chosen for FCR will not affect the design of the piping network; it only changes the net cost per unit energy.

B) ACHL = Annual cost of heat loss ($/yr)

$$ACHL = \frac{HL \times PE \times CCP \times FCR}{3413 \times KWHeYR}$$

where

    HL   = heat loss in 1 year (BTU/yr)

    PE   = overall plant efficiency

    KWHeYR = total plant electric generation (KWHe/yr)

    CCP   = total capital cost of providing the thermal power ($) - no storage costs are included

The heat loss in 1 year is determined by the collector fluid input and output temperature, the pipe and insulation parameters, ambient conditions and plant operating hours.

C) ACPP = annual cost of pump power ($/yr)

$$ACPP = \frac{PW \times CCP \times FCR}{KWHeYR}$$

where PW is the pumping power due to pressure losses in 1 year (KWHe/YR). The calculation of the pumping power over 1 year's operation depends on the fluid temperature, pipe diameter, and mass flow rate.

The estimated overall cost of the solar plant is composed of the following items:

- Collectors
- Land
- Turbine-Generator
- Heat Rejection Equipment
- Heat Exchanger
- Moisture Separator (when required)

- Piping and Piping Components
- Insulation
- Valves
- Structures and Facilities
- Miscellaneous Plant Equipment

A breakdown of the costs used for each of the items is presented in Appendix A.

To evaluate all these costs, the yearly performance of the system must be computed in terms of total energy collected, heat loss, and pumping energy per year. It should be pointed out that the mathematical model does not include storage and its cost.

The existing model derives its data from the load-duration curves of Section VI. Figure 109 shows a typical curve for an entire collector field. The loss lines shown along the abscissa are the loss duration curves due to the three major loss sources. These are: radiation from the receiver surface, conduction through the energy transport pipe walls, and pump work associated with the transport network. Each of the loss terms is added to the loss plotted below it. The pump work is the only time-dependent parameter (heat losses are functions of temperature only and the temperatures are essentially constant for all operating conditions).
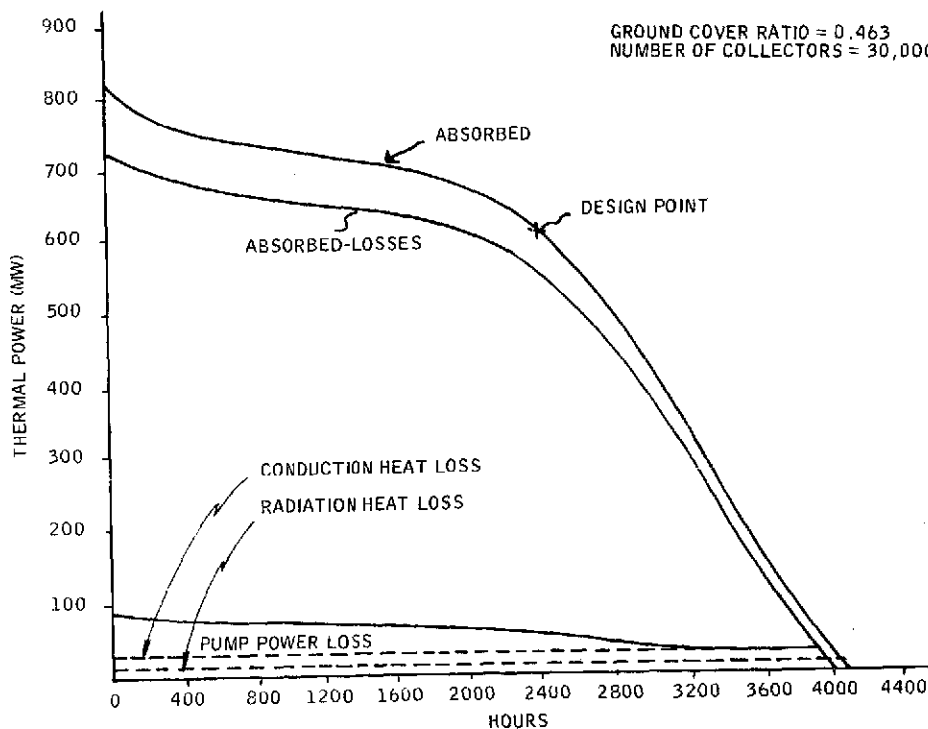
Figure 109. Load Duration Curve for Paraboloid of Revolution

It is not practical to perform a running time integral of pump work over a year for each candidate design pipe diameter and insulation thickness for each pipe section in the field. The approximation that pump work varies as the cube of the mass flow rate (see Equations 9 and 12) can be used to evaluate the yearly pump work at one design condition. A design point at the cube root of the time integral of Q_{coll}^3 (called the root mean cube point) is used to obtain the average pump work over 1 year of operation.

A computer program performs the field design using the above methodology. The costs used in the study are detailed in Appendix A. In practice, a pipe diameter and insulation thickness is chosen and the heat and pump work losses are calculated along a section. The annual cost of the pipes and insulation (including transportation and installation) is found for the section and the annual cost of the losses is computed according to the cost equations. The total cost is simply the summation of these annual costs. The pipe diameter and insulation thickness are incremented in discrete sizes and the total costs are calculated until a minimum has been found for each section of piping in the network. To cost out the energy losses, the total capital costs of the plant are given an estimated initial value, the field is designed and the total capital costs are again computed. An iteration of the energy transport system design is then performed as before.

RESULTS

The computer program using the design methodology described was exercised to consider the pipe and insulation layout for the solar collector fields containing parabolic trough collectors with north-south, east-west, or polar orientations, and for the parabolic dish collector. Both the pool-boiling and pressurized water concepts were examined. The cases were run with various collector spacings, through a range of plant capacities and with various degrees of regenerative heating of the output condensor fluid.

The following parameters, unless otherwise stated, were held fixed throughout the exercise of the code:

- Ambient air temperature   80°F
- Air speed   15 ft/sec
- Insulation type   Calcium Silicate
- Turbine inlet conditions - pool boiling concept
  - T_{inlet} 543°F
  - P_{inlet} 985 psia
- Turbine inlet condition - pressurized water concept
  - T_{inlet} 585°F
  - P_{inlet} 925 psia
- Heat rejection (wet cooling)   120°F water return
- Regenerative heating ratio   0.8
- Heat exchanger   20°F pinch point

All integrated collector absorbed power data used are for 1/4 degrees rms errors in optics and tracking with the clear air insolation model.

A range of steam cycle parameters and the heat exchanger conditions are calculated for various turbine conditions in Appendix B.

Ground Cover Ratio Selection

For each of the possible collector field systems, the choice of the best ground cover ratio (GCR) is determined by trading off the cost of pipes, insulation, and land against the cost of collectors, turbine-generator, and associated equipment. From the standpoint of collectors only, the best GCR is the one at which no shadowing occurs so that maximum energy is collected. In this case, individual collectors are spaced relatively far apart, requiring large land area and a lengthy piping network. As the ground cover ratio is increased the collectors begin to shadow each other, producing less energy per collector, but at the same time the land area and piping length are reduced. At some point the increase in GCR reduces the energy collected to a point where the cost of the additional collectors needed to supply a given energy outweighs the cost reduction gained in piping length and land area. At this point the summation of costs per energy delivered is at a minimum.

The tradeoff criteria are quantitatively shown in Figure 110. The cost of land is minimal compared to the connecting pipe costs. These latter costs are nearly constant since the number of connections increases while the length per connection decreases with increasing GCR. The increase in balance of plant cost is due to the increasing maximum capacity which must be provided as the GCR is increased. As the collectors are spaced closer together, the load-duration curve becomes more sharply sloped (see Section VI), and the peak energy must be greater to obtain a constant integrated energy. As shown in Figure 110, the summation of the plant costs reaches a minimum at a ground cover ratio of 0.45 for the pressurized water system with a polar mount trough collector field.

Figures 111 through 113 show the results of other ground cover ratio sweeps. The ordinate shows mills/Kwhe, without storage costs, in terms of 1974 dollars. The $1500 per collector pressurized water cases were run with a 550°F turbine inlet temperature. Comparing the results of Figure 111 to 112 shows that the pool-boiling concept is less costly per Kwhe. However, these results do not show storage costs nor assume that the pool boiling steam control is more costly than the pressurized water control. Because of the additional expense associated with internal storage and control in the steam case, it was eliminated from further consideration in working toward a baseline (see Section XI).

The pressurized water system results at $1500 per collector cost (Figure 111) shows that the east-west and north-south trough fields can be eliminated from further study since the polar-trough configuration is less costly overall, assuming that the polar trough can be manufactured at the same price as east-west of north-south troughs. This seems reasonable since the only difference is in the added support beams. The optimal GCR's for the various fields shown are listed below:

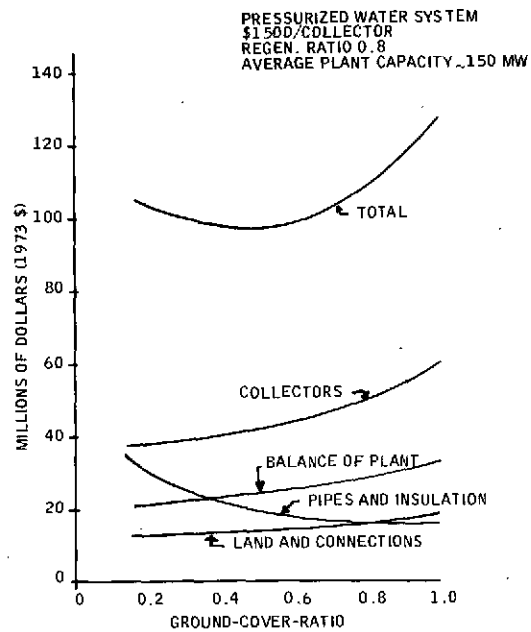| Concept	Collector Type	Cost/Collector	Optimal GCR
Pressurized Water	East-West	$1500	0.54
Pressurized Water	North-South	1500	0.50
Pressurized Water	Polar	1500	0.45
Pressurized Water	Dish	1500	0.48
Pressurized Water	Polar	5000	0.33
Pressurized Water	Dish	5000	0.40
Pool Boiling	Polar	1500	0.40
Pool Boiling	Dish	1500	0.45

Figure 110.   Plant Costs Versus Ground-Cover-Ratio
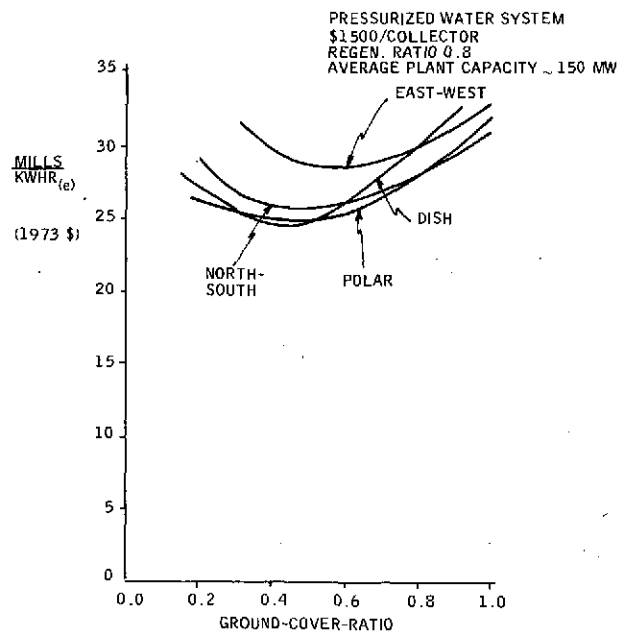for a Polar Trough Collector Field

Figure 111.   Energy Cost Versus Ground-Cover-Ratio
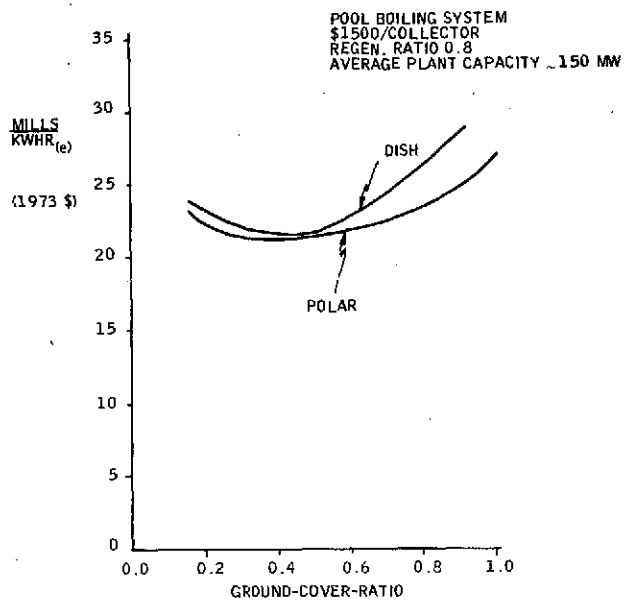
Figure 112. Energy Cost Versus Ground-Cover-Ratio
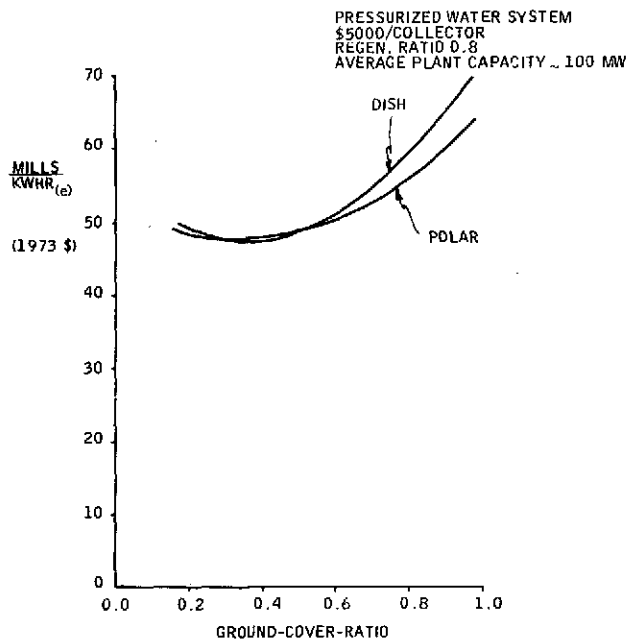
Figure 113. Energy Cost Versus Ground-Cover-Ratio

150

In the pressurized water polar trough and two-axis dish cases, increasing the collector cost from $1500 to $5000 shifted the optimal GCR toward a less-shadowed, lower GCR. Another cost of $3500 per collector was run for the polar trough collector and the locus of optimal ground cover ratios is shown in Figure 114. As the collector cost estimate is increased, the cost of pipes and insulation becomes a smaller portion of the total plant cost. Thus, the optimal ground cover ratio decreases as collectors become more expensive.

Other variables which may affect the selected optimal ground cover ratios include the plant size, storage costs, turbine conditions, heat rejection, etc. That is, variables which can change the total plant cost change the annual energy costs and the proportion of costs. For instance, adding storage costs and assuming they are constant for all GCR's would weight the energy losses higher (pipes and insulation would be more expensive) so that the optimal GCR would be lower.

Plant Size Selection

Economies, or diseconomies, of scale in a solar plant are governed by the investment costs in piping, insulation, and turbine/generator/heat rejection systems and by the energy transport system losses as a function of plant size. The pricing of power plant components given in Appendix A was generated to study the solar plant economies of scale in a range of plant sizes from 100 to 1000 $Mw_{(e)}$. For study purposes, the average plant capacity was defined to be the yearly generator output averaged over 4000 hours. That is, the thermal load-duration curves of Section VI were used to determine the integrated thermal power minus heat losses multiplied by an appropriate cycle efficiency. This energy is simply divided by 4000 hours to give the defined average plant capacity in megawatts.

The results of the plant size parameter variation are shown in Figures 115 through 117. In each case, the collector types were run at the previously determined optimal ground cover ratios. These optimals are subject to some change with plant size but such a change would have a negligible effect (less than 1 mill/Kwh) on the computed energy costs. The results shown in Figures 115 through 117 indicate that the optimal average plant capacity is below 100 Mw. The dashed curve below 100 Mw is extrapolated since the pricing data for balance of plant costs is not valid in this range.

Comparing Figures 115 to 116, shows that the rise in energy cost with increasing plant size is much sharper for the pressurized water concept than it is for the pool-boiling concept. The reason for this sharper slope is that the pipe material, welds, and handling charges increase more rapidly with increasing pipe size for the higher-pressure, hot water concept than for the lower-pressure, pool-boiling concept. The cost data for both concepts are given in Appendix A. Since larger plants require larger pipes, the rise in pipe and insulation cost with increasing pipe size is not as rapid for the pool-boiling concept.

The diseconomy of scale for solar power plants is mainly due to the increasing investments in pipe and insulation coupled with decreasing piping network efficiency. A breakdown of the $/kw investment costs is provided in Figures 118 and 119 for the pressurized water system concept at $1500 and $5000 per collector. As shown, the pipe and insulation costs are the major source of the increasing energy cost with plant size.

A brief examination of the piping requirements as a function of plant size clearly indicates the reason for the increase. Consider a hypothetical solar plant which has collectors along a single pipe length with a uniform flow input along the length. To double this solar plant's power output the number of collectors must nominally be doubled, which in turn will require twice the pipe length. This would leave the cost per kilowatt unchanged if the average pipe size were unchanged.

However, the added piping sections will be larger than the original piping (see Figure 120) and will cause the average pipe size to be increased. The end result is an increase in cost per foot of piping and the $/Kw investment in pipes and insulation also rises.

POLAR TROUGH
PRESSURIZED WATER SYSTEM
REGEN. RATIO 0.8
AVERAGE PLANT CAPACITY ~ 150 MW

MILLS/KWHR$_{(e)}$

(1973 $)

$5000/COLL.

$3500/COLL.

$1500/COLL.
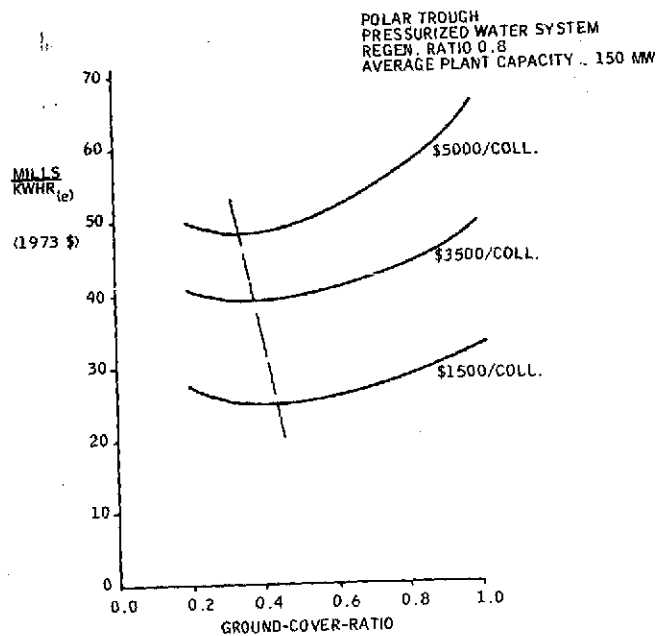
GROUND-COVER-RATIO

Figure 114.   Energy Cost Versus Ground-Cover-Ratio

PRESSURIZED WATER SYSTEM
$1500/COLLECTOR
REGEN. RATIO 0.8

MILLS/KWHR$_{(e)}$

(1973 $)

TWO-AXIS DISH @ GCR = 0.48
OR
POLAR TROUGH @ GCR = 0.45

AVERAGE PLANT CAPACITY (MW)
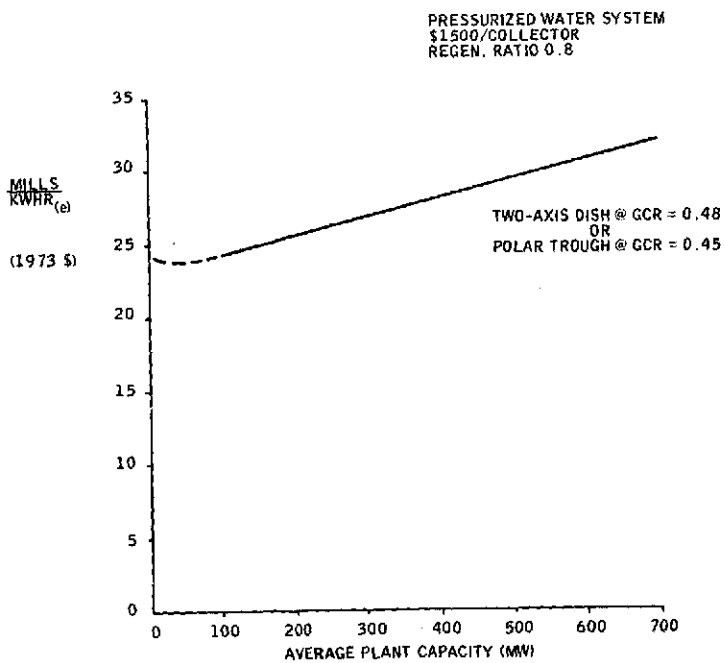
Figure 115.   Energy Cost Versus Plant Size

152

MILLS
KWHR(e)

(1973 $)

TWO-AXIS DISH @ GCR = 0.45

POLAR TROUGH @ GCR = 0.40

AVERAGE PLANT CAPACITY (MW)
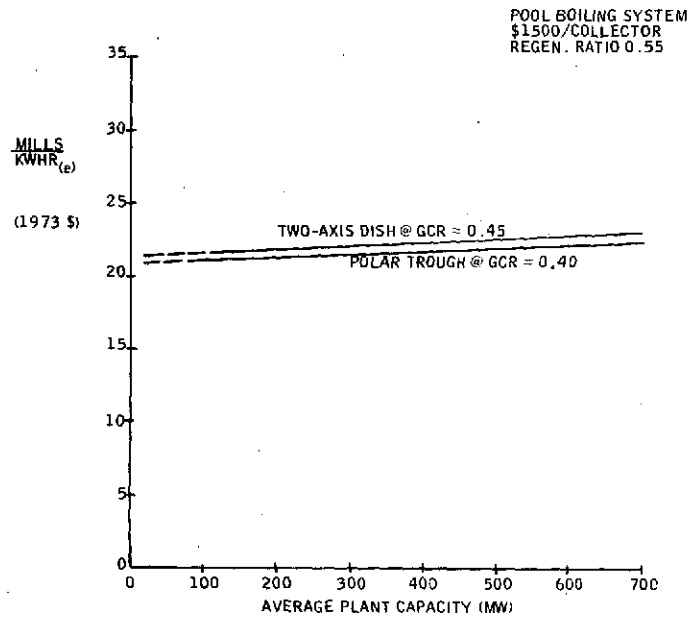
Figure 116.   Energy Cost Versus Plant Size

PRESSURIZED WATER SYSTEM
$5000/COLLECTOR
REGEN. RATIO 0.8

MILLS
KWHR(e)

(1973 $)

TWO-AXIS DISH
GCR OF 0.40

AVERAGE PLANT CAPACITY (MW)
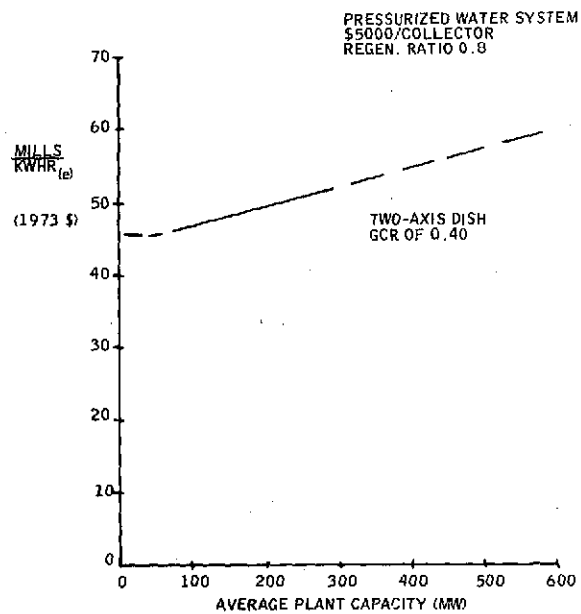
Figure 117.   Energy Cost Versus Plant Size (Total)

153
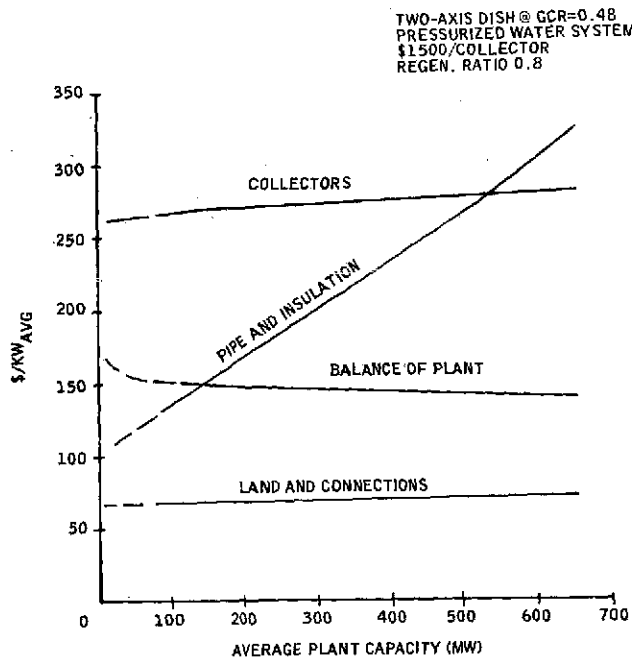
Figure 118. Energy Cost Versus Plant Size
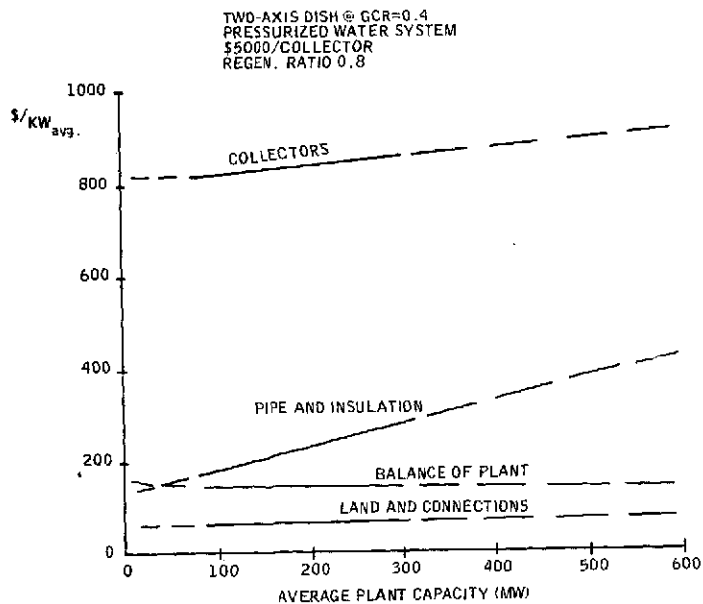
Figure 119. Energy Cost Versus Plant Size
(By Components)
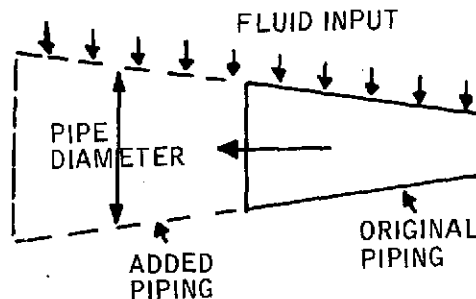
Figure 120. Added Piping Versus Original Piping

Actually, the hypothetical case presents somewhat of an oversimplification of the factors involved in the rising costs. Since the cost of energy rises with increasing plant size, the piping network sections will be designed to lose less energy per section than in smaller plants. But, because the larger plants require more of the larger diameter pipes than the smaller plants, the percentage of power lost in the total piping network will be increased. This point is sometimes confusing so an example is presented below to help clarify the point.

Consider a two-axis dish collector costing $5000 in a field with a ground cover ratio of 0.40. The system uses pressurized water as the heat transport fluid. Consider the hot water collector branch header designs for a 100 and a 150 Mw average plant capacity. The pipe diameters designed for each plant, along with the pressure losses incurred along each branch header, are shown in Figure 121. The mass flow rates along each branch header are identical out to Section 23 where the piping ends for the 100 Mw plant. The figure shows that the next largest pipe size was selected as optimal earlier upstream along the 150 Mw branch header than along the 100 Mw branch header. Since the cost of energy for the 150 Mw plant size is higher than for the 100 Mw plant size, it is expected that larger pipes would be selected to keep the pressure losses lower in sections having the same mass flow rate. Thus, along the branch headers, the 150 Mw plant will have a larger average pipe diameter not including the added pipe sections. In this case, the 100 Mw branch header has 23 individual pipe sections and the 150 Mw branch header has 28 sections. The additional 5 sections on the 150 Mw branch header are all 3.36 inch ID pipes.

Note that the pressure gradient along these last sections is higher than at any other point along the branch header. This is because the section pipe costs increase more than linearly for pipe diameters over 2-1/2 inches (see Appendix A). Steps up in pipe size are delayed longer and loss gradients, dp/dx, dQ/dx, reach higher values as bigger pipes are designed. The end result is that larger average plant capacities will have larger percentage energy losses. This effect is shown in Figure 122.

The rising $/Kw investment cost (Figures 118 and 119), for collectors can be explained by the decrease in piping network efficiency. Again consider doubling the size of a solar power plant. By doubling the number of collectors the absorbed power is doubled but, as shown in Figure 122, the percentage of power lost is also increased. Slightly less than twice the average power would, therefore, be available. To obtain the additional power required to double the average plant capacity, more collectors would be necessary and the $/Kw investment for collectors is therefore higher for the larger plant size.

NOTE: EACH SECTION IS 90 FEET LONG
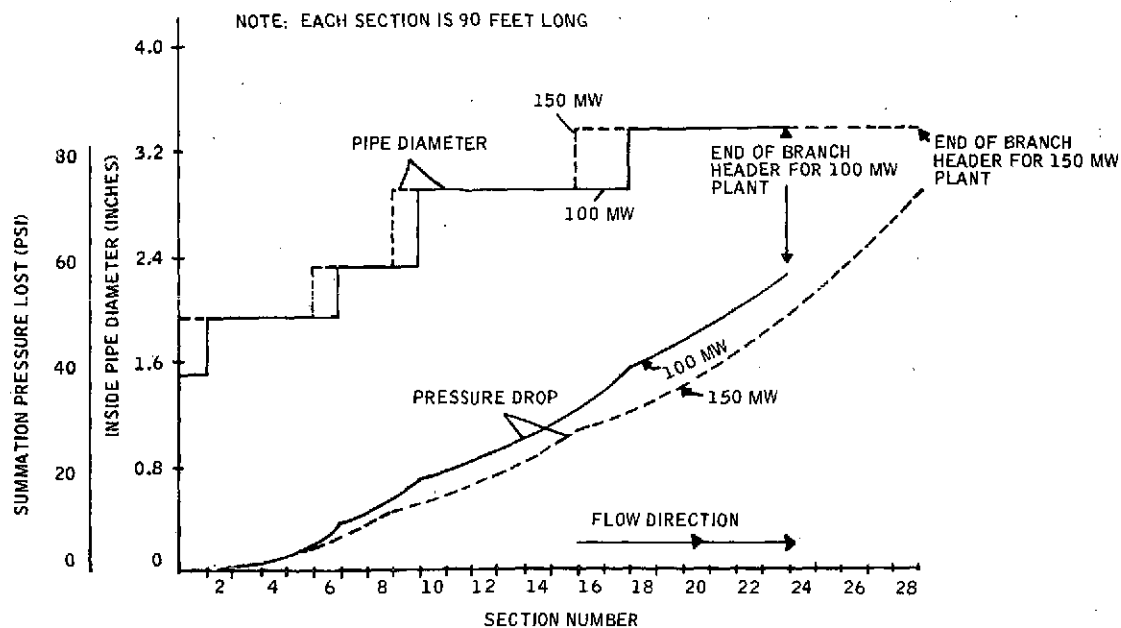
Figure 121. Pressure Losses Incurred

TWO-AXIS DISH @ GCR=0.48
PRESSURIZED WATER SYSTEM
$1500/COLLECTOR
REGEN. RATIO 0.8
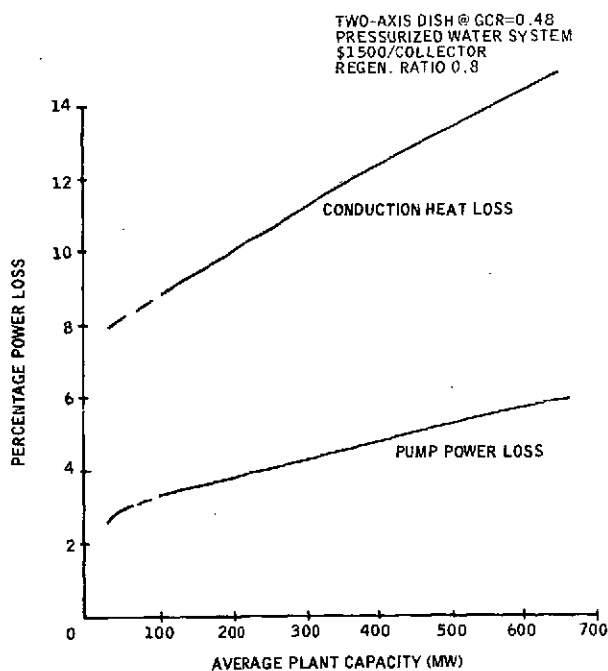
Figure 122. Power Loss Versus Plant Capacity

Degree of Regenerative Heating Selection

In fossil or nuclear fuel power plants the optimal feedwater temperature ratio, FTR, (also referred to as the regenerative heating ratio) is 0.8. For a solar plant distributed collector system the feedwater must be pumped over greater distances and the optimal FTR may be different than for the conventional systems. At lower feedwater temperature ratios, the feedwater temperature is lower. The advantages of a lower feedwater temperature for a distributed system are a reduced heat loss in the feedwater piping and an increased enthalpy change across the collectors. The increased enthalpy change may allow a lower mass flow rate to be used, thus pumping power can be reduced. In effect, the lower feedwater temperatures can reduce the investment which must be made for pipes and insulation. The disadvantage of using less regenerative heating is that the net turbine-generator efficiency is reduced. This implies that a greater thermal power must be collected at lower FTR values. (See Appendix B for the efficiency and temperature variations as a function of the feedwater temperature ratio.) By comparing the net energy costs as a function of the degree of regenerative heating, the economic optimum value of the final feedwater temperature can be found.

A sample of the results of exercising the energy transport system computer code for various degrees of regenerative heating is shown in Figures 123 and 124. For the pressurized water system, the net energy cost for feedwater temperature ratios from 0.5 to 0.8 is almost constant. An optimal FTR of approximately 0.65 can be chosen, but the variation of energy costs with regenerative heating is weak. The same conclusion can be made for the pool-boiling system results as shown in Figure 124. In this case, the optimal feedwater temperature ratio is around 0.55. This is slightly less than for the pressurized water system because the collector input temperature is higher than the final feedwater temperature when a heat exchanger is used. Some of the advantages of reducing FTR are lost at higher temperatures.

Energy Transport System Performance

Throughout the previous subsections, the performance of the piping network has been discussed as it affected the optimization parameters. The performance of a single solar power plant is discussed below. A pressurized water system is examined at an average plant capacity of 100 Mw. The 100 Mw plant is chosen as the optimal within the limits of the plant sizes being considered under this contract. The solar plant design conditions are shown below.

Solar Plant Conditions

Two-axis dish at ground cover ratio: 0.40

Turbine-generator (wet cooling)

Nameplate generator capacity: $125 \, Mw_{(e)}$

Inlet temperature: 585°F

Inlet pressure: 925 psia

Feedwater temperature ratio: 0.8

Efficiency: 0.35

Collector outlet temperature: 626°F

Collector inlet temperature: 547°F

TWO-AXIS DISH
PRESSURIZED WATER SYSTEM
AVERAGE PLANT CAPACITY 150 MW

MILLS
KWHR(e)

(1973 $)

GCR 0.40
$5000/COLL

GCR 0.48
$1500/COLL

FEEDWATER TEMPERATURE RATIO
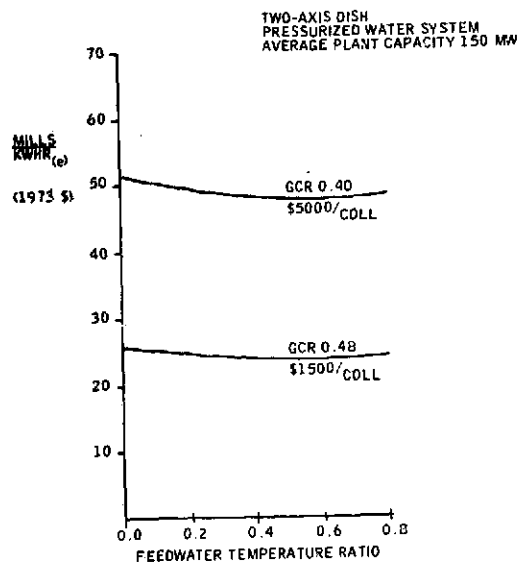
Figure 123. Energy Cost Versus Feedwater
Temperature Ratio

POOL - BOILING SYSTEM
$1500/COLLECTOR
AVERAGE PLANT CAPACITY 150 MW

TWO-AXIS DISH AT GCR = 0.45

POLAR TROUGH AT GCR = 0.40

MILLS
KWHR(e) (1973$)

FEEDWATER TEMPERATURE RATIO
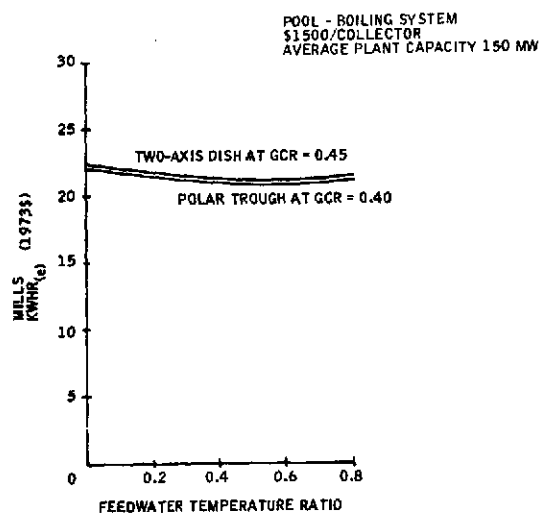
Figure 124. Pool-Boiling System
Results

158

From these specifications, the energy transport system computer program designed a field of 16,560 collectors, with a piping network having a total of 514,645 feet of header pipes and 641,700 feet of 1/2 inch connecting pipes. The piping is inventoried below by pipe diameter:

Piping Inventory

Nominal Pipe Diameter	Feet Required
1/2 inch	641,700
1-1/2	21,614
2	108,072
2-1/2	86,458
3	172,915
3-1/2	108,072
8	417
10	1,529
12	1,390
14	1,668
16	2,502
18	10,008

The piping and insulation layout is described in detail in Section X.

At this design point, the performance of the energy transport system is summarized below:

Yearly Average Performance Summary[*]

Thermal Power Collected:	291.19	$Mw_{(t)}$
Thermal Power Lost:	25.79	$Mw_{(t)}$
Percent Thermal Power Lost:	8.75	
Electric Power Generated:	93.03	$Mw_{(e)}$
Electric Power used in Pumping:	2.34	$Mw_{(e)}$
Percent Electric Power Lost:	2.51	

[*]Averages are over the total plant operating hours in one year.

The temperature and pressure in the piping network as a function of position in the field is shown in Figure 125. The figure shows the temperature and pressure along the piping which extends farthest from the steam generator. The above piping network performance data are based on a system mass flow rate which approximates the mass flow rate at the average annual pumping power level. The instantaneous pump power varies approximately as the cube of the mass flow rate. In operation, the absorbed power will vary during a year's or day's operation, causing the system's mass flow to vary. This will affect the system performance. To reasonably approximate the off-design performance, a simplified approach will be used.

The load-duration curve for the dish collector field under consideration is shown in Figure 126. Design point heat, temperature, pressure and pumping power losses were calculated using the steady-state equations previously presented. Off-design performances are calculated using the fact that the mass flow is directly proportional to the absorbed power. Thus, the absorbed power($Mw_{(t)}$) can be used in place of the mass flow rate in the loss equations. The off-design performance calculations are approximated as:

PRESSURIZED WATER SYSTEM
TWO-AXIS DISH @ GCR = 0.40
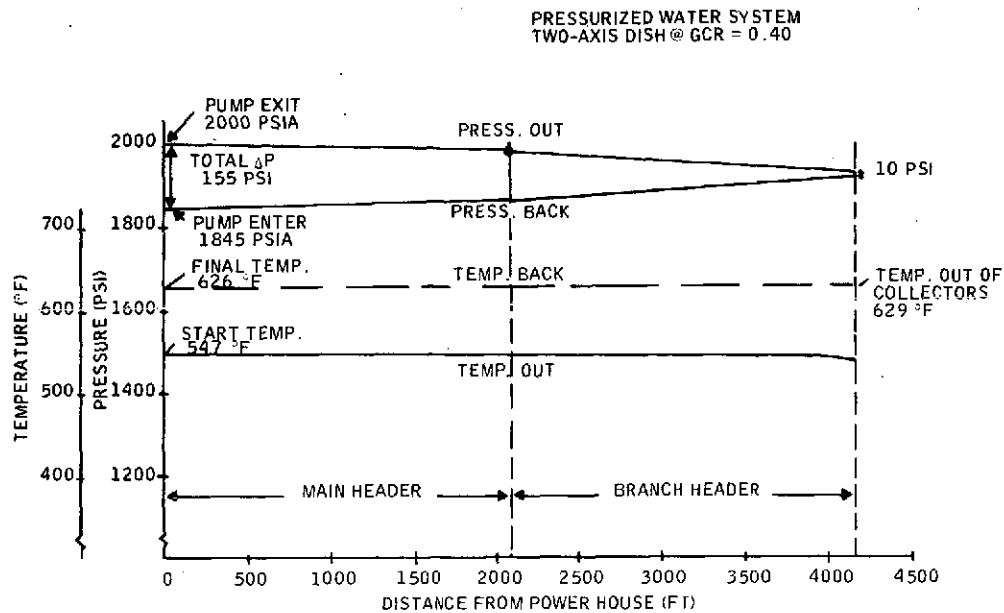
Figure 125. Design Point Pipe Network Performance

PRESSURIZED WATER SYSTEM
TWO-AXIS DISH @ GCR=0.4
16,560 COLLECTORS
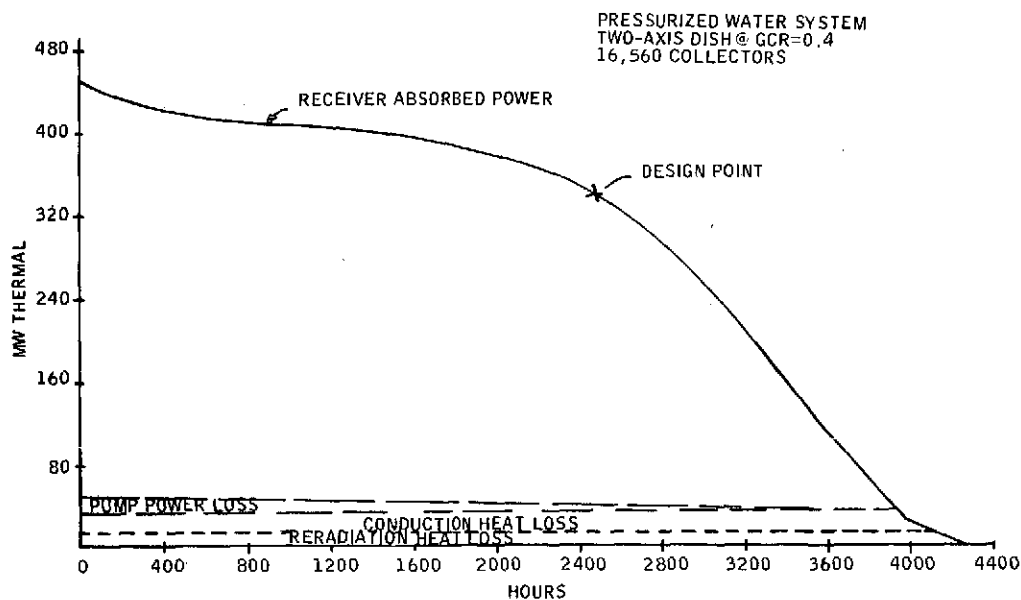
Figure 126. Thermal Load-Duration Curve for a Solar Plant Average
Capacity of 100 $MW_{(e)}$

$$\Delta P = \Delta P^* \left(\frac{Mw^2}{Mw^{*2}} \right) \qquad (35)$$

$$PW_{loss} = PW^*_{loss} \left(\frac{Mw^3}{Mw^{*3}} \right) \qquad (36)$$

$$Q_{loss} = Q_{loss}^* \qquad (37)$$

$$\Delta T = \Delta T^* \left(\frac{Mw^*}{Mw} \right) \qquad (38)$$

where the starred (*) superscript indicates the losses at the design point.

The piping network efficiency is defined as:

$$\eta_p = 1 - \frac{Q_{loss} + PW_{loss}}{Mw} \qquad (39)$$

Using the off-design approximations,

$$\eta_p = 1 - \frac{Q^*_{loss}}{Mw} + \frac{PW^*_{loss} Mw^2}{Mw^{*3}} \qquad (40)$$

The design-point conditions are given in the previous performance summary table and in Figures 127 and 128. The load duration curve of Figure 127 is used to obtain off-design absorbed power values ($Mw_{(t)}$). Figure 128 shows the piping network performance parameters during the year's operation. The temperature at the heat exchanger entrance drops off from 629°F at 440 $Mw_{(t)}$ to 620°F at 120 $Mw_{(t)}$ and 600°F at $Mw_{(t)}$ where the absorbed power and mass flow are extremely low. The problem associated with the temperature roll-off is that the turbine inlet conditions are affected. However, the turbine inlet temperature can be held constant by controlling the mass-flow ratio of turbine side to collector side.

Figure 127 was used to generate a plot showing approximate daily performance of the network. Figure 128 shows how the performance parameters vary throughout the day for 3/15.
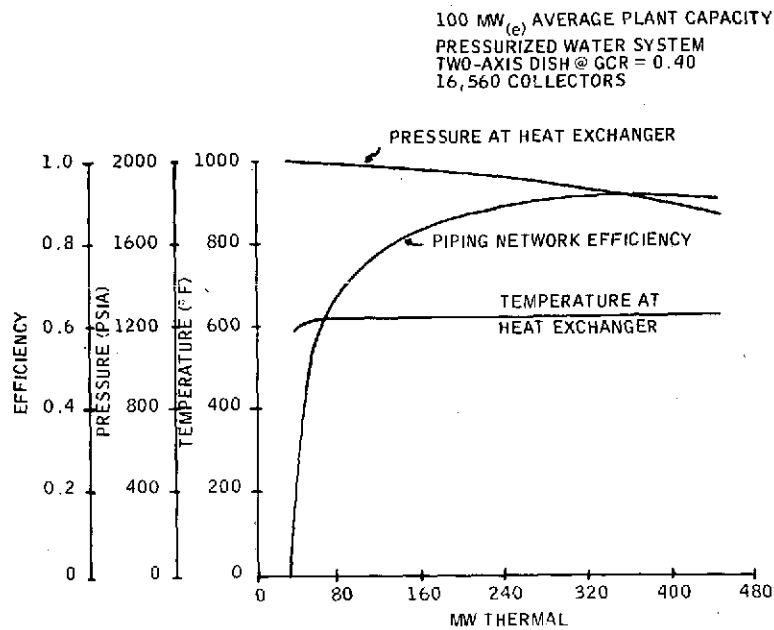
Figure 127. Off-Design Point Energy Transport Performance
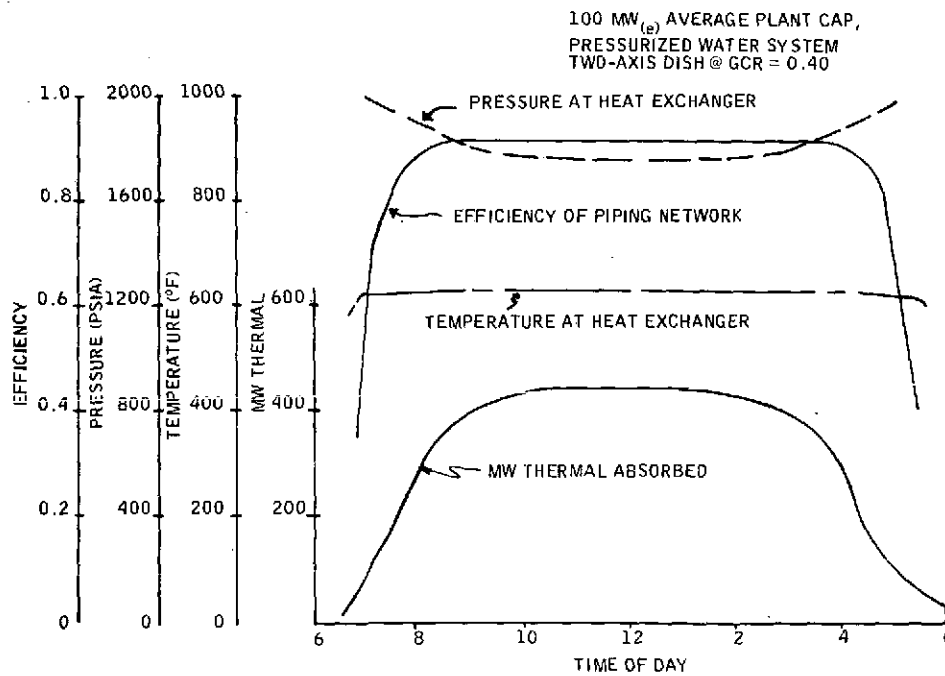
Figure 128. Daily Piping Network Parameter Variation

CENTRAL RECEIVER RISER AND DOWNCOMER DESIGN

In a central receiver, superheated steam generating plant, the turbine-generator, condenser, and feedwater heating system will be located adjacent to the base of the tower. The feedwater and steam will be transported up and down the tower in a riser and downcomer system. In designing this system, the following choices must be made:

1. Single-versus-multiple risers and downcomers
2. Pipe size
3. Method of absorbing thermal expansion

For the anticipated 50-200 Mw plant, both the feedwater and the steam could each be handled by single, commercially available pipes. A multiple-pipe arrangement would have a higher capital cost, a higher installation cost, and would require more pump power. Since multiple pipes have no significant advantages, a single pipe is superior.

The sizing of any pipe requires analyzing the economic tradeoff between the higher capital cost for a larger pipe, and the higher pressure drop for a smaller pipe. Thus, it is necessary to know the cost of pump power, which requires knowing both plant cost and plant annual output. In addition, tower height must be known as a function of plant output. Since this is known only approximately, this analysis for solar generating plants cannot be performed accurately at this time. An alternative, less accurate method is to assume a "reasonable" pressure drop in the pipes and to design the pipes to that requirement. This method has been used.

Since these pipes will operate at elevated temperatures, they will experience thermal expansion. Two methods of absorbing this thermal expansion have been considered:

1. Expansion loops
2. Bellows-type expansion joints

A typical expansion loop design is shown as a solid line in Figure 129. As the temperature is increased, the pipe expands and assumes the shape indicated by the dashed line.

A typical expansion joint design is shown in Figure 130. As the pipe is heated and expands the joints absorb the motion with a bellows action.

Although the expansion joint design has a lower capital cost, bellows-type expansion joints are not commercially available with a pressure-temperature rating above 400 pounds per square inch/400 degrees Fahrenheit.

The present study uses an expansion loop design.

Since the pressure drop depends on the number of bends and total pipe length, the pipe size depends on the expansion loop design. The expansion loop design, however, depends on the pipe size. Therefore, the design of the pipe size and expansion loop parameters is an iterative process.

The assumed frictional pressure drop was 50 pounds per square inch in the riser and 50 in the downcomer. The operating temperature ranges were 400 Fahrenheit for the riser and 900 Fahrenheit for the downcomer. Black & Veatch has acquired considerable expertise in calculating and designing pipes subject to thermal expansion. Computer programs which calculate expansion loop parameters for a given pipe size were iterated with pressure drop calculations until suitable designs were obtained. Resulting pipe sizes are given below:

Figure 129. Schematic Expansion Loop Design
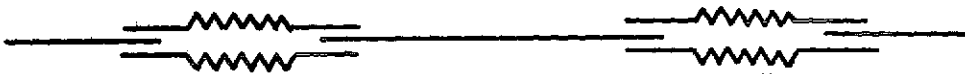
Figure 130. Schematic Expansion Joint Design

Plant Output	Tower Height	Riser Pipe	Downcomer Pipe
60 MW	750 ft	6 inch SCH 80	18 inch SCH 80
215 MW	1500 ft	10 inch SCH 80	24 inch SCH 80

The risers will be A-106 carbon steel and the downcomers will be 1-1/4 percent chrome - 1/2 percent molybdenum grade P-11 alloy steel.

The detailed expansion loop parameters, along with the detailed hanger design, are presented in Section X. Cost calculations for the riser and downcomer for the 1500 foot tower are also presented.

The pipe material, insulation, welding, fittings and erection costs were obtained from industrial firms with wide experience in pipe fabrication and erection. Hanger installation costs are based on one dollar per pound of hanger, a figure developed by Black & Veatch

With the tower height, riser design, and downcomer design known, the pump power can be calculated. The pump power used to obtain turbine throttle pressure is already included in the calculations of net plant heat rate and cycle efficiency (see Section IX). The pump power calculated here is the power associated with the static and dynamic losses in the tower. Since both the pump power and the plant output are almost exactly proportional to flow rate, the pump power is calculated as a fraction of plant output. The results, based on a pump efficiency of 85 percent, are:

Tower Height (feet)	Rated Capacity (MWe)	Pump Power (fraction of output)
750	60	0.0040
1500	215	0.0068

SECTION VIII

ENERGY STORAGE/TURBINE-GENERATOR AND HEAT REJECTION STUDIES

ENERGY STORAGE STUDIES

The objective of this task was to identify and conceptually define the most promising energy storage system for solar-thermal power generation. The hot water thermal storage concept was selected for short-term storage to provide power during brief solar outages. The basic concept has the following advantages:

- Well-developed technology
- Location independence
- Ease of heat transfer
- Minimum corrosion difficulties
- Practically infinite lifetime

These advantages make the hot water storage an attractive candidate. The design and analysis of a specific hot water storage system are described below.

BASELINE DESIGN

The energy storage system selected as the design for a solar-powered central electric power plant is shown in Figures 131 and 132. This is a multi-tank hot water stratified system. The tank size of 11 feet outside diameter x 41 feet outside length was dictated by transportation ease, allowing fabrication of factory assembled units.

During actual operation, some tanks will have cold return water flowing in from the bottom, hot supply water out from the top, while others will be idle, either holding "spent" return water or supply water ready to be used. This will minimize mixing losses during partial discharge operation and will ease control problems. Valves on each cylinder will control tank flow.

Tank Design for Hot Water Storage

The thickness, t, of a cylindrical shell for use as a pressure vessel can be calculated from:

$$t = \frac{PR_o}{S + 0.4P}$$

where

t = thickness of shell plate, inches

P = design pressure, psi

R_o = outside radius of shell, inches

S = maximum allowable stress, psi

166
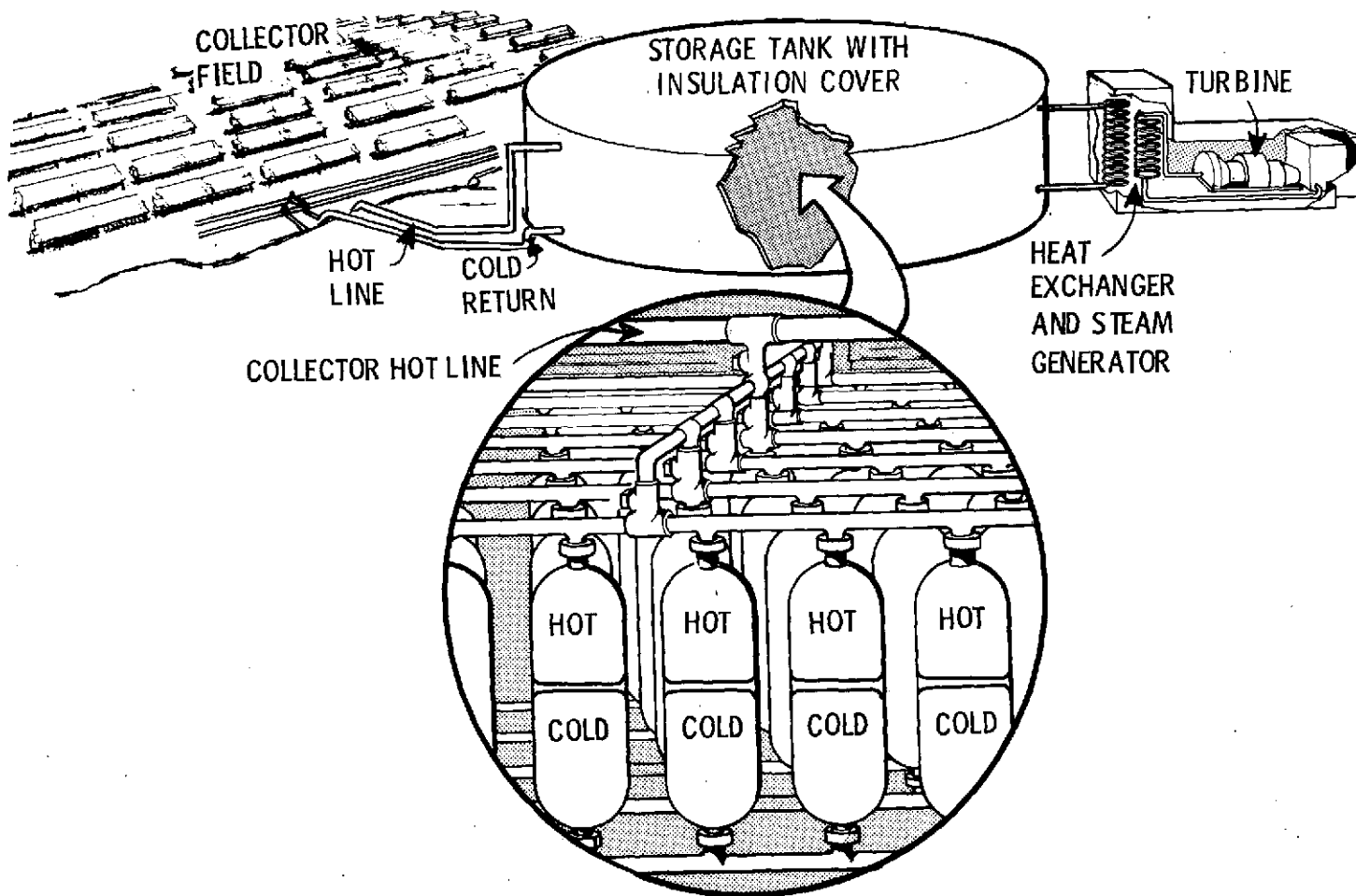
Figure 131. Hot Water Storage System
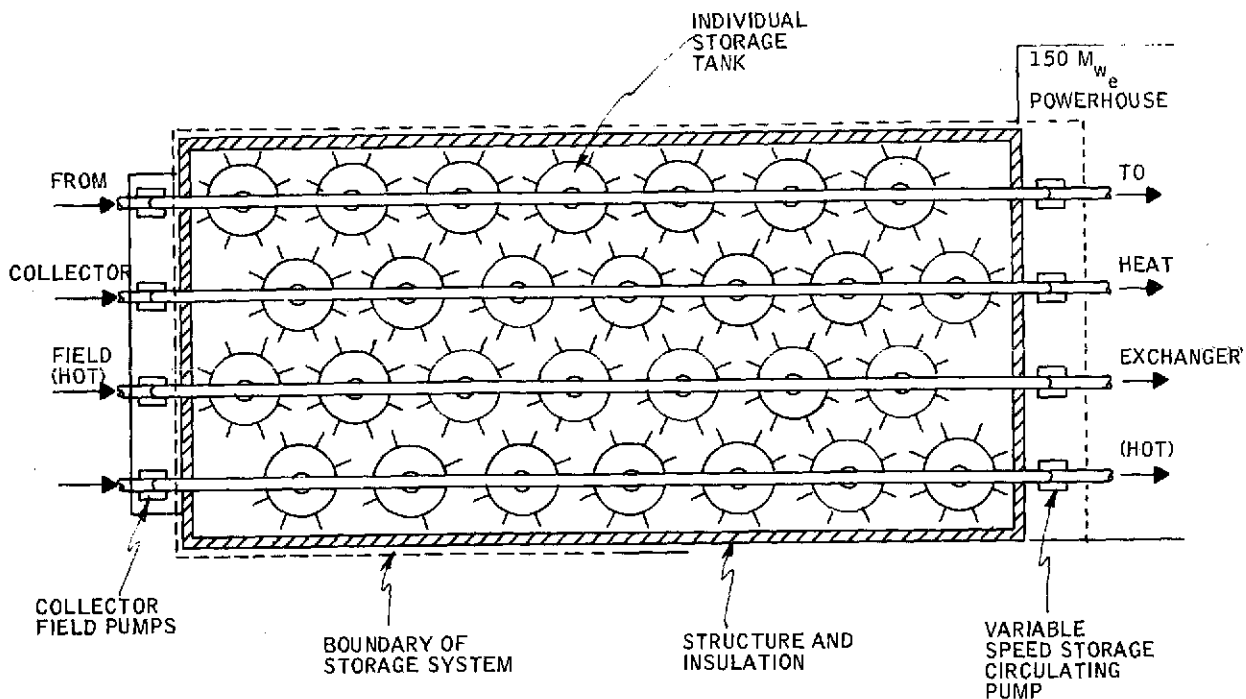
(Top View - One Half of System)
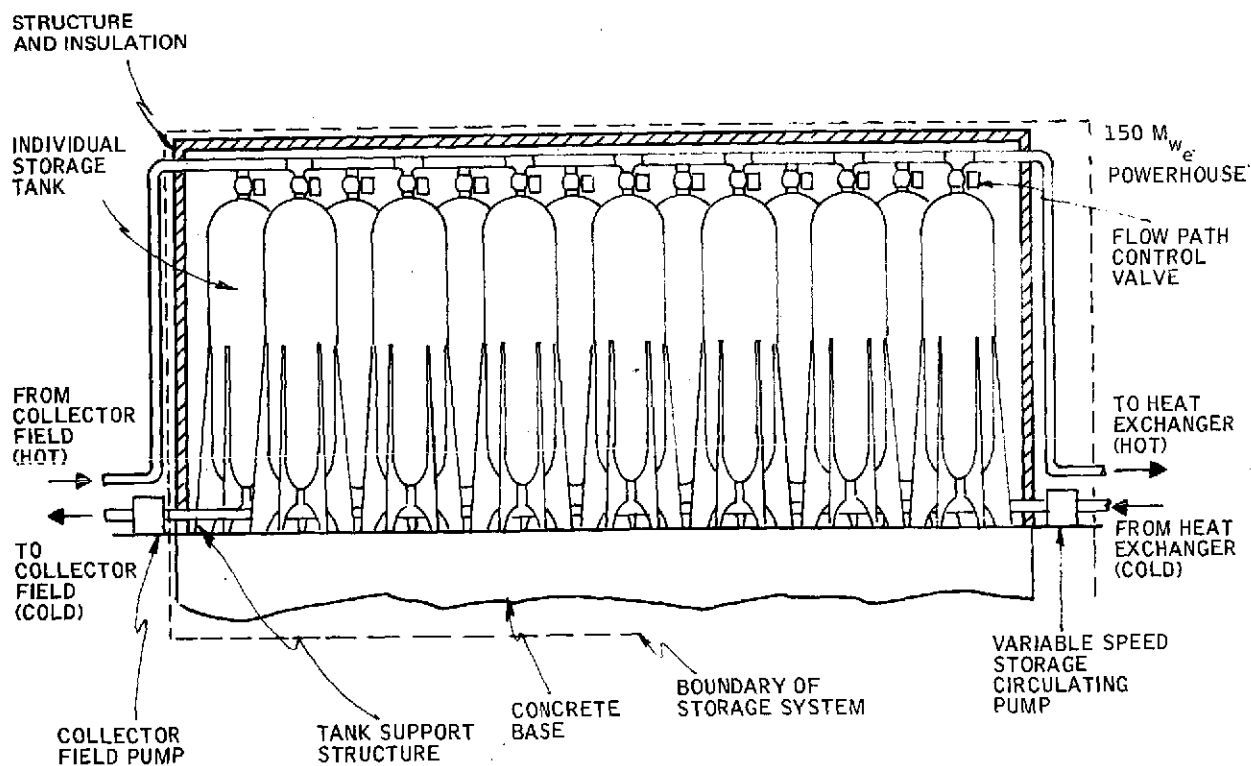
(Side View - One Half of System)

Figure 132. Storage System

One common metal used to construct pressure vessels for nuclear reactors is SA-533, Grade B - Class 1. This is a low-alloy steel with the following chemical constituents:

Carbon	0.25 percent, maximum
Manganese	1.15-1.50 percent, maximum
Phosphorous	0.035 percent, maximum
Sulfur	0.040 percent, maximum
Silicon	0.15-0.30 percent, maximum
Molybdenum	0.45-0.60 percent, maximum
Nickel	0.40-0.70 percent, maximum

For metal temperatures not exceeding 750°F, the maximum allowable stress is 20,000 psi. Using this value for the design of a 10-foot inside diameter and 40-foot inside length with hemispherical heads cylindrical vessel, the wall thickness can be calculated as a function of the desired pressure. In addition, the mass of the metal which acts as a heat sink can be determined. Thus,

Design Pressure (psi)	Shell Thickness (inches)	Metal Mass (lbs x 10^3)	Internal Vessel Volume
2000	6.38	349.7	2878

The potential volume efficiency loss problem, caused by high tank mass lowering the differential enthalpy of the contained water, is resolved by an analysis which is presented later.

The tank design and the design parameters are shown in Figure 133 and Table XXV, respectively. Performance specifications for the system are given in Table XXVI, while the cost estimates are shown in Table XXVII.

Operation

The energy from the distributed collectors is collected and transported in the field as pressurized water. When the collected energy is taken directly from the field to drive the turbine, it goes through a heat exchanger and steam generator. When the turbine is run from stored energy the stored water is run through the same heat exchanger. Slight temperature drops which occur in storage are compensated in the heat exchanger so that the turbine receives identical temperature and pressure steam whether stored energy or energy direct from the collectors is used. Figure 134 shows how this is accomplished. The pinch point can be thought of as a pivot point on the pressurized water lines.

The slope of the water lines is set by the mass flow ratio (ratio of mass flow through the collectors, or from the storage tanks, over the mass flow through the turbine). To minimize pump work, this ratio was set as small as possible. The limit on how low the mass flow ratio can go is the upper temperature limit for the pressurized water at the working pressure. After the water has been stored, it suffers a drop in temperature. To yield the same turbine inlet temperature, the mass flow ratio is increased, reducing the slope and, hence, reducing the required water temperature. Notice that at higher mass flow ratios, a given quantity of stored thermal energy (or given mass of water) will not run the turbine as long a time. The potential electric energy of the water is lost while its thermal energy is not. The main advantage of collecting energy and storing energy in the same fluid is that it does not require two heat exchange processes in series. Furthermore, for pumping economy, the energy is collected at temperatures well above the minimum necessary to produce steam at design turbine inlet conditions. This means that there is a relatively wide temperature margin over which the temperature drop in storage can be accommodated.

170
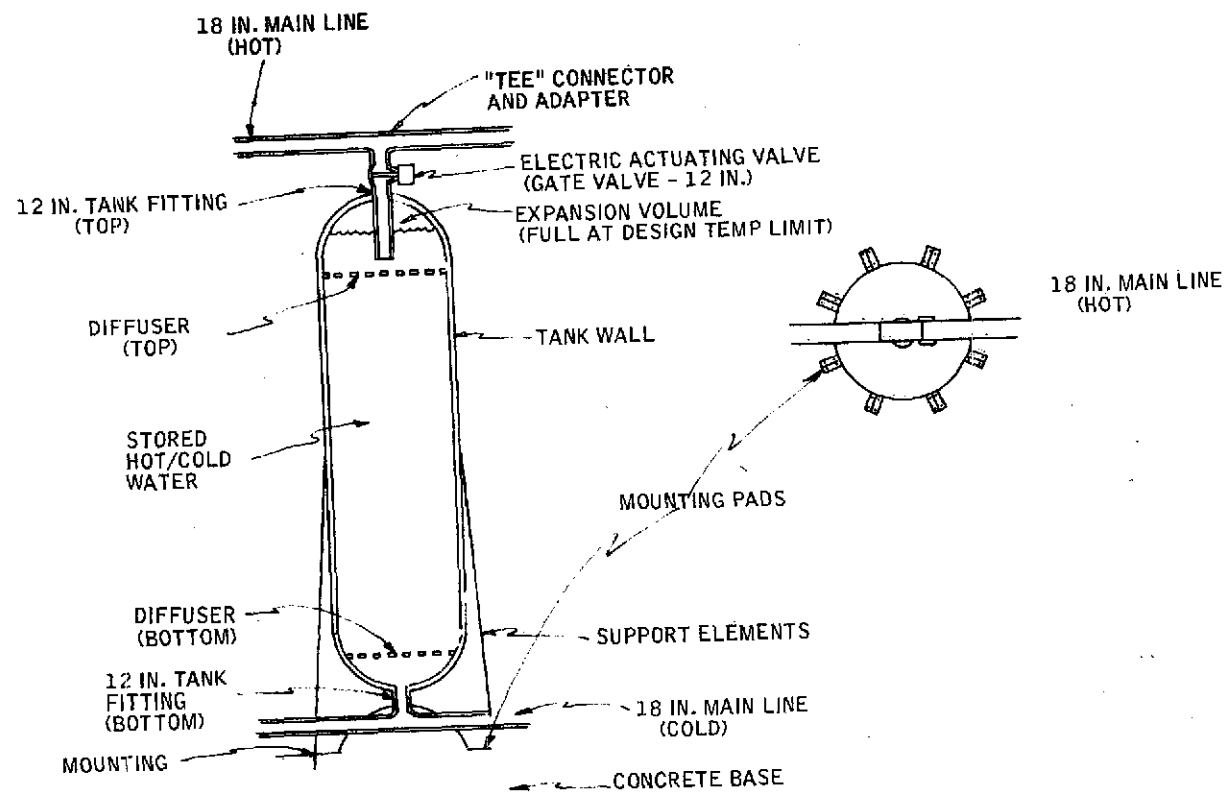
Figure 133. Tank Design

Table XXV. Tank Design Specifications

Type:	Cylindrical with Spherical End Caps
Size:	Volume: 2878 Ft^3
	Dimensions: 11.06 ft O.D. - 41.06 ft. L.O.A.
Material:	SA-533 Grade B Class 1 Steel
Weights:	Empty: 350,000 Lbs (Without fittings)
	Unit Shipping: 350,000 Lbs (includes structure, piping, valving, diffusers)
	Installed W/Water: 480,000 Lbs

Fittings Required:

    (2) Inlet/outlet pipes (12 inches)   (2) Diffusers

    (1) Gate valve, 12 inches electric   (8) Tank support brackets

    (2) 18 inches main to 12 inches side tees

Design Limits:

    Pressure: 2000 P.S.I.

    Temperature: 626°F

    Valve Opening Time: < 30 sec

    Tank Discharge Time: 3.16 min

    Sideward Acceleration: 0.6 G (4 x Earthquake Zone 3)

Table XXVI. Specifications

System Design:

    Type: Multiple tank sequential discharge (pressurized water)

    Arrangement: 8 parallel x 7 time sequential (Total: 56 tanks)

    Controls:

        Flow Path: Individual on/off electric actuated gate valves

        Flow Rate: Variable speed pumps (8 total; 1/parallel line)

System Performance:

    Input/output: 0.99 + (pump losses only)

    Storage: 0.99+/Hr

System Rating:

    Power Output: 150 Mw$_e$ (444 Mw$_t$)

    Time of Run: All tanks (56): 33 min (615°F)

Table XXVII. Cost Estimate

Tank Cost:			
Material (320,000 at 0.30/lb	=	$	96,500
Fabrication labor (equals material)	=		96,500
Value Cost	=		11,000
Tee cost (2)	=		1,000
Shop welds (3)	=		280
Single Tank Subtotal		$	204,280
System Cost:			
Tanks (56)	=	$11,440,000	
Transport (20 percent tank cost)	=	2,290,000	
Base (concrete, material and installation)	=	44,000	
Tank installation ($10,000/tank)	=	560,000	
Connecting pipe assembly (280 extra welds)	=	77,000	
Pump cost (8 at $50,000)	=	400,000	
Pump installation (50 percent)	=	200,000	
Structure (2 at $50,000)	=	100,000	
Insulation (0.72/ft^2 at 3 ft)	=	37,000	
Insulation installation (200 percent)	=	74,000	
Total Capital Cost		$15,222,000	
Capital cost/kw-hr		$	203
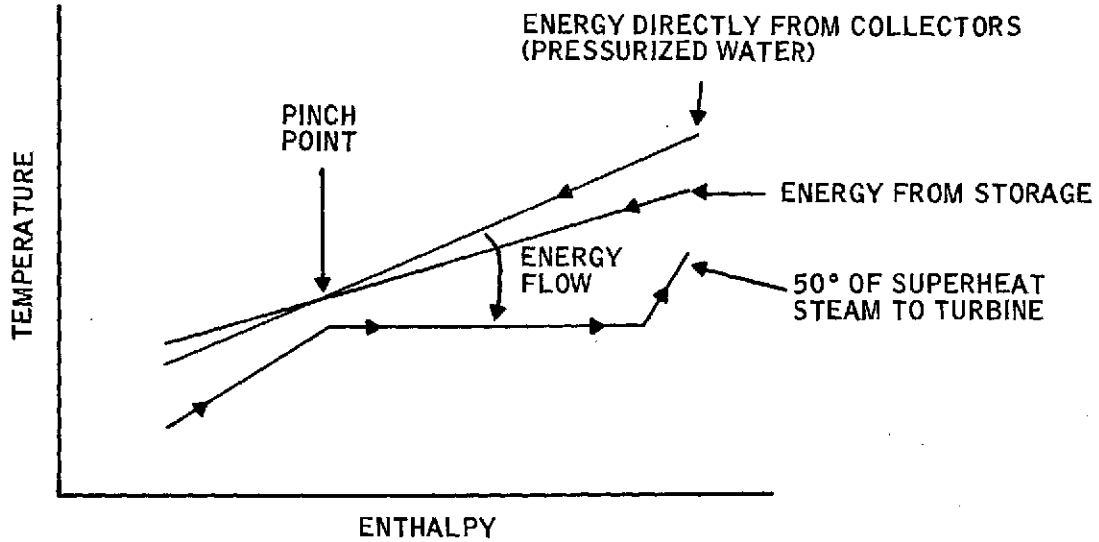
Figure 134. Temperature Drop Configuration

SYSTEM PERFORMANCE

The system performance was calculated to ascertain the expected temperature drop in storage. It should be pointed out that the basic loss mechanism in the stratified tank concept is, in fact, not a loss of energy but a degradation of the quality of the energy. That is, the temperature of the water is reduced when it comes into contact with, and equilibrates with the cool metal tank walls. After each time the stored energy is used, the tank is refilled with cooler water, which then cools the tanks again before the next filling. The heat loss rate to the environment is low and can be ignored. With this assumption, the simultaneous equation set for all the equilibrium temperatures in the system can be defined.

Basically, the tanks are in one of two equilibrium states when they are charged or discharged. First, each tank is filled with a weight of water (W_W) at the collection temperature (T_{coll}). After the water comes into equilibrium with the metal walls of the tank (at temperature T_H), a quantity of energy (E_T) has been transported from the water to the metal where (E_T) is given by

$$E_T = W_W[H(T_{coll}) - H(T_H)] \tag{41}$$

where $H(T_i)$ is the enthalpy of water at temperature (T_i) and pressure equal to the system operating pressure (2000 psi). In this process, the temperature of the metal walls goes from the cold-state temperature (T_c) to the hot-state temperature (T_H). The amount of heat added to the metal walls (E_T) is given by

$$E_T = W_S C_{p_S}(T_H - T_c), \tag{42}$$

where W_S is the weight of the steel in the tank walls and C_{p_S} is the specific heat of the steel. Since the losses to the environment are assumed negligible, the heat gained by the metal is equal to the heat lost by the water. Clearly then, we can combine Equations (41) and (42) to yield:

$$W_S C_{p_S}(T_H - T_c) = W_W[H(T_{coll}) - H(T_H)] \tag{43}$$

173

As the tank is discharged from the top, it is filled from the bottom with the same weight of water (W_W) at the temperature of the returning fluid from the heat exchanger (T_{ret}). The water initially at (T_{ret}) comes into equilibrium with the metal tank walls which were initially at (T_H). Thus, when the tank comes to its cold equilibrium state the water gains an amount of energy (E_T) given by

$$E_T = W_W [H(T_c) - H(T_{ret})] . \tag{44}$$

When the metal walls cool down to (T_c), they give up an amount of energy given by

$$E_T = W_S C_{p_s} (T_H - T_c) . \tag{45}$$

As before, we combine 4 and 5 to yield

$$W_S C_{p_s} (T_H - T_c) = W_W [H(T_c) - H(T_{ret})] . \tag{46}$$

Equations (43) and (46) represent two equations in three unknowns (T_H, T_c), T_{ret}). The additional required equation for (T_{ret}) comes from the heat balance on the heat exchanger.

The energy flow chart for a heat exchanger and steam generator was shown in Figure 134. To organize the calculation, the schematic diagram (Figure 135) of the system is broken into a counter flow heat exchanger and a steam generator. The pinch point constraint is then clearly visible in the schematic. The thermal power transferred to the boiling steam is (P_T) where:

$$P_T = \dot{m}_T H_V \tag{47}$$

and $\dot{m}_T$ is the mass flow through the turbine, T_{inlet} is the turbine inlet temperature, and $H_V(T_i)$ is the heat of vaporization of water at the turbine operating inlet pressure and temperature. This power is supplied by the temperature change of the following storage fluid from the inlet to the outlet of the steam generator:

$$P_T = \dot{m}_s [H(T_H) - H(T_{inlet} - \Delta T)], \tag{48}$$

where $\dot{m}_s$ is the mass flow rate from the storage tanks. Clearly, Equations (47) and (48) can be combined to yield:

$$\dot{m}_T H_V = \dot{m}_s [H(T_H) - H(T_{inlet} - \Delta T)] . \tag{49}$$

By the same argument, we can form a heat balance on the counter flow heat exchanger to yield:

$$\dot{m}_T [H(T_{inlet}) - H(T_{RH})] = \dot{m}_s [H(T_{inlet} - \Delta T) - H(T_{ret})] , \tag{50}$$

where T_{RH} is the temperature of the water from the regenerative heaters.

Equations (43), (46), (49), and (50) form four nonlinear simultaneous equations in four unknowns T_H, T_c, T_{ret}, and (m_s/m_t). The variables which affect the solution are (W_S/W_W), T_{inlet} and T_{RH}, which is a function of the regenerative heat ratio. Notice that only the ratios of storage to turbine mass flow (m_s/m_t) and metal-wall-weight to stored-water-weight appear in these equations. This allows a solution of the equations which is independent of the scale of the system. We have programmed a solution algorithm which uses a modified Newton-Raphson iteration scheme, for this equation set. We found solutions at various thicknesses of tank walls.

The effect of increasing wall thickness is to reduce the temperature of the stored fluid and require a higher mass flow ratio (m_s/m_t). The higher mass flow means that effectively the turbine run time which can be obtained from a fixed-volume storage tank is reduced as the metal wall thickness is increased. The results of the calculation are shown in Figure 136.

174
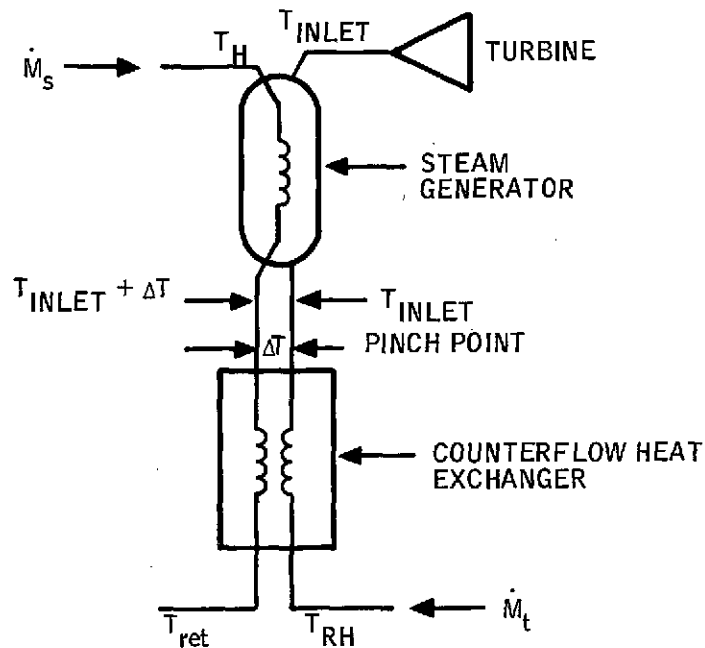
Figure 135. System Schematic

The thickness is shown to provide a physical insight into the design but the physical parameter which actually determines the efficiency is the ratio of weight-of-metal-tank-walls to weight-of-water-stored (W_S/W_W). This ratio can be shown to be proportional to the ratio of internal tank pressure over design tensile stress in the tank walls. Thus, the result of an $\sim$ 80 percent efficiency to satisfy boiler code for this size tank actually holds for any size tank with a 2000-psi internal pressure and the stress limit defined by the boiler code.

CANDIDATE ENERGY STORAGE SYSTEMS

Water

Storage of energy as sensible heat in water can be accomplished in a temperature range of 50°F to 650°F. At the higher temperatures, the vapor pressure is high and the storage containment will require heavy equipment. Because of equipment costs, water may be best suited to the lower temperature range, perhaps 450°F and below.

When a sufficient temperature change is practical for water storage, the storage heat capacity per unit volume and weight is competitive with the heat of fusion of many salts. Furthermore, water is a relatively abundant, low-cost material which presents no high risk to environmental concerns or technology development. The major problem with implementing many water storage schemes is the cost. Major cost items are the storage tanks, insulation, piping and any required heat exchangers.
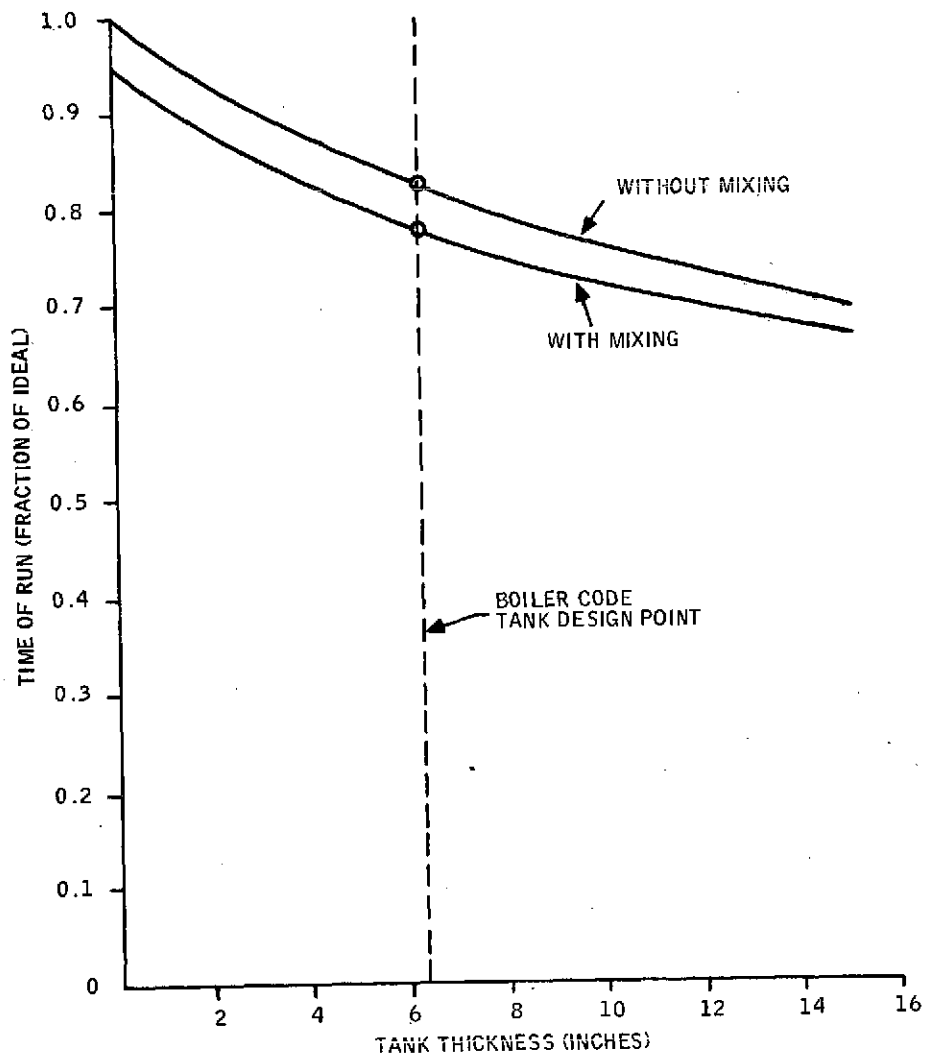
Figure 136. Storage Volume Efficiency

Aquifer

An aquifer can be used for sensible heat storage by drilling a number of pairs of widely spaced wells into an aquifer of suitable depth. Water can then be withdrawn from the deeper wells and heated by a thermal energy source. The hot water would then be injected into the shallow wells where, according to one-dimensional analysis, "inverted cones" of hot water/rock are formed. The hot water can be withdrawn when needed and the cold water returned would be re-injected into the deeper wells.

The major cost items are the drilling, the pumps and transport requirements. The major problem with the storage scheme is the fact that it is very much site dependent and could have adverse environmental impacts.

Blast Cavity

The blast cavity is another alternative scheme for sensible heat storage in water. A deep well is drilled into hard, nonporous rock (granite), and a large-scale explosive charge (100 kiloton atomic device) is detonated, fracturing rock and allowing injection of heated water which can then be used in the same manner as the hot water tank. A second hole is "slant" drilled (current oil exploration technology) to the "bottom" of the cavity allowing cavity water stratification. The major costs are the drilling, transport and pumping. Further costs are associated with operational radiation control and leaching control from fractured rock. The concept uses the natural insulation and containment provided by the surrounding rock, but it may have an adverse environment impact and its application definitely depends on location.

Preliminary cost estimates of the blast cavity approach indicate that it is economically promising for large-volume storage at suitable locations.

Eutectic Salt

The thermal storage of energy by molten eutectic salts, using phase change, is a thermodynamically attractive concept since much of the energy is transferred across relatively small temperature changes. A salt storage using high-temperature steam as the heat source and saturated steam as the application is charted in Figure 137.

How much of a temperature drop actually occurs depends on the design geometry and the thermal conductivity of the materials selected.

Major cost items are the salt and the containment structure. The primary technical problems are the corrosion and compound separation characteristics of most salts. (Appendix C presents some basic salt mixtures currently being investigated.)

Metal

Metal (aluminum at low pressure) can be contained in a tank in which the heat transport piping is located. Heated transfer fluid passes through the pipes, melting the metal and storing the heat. When heat is required, cooler transfer fluid is passed through the pipe network, extracting the energy. Heat transfer efficiency is high because of the conductive nature of the molten and solidified aluminum. Major cost items are the aluminum, the piping network, and the containment vessel and insulation. This system, while it presents basically the same favorable features as eutectic salts, does not have their corrosion problems, but it does face a probable material resource shortage.

Organic Compound

The organic compound system is the same as the eutectic salt system, except that it entails less of a corrosion control problem. It seems suited for low-temperature thermal storage. Major cost items are the special wax-plastic material, and the containment structure and insulation.
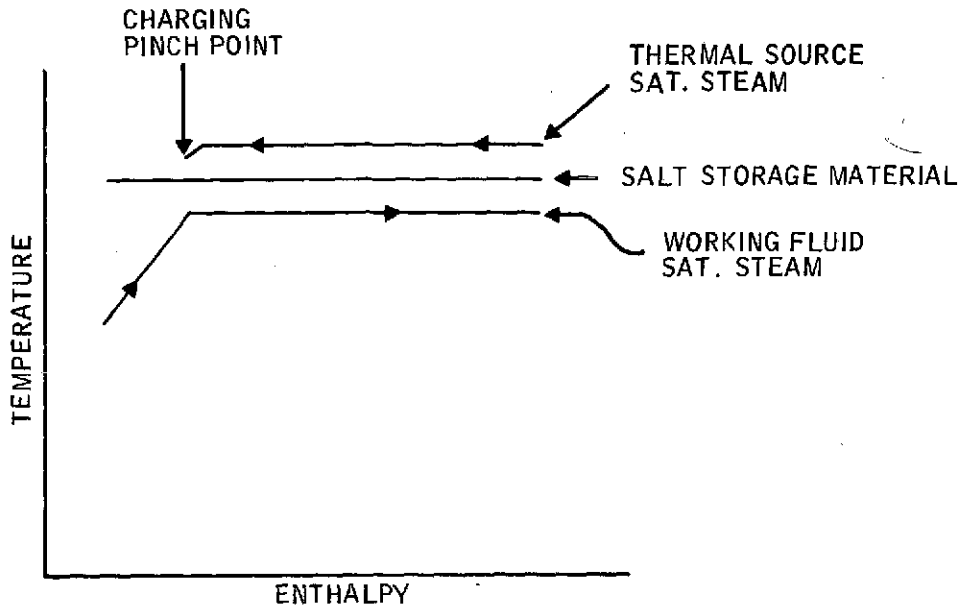
Figure 137. Energy Storage by Molten Eutectic Salts

Salt and Metal

For very high temperature thermal storage, a combination of molten salt and a stratified tank high-temperature liquid metal storage is possible.

The energy flow in the combined salt and liquid metal system is shown in Figure 138. Thermodynamically, this is a good fit, but the liquid metal pumps and heat exchangers associated with this system are very expensive.

Steam Accumulator

The steam accumulator concept has actually been used as a steam storage system. High-pressure steam is mixed with water and allowed to condense in a pressure vessel. As more steam is added, the mass of water eventually reaches the boiling point at the charging pressure. To discharge the steam, the pressure is dropped and the water flashes back to steam. The fraction of the water which can be flashed into steam is determined by the pressure drop.

Unfortunately, most modern turbo-machinery is sensitive to inlet pressure and temperature variation. To have a large enough pressure drop to flash a significant amount of water into steam, the system must be charged with a higher pressure (and, hence, higher temperature) energy source than the turbine inlet conditions require.

Superheated steam can be used to charge a steam accumulator storage system, at least in theory, but only saturated steam could then be withdrawn from it.

The complication of heat storage when the energy source is saturated or superheated steam derives from two sources: the constant temperature heat exchange during phase change; and the lack of a heat exchanger between the energy supply and the turbine to compensate for termpeature drops in the storage system.

The temperature drops associated with the phase change are shown in Figure 139.
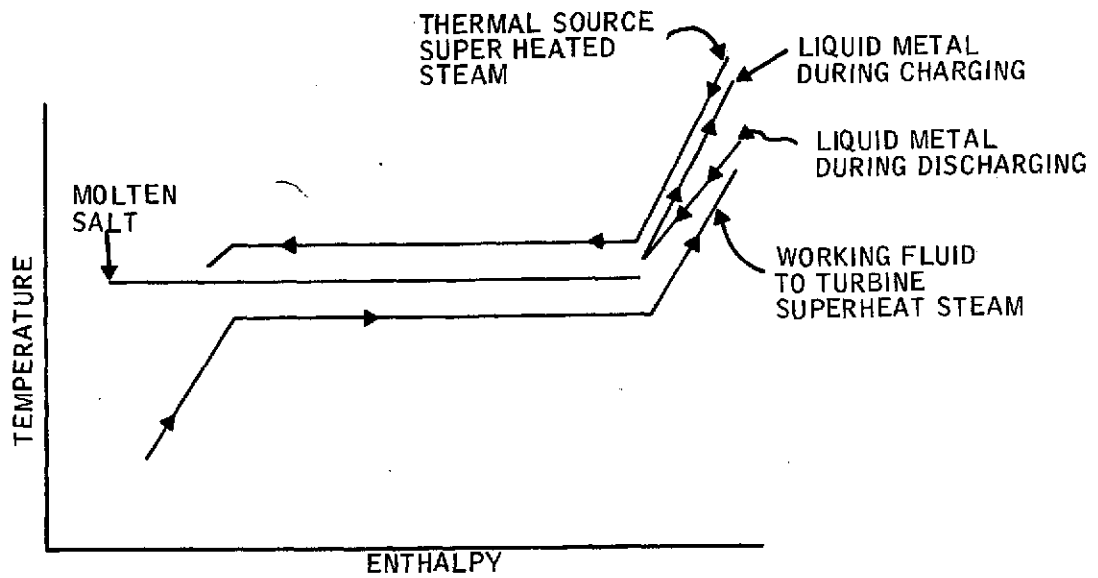
Figure 138. Energy Flow in Combined Salt and Liquid Metal System
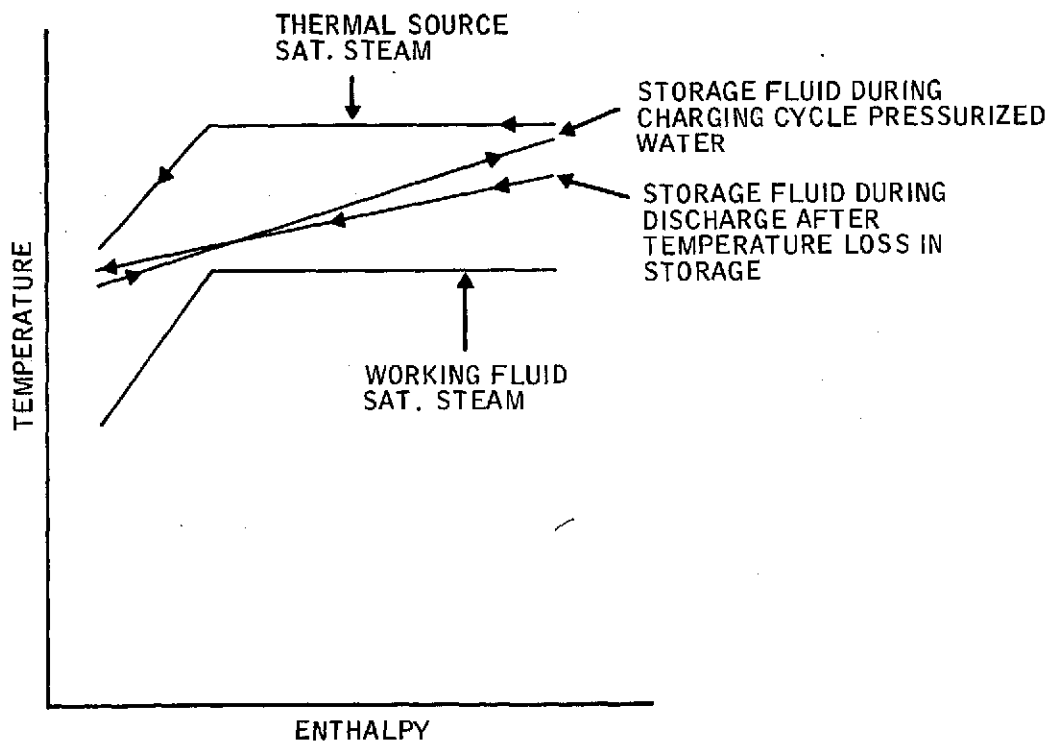
Figure 139. Temperature Drops Associated with Phase Change

Clearly, a hot water saturated steam storage system can be built but it will significantly degrade the energy it stores, with attendant losses in electric energy potential of the stored thermal energy.

Liquid Hydrogen

Hydrogen is formed by electrolysis of water and it is stored in tanks to be used by hydrogen-air fuel cells. Major cost items are the fuel cells, the electrolysis unit, the hydrogen tank and equipment, and the I/O rectifiers and inverters. The system costs and potential safety hazard conflict with its natural gas system compatibility and the availability of the generation-storage technology.

Flywheel

Several flywheel designs appeared as attractive external storage system alternatives, but the system design required a thermal buffer to the turbine inlet. The possibility of a flywheel utilization in future system studies and designs is not to be excluded.

Salt Battery

Two types of batteries are considered competitive: the sodium-sulfur battery and the lithium-chloride battery. Both have the necessary material availability. They require extensive development to increase operational lifetime but otherwise they appear technically acceptable. As with other external storage system concepts, they should be further investigated.

Superconducting Magnet

The University of Wisconsin design of a magnet with aluminum conductors and epoxy insulation segments shaped into a single torus with the major structural support provided by native rock (granite) was investigated. Cost data were provided by the University of Wisconsin with appropriate input-output devices included and the cost of this system appeared high. However, cost reductions seem possible.

Compressed Air

The compressed air system consists of a motor-generator, a turbo-expander and a turbo-compressor feeding the compressed air into a natural underground storage site (oil, gas, or capped water well or other such closed formation). With a favorable site, relatively low costs are possible; the technology is available, but expected storage efficiency is hard to determine. An unfavorable site requiring a man-made cavity, tank, or hydraulic bladder (water pressure from a surface lake) would raise its cost by a factor of 2 to 3. The only major cost items for a "natural cavity" system is the compressor-expander and motor-generator set.

Pumped Hydro

This external system would appear the most attractive but the associated problems of water availability and location dependence balance out its advantages.

TURBINE-GENERATOR AND HEAT REJECTION STUDIES

Physically, the turbine-generator system is separate from the heat rejection system. However, due to the nature of the steam cycle, the overall system efficiency is based on a coupling of the two components. For this reason the two systems will be treated together in this section.

180

TURBINE-GENERATOR

Distributed System

The choice of a turbine-generator for the distributed system is a 925 psia/585°F machine. This is an 1800 rpm, non reheat turbine currently being manufactured for use with nuclear reactors. Steam entering the high-pressure turbine possesses 50°F superheat. At the present time this particular turbine is not made in ratings smaller than 175,000 Kw(e), but the capability exists to produce it in smaller sizes.

The reason for the use of a saturated steam turbine (50°F superheat is almost negligible, providing only an assurance of dry steam at the turbine throttle) is the difficulty of generating superheated steam with a dish collector. The maximum temperature available using pressurized water is only 700°F, so no significant amounts of superheat could be expected under any conditions.

Other turbine cycles besides the one selected are available for use with saturated steam. However, if no superheat is provided, a moisture separator must be used prior to the steam entering the turbine. For this reason the turbine cycle with slightly superheated steam was chosen.

Central Receiver

The turbine-generator selected for use with the central receiver is an 850 psig/900°F machine. Based on the receiver design presented in Section VI, pressures higher than 1000 psia were eliminated from consideration. Thick-walled tubing suffered the disadvantage of lower temperature steam produced because of the metallurgical limitations of the wall material.

Turbine cycles with pressures lower than 850 psig were not used for the central receiver system because of the lower cycle efficiencies. The 850 psig/900°F turbine is currently being manufactured for use in small electric generating stations. This turbine is a 3600 rpm, non reheat machine.

HEAT REJECTION SYSTEMS

The initial heat rejection studies included the use of wet cooling towers, dry cooling towers (air cooled heat exchangers), a cooling lake, and once-through cooling. The choice of Inyokern, California, as the site of the solar-electrical station eliminated the cooling lake as a serious contender because of very high evaporation rates. In addition, once-through cooling would require a large portion of the volume of water in the Los Angeles Aqueduct to flow through the electric generating plant. For these reasons cooling towers are the preferred method of cooling the condensers.

Dry cooling towers are much more costly than wet towers, and the steam cycle efficiency is significantly lowered if dry towers are used. However, wet cooling towers require an adequate water supply. Following an investigation of the water resources in the siting region, the major conclusions drawn from the available information are:

1) For the near term, cooling water for large thermal power plants located in desert regions will be obtained by negotiated diversions from existing aqueducts.

2) For the long term, dry or wet/dry cooling tower technology must be developed to mitigate anticipated cooling water demands.

The following subsection contains information relating to both wet and dry cooling towers.

STEAM CYCLE EFFICIENCIES FOR WET AND DRY COOLING TOWERS

The thermal efficiency of a steam cycle depends on the inlet conditions to the turbine, condensing temperature, temperature of the feedwater returning to the heat source, and the mechanical efficiency of the system components. For a given steam cycle it is important to know the cycle efficiency using both a wet cooling tower and a dry cooling tower. Only then will a cost comparison between various conceptual systems be meaningful.

The condensing temperature using a dry cooling tower was taken to be the ambient air temperature plus 65°F. Using a wet cooling tower the condensing temperature is equal to the ambient wet bulb temperature plus 48°F. Figure 140 illustrates the rationale behind these condensing temperatures. The returning feedwater temperature was taken to be 400°F for all cases.

Steam cycle efficiencies were calculated using both a wet cooling tower and a dry cooling tower for the 925 psia/585°F turbine and the 850 psig/900°F turbine. The results of the cycle efficiency are presented in Figures 141 and 142. Figure 141 shows the cycle efficiency as a function of the ambient wet bulb temperature using a wet cooling tower. The steam cycle efficiency using a dry cooling tower as a function of the ambient air temperature is shown in Figure 142.

It is difficult to compare the results given in Figures 141 and 142 without a temperature duration curve. Using the temperature duration curves and wet bulb duration curves for China Lake, California, an efficiency duration durve was generated. Figures 143 and 144 give the thermal cycle efficiency duration curves for the two steam cycles using both wet and dry cooling towers.

DRY COOLING TOWER
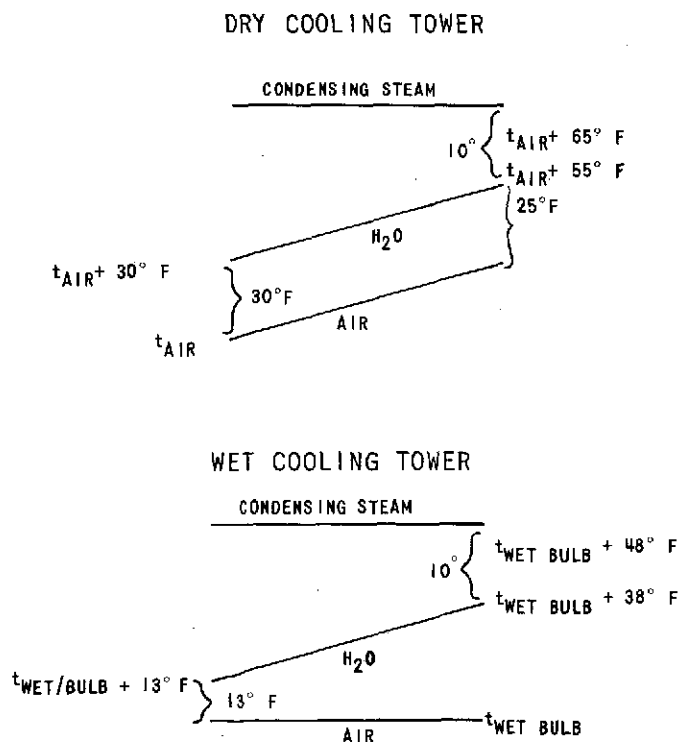
WET COOLING TOWER

Figure 140. Steam Cycle Condensing Temperatures

Figure 141. Steam Cycle Efficiency Using a Wet Cooling Tower
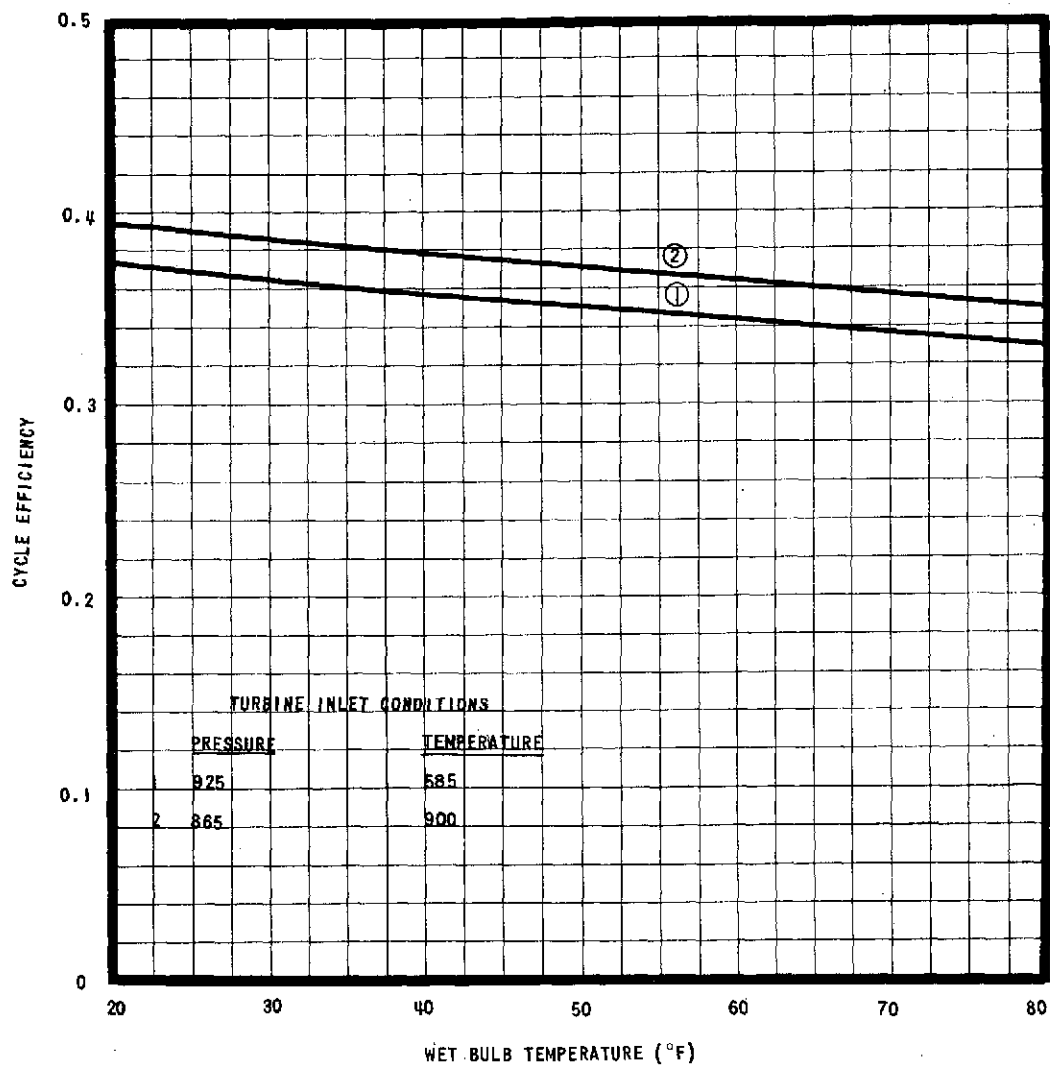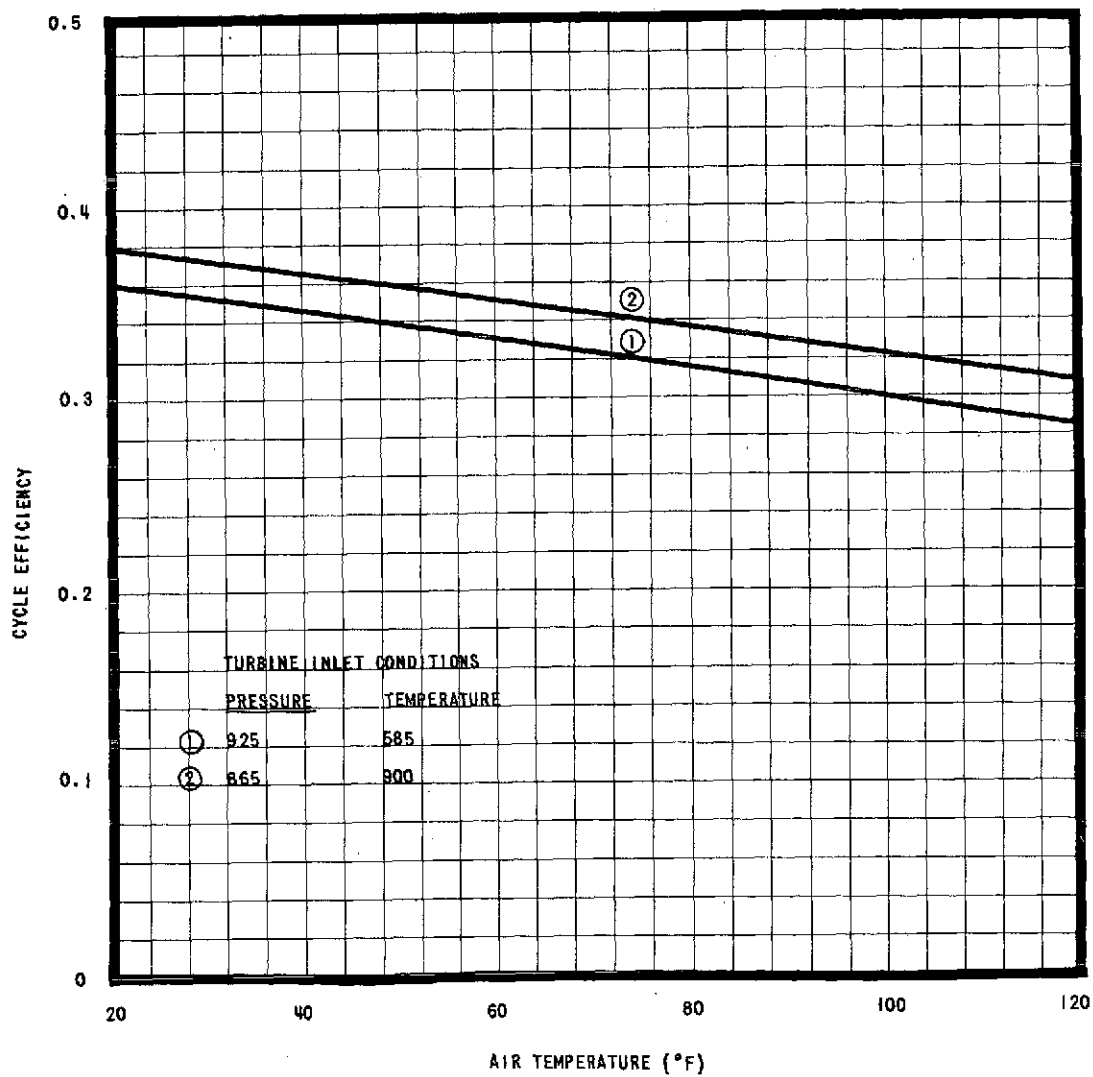as a Function of the Wet Bulb Temperature

Figure 142. Steam Cycle Efficiency Using a Dry Cooling Tower as a
Function of the Ambient Air Temperature
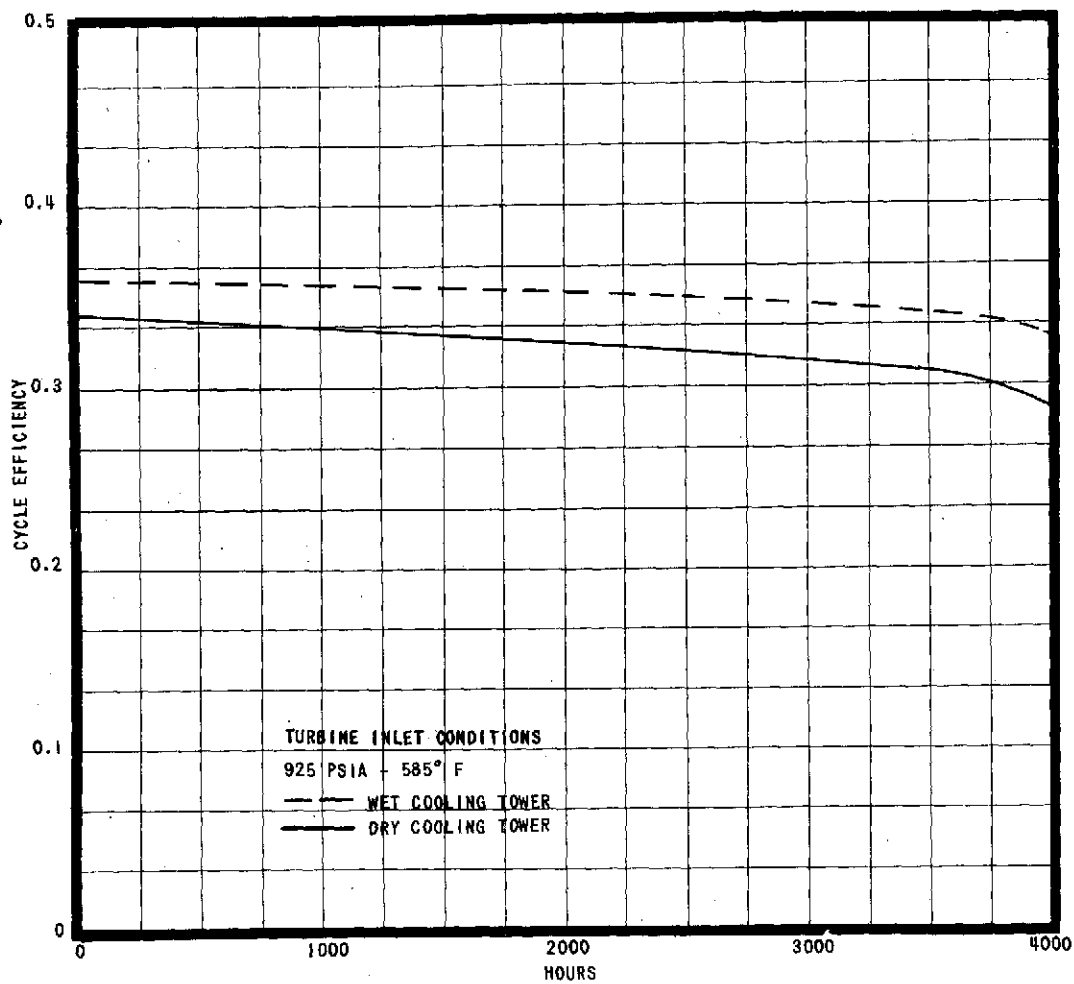
Figure 143. Efficiency Duration Curve for the 925-585 Steam Cycle Operating at China Lake, California
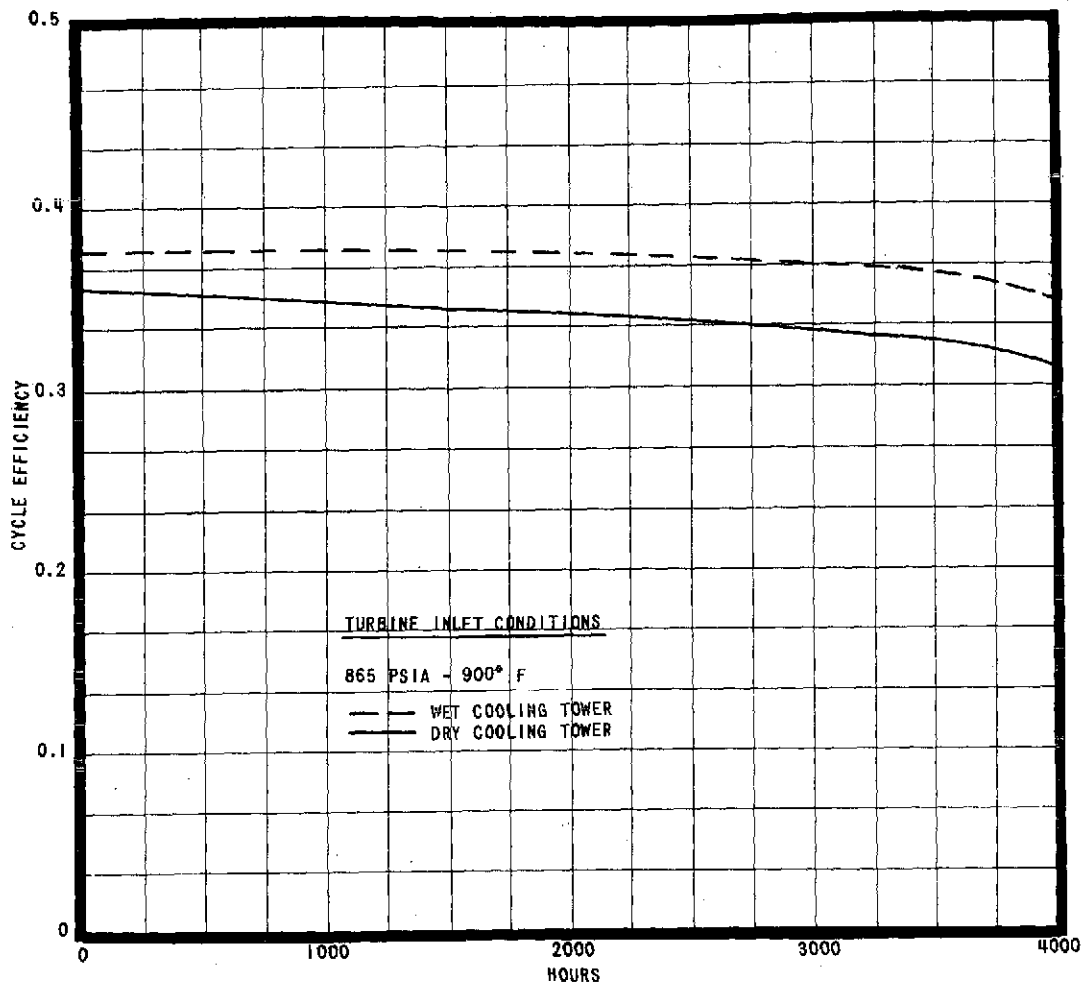
Figure 144.   Efficiency Duration Curve for the 865/900 Steam
Cycle Operating at China Lake, California

SECTION IX

MARGIN ANALYSIS

The pioneering work on solar power plant mission analysis performed by Aerospace Corporation, El Segundo, California (Reference 8), pointed out the relationship between energy storage capacity, plant and power grid reliability and required backup plant capacity. The present effort initially focused on the physical relationships between the various subsystem elements and the total plant performance. However, since the storage capacity question had to be addressed in detail, attention had to be paid to grid-wide issues, such as grid reliability.

On the other hand, margin analysis determines by probabilistic methods the amount of generating capacity which must be installed on a power grid above and beyond the expected peak power demand, so that the entire grid will meet its reliability requirements. The motivation lies with the large capital investment and expenditure associated with the construction of the additional plants (margin) for reliability.

The power industry specification on grid reliability is one day of outage in ten years of operation. This is a much stricter reliability specification for a grid as a whole than that achievable by even the most reliable single plant on the grid. The issue becomes important to solar energy because the solar heat source is inherently less reliable than conventional heat sources because of the vagaries of weather and the daily and seasonal variation in solar flux.

Two techniques exist for maintaining the reliability of the grid with a large solar plant on the line. The solar plant can be "backed up" with a conventional plant which is pressed into service as needed after the available instantaneous solar power has been supplied to the grid. The second method is to control the delivery of power to the grid so that the collected energy can be stored when it is available and not needed to meet the grid demand. This stored energy then becomes available for electricity generation when the demand is again high and direct solar insolation is not available.

Thus, the output of the plant becomes independent of the insolation for time periods equal to the storage capacity in effective electric kWhr(e) divided by solar plant capacity in kW(e). If these periods can coincide with high-demand times, then the solar plant will appear to the grid to be as reliable as any conventional plant. At low-demand times, the "left-over" conventional plants can accommodate the demand with a sufficient safety margin. This plant-grid interface was studied as a function of the following list of solar power plant design issues to attain the cost optimal balance between storage capacity and backup capacity:

- Storage capacity

- Number of extra collectors needed to maximize storage capacity utilization

- Importance of early morning collector throughput rate; this affects collector number and spacing

- Nightly discharge of stored energy into the grid versus use of stored energy only when a solar outage is coincident with a high demand period

- The use of spinning reserve capacity to backup the solar plant at off-peak demand times without incurring extra capital investment for margin plants

The basic grid reliability specification of 1 day of outage in 10 years is often quoted. Since there are many possible meanings which could logically be assigned to this specification, a more rigorous statement must be established. By definition then this means that the most likely outcome of a 10-year survey of grid power output is that for 24 hours during that time the total instantaneous demand would exceed the instantaneous capacity because of outage of power plant(s). The outages due to distribution failure are not included. More simply stated, the expectation value of outage duration due to power plant failure is 1 day in 10 years. An outage is defined to be any time the available capacity (spinning reserve included) is less than the demand by any amount. Thus, a 1000 Mw shortage is taken to count the same as one of 5000 Mw.

There is no specification on the distribution of outage duration. The 10-year power output sample can be considered to be a statistical experiment. If this experiment could be performed many times with the same demand and the same power plant complement, the outcome (total hours of outage) would be different for each experiment. The most likely outcome should be 1 day in 10 years, but longer and shorter durations would occur.

The specification means that the slope of this bell-shaped distribution must be zero (a maximum) at one day in 10 years. There is no specification on either the magnitude of the distribution at 1 day in 10 years or the rolloff around it.

The derivation of the probability integral for the expectation value of outage duration must assume that all relevant terms are continuous and integrable as needed. If the grid experiences an instantaneous risk of outage of P_F which remains constant during a small time interfal dt, then by the definition of failure probability the most likely duration of an outage during dt is dH where

$$dH = P_F dt \qquad (51)$$

Thus, if P_F varies over the time interval 0 to T the expectation value of outage over the interval is H, where

$$H = \int_0^T dH = \int_0^T P_F(t)dt \qquad (52)$$

If P_F were a constant, then its value must be chosen such that H, for T = 10 years, is

$$P_F = \frac{1}{3650} = 0.00027 \qquad (53)$$

Clearly, P_F is not a constant but a function of the detailed reliability of each plant on the grid and the total demand on the grid.

Calculation of the backup capability due to the presence of a solar plant on the grid is performed in two steps. The integral of Equation (51) is evaluated for a year's demand assuming various levels of margin are available. The value of margin which satisfies the reliability specification is found by interpolation between calculated points. Then a solar plant is added to the grid and the process is done again. The increase in margin from the first to the second calculation is the backup capacity due to the solar plant.

In the utility industry there is a commonly used algorithm for calculating the risk of failure (P_F) as a function of demand on any general complement of plants. An example of the output of the algorithm is shown in Figure 145. This plot is P_{FAIL} plotted against demand (in Mw). The nominal grid rated output (GROP) is 31,029 Mw. This is also the highest demand level which the grid is expected to experience. The assumptions used to calculate the curve are:

- The spinning reserve is 20 percent of the instantaneous demand whenever the damand is low enough to maintain a sufficiently large margin of installed capacity.

- The plants are brought on the line in the order of largest to smallest as the demand rises.

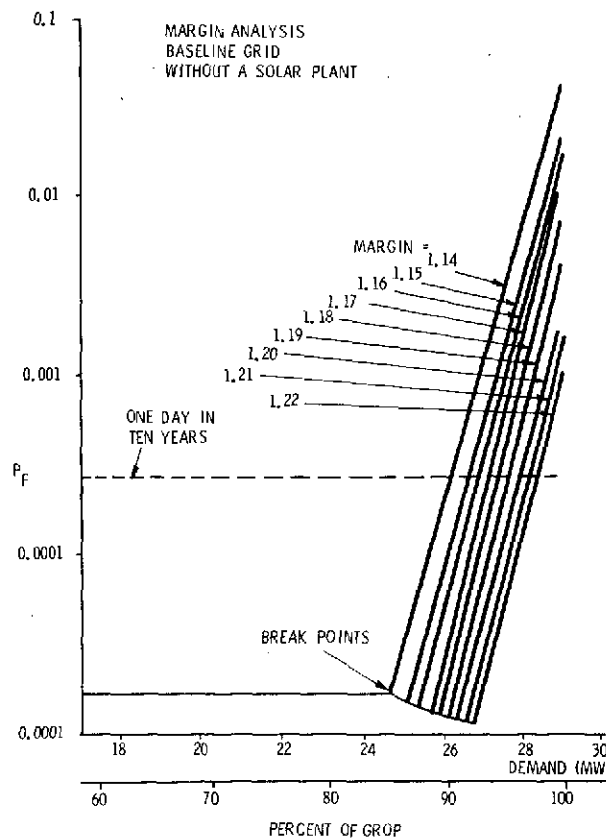- The plants are brought off in the reverse order as demand falls.

Figure 145. Algorithm Output

Notice in Figure 145 that the curve breaks into a family of curves at high demands. Each of these curves represents a different assumed value of installed margin capacity beyond the minimum capacity needed to meet GROP level demand. Recall that it is this extra margin capacity which must be traded off against storage capacity. When the curve breaks into a family of curves, this represents the reduction in spinning reserve capacity as the power dispatcher "runs out of plants" to maintain the high (in this case 20 percent) spinning reserve fraction. Clearly, the lower total installed capacity scenarios have the lower break-points and incur more risk as the demand approaches GROP.

The spinning reserve capacity normalized by the instantaneous demand is plotted versus the demand normalized by the GROP level in Figure 146. This plot represents an analytical model of the power dispatcher's method of scheduling spinning reserve. Note that the instantaneous spinning reserve capacity is not affected by the installed margin until after the breakpoint demand level has been passed. The output of the solar plant is most important to maintain grid reliability when the demand is at or above the breakpoint.

The calculation of the baseline margin requirement for the grid without a solar plant uses the curve in Figure 145 as the integrand function in Equation (52). The process is a simple forward time integration of Equation (52) and it can be performed numerically on the computer. At each time step, the demand data are read from a tape provided by Aerospace Corporation, El Segundo, California. The risk of failure P_F is found from a table-look-up-interpolation routine which contains the data points from Figure 145.

The summation for the integral in Equation (52) is then incremented using the P_F data for that time step. This process is contained for 24 hours a day all year to yield the year's expected outage duration.

The simulation of a solar plant on the grid involves the calculation of risk (P_F) as a function of demand and instantaneous solar plant output. The method is to select one of the plants on the grid to simulate the solar plant. It is placed in the list of plants on the grid with an associated mechanical failure probability similar to a conventional plant. A set of P_F versus demand curves similar to Figure 145 are run out by the "algorithm" method, assuming various levels of output from the solar plant. A P_F versus demand curve was run out for a range of solar plant outputs from 1000 Mw to 0 in 200 Mw increments (i.e., five graphs). For example, Figures 147 and 148 show two of the five curves used in this study. The solar plant is at 800 Mw output level in Figure 147 and no output is available in Figure 148. Note that as the amount of power available from the solar plant is reduced, the breakpoint is incurred at a lower demand level and the risk goes higher at GROP for each level of margin. Note also that, below the breakpoint demand, the risk of outage is independent of solar plant output. Below the breakpoint, the solar plant is not needed to form the complement of conventional spinning reserve plants.

To evaluate the outage integral [Equation (52)] over a year of operation, the integral is added to a solar plant simulation program. At each time point in the integration, the solar intensity and the demand data are read off the data tapes provided by Aerospace Corporation. The code then uses its math model of the collector, piping, turbine-generator, etc. to find the solar plant output possible at that instant.

If required, the simulation may draw energy from storage or add to it depending on the plant control scenario being simulated. The control philosophy simulated to obtain the results presented here is:
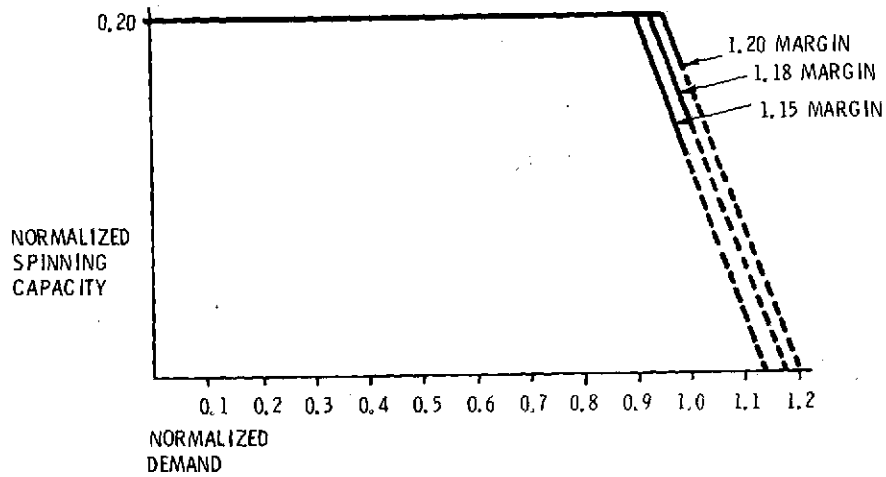
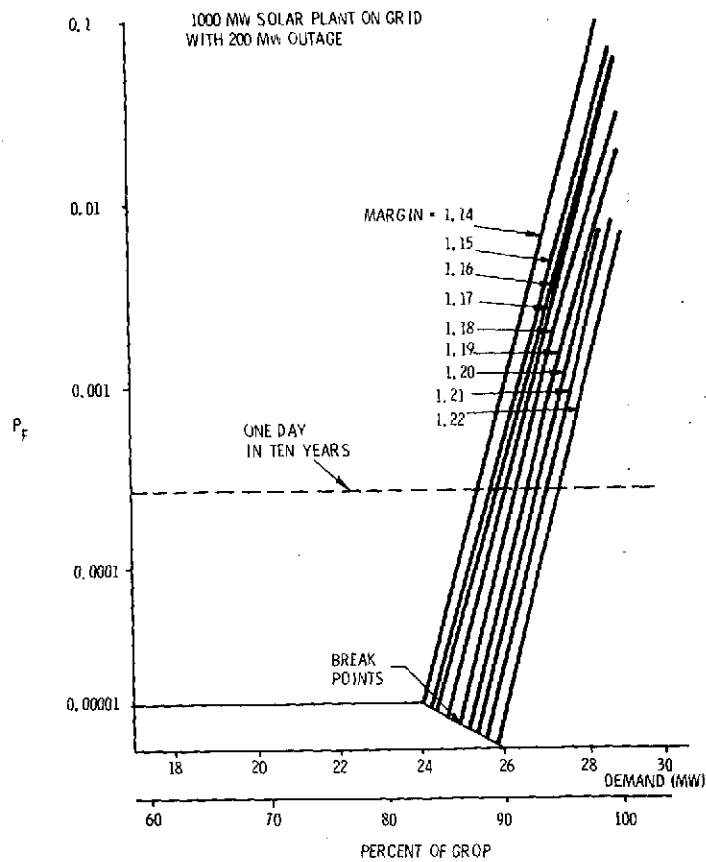Figure 146. Spinning Reserve Capacity versus Normalized Demand
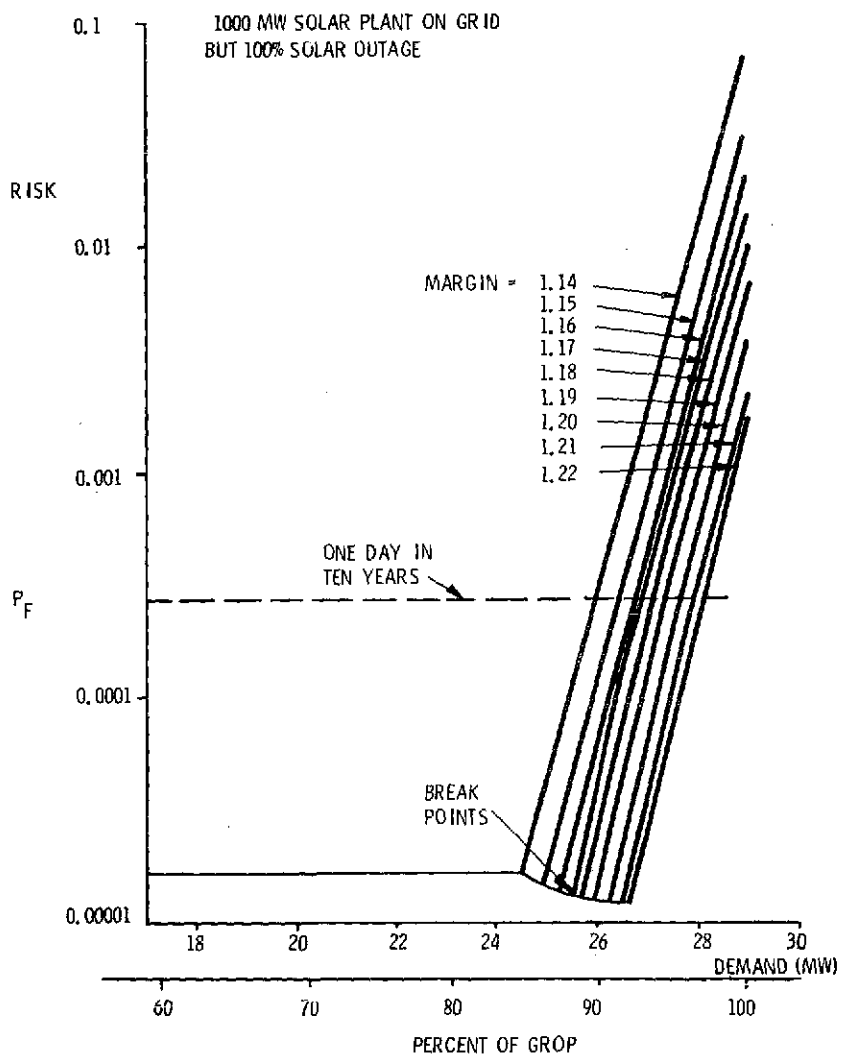

Figure 147. Demand Curve with 800 Mw Output

Figure 148. Demand Curve with No Output

If the demand on the grid is below the breakpoint, all available thermal power is stored until the storage is full. Once the storage is fully charged, all collected thermal power is converted to electricity and sent out on the grid (subject to turbine capacity limits). When the demand is above the breakpoint, it becomes essential to have the solar plant producing power for the grid. Thus, when the demand is above the breakpoint, power is taken from storage as needed to keep the turbine operating at the specified minimum value (taken to be 20 percent of turbine capacity); in fact, power is drawn from storage only when the demand is above the breakpoint and the grid is incurring outage risk. On those occasions when the collected thermal power is greater than the capacity of the turbine/generator to convert it to electricity, the excess is stored if storage is not already full.

Thus, the instantaneous solar flux available and the status of the storage determine the output of the solar plant. The set of curves of (P_F) as a function of demand and solar plant output are interrogated for P_F. The H integral [Equation (52)] is then integrated along with the other differential equations that represent system parameters (such as storage content) and system performance measures (such as integrated output energy). The H integral is carried out simultaneously for each curve in the margin capacity set. This yields the H total per year for each value of installed margin in one integration pass through the year's demand and insolation data. By interpolation between the H values obtained, we can find the value of margin capacity which satisfies the 1-day-in-10 years criteria on H. Thus, with each year's simulation the detailed plant performance, the effect of storage capacity, and the backup capacity which must be installed on the grid to back up the solar plant are calculated.

The expectation value of outage (H) is integrated 24 hours of the day whether the solar plant has output or not. This leads to a problem in defining a classification for the plant. The outage risk (P_F) is integrated over all 24 hours as would be the case for a base load plant. The runs we have made indicate, however, that plants with low-storage capacity are cost optimal. A plant with 1/2 hour storage simply follows the daily demand peaks and the storage supplies energy when needed to keep the failure risk low. In this sense it is a peaking or demand-following plant.

The demand tapes can be loosely characterized as showing a mid-morning peak and an evening peak which occurs after sunset. The goal of the plant control strategy is to make the availability of stored energy coincident with this second demand peak.

The curves of Figure 149 represent the results of a year's time integration for a series of plant designs with a 1000 Mw capacity turbine and various amounts of collector area and storage capacity. The curves are for from 5 to 10 square kilometers of collector aperture area.

The physical interpretation of the curves is that as the collector aperture area went from 5 to about 7 square kilometers, the extra area above the minimum to run the turbine was used to charge storage. Above 7 Km^2, the extra area was not used. It turns out that the 7 Km^2 system had enough collector capacity to fully charge the storage to run the turbine at its minimum rate of output (20 percent of capacity or 200 Mw) all through the night peak of demand. The 20-percent output limit when the plant is run solely from stored energy attempted to make the stored energy last as long as possible during high demand times. More collector area was wasted because even though energy could be stored, it could not be used during relatively short peak demand times at the minimum discharge rate. If the minimum rate were increased then more energy would be used each night and the additional collector area would have reduced the backup requirement. This minimum rate of operation during night peak also caused the backup capacity required to remain essentially constant with storage time beyond 1 hour and more than 8 Km^2 of collector area.
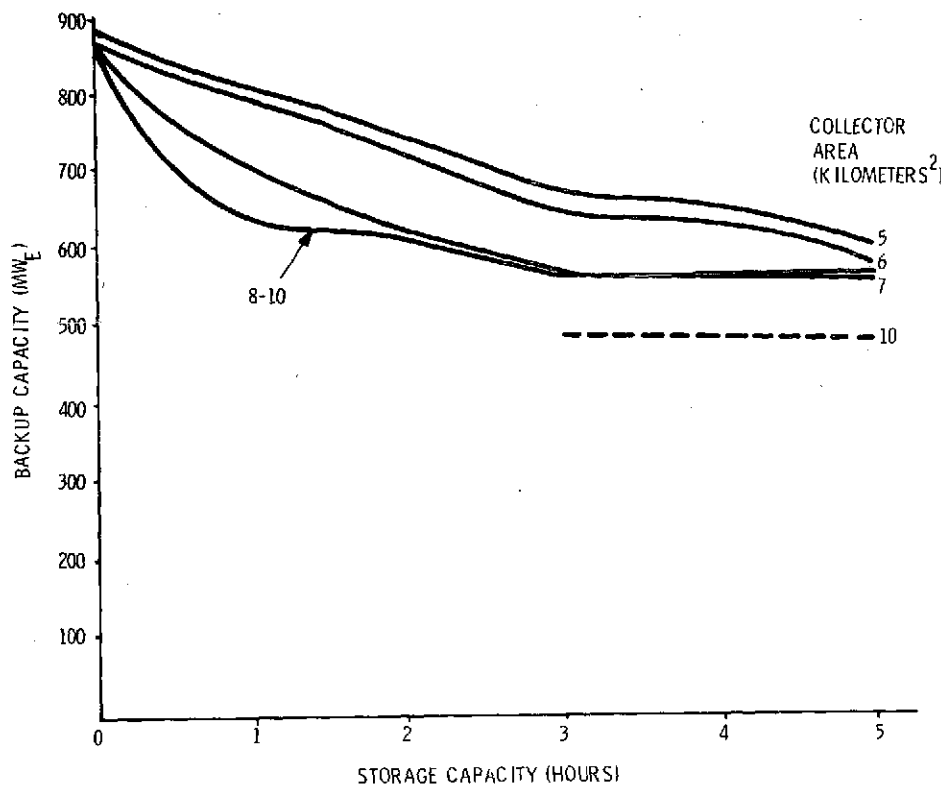
Figure 149. Year's Time Integration for Series of Plant Designs

Clearly, the control strategy should be modified to run the system at higher output levels during the night peak operation times for systems with large storage capacity and collector area. This was done for a system with 10 Km^2 of collector area and a range of storage capacities from 3 to 5 hours.

The dashed curve in Figure 149 represents a system in which the turbine is either fully on or fully off. Thus, when storage is used for the night peak demand, it is drained as fast as possible. This significantly reduced backup capacity; further reduction is possible if more collector area was used. The dashed line would also curve downward if the increasing storage capacity of the collector area was increased beyond 10 Km^2.

This calculation is essentially conservative, i.e., the solar plant is given capacity credit only for the actual power delivered at any instant. This is clearly correct when integrating total energy delivered to the grid, but not so clearly correct when integrating expected value of outage. For example, whenever the turbine is on and spinning, and there is energy in storage, the plant output could be quickly increased to full capacity to compensate for a forced outage. Thus, a more liberal interpretation of capacity would have the plant counted at full capacity whenever it is at any non-zero power output level and there is any non-zero energy in storage. This may be too liberal while the position taken to generate Figure 149 may be too conservative. A middle-ground approach is clearly desirable. In this instance, the simulation of the system should be extended to include increases in solar plant output to cover forced outages that actually occur. Then, if full capacity credit is given whenever storage is full, the worth of the storage system will not be over- or under-estimated. For the conservative interpretation, the storage is drained whether a forced outage occurs or not. Thus, only partial capacity credit is given for too short a time each day. For the liberal interpretation, the storage is drained perhaps more slowly than could safely be done if outages occur so that full capacity credit is given for a longer time than is appropriate.

194

The data of Figure 149 are the fundamental design data, and these results are derived from first principles. To actually decide on a design, however, we must apply price information to each point on the curves of Figure 149 and find the minimum cost system. Introducing pricing data increases the uncertainty of the results, but it is nevertheless worthwhile. Space does not permit a detailed explanation of the pricing methodology but the results are based on cost summation of each piece part of the system. Wherever applicable, boiler codes and wind load safety factors were applied. This added significantly to the cost of piping and storage.

The fundamental dependent variable is mills-per-kilowatt-hour produced and it is plotted versus collector area and storage capacity in Figure 150. The total price of the kilowatt hours generated includes the price of the collectors, turbine/generator, storage system and required backup capacity to maintain grid reliability. The prices used are 1.67×10^8 dollars per square kilometer of collector aperture, 301 dollars per kilowatt hour electric of storage, 116 dollars per kilowatt capacity for turbine/generator/heat rejection and balance of plant, and 120 dollars per kilowatt of back-up capacity. The backup plants were taken to be oil or gas fired gas turbines. The only items left out of the cost summary data were the cost of fuel used in the backup plant and the amount of energy produced by the backup plants.

The most important feature of the curves is that the minimum energy cost occurs at zero storage with just enough collector area to run the turbine. This result basically reflects the very high cost of pressurized hot water storage tanks which meet boiler code specifications and the relatively low cost of backup gas turbines. Previous work at Aerospace Inc. used storage and collector costs which were lower relative to the backup cost and hence the optimal storage capacity was non-zero. If other compatible storage systems can be developed with lower cost, then these results will also change. There is speculation that even at these prices (if the cost of fuel (oil or gas) for the backup plants were included in the total prices) the optimal storage capacity would be non-zero. Accordingly, we have developed a statistical methodology for calculating the expected value of energy required from the margin plants on the grid.

The expected value of energy required from the margin plants is (E_m), where:

$$E_m = \int_{Time} [D - C]\, dt \qquad\qquad (54)$$

Where D is the instantaneous demand and C is the most likely capacity of the plants which are responsible for meeting the demand (not including the margin plants).

The term C can be pre-calculated using the "algorithm" for a range of demand and solar plant capacity values, as was done for P_F in Equation 53. The pre-calculated data can then be loaded into the yearly simulation program and used with suitable table lookup routines to determine the integrand of Equation 53 at each time step of the year's integration. A difference between the expected value of energy required from the margin plants (E_m) for a grid with and without a solar plant on line is an estimate of the extra energy required from the margin plants, that is needed to backup the solar plant. The fuel cost to produce this energy can be calculated using the average efficiency and fuel cost for the margin plant inventory. This cost could then be added to the sum of grid incurred costs due to the presence of a solar plant on line. The energy produced by the margin plants must also be added to the total energy generated by the solar plant. In this way, the solar plant and its backup system is treated as a complete energy producing system and its total output price is compared with a conventional plant. The calculations and modifications to existing software to include this cost have not been accomplished to date.

The strategy used to control the turbine output level and the input and retrieval of power from storage has as large an effect on system cost and performance as any other system design issue.

The high prices associated with pressurized, hot water storage, yield a cost optimal design with no storage capacity. Storage may nevertheless be necessary for plant stability and control issues related to high frequency solar transients.

The interpretation of solar plant instantaneous capacity is not fully resolved as it affects margin calculation methodology. This issue should be decided with input from all concerned parties and a standard interpretation should be set.

The quantity of fuel consumed and energy produced by the margin plants while they are substituting for the solar plant can be calculated by methods similar to and compatible with current analysis methods. This issue should be included in future margin studies.

DISH COLLECTOR SYSTEM AND
HOT WATER STRATIFIED TANK
STORAGE
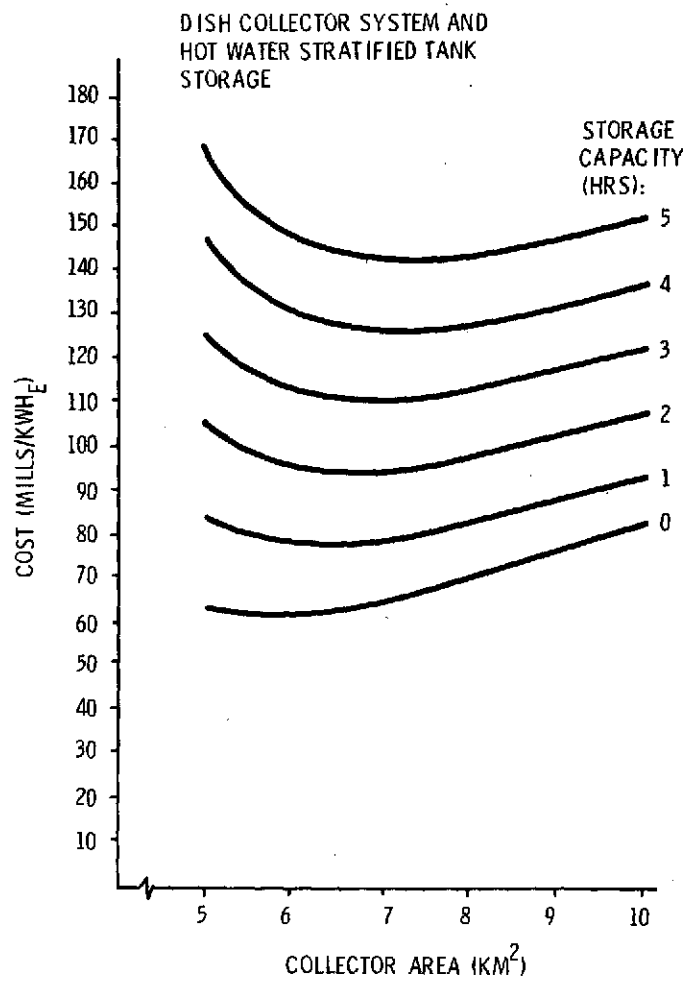
Figure 150.   Cost (Mills/Kwh) versus Collector Area (KM^2)

197

SECTION X

REFERENCE SYSTEM BASELINE DESIGNS

Reference systems for both the distributed and central receiver system concepts are described in this section. Each reference system has been chosen to represent the most promising design studied although each system is not necessarily optimal with respect to all the subsystems. Furthermore, the degree to which the two reference systems have been optimized varies, the distributed system being more developed because of the lead time in analysis.

In the reference system descriptions, no attempt is made to specify the solar plants control strategy. This strategy has a significant effect on system cost and performance but the work done on storage and margin analysis (Section VIII), has not yet fully resolved the issue of optimal strategy. Current judgment is that thermal storage for stability (the order of one-half hour for cloud passage) is desirable if not a requirement. The plant reliability would then be maintained by conventional back-up capacity or a compatible storage scheme. The cost for storage/reliability has not been included in the reference systems presented.

DISTRIBUTED SYSTEM

This section gives a description, specification, and cost analysis for the first reference system, the distributed dish collector-pressurized water system utilizing a 925 psia, 585°F steam cycle. The optimum solar collector spacing, piping network, and plant size was determined by a parametric computer analysis of the overall system (see Section VII.

Overall System Description

The design of the distributed system employs dish collectors to gather the radiant energy of the sun. For the reference design, a 100 Mw'(e) average plant capacity was chosen. Water under a pressure of 2100 psi is circulated through the collectors and returned to a once-through steam generator. The system parameters are given in Table XXVIII. The collectors are arranged in a square, quartered field with the steam generator, turbine-generator, and the balance of the plant (minus the heat rejection system) located at the center of the quartered field. The overall system is shown in Figure 151. The major functional elements of the balance of plant are:

- Conventional steam generator (10,000 tubes)

- Conventional 925/585 non-reheat turbine generator

- Condenser

- Condensate pump

- Deaerator

- Feedwater heaters

- Boiler feed pump

- Circulating water pumps (primary loop)

- Substation

198

PRIMARY HEAT TRANSPORT PRESSURIZED CYCLE
(WATER)

SECONDARY WORKING CYCLE
(STEAM)

TEMPERATURE
FLOW VALVE

TEMPERATURE
DETECTOR

585 F
(50° SUPERHEAT)
925 PSIA

TURBINE

GENERATOR

626 F

2000 PSIA

STEAM
GENERATOR

SURFACE
CONDENSER

SOLAR COLLECTORS
– TWO AXIS DISH –

453 F

925 PSIA

120 F

3.5" Hg

WET COOLING
TOWER
(MECHANICAL
DRAFT)

REGENERATIVE
HEATERS

547°F

2150 PSIA

HOTWELL
PUMP

HEAT TRANSPORT
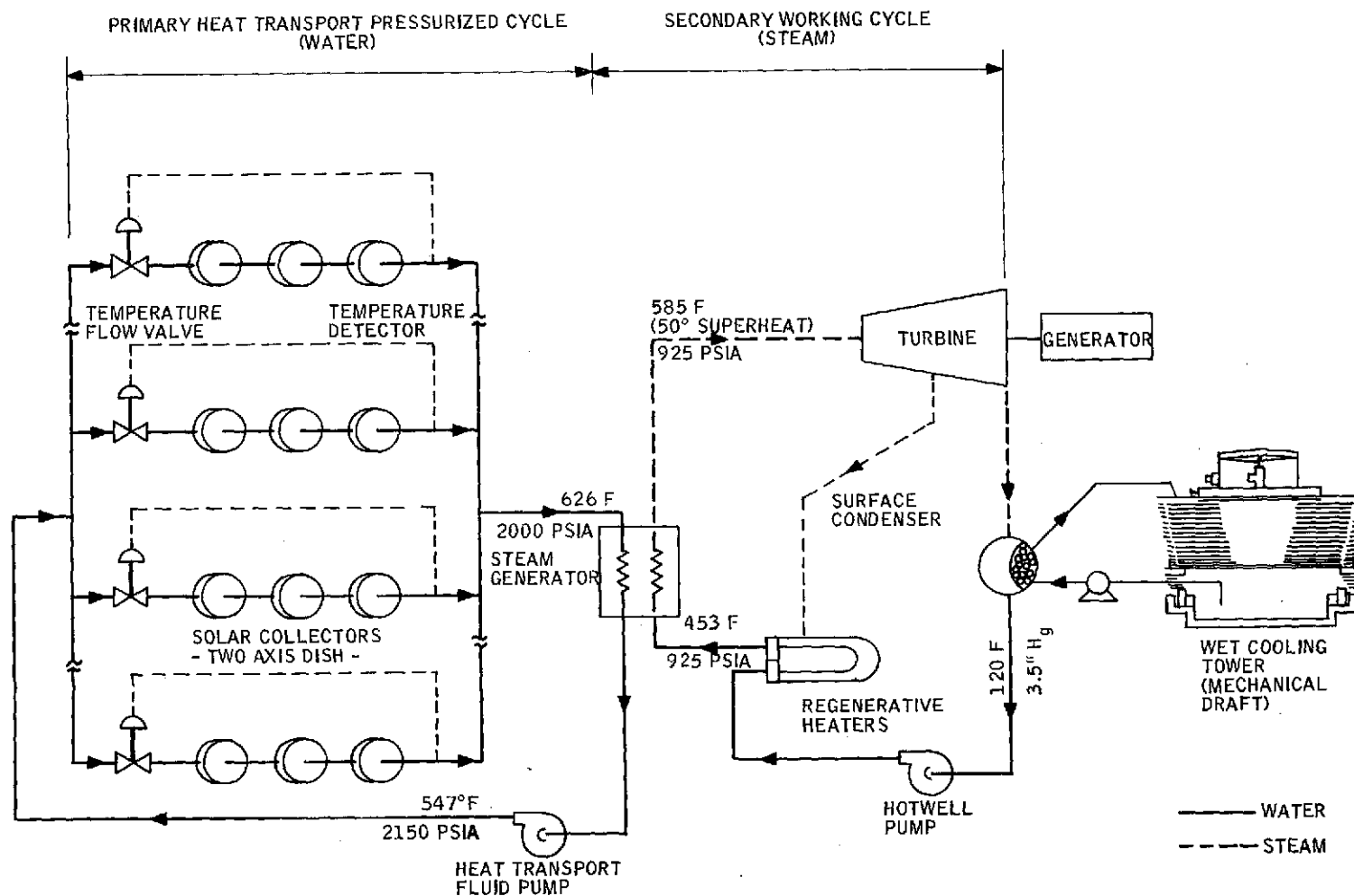FLUID PUMP

————— WATER

– – – – – STEAM

Figure 151.   Paraboloid of Revolution Disc Collector
Overall System Schematic

199

Table XXVIII. Dish Collector Distributed Reference
System Characteristics

Collector Field Geometry	Square
Collector Field Length	2080 feet
Number of Collectors	16,560
Collector Aperture Area	420 ft^2
Collector Field GCR	0.40
Collector Output Temperature	626°F
Collector Inlet Temperature	547°F
Turbine Inlet Steam Conditions	925 psia/585°F
Feedwater Temperature Ratio	0.8
Heat Rejection	Wet cooling
Peak Power	381.5 MW(th)
	143.4 MW(e)
Annual Energy	1.25 x 10^6 MWH(th)
	0.39 x 10^6 MWH(e)

The heat rejection is provided by a wet mechanical draft cooling tower system. This
system is located exterior to the collector field to avoid fogging and to provide close
proximity to the water supply.

Turbine-Generator/Heat Rejection System

Turbine-Generator -- The turbine-generator is a conventional, 925 psia/585°F, 1800
rpm, non-reheat steam turbine. Turbines applicable for this cycle are listed in the
General Electric Price Book for sizes from 175 MW to 1000 MW and in the Westinghouse
Price Book from 200 MW to 1500 MW. Associated with the turbine is a condenser which
maintains a turbine back pressure below 3.5 inches of mercury. Before entering the
steam generator, the feedwater is heated by extraction steam in six feedwater heaters
to a temperature of about 420°F, depending on the ambient temperature. The feedwater
pressure is provided by a conventional condensate pump and boiler feed pump. Fig-
ure 152 shows a turbine-generator heat balance for a typical 925 psia/585°F steam cycle.

Heat Rejection -- Heat is rejected from the condenser by a circulating water system
using wet, mechanical draft, cooling towers. These cooling towers are commercially
available in any desired size. The peak circulating water flow for the 100 MW(e) rated
capacity is estimated at 51,000 gallons per minute (gpm), and the peak make-up water
requirement is estimated at 1300 gpm. This makeup water replaces that water lost from
the circulating water system as evaporation and blowdown in the cooling towers.

Dish Collector Design

The detailed description of the baseline dish concentrator/collector design is given in
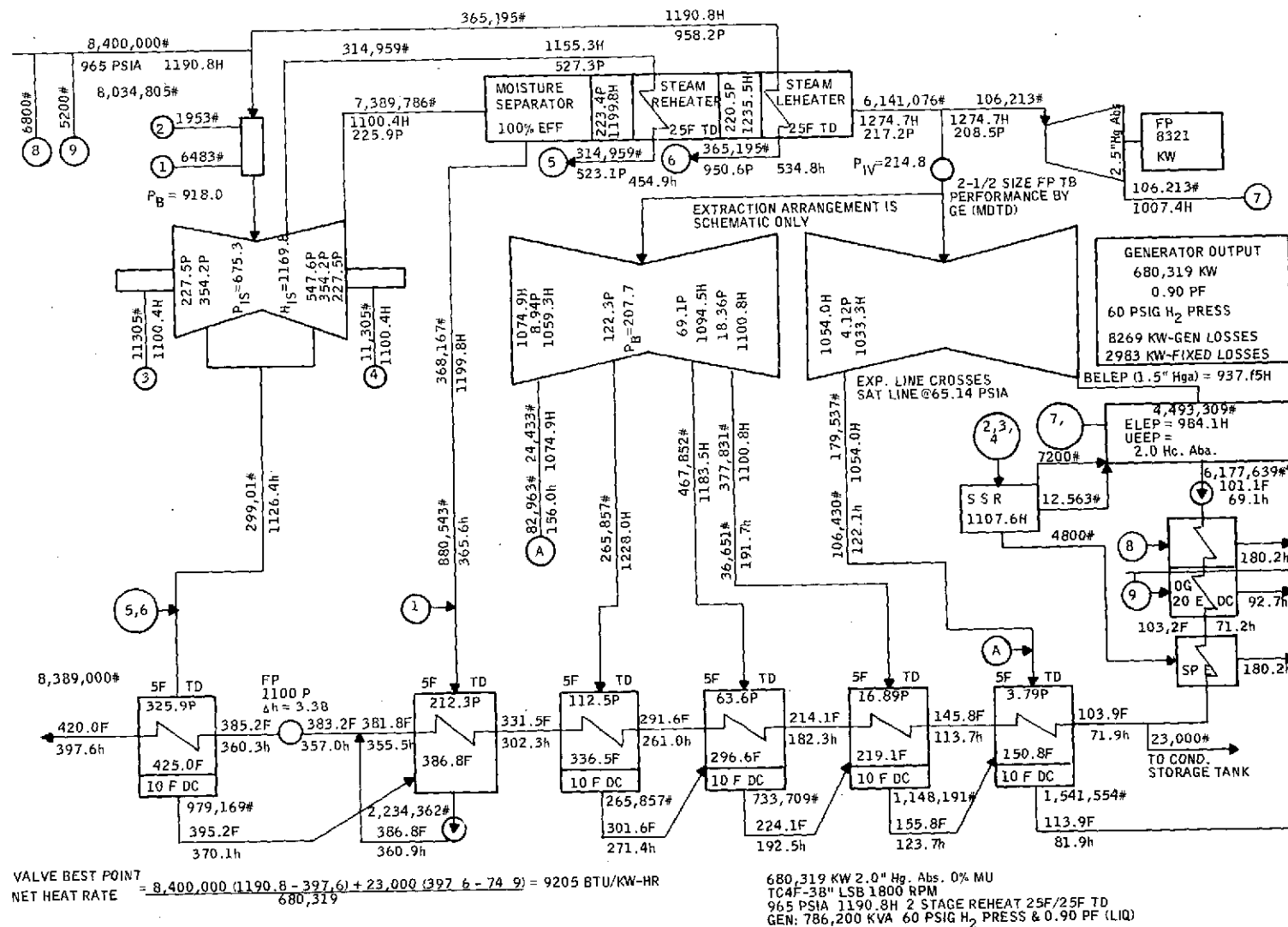Section VI.

Figure 152. Turbine-Generator Heat Balance for a Typical 925 psia/585°F Steam Cycle

Piping Specifications

The piping network for the distributed dish-pressurized water reference system was designed using the methodology described in Section VII. The piping used is seamless carbon-steel pipe to Specification ASTM-A-106, Grade B. Schedule 80 pipes are used for nominal diameters less than 4 inches and schedule 120 pipes are used for diameters larger than 4 inches, according to the requirements of the Power Piping Code - 1973. The insulation is calcium silicate with 0.016 inch thick aluminum jackets. Appendix A contains the detailed price and material properties for the pipes and insulation.

For the 100 $MW_{(e)}$ average capacity plant, the two-axes dish collector spacing was chosen at a ground cover ratio of 0.40. The spacing of the collectors along a branch header is shown in Figure 153. Each collector is connected to the branch header by 1/2 inch connecting pipes which allow for a flow of water under high pressure. The mass flow rate through each collector is governed by an output temperature regulated control valve. A shutoff valve on each connecting line allows for individual collector maintenance when necessary. Branch header piping sections are designed to be shipped in 90-foot lengths with sockolets shopwelded at 15-foot intervals. Expansion loops are field welded between each of these units.

The computer results for pipe diameters and insulation thicknesses to be installed along the transport system network are shown in Figures 154 and 155. In the computer study, the maximum pipe size was restricted to 18-inch pipes because it was felt that the purchase of larger pipes would not reduce the dollars per square foot of flow area. Thus, the results shown for the main header piping and insulation sizes are in terms of equivalent sizes above the 18-inch pipe. For instance, two 18-inch pipes were accepted as roughly the equivalent in cost and and flow area of one 25-inch pipe. At the steam generator exit there are three 18-inch pipes feeding water to each side of the collector field. Three 18-inch and one 12-inch pipe carry the hot pressurized water to the steam generator entrance. In the entire collector field there are 120 hot and cold branch headers coming off the two main headers. Each branch header has a total of 23 sections like the one shown in Figure 154. The performance characteristics of the piping network are described in Section VII.

Plant Costs

Costs for each of the subsystems described earlier in this section were estimated using the cost methodology described within the sections and in Appendix A. Table XXIX gives a cost summary for the dish collector reference system.

The header piping and insulation layout was designed using the methodology described in Section VII with a 420 ft^2 collector cost of $5000/collector. Energy storage costs were omitted in the energy transport design studies. As energy storage costs are included, or collector costs are updated, the design of the piping network is subject to change (see Section VII). The cost of the network specified earlier in this section was computed using the unit costs of Appendix A.

For the 100 MW(e) average plant capacity, a turbine-generator with nameplate generating capacity of 125 MW(e) is installed to provide the capability to use the greater than average solar insolation. The cost of the turbine-generator/heat rejection equipment, balance-of-plant costs and steam generator costs are based on the 125 MW(e) turbine-generator installation. Cost data are taken directly from Appendix A.

The total solar power plant cost shown in Table XXIX is computed for a 420 square foot collector costing $5000 (approximately $12/$ft^2$). Since no structural analysis or cost optimization of dish collector designs has been completed, this figure is somewhat arbitrary. Because of the uncertainty in collector cost the total plant cost is best reported as a function of collector cost. The reference system net energy cost is shown in Figure 160.
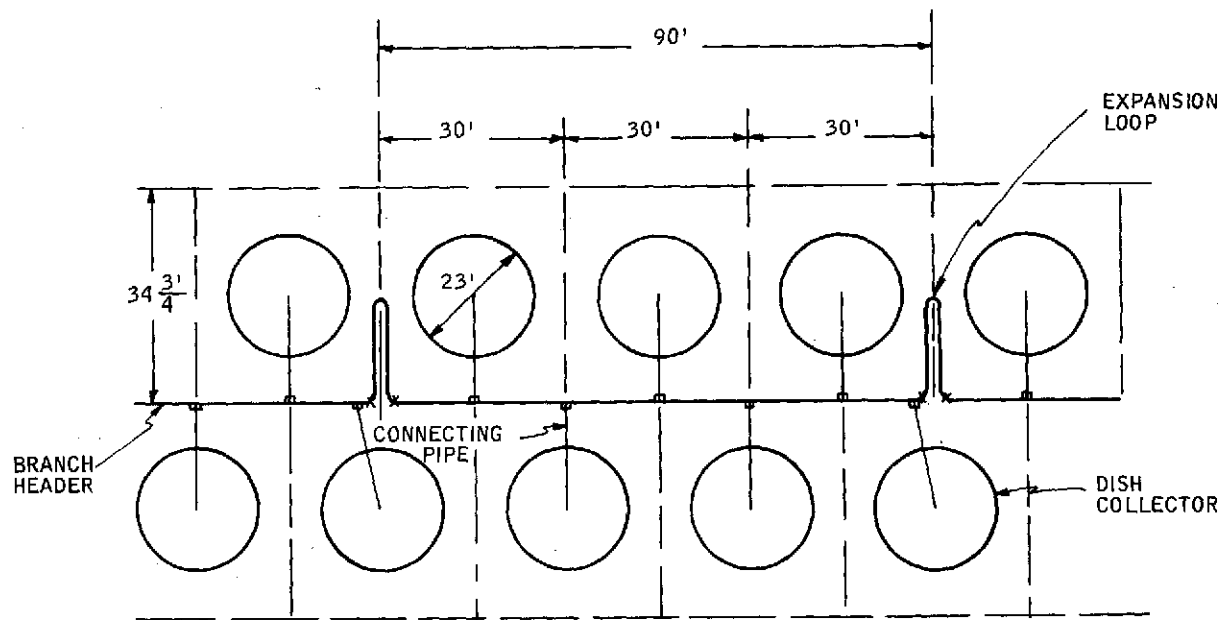
202

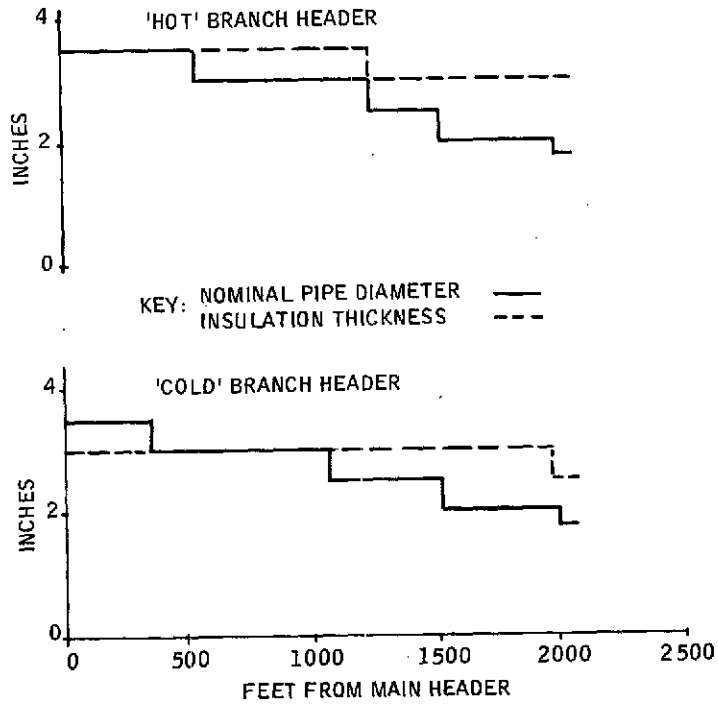Figure 153. Two-axis Dish Branch Header Layout at GCR = 0.40

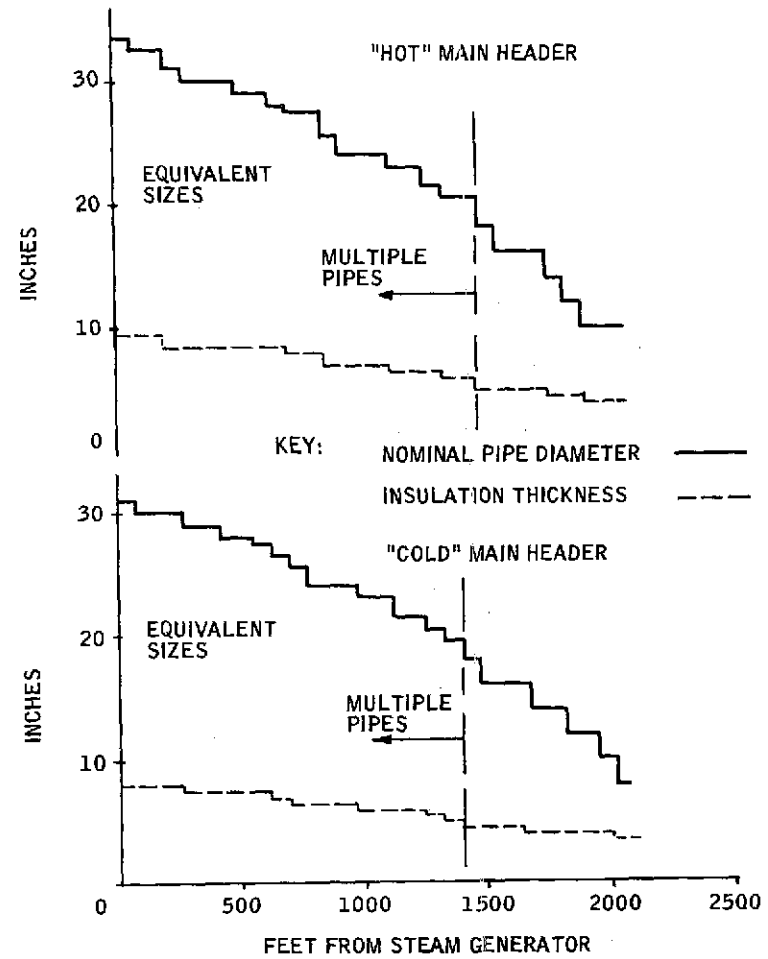Figure 154. Branch Header Pipe and
Insulation Sizes

Figure 155. Main Header Pipe and
Insulation Sizes
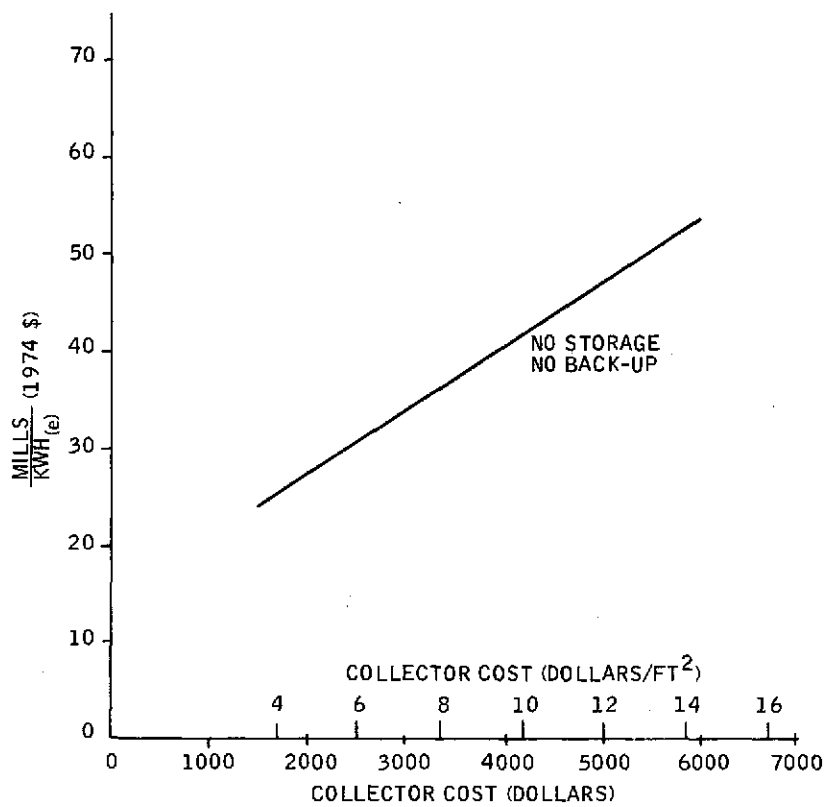
Figure 156. Distributed Dish Reference
System Energy Cost

Table XXIX. Distributed Dish Collector Reference
System Design Costs

100 MW(e) Average Plant Capacity

Land	$ 0.32 x 10^6
Header Piping	13.00
Header Insulation	5.47
Connection Piping and Insulation	3.81
Valves	2.40
Steam Generator/Pump	2.05
Turbine-Generator/Heat Rejection	7.22
Balance-of-Plant	5.24
Subtotal (without collectors)	$39.51 x 10^6
Total Plant Cost at $5000/collector (420 ft^2)	$122.31 x 10^6

The energy cost is found by dividing the annual plant cost by the net electric energy available to the grid in a year's operation. The annual plant cost is based on a fixed charge rate of 15 percent.

$$\text{Annual cost} = 0.15 \left(\$39.51 \times 10^6 + \text{cost of collectors} \right)$$

The energy cost numbers are all based on direct (1974) dollars.

CENTRAL RECEIVER

Overall System Description

This point design, capacity 215 Mw(e) peak, employs a Crescent receiver atop a 1500-foot reinforced concrete tower. The heliostat field is a circular annulus with an outside radius of 3100 feet and an inside radius of 580 feet. Figure 157 is an artist's perspective of the plant. The view is looking northwest at the Inyokern South site. Figure 158 shows the reference site layout. Tie-in to the existing 230 kv transmission line which crosses the Inyokern South site is shown for reference purposes. Mechanical draft wet cooling towers are located exterior to the heliostat field to avoid fogging and deposition of particulate matter on the heliostats.

Referring to Figure 157, water is transported up the tower in a carbon steel riser to the crescent receiver where it is converted to 900°F superheated steam. The steam is transported back down to the base of the tower in an alloy steel downcomer. The balance of the plant, with the exception of the heat rejection system, is located at the base of the tower interior to the heliostat field annulus. An architect's conception of the balance of the plant is shown in Figure 159. The major functional elements of this part of the plant are:

- Conventional 850/900 non-reheat turbine-generator
- Condenser
- Condensate pump
- Deaerator
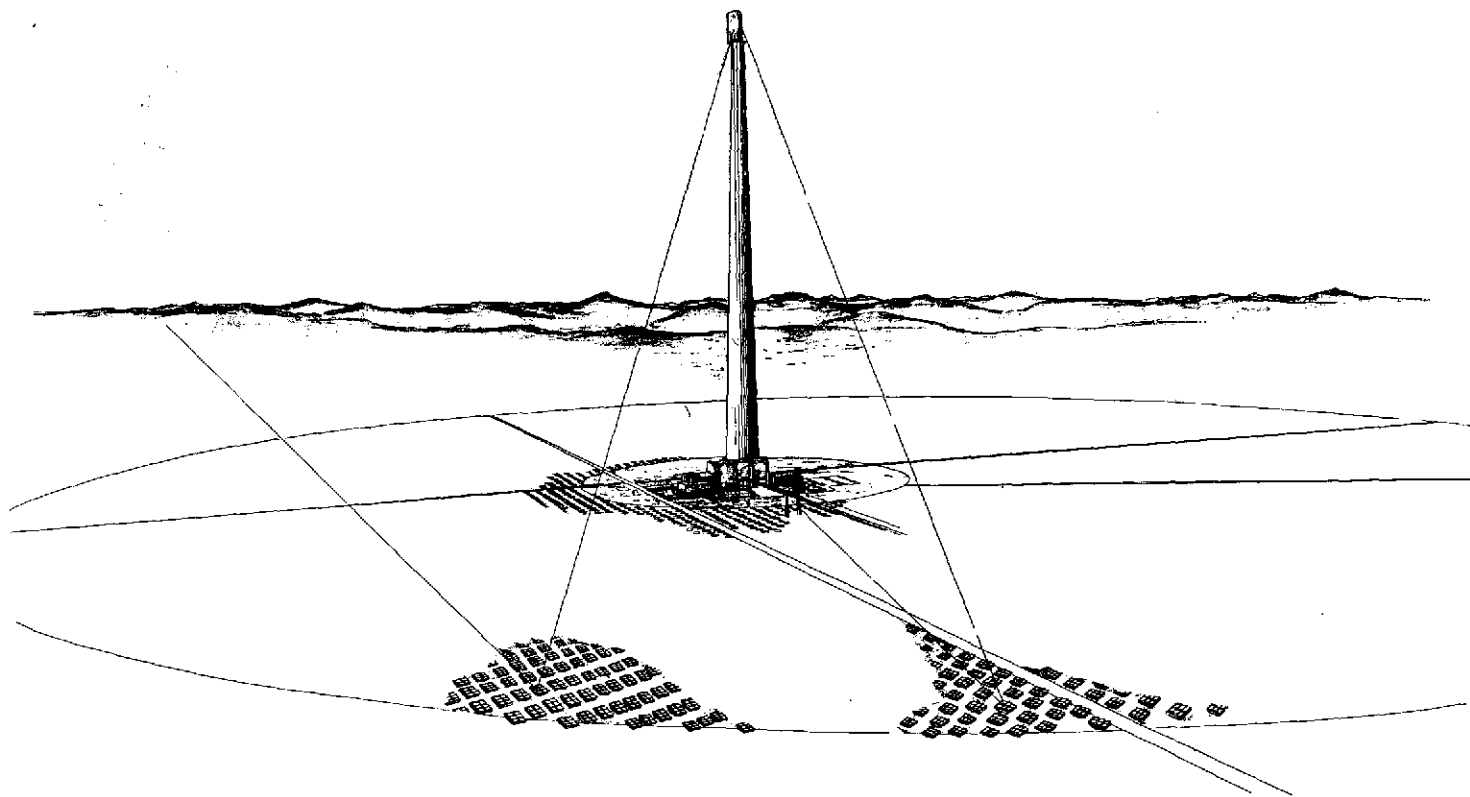
Figure 157. Artist's Perspective of Reference Central Receiver Solar Electric
Generating Facility -- View Looking Northwest

MAKEUP WATER LINE

COOLING TOWER

CIRCULATING WATER PIPES

HELIOSTAT FIELD

RECEIVER TOWER

SUBSTATION

GENERATING PLANT

230 KV TRANSMISSION TIE

ACCESS ROAD

N

W   E

S

WIND ROSE
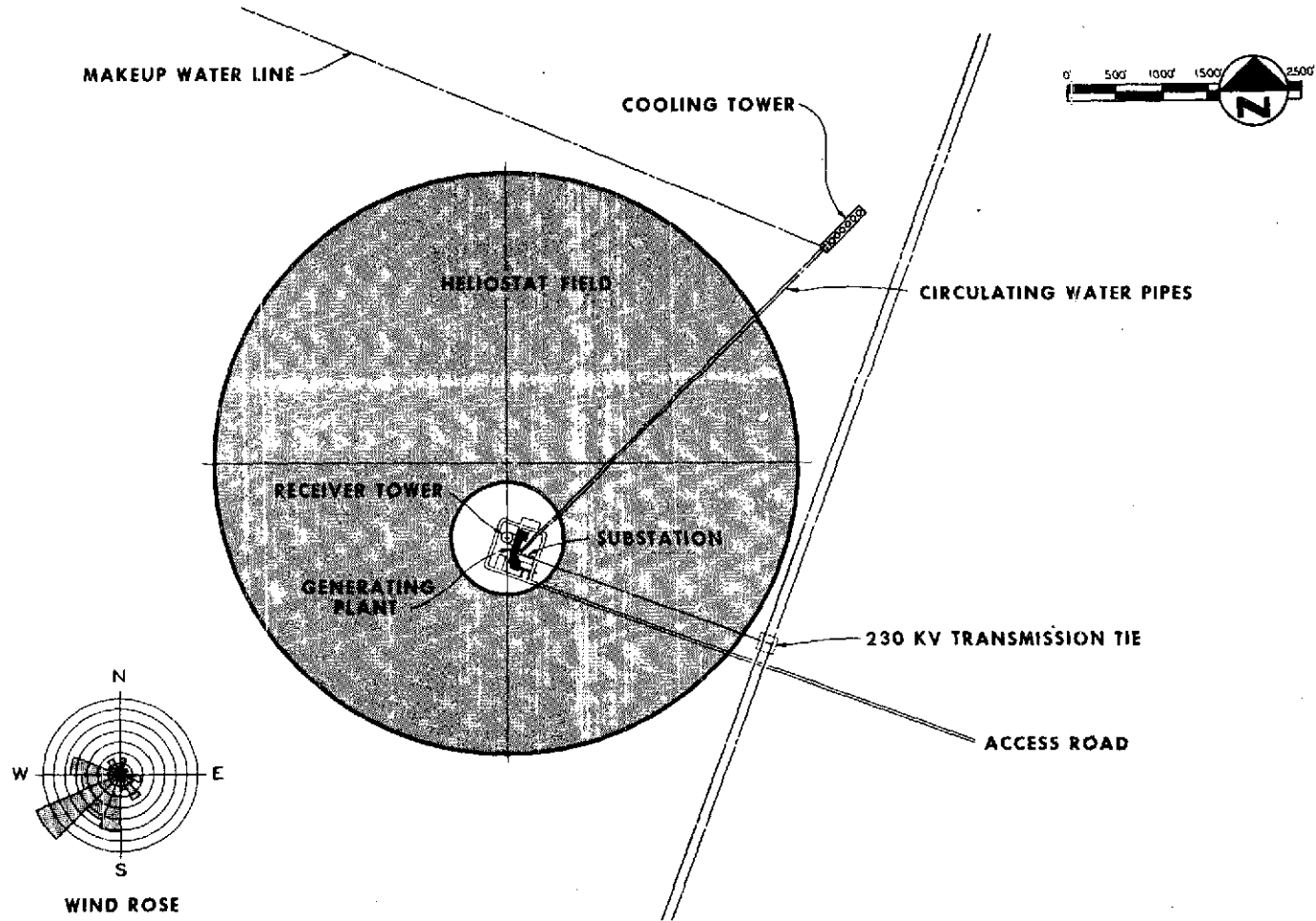
Figure 158.   Site Layout for Central Receiver Reference System Solar Electric
Generating Facility, Inyokern South Site
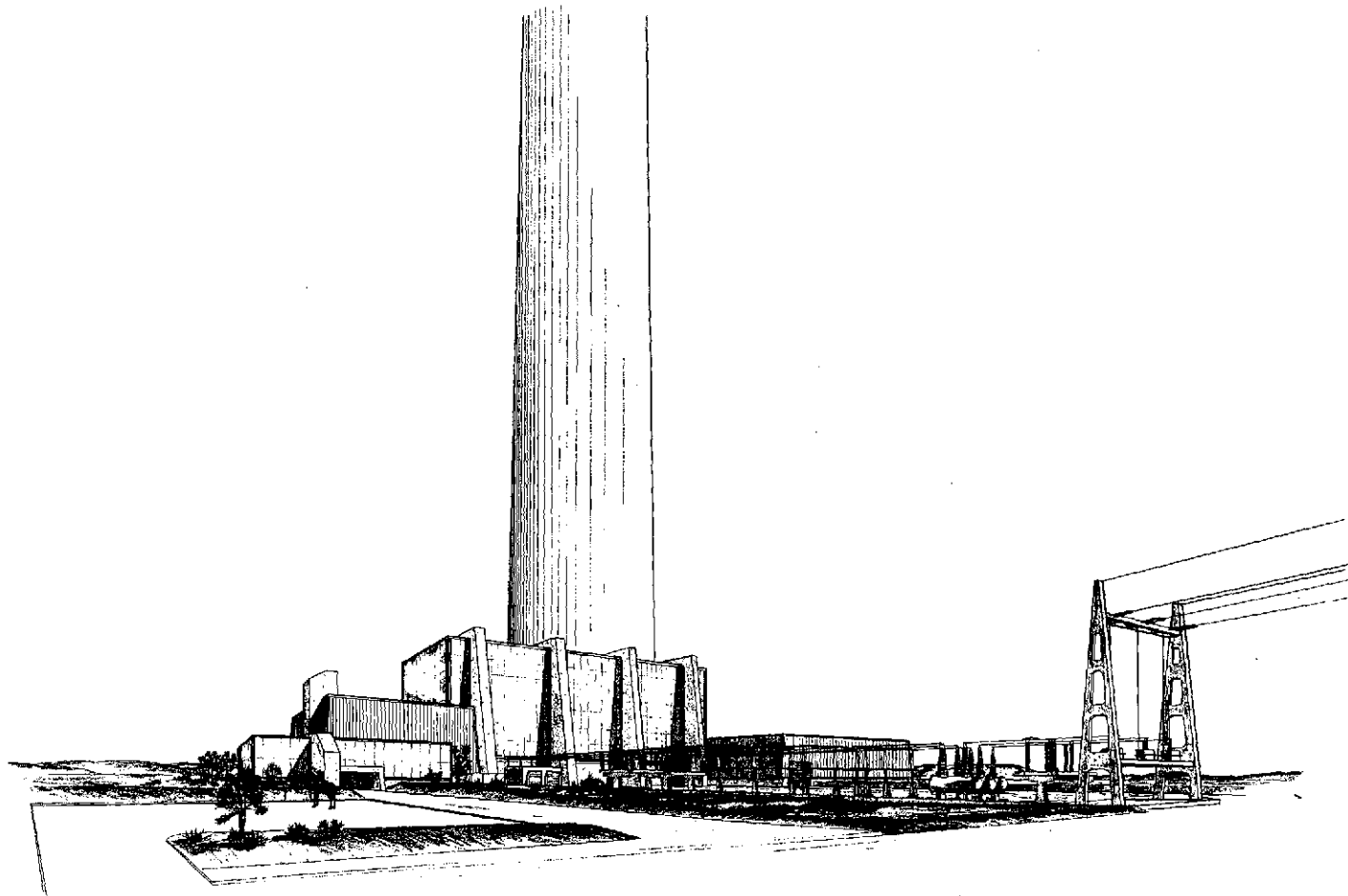
Figure 159. Architect's Conception of Reference Central Receiver Solar
Electric Power Plan, View Looking Northwest

- Feedwater heaters

- Boiler feed pump

- Water treatment facility

- Auxiliary power system

- Transformers and electrical switchgear

- Plant control

- Support facilities

Sufficient design of the reference plant was carried out to show the most important details of the physical layout. Plans for the three main floors are shown in Figures 160 through 162. These plans are suitable for a 200 Mw(e) steam generating plant and include the additional facilities required for solar thermal conversion to electricity. Particular details of interest include the heliostat control computer adjacent to the control room in Figure 162; the elevator and stairway access to the riser and downcomer piping in the receiver tower, Figure 162; the supporting machine shop and maintenance areas shown in Figure 160; and the visitor center and media room (projection, lecture, and interview facilities) shown in Figure 164. A cross-section of the main plant building is shown in Figure 163.

The Central Receiver Reference System Characteristics are given in Table XXX.
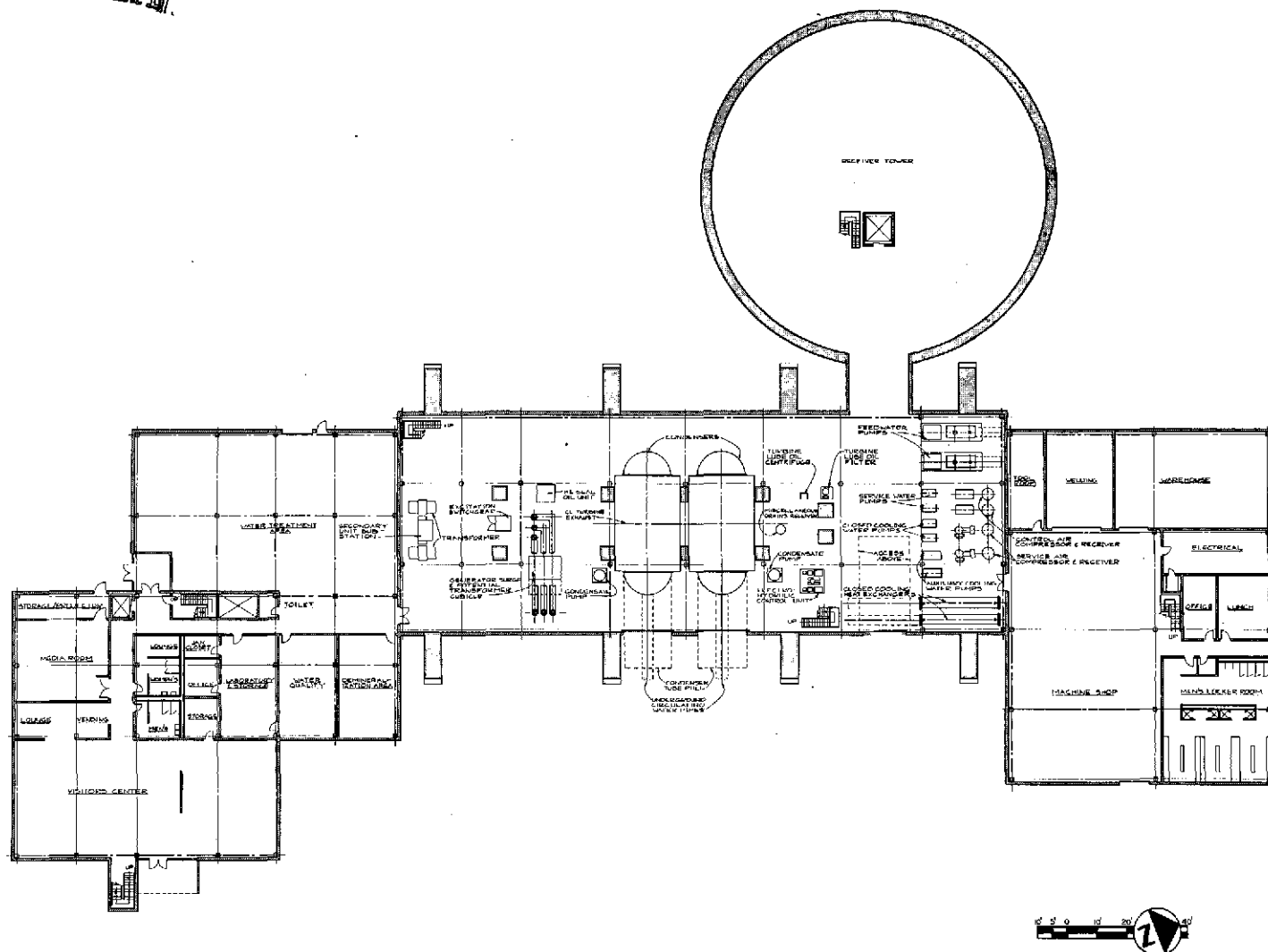
Figure 160. Ground Floor Plan Reference Central Receiver
Plant

212
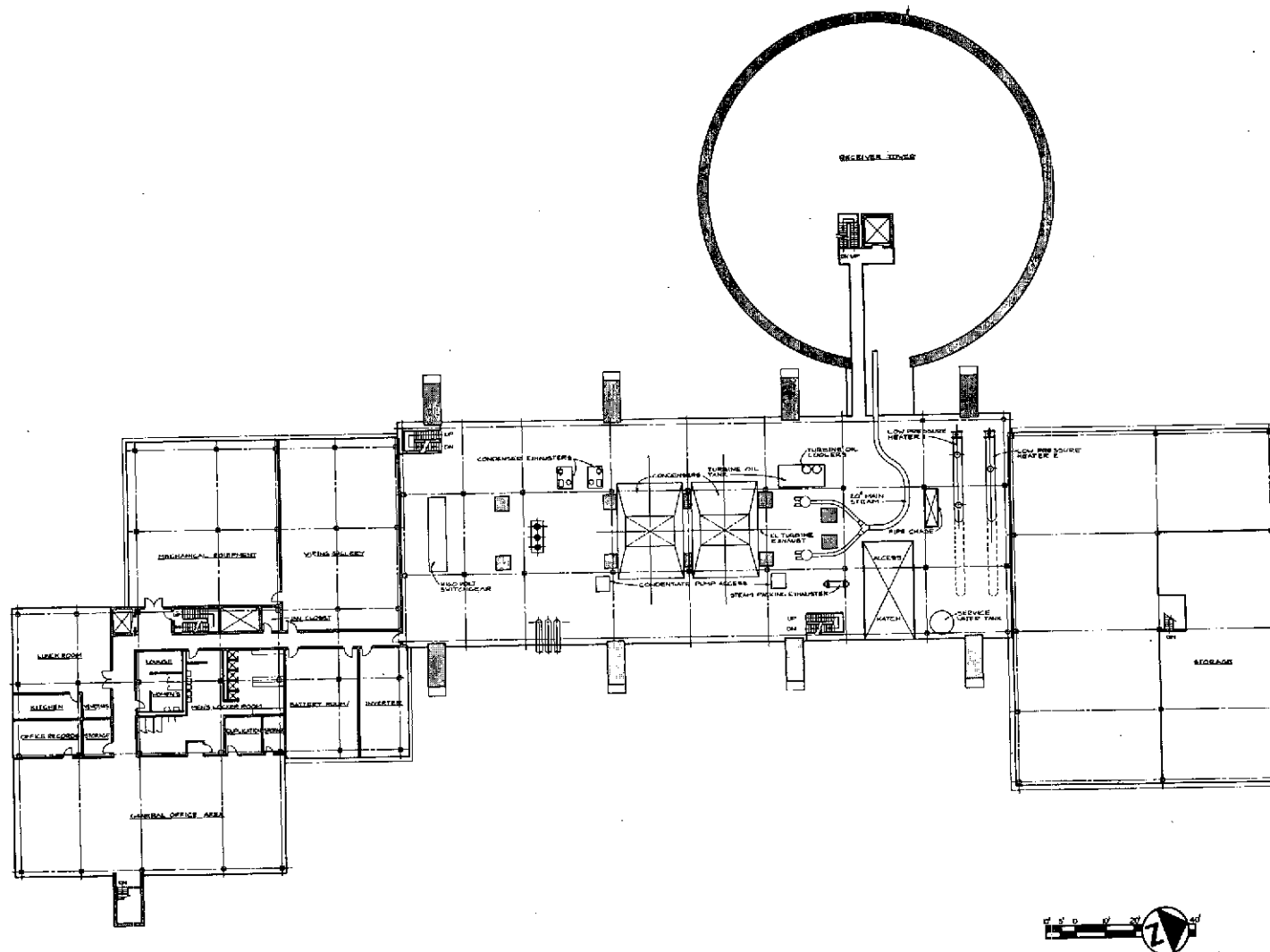
Figure 161. Mezzanine Floor Plan Reference Central
Receiver Plant
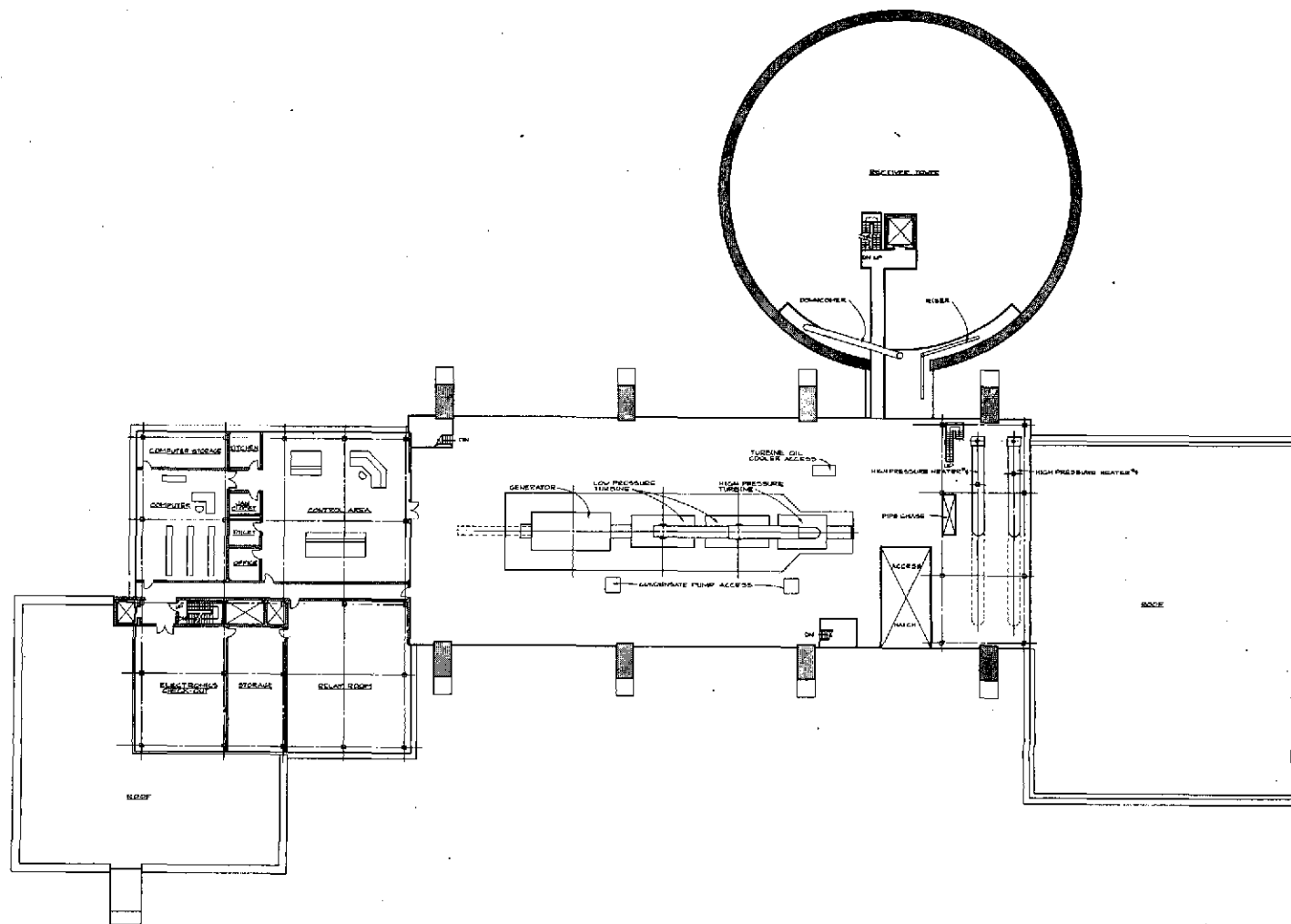
Figure 162. Operating Floor Plan Reference
Central Receiver Plant
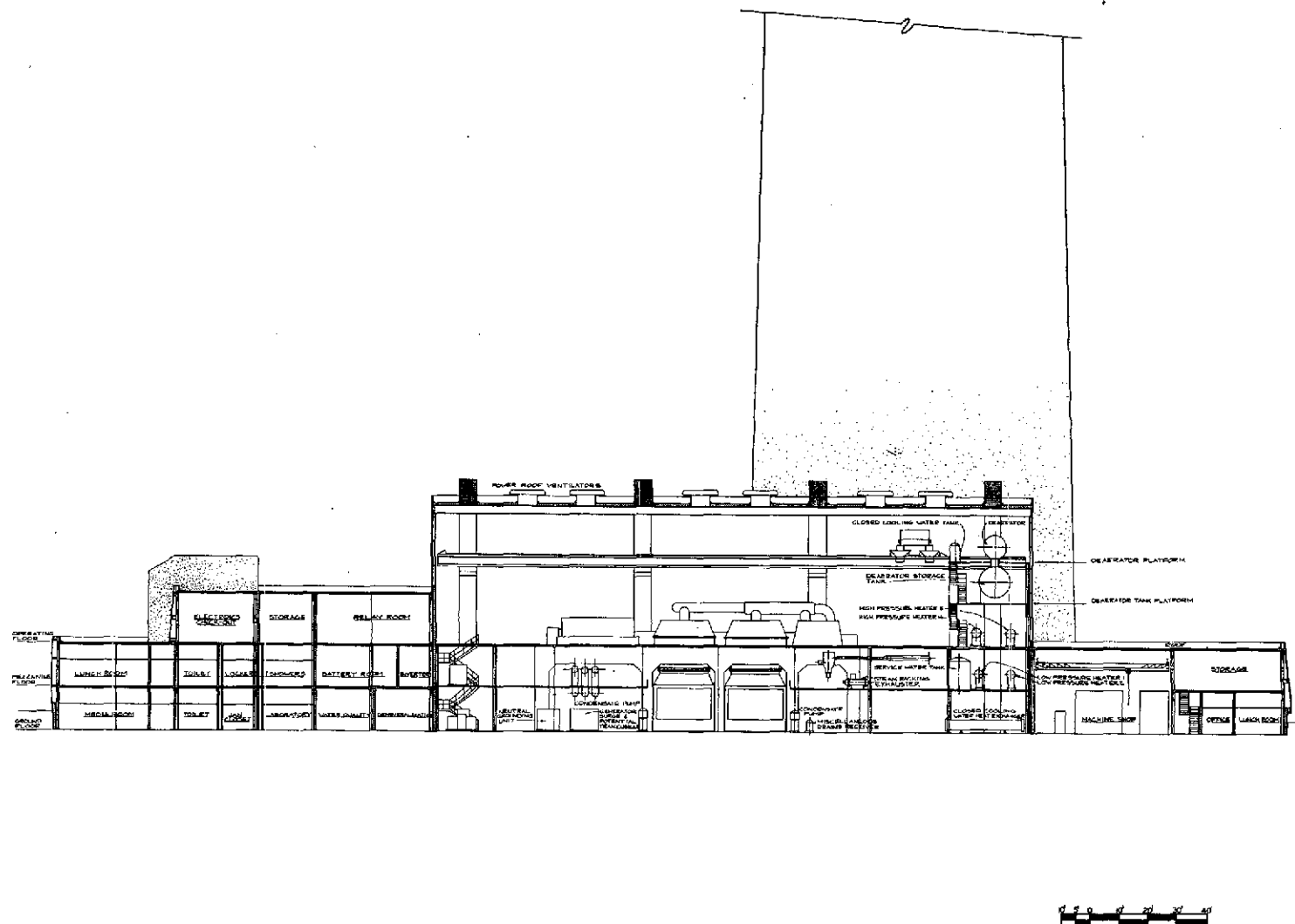
Figure 163. Cross Section of Main Plant Building

Table XXX. Central Receiver Reference System Characteristics

Tower Height	1500 feet (457 m)
Mirror field: outer radius	3100 feet (945 m)
Mirror field: inner radius	580 feet (177 m)
Mirror pattern	Uniform Spacing
Mirror GCR	0.456
Total mirror area	1327.9×10^4 feet^2 (123.36×10^4 m^2)
Receiver type	Crescent
Receiver height	100 feet (30.5 m)
Receiver width	70 feet (21.3 m)
Turbine inlet steam conditions	850 psig/900°F
Feedwater temperature ratio	0.8
Peak (6/15 noon) power	580 MW(t) 215 MW(e)
Annual Energy	1.586×10^6 MWH(t) 0.587×10^6 MWH(e)

Turbine-Generator/Heat Rejection System

Turbine-Generator -- The turbine-generator is a conventional, 850 psig/900°F, non-reheat, superheated steam turbine. Turbines using this cycle are listed in both the General Electric and Westinghouse Price Books for sizes from 20 MW to 200 MW. The most popular size is about 60 MW. Associated with the turbine is a condenser which will be designed to maintain a turbine back pressure below 3.5 inches of mercury. Prior to entering the central receiver, the feedwater will be heated, by extraction steam, in five conventional feedwater heaters to a temperature of about 411°F, depending on the ambient temperature. The feedwater pressure is provided by a conventional condensate pump and boiler feed pump. Because of the static and dynamic pressure losses in the central receiver tower, the boiler feedpump will be designed to provide a higher pressure than is normally required for this steam cycle. Because the fourth and fifth feedwater heaters are downstream from the boiler feedpump, these two heaters will be designed to withstand higher feedwater pressures than is normal with this steam cycle. These higher pressure pumps and heaters are commercially available for use with higher pressure conventional cycles, for example, 1250 psig/950°F. A turbine-generator heat balance for a typical 850/900 steam cycle is shown in Figure 164.

215
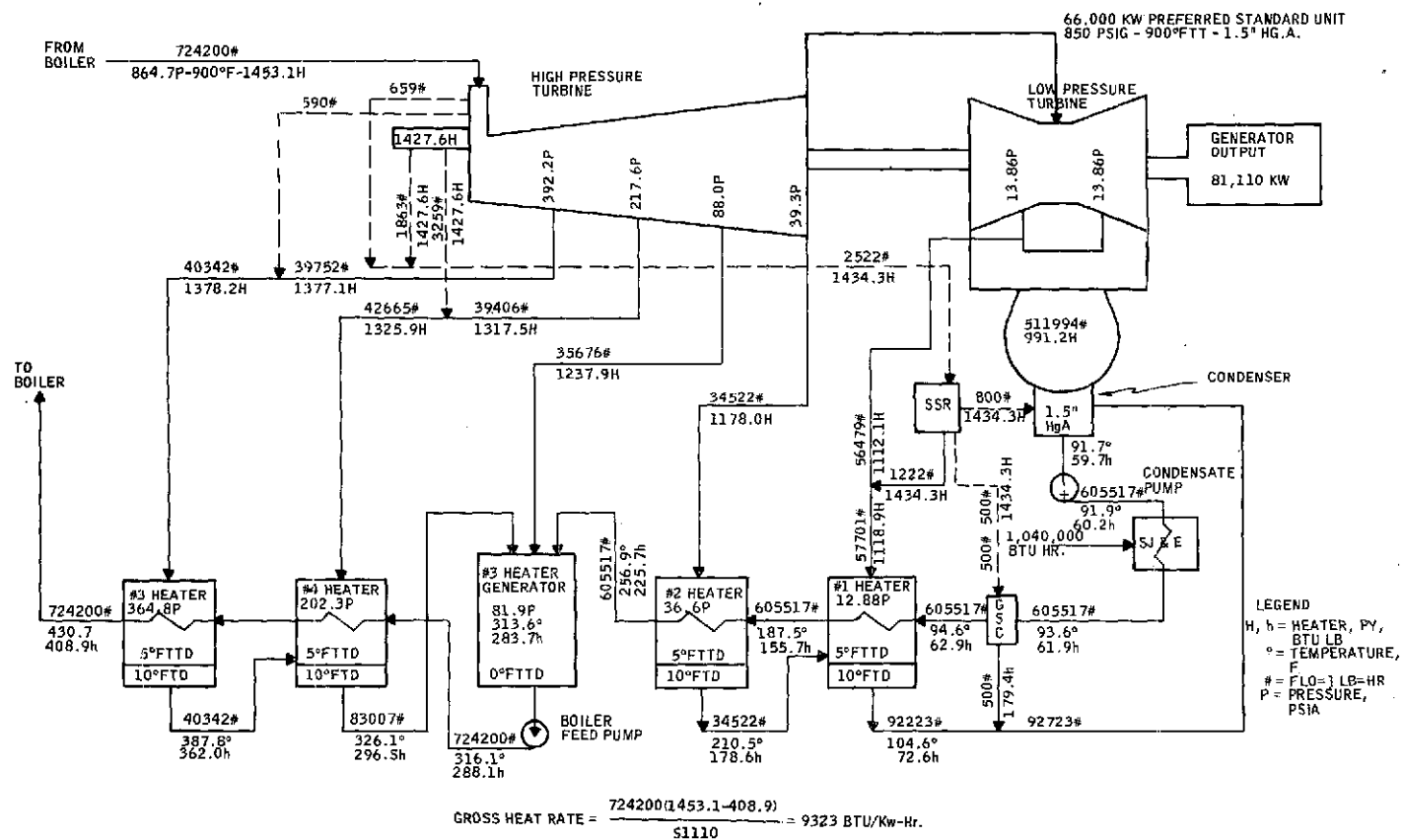
Figure 164. Turbine-Generator Heat Balance for Typical 850/900 Steam Cycle

Heat Rejection -- Heat will be rejected from the condenser by a circulating water system using wet, mechanical draft cooling towers. These cooling towers are commercially available in any desired size. The peak circulating water flow for the 215 MW(e) rated capacity is estimated at 110,000 gallons per minute (gpm), and the peak make-up water requirement is estimated at 2800 gpm. This make-up water replaces that water lost from the circulating water system as evaporation and blow-down in the cooling towers.

Horizontal Rotating Heliostat Design

The detailed description of the design of the horizontal rotating heliostat is given in Section VI.

Receiver/Tower Specifications

Tower Specifications -- For the reference system point design, there are three sets of tower specifications, one each for seismic zones I, II, and III. These specifications are given in the following tabulation:

Seismic Zone	I	II	III
Tower height (ft)	1500	1500	1500
Diameter at top (ft)	40	40	40
Diameter at base (ft)	96	104	116
Cost (10^6 $)	8.0	8.0	8.8

Riser/Downcomer Specifications -- For the reference system point design, the riser and downcomer are each a single pipe. Each pipe consists of a series of identical expansion loop modules. A single module is shown for the riser in Figure 165 and for the downcomer in Figure 166. A total of 8 riser modules and 16 downcomer modules are required for a 1500-ft tower. A schematic drawing of the piping arrangement in the tower is shown in Figure 167. Detailed drawings of the anchors, guides, and vertical restraints are shown in Figure 168.
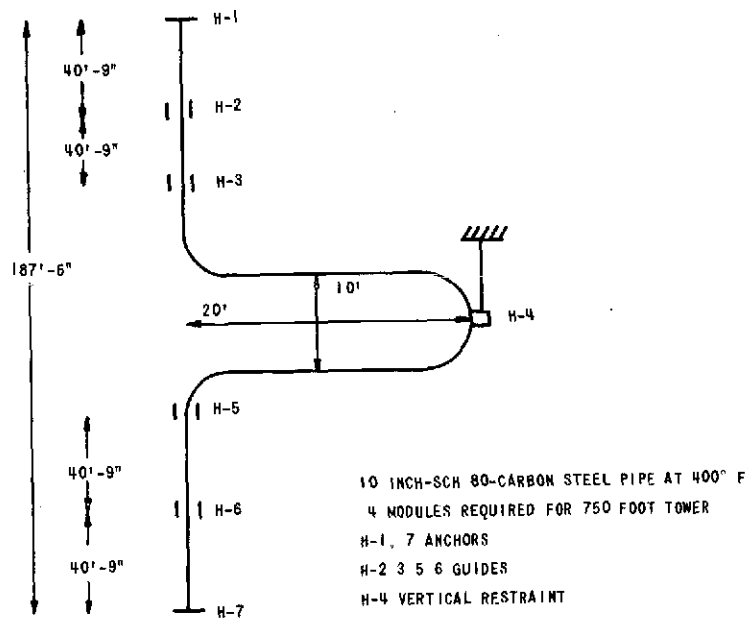
Figure 165. Riser Module for 215 MW(e)
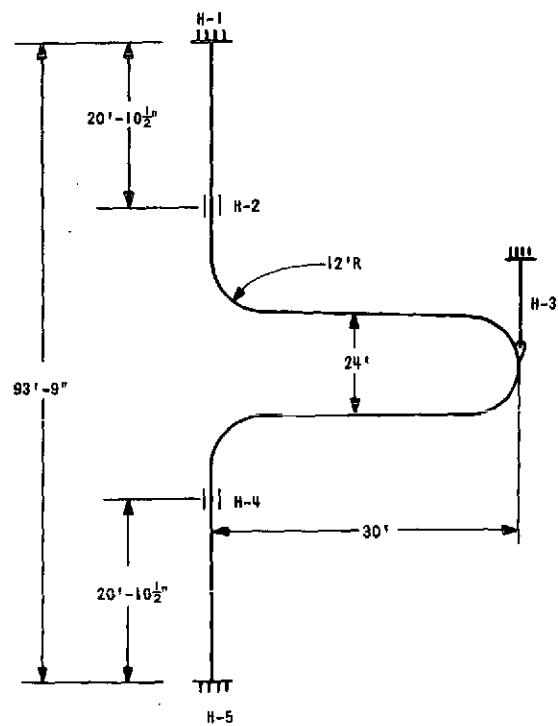
Figure 166. Downcomer Module for 215 MW(e)
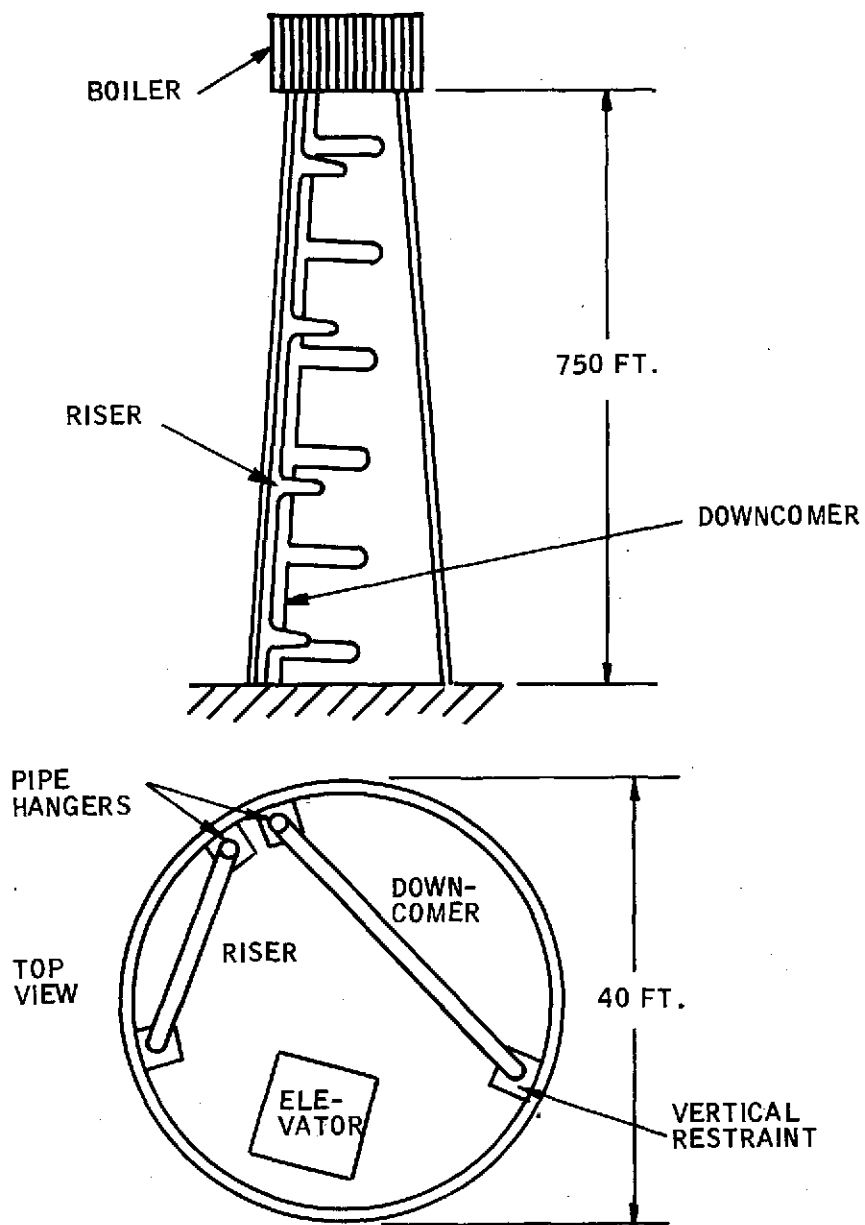
Figure 167. Water/Steam Tower Piping Configuration
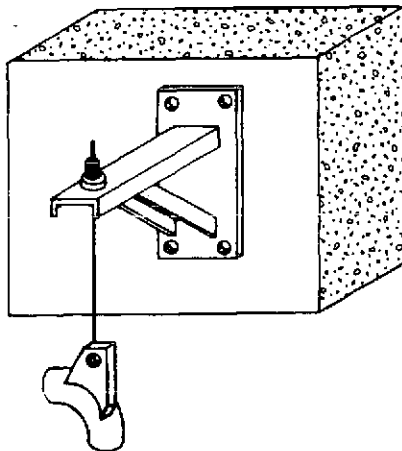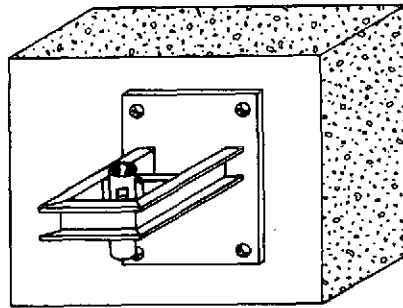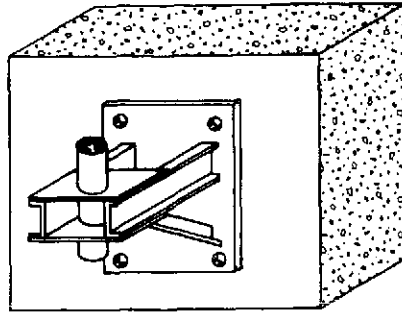
Figure 168. Detailed Drawings of Anchors, Guides, and Vertical Restraints

Receiver Specifications -- For the reference system point design, a Crescent receiver design is used (Figure 95). Receiver specifications are listed below.

Cylinder height:	100 feet
Cylinder radius:	35 feet
Cylinder enclosure angle:	180 degrees
Tube OD:	2.375 inches
Tube ID:	1.939 inches
Tube material:	316 Stainless Steel
Tube spacing:	3.0 inches
Number of tubes:	438
Water inlet velocity:	0.95 feet/second
Water inlet temperature:	411°F
Steam outlet temperature:	900°F
Maximum tube temperature:	< 1200°F
Receiver pressure drop:	2 psi
Capacity rating:	215 MW(e)
Total weight (including supports):	145 tons

Plant Costs

Costs for each of the subsystems were calculated for the point designed described above. A cost summary for the central receiver reference system is shown in Table .

The total cost of riser/downcomer piping was calculated from the cost of the individual modules shown in Figures 165 and 166. Breakdown of the module costs, including erection, is:

- 10-inch Schedule 80 Riser Module

Hangers	$ 2,700
Straight-run pipe	2,732
Elbows	1,772
Welds	1,290
Insulation and handling	5,389
	$13,883

- 24-inch Schedule 80 Downcomer Module

Hangers	$ 2,225
Straight-run pipe	12,418
Elbows	10,942
Welds	53,707
Insulation and handling	6,071
	$85,363

There are eight riser modules and 16 downcomer modules in the 1500-foot tower. The total cost of piping is, therefore:

$$8 \times \$13,833 = \$\quad 111,064$$
$$16 \times \$85,363 = \$1,365,808$$
$$\text{Terminal welds and hangers} = \underline{\qquad 7,900}$$
$$\text{Total Cost} = \$1,482,772$$

For the central reveiver, a 215 MW(e) capacity rated turbine-generator is installed. The cost of this subsystem was taken from Appendix A along with the heat rejection and balance of plant costs for a 215 MW(e) capacity rating.

As shown in Table XXXI, the heliostate cost is the largest cost item in the reference system design. Since an undisputed heliostat cost figure is not available, the total plant cost is best reported as a function of the heliostat cost. The net energy cost of the reference system is shown in Figure 169 as a function of heliostat cost. The energy cost is based on a fixed-charge rate of 15 percent, and is based on direct (1974) dollars.

Table XXXI.   Central Receiver Reference System Design Costs
147 MW(e) Average Plant Capacity

Land	$\$0.554 \times 10^6$
Piping/insulation	1.483
Crescent receiver	3.160
Tower	8.800
Turbine-generator/heat rejection	12.200
Balance of plant	9.245
Subtotal (without heliostats)	$\$35.44 \times 10^6$
Total plant cost at $6.95/ft^2 for heliostats	$\$92.435 \times 10^6$

Figure 169. Central Receiver Reference System Energy Cost

SECTION XI

CONCLUSIONS

A rigorous comparison of 11 candidate system design concepts, including both distributed and central receiver systems, showed the water-superheated steam (850 psig/ 900°F) central receiver system to be the preferred concept. This concept was selected primarily on economic grounds with the prime cost factor, exclusive of storage, being the mirrors. Flat surface heliostats are significantly less expensive th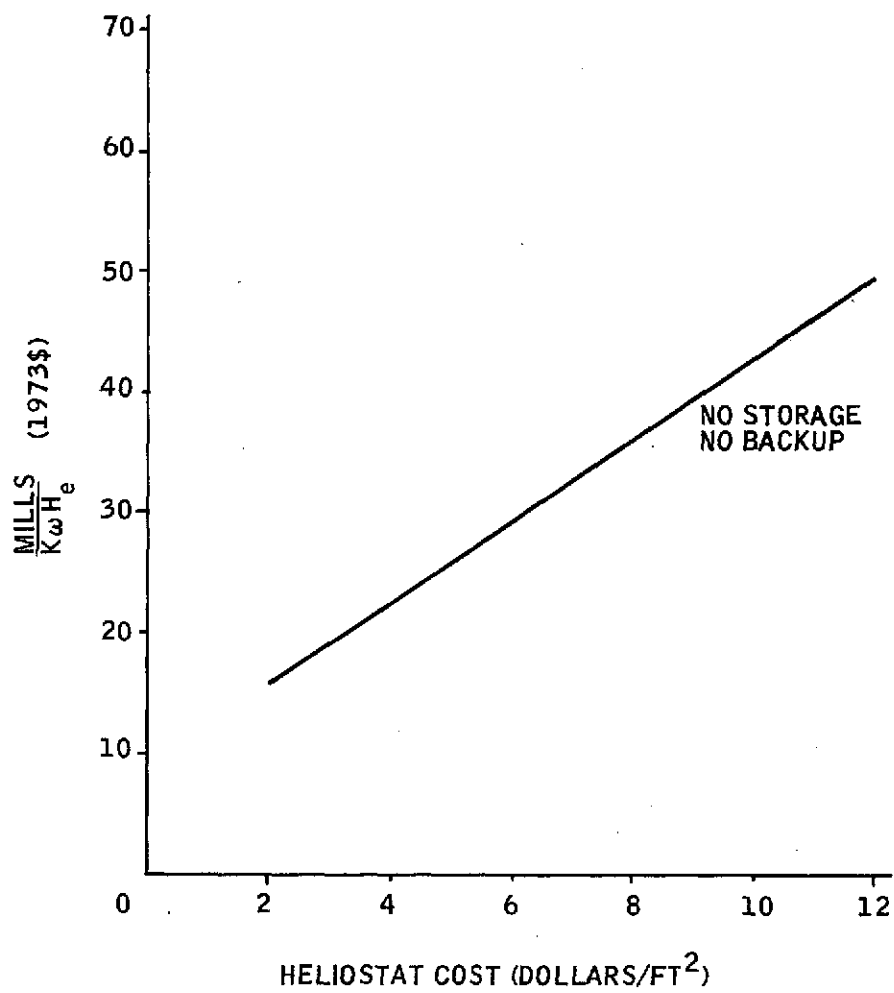an curved parabolic trough or paraboloidal dish collectors. Although the water-steam central receiver was not optimized with respect to power level in this study, all indications are that the optimum size will be of the order of 100 Mw(e) or less.

Three other central receiver concepts were investigated: (1) a closed Brayton cycle using helium, (2) a combined Brayton/steam Rankine cycle, and (3) a liquid sodium/ steam Rankine cycle. The water-superheated steam Rankine cycle was rated superior on the basis of an optimum combination of conversion efficiency, cost of conversion equipment, and maximum use of available technology.

Distributed system designs using several different type collectors were evaluated and compared. In order of decreasing economic desirability they are: paraboloid of revolution dish, polar-mounted parabolic trough, north-south trough, east-west trough, and flat plate collectors. These distributed systems showed a trend towards optimization at a size below the range of our investigations (i.e., under 100 Mw(e)). It is possible that these systems could become economically competitive in the low megawatt capacity range.

The major economic issue related to the implementation of solar electric generating plants is their high capital cost. The low density of solar energy at the earth's surface requires that large arrays of solar collectors (heliostats) be used for significant power generation. These collectors account for approximately 70 percent of the total solar plant costs. Consequently, design of low-cost, efficient collectors is the prime leverage item for reducing solar thermal conversion costs to competitive levels. Furthermore, the number of collectors required can be reduced by the use of higher efficiency conversion cycles.

The best siting region for central station solar power plants is in the Southwestern United States where the direct component of insolation is highest. The reference site for this study is Inyokern South, located approximately 10 miles southwest of Inyokern, California. Operation at this site would require a negotiated diversion of water from the Los Angeles Aqueduct in order to meet the make-up water requirements for evaporative forced draft cooling towers. Water availability seriously limits the number of potential sites in the Southwest unless advanced solar conversion systems with minimal water requirements are developed. The use of dry cooling towers with conventional steam turbomachinery has a significant negative impact on total plant costs, primarily through lowered cycle efficiency.

The major environmental impacts of siting solar thermal conversion plants appear at this time to be:

- Large land area requirements and consequent land usage displacement

- Water requirements for systems utilizing conventional steam cycles

- Effect of large-scale construction practices on the desert biome

For all central receiver and distributed collector concepts, several storage subsystems were investigated but no satisfactory match-up was clearly identified. We believe that a minimum half-hour storage capacity must be a system requirement to enable controlled response to transient inputs. Furthermore, the charge/discharge strategy of storage utilization was shown to be one of the critical design parameters affecting the economic competitive capabilities of the solar thermal systems.

For a central receiver system, the receiver subsystem design is among the most important issues. A fully exposed, crescent-shaped receiver is the most promising design for our reference central receiver system. Although a cavity-type receiver is an attractive alternative, especially from the standpoint of convection and reflection losses, the crescent receiver simplicity of design, erection, and control, the minimal thermal stresses, and the time invariant heliostat aim strategy which can be used, lead us to prefer the crescent receiver at this time.

The flux distribution on the receiver is another critical parameter as it controls the receiver heat transfer characteristics. Our studies have shown that receiver flux control, heliostat design and aim strategy are closely coupled. With the crescent receiver design, a nearly axisymetric flux distribution was attained independent of time of day/year using a time invariant aim strategy.

A careful development of costs for all materials, components, and subsystems shows that the cost of electrical energy from the central receiver system is competitive with conventional peaking power in certain parts of the United States. This comparison is strongly sensitive to collector costs.

Based on both technical and economic considerations, we conclude that the dynamic conversion of solar generated heat to electricity is a feasible and potentially competitive energy source. No technical barriers to its implementation exist; the major prerequisites for economic viability are the design and production of low-cost hardware.

SECTION XII
RECOMMENDATIONS

Based on the results and the experience attained in the course of this study program, we believe that further work should be undertaken in both the central receiver and the distributed collector systems. For the water-superheated steam crescent central receiver we specifically recommend the following:

- Heliostat aim strategy should be refined to attain flux distributions that fully satisfy the design constraints.

- Thermal stress studies should be undertaken to ensure compatibility with materials requirements.

- A transient control philosophy for all subsystem interfaces should be developed.

- Storage concepts should be designed to enable off-design conditions operation.

- A charge/discharge storage strategy should be developed for economic optimization.

- Low-cost heliostats should be designed and developed.

- Overall system scaling and sensitivity studies should be undertaken.

- Conceptual design studies should be extended to alternate configurations capable of using the high-flux/high-temperature potential of the central receiver.

In detail, the aim strategy effort should address such issues as the side-to-side flux balance, receiver size minimization and scale effects. The issue of flux control problems with small-scale facilities such as the proposed test facility or the POCE should be addressed. It is conceivable that systems smaller than those studied in this present work will require a modification of the aim point strategy. The introduction of focusing heliostats may also require a modified aim strategy. If these developments do present flux control problems, a thorough study should be very important in planning the future areas of hardware development.

To date, the flux control and system design work has primarily centered around steady-state operation. The next logical concern is transient response. Under conditions of broken cloud cover, a flux imbalance from side to side across the tube walls is possible. The extent to which this flux imbalance is really a problem and the control strategy which will ensure the integrity of the system should be identified. At most, they may require an array of insolation sensor equipment in the mirror field to detect cloud passage and to effect a symmetric defocus of the heliostats to balance the flux loss.

Implied in this work is a detailed thermal stress calculation to assess the problem. A transient control study should also be undertaken for the turbine generator, and heat storage subsystems. The valving and control system, which has to ensure steady operation from storage and direct collection during broken cloud cover operation, may impose serious design and operating limitations which have not yet been identified. Detailed storage design studies should be initiated to examine both the backup capacity displacement and system transient control functions.

Storage to date has been examined in terms of compatibility with the turbine inlet conditions for standard modern turbine equipment. This restricted the study to storage systems which could deliver energy at essentially the same temperature as the energy delivered directly from the collectors. The possibility of practical "dual-cycle" four-flow turbines which can accommodate a wide range of inlet temperatures and pressures greatly extends the range of possible storage concepts. For example, superheated steam directly from the central receiver could be used during sunshine hours and saturated steam generated from a lower temperature storage medium such as Therminol 66 could be used in the same four-flow turbine system. Charging of the storage system could be accomplished from bypass or extraction steam during sunshine hours.

The other important area for further storage system investigation is the charge/discharge storage control strategy, since the extent to which a given storage capacity can displace fossil backup equipment capacity is as strongly influenced by the utilization strategy as it is by any other design parameter.

The heliostat module is the single most important item in the overall system cost. Efforts should be directed toward the design and development of low-cost heliostats with particular attention to the economic optimization of the heliostat operational functions.

Conceptual central receiver design studies should be undertaken to identify configurations which can use the high-flux/high-temperature capabilities of the central receiver. In particular, there are open-cycle gas turbine engines available which can operate up to 1800°F. If a high-temperature and high-performance receiver, using perhaps the latest developments in ceramics, can be designed, the gas turbine systems will become very attractive. They will have high efficiency and low cost, can be mounted at the tower top because of their low weight, and will require no cooling water for waste heat rejection. The importance of cooling water scarcity in the Southwest should also motivate further work on dry and wet/dry cooling tower technology.

The present study was chartered to investigate solar plants in the range from 100 to 1000 megawatts electric, but the smaller-size plants appear to be attractive. Therefore, overall system scaling and sensitivity studies, using the Monte Carlo simulation capabilities, should be carried out. This effort should examine focusing heliostats and the impact they will have on flux control.

In relation to the distributed collector systems, we recommend the following:

- A low-cost paraboloid of revolution dish collector should be designed and developed.

- Storage concepts fully compatible with the distributed systems should be identified to achieve economic optimization.

- Total energy systems studies should be carried out.

- Process heat capability utilization studies should be undertaken.

- Overall system scaling and sensitivity studies should be initiated.

We further recommend that an effort be made to identify and define federal policy in relation to federal land use for solar power plants in the Southwest.

It is also important that studies be undertaken to identify the environmental, socio-political, and economic impacts of solar power plants. Associated with the latter effort, studies should be undertaken to extend the geographic limitation of the present study beyond the Southwest of the Continental United States to other regions of the country, especially those characterized by median levels of insolation.

REFERENCES

1) "Site Selection Guide for Solar Thermal Electric Generating Plants", Special Report prepared for NASA-Lewis Research Center (Contract No. NAS3-18014) by Black & Veatch Consulting Engineers, Kansas City, Missouri, June 1974.

2) "Selecting Preferred Sites for a Solar Power Station Using Solar/Climatic Data", Special Report prepared for NASA-Lewis Research Center (Contract No. NAS3-18014) by Honeywell Systems & Research Center, 2600 Ridgway Parkway, Minneapolis, Minnesota, June, 1974.

3) "On-Site Survey of Candidate Solar/Electric Power Plant Sites", Special Report prepared for NASA-Lewis Research Center (Contract No. NAS3-18014) by Honeywell, Inc./Black & Veatch, June 1974. (Available through Honeywell Systems & Research Center, Minneapolis, Minnesota).

4) Moon, J. D., and Sampson, R. L., "Computer Analysis of the Flat Plate Solar Collector and the Absorption Refrigeration Cycle", Honeywell Systems & Research Center, Minneapolis, Minnesota, No. 2810-3701, F4007-ID, April 1973. (Informal Honeywell report)

5) "Research Applied to Solar-Thermal Power Systems", University of Minnesota/ Honeywell, Progress Report No. 1, NSF/RANN/SE/GI-34871/PR/72/4.

6) "Research Applied to Solar Thermal Power Systems", University of Minnesota/ Honeywell, Progress Report No. 2, NSF/RANN/SE/GI-34871/PR/73/2, pp. 68-69, Figures 3-40 and 3-41.

7) R. Hilpert, "Wärmeabgabe von geheizten Drähten und Rohren," Forsch. Gebiete Ingenieurw., Vol. 4 (1933), p. 215.

8) Kreith, Frank, Principles of Heat Transfer, Scranton: International Textbook Company, 1959, p. 376.

APPENDIX A
DISTRIBUTED SYSTEM SOLAR POWER PLANT COSTS

The major costs of a distributed solar collector power plant are for:

- Turbine-generator/heat rejection equipment

- Balance of plant

- Steam generator

- Land

- Energy transport system

- Solar collectors

The cost estimates for each of the above items follows:

TURBINE-GENERATOR/HEAT REJECTION

Capital costs (including erection) of the steam turbine-generator, condenser, and cooling tower as a function of gross electric generating capacity are given in Figure A-1. These costs were obtained from the experience of Black & Veatch in the purchase and installation of steam power plant equipment with turbine inlet conditions between 1000 psi/500°F and 1450 psi/1000°F. The costs were corrected for inflation so that the curve in Figure A-1 represents 1974 dollars. These are average prices for standard steam cycles and are unlikely to be in error by more than 10 percent.

The costs in Figure A-1 are only valid if the heat rejection system is a wet cooling tower. Either wet or dry cooling towers could have been selected, but higher efficiency wet cooling was chosen for both the distributed system and the central receiver system for a meaningful comparison. The use of dry cooling towers would increase the costs in Figure A-1.

BALANCE-OF-PLANT

The balance-of-plant includes the:

- Turbine-generator base

- Condenser base

- Structural supports and bases for the feedwater heaters and deaerator

- Controls for the turbine-generator, pumps, and valves

- Control room

- Plant building

- Electrical substation used to transform the generated power to a state suitable for transmission

229
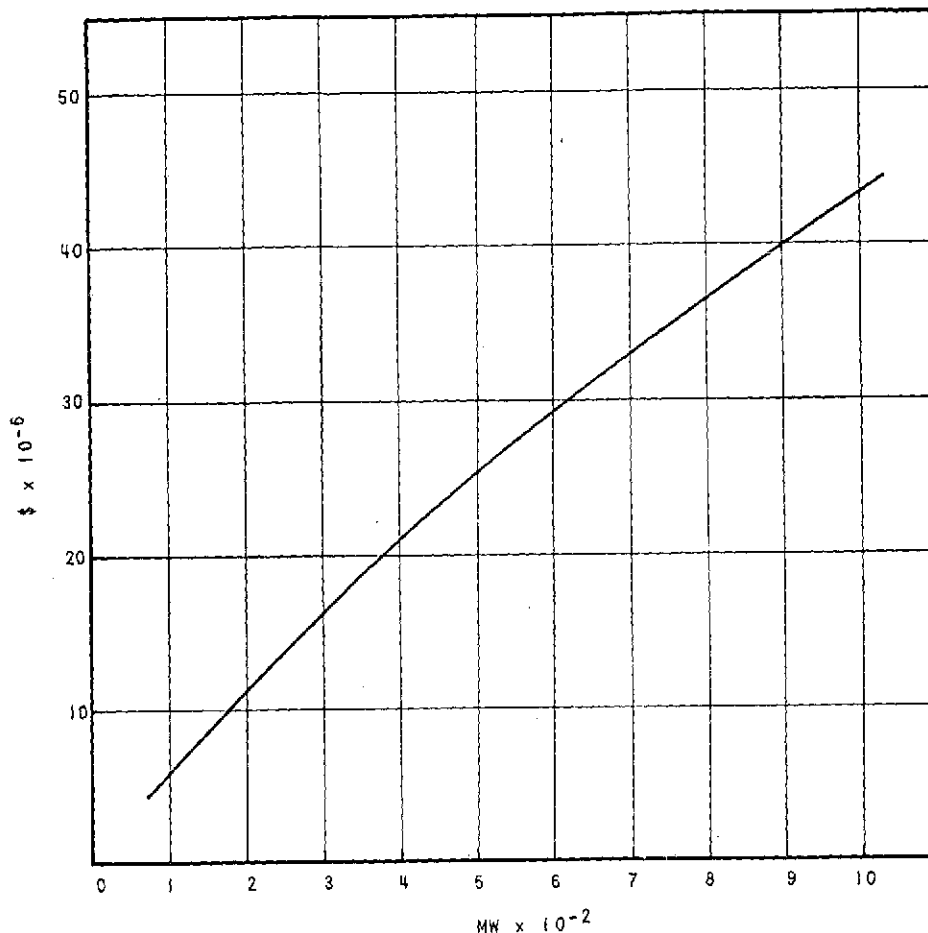
Figure A-1. Cost (Including Erection) of Steam Turbine-
Generator, Condenser, and Wet Cooling Tower
as a Function of Electric Generating Capacity

While it is beyond the scope of this project to prepare design specifications for this
balance-of-plant equipment, it is possible to estimate its cost.

To determine the balance-of-plant costs, five units which Black & Veatch has recently
designed were examined. For each of these plants, a comprehensive price breakdown is
available. The cost of the boiler, fuel handling equipment, pollution control equipment,
and the associated construction costs were subtracted from the total plant cost. The
experience of Black & Veatch is that 60 percent of the general construction and structural
steel costs are associated with the boiler. The remaining costs were escalated at a rate
of 8 percent, compounded annually. The cost of the steam turbine-generator, condenser,
and cooling tower (Figure A-1) was subtracted from these cost figures. This yielded
costs of $60, $45, $52, $42, and $40 per kilowatt$_{(e)}$ of installed capacity for the five

plants. These costs are shown in Figure A-2 as a function of installed capacity, and are
based on an operational date of 1975. They agree with current estimates of Black &
Veatch project managers. An average value of $42/Kw(e) for balance-of-plant costs is
valid within the range of 100-700 Mw(e).

230
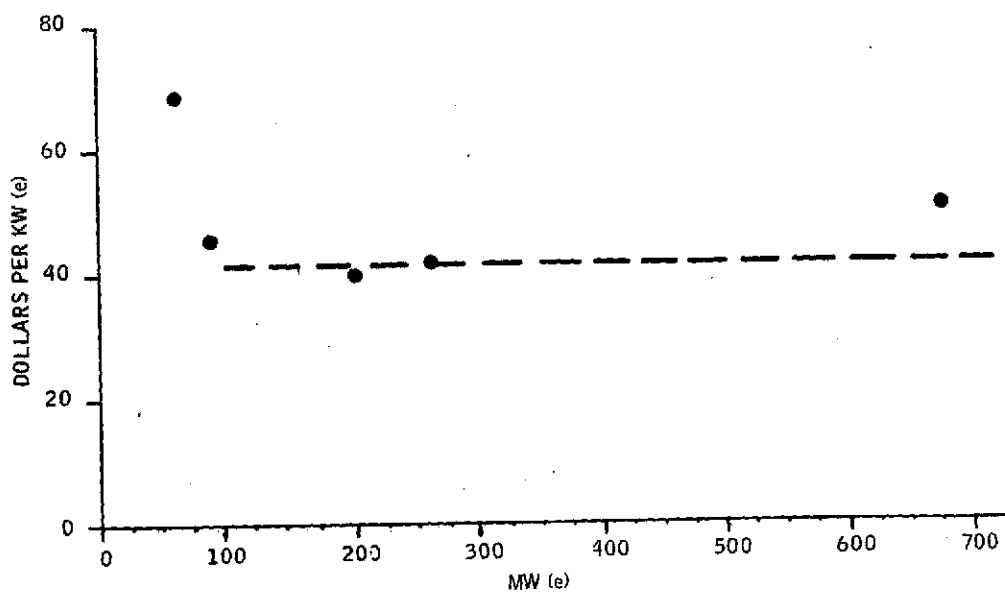
Figure A-2. Costs as a Function of Installed Capacity

STEAM GENERATOR

Based on steam generators currently in use, a cost of $16/Kw(e) was used in pricing the solar plant steam generator. The Kw(e) number is the turbine generator nameplate capacity.

LAND

The land area required for the collectors and steam turbine generator components was estimated at $800 per acre.

ENERGY TRANSPORT SYSTEM

Insulation

The type of insulation used depends on the maximum temperature of the pipe, price of the insulation, and the amount needed. Three insulation materials were investigated in detail: calcium silicate; mineral wool; and fiberglass. The distributed system uses calcium silicate, but the properties and costs of all three are given for completeness.

Calcium Silicate -- Calcium silicate is the standard insulation used in power plant piping. The type being considered is Thermo-12, made by the Johns-Manville Company. Thermo-12 is a rigid, white, hydrous calcium silicate insulation molded into sections. It does not contain asbestos. The temperature limit is 1500°F.

Pipe insulation is a solid, hollow cylinder whose inner and outer radii are r_1 and r_2, respectively. The equation for the temperature profile through the insulation is:

$$T_r = \frac{T_1 \ln (r_2/r) + T_2 \ln (r_1/r)}{\ln (r_2/r_1)}$$

where T_1 and T_2 are the temperatures at r_1 and r_2. Since the thermal conductivity of the insulation is a function of temperature, the heat flow per unit length can be determined by an integration procedure. The thermal conductivity is shown as a function of temperature in Figure A-3.

The price for insulation includes the cost of the material, jacket, and installation. Installation price is assumed to be equal to the price of the insulation. Aluminum jackets 0.016-inch thick are recommended. The installed price is given in Table A-1.

Mineral Wool

Mineral wool is made of long-fibered spun material formed in flat units reinforced on one side with wire mesh. The type that was considered is Pres-Lok, made by the Keene Corporation. A typical analysis of the wool gives:

SiO_2	42 percent
Al_2O_3	12 percent
CaO	30 percent
MgO	8 percent
FeO	8 percent

232
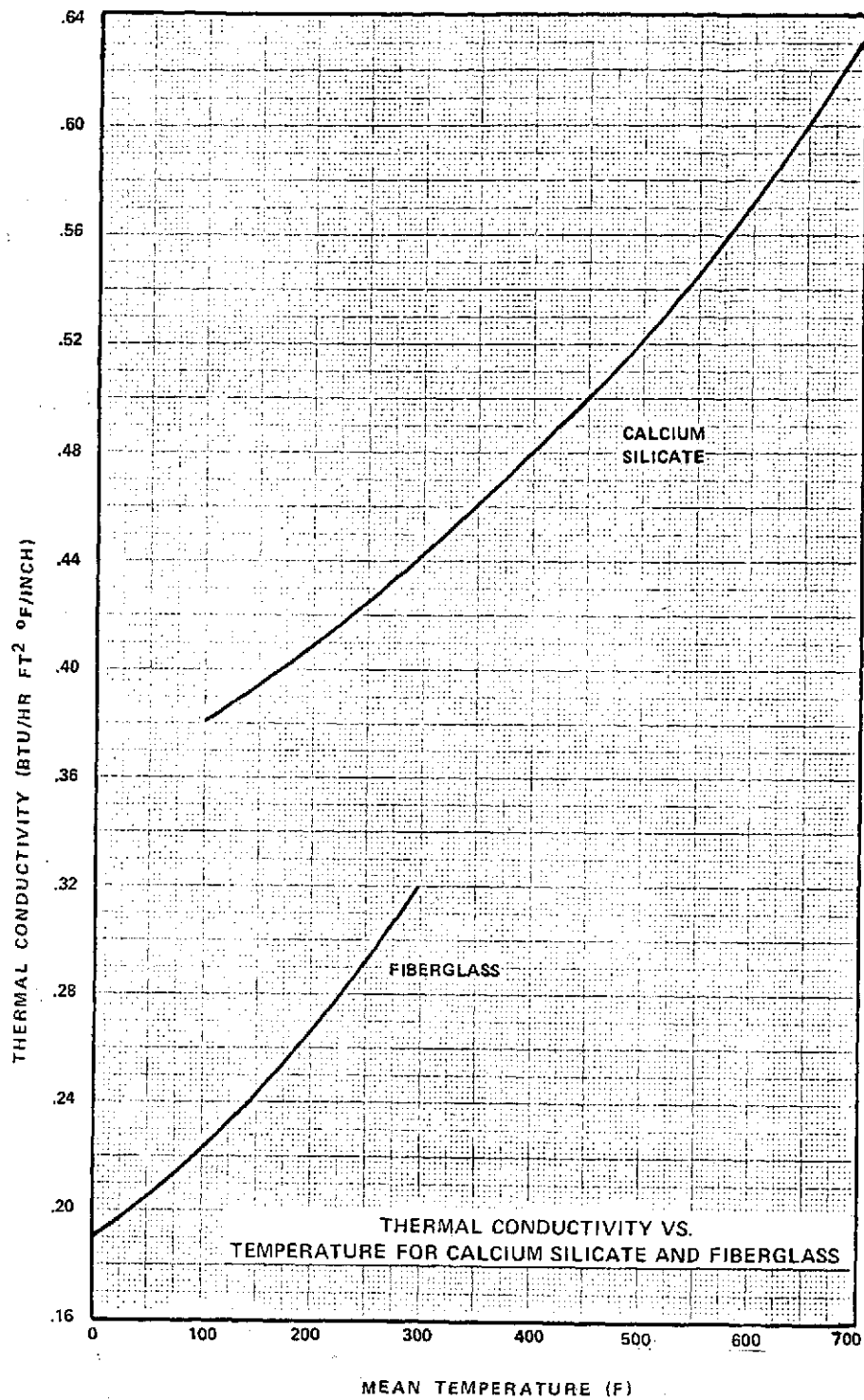
Figure A-3. Thermal Conductivity versus Mean Temperature

Table A-1. Calcium Silicate Insulation Price (Installed)

Pipe Size inches	Insulation Thickness Prices ($/100 feet installed)						
	One inch	1-1/2 inches	2 inches	2-1/2 inches	3 inches	3-1/2 inches	4 inches
1/2	142	217	303	352	409	577	725
1	158	234	328	377	458	614	770
1-1/2	176	258	364	409	503	651	806
2	188	278	377	423	528	671	827
2-1/2	205	303	405	454	561	700	859
3	221	311	426	491	597	745	917
3-1/2	241	335	458	536	642	781	949
4	266	348	483	573	679	843	1011
5	297	384	540	655	765	912	1131
6	319	401	556	704	822	992	1207
8	409	482	650	807	973	1179	1404
10	462*	586	788	970	1146	1404	1651
12	545*	675	912	1096	1295	1563	1823
14	618*	765	998	1221	1428	1675	1944
16	728*	864	1108	1343	1575	1841	2134
18	811*	950	1206	1460	1716	2011	2305
20	893*	1029	1322	1580	1838	2154	2473
22	970*	1075*	1420	1698	1981	2217*	2545*
24	1064*	1142*	1489	1738*	2042*	2370*	2686*

* Based on Owens/Corning Fiberglass Prices.

It does not contain asbestos. The temperature limit is 1200°F. The thermal conductivity is presented in Figure A-4.

Mineral wool is light weight, moisture resistant, and noncombustible. It is recommended for use only on pipes equal to or greater than 4 inches. Smaller pipes should be insulated with calcium silicate.

The prices listed in Table A-2 for mineral wool include a 0.016-inch aluminum jacket and installation. Prices for pipes below 4 inches in diameter are for calcium silicate.
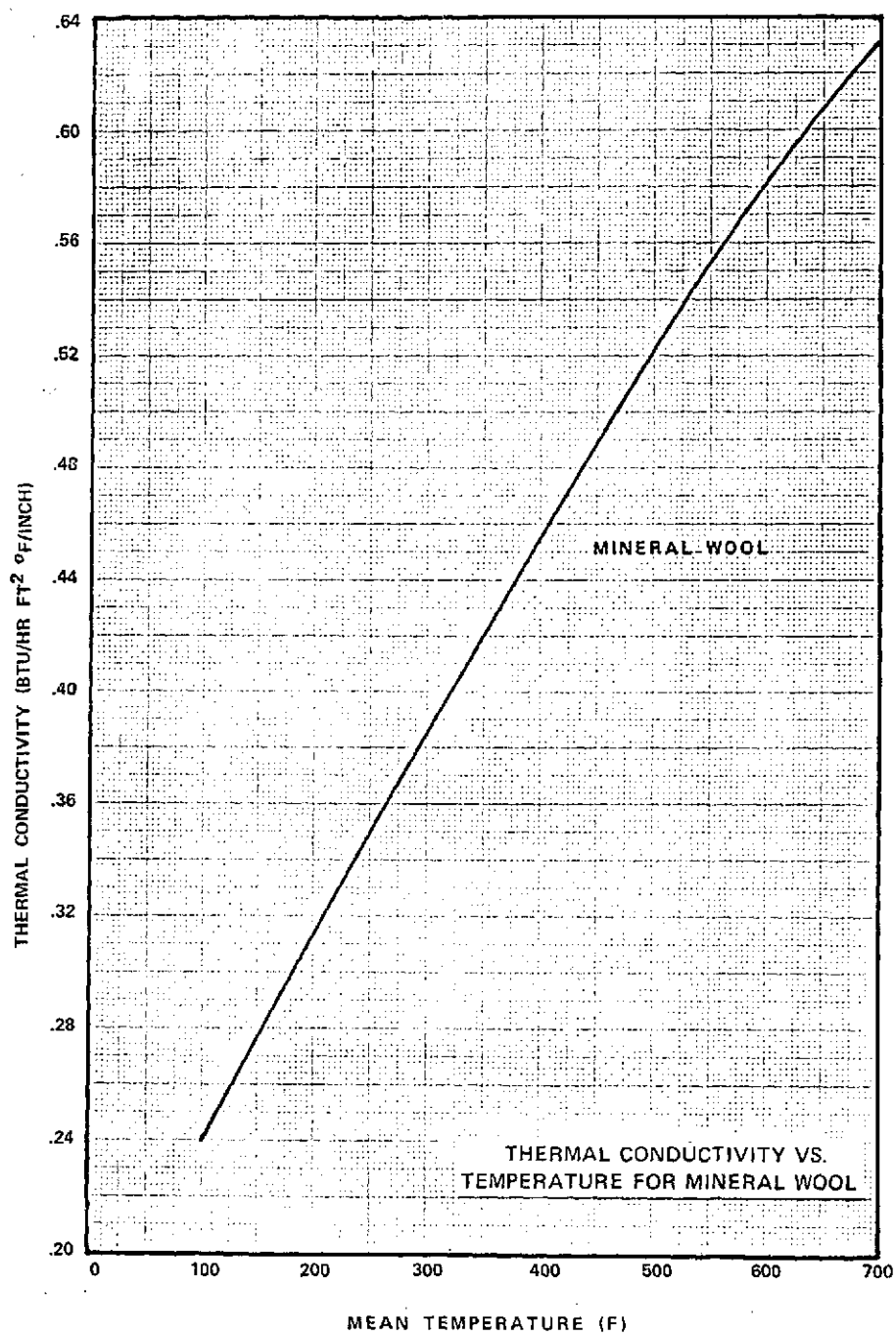
Figure A-4. Thermal Conductivity versus Temperature
            for Mineral Wool

Table A-2. Mineral Wool Insulation Price (Installed)

Pipe Size inches	Insulation Thickness Prices ($/100 feet Installed)						
	One inch	1-1/2 inches	2 inches	2-1/2 inches	3 inches	3-1/2 inches	4 inches
1/2							
1							
1-1/2							
2							
2-1/2		Use Prices for Calcium Silicate Insulation					
3							
3-1/2							
4	271	355	494	587	694	863	1036
5	304	393	553	669	783	934	1153
6	325	409	569	719	843	1012	1233
8	417	491	666	821	992	1202	1431
10	*	595	803	988	1168	1438	1689
12	*	683	927	1121	1321	1601	1867
14	*	781	1021	1250	1463	1719	1995
16	*	883	1134	1376	1614	1889	2191
18	*	970	1234	1495	1759	2063	2367
20	*	1067	1353	1619	1885	2210	2539
22	*	1137	1453	1741	2032	2372	2726
24	*	1028	1524	1851	2181	2535	2877

* Prices unavailable.

Fiberglass

Fiberglass pipe insulation is made from long, fine, flame-attenuated glass fibers, bonded with a thermosetting resin. The type that was considered is Metal-Lok, made by the Johns-Manville Company. The temperature limit is 500°F, and the thermal conductivity is given in Figure A-3.

The prices listed for the fiberglass in Table A-3 include a 0.016-inch aluminum jacket and installation. Where double-layer insulation is required, only one jacket is purchased.

Table A-3. Fiberglass Insulation Prices

Pipe Size inches	Insulation Thickness Prices ($/100 feet installed)						
	One inch	1-1/2 inches	2 inches	2-1/2 inches	3 inches	3-1/2 inches	4 inches
1/2	141	195	247	331	392	515	*
1	150	209	270	348	437	545	*
1-1/2	163	227	317	381	473	588	715
2	173	241	326	398	501	622	726
2-1/2	185	269	330	427	515	636	744
3	197	275	364	450	535	668	801
3-1/2	221	294	392	477	591	726	865
4	240	304	411	499	602	752	887
5	265	334	455	558	666	801	1002
6	283	347	480	596	743	903	1059
8	365	424	558	697	930	1031	1221
10	424	524	680	817	1070	1260	1441
12	508	587	777	934	1169	1361	1588
14	585	685	873	1035	1262	1490	1688
16	682	757	949	1136	1384	1615	1850
18	739	830	1028	1225	1507	1754	1992
20	807	890	1125	1329	1620	*	*
22	876	965	1203	*	*	*	*
24	954	*	*	*	*	*	*

* Prices unavailable.

PIPING

Data in Tables A-4 through A-11 were generated to estimate piping costs of a distributed collector field piping network. Costs are divided into unit costs for various sections, and tasks-to-be-performed for pipe installation. A typical branch header unit is shown in Figure A-5. Transportation of the unit by railroad cars limits the length of the unit to approximately 80 feet. As much as possible is shop-fabricated with expansion loops. Connecting pipes are field-installed.
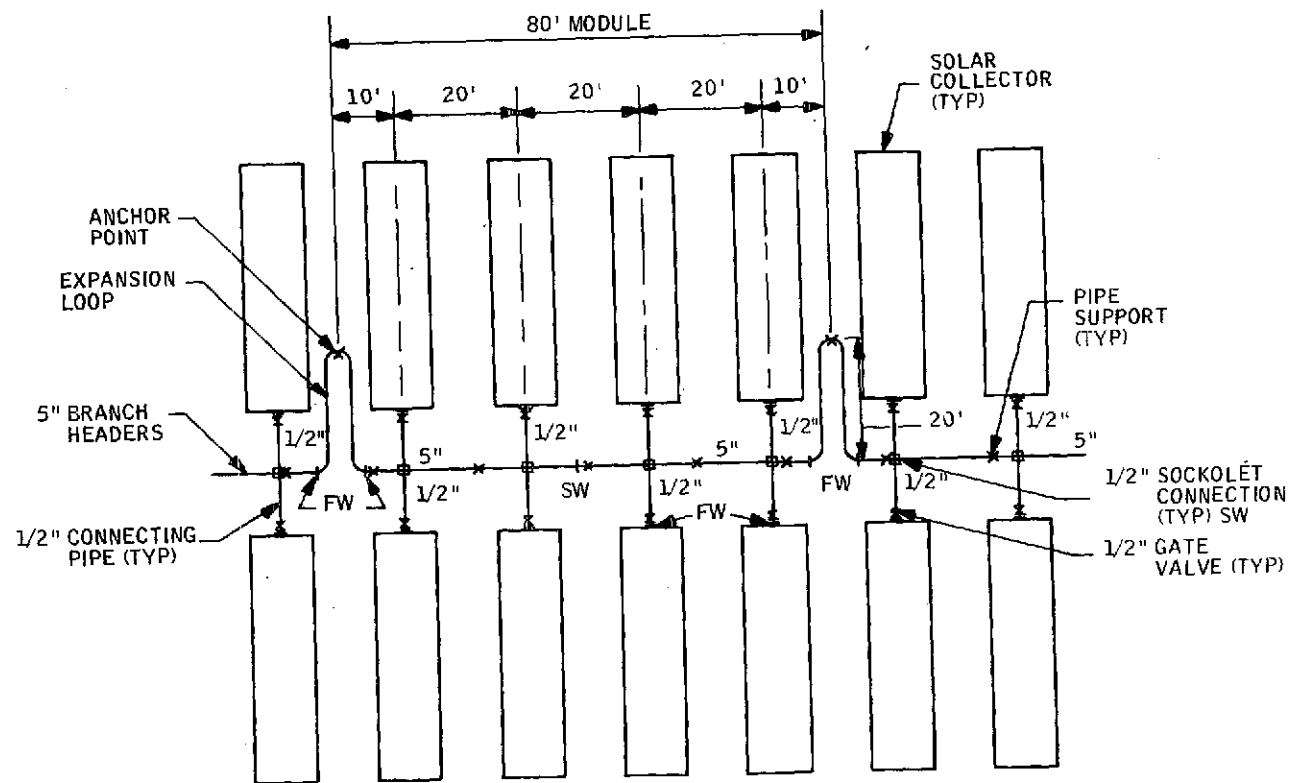
Figure A-5.   East-West Collector Configuration

Table A-4. Expansion Loop Lateral
Distance Specification

Size of Branch Header	Temperature	
	550°F (Concept No. 2)	625°F (Concept No. 3)
1/2 in.	8 ft.	9 ft.
1	9	10
1-1/2	11	12
2	12	13.5
2-1/2	13.5	15
3	15	16.5
3-1/2	16	17.5
4	17	18.5
5	18.5	21
6	20.5	22.5
8	23.0	26.0
10	26.0	29.0
12	28.0	31.5
14	29.5	33
16	31.5	35.5
18	33.5	37.5

Table A-5. Pipe Bending Cost

Nominal Pipe Size	Bending Labor Cost
2 in. and smaller	$113
2-1/2	137
3	164
4	208
6	315
8	460
10	584
12	779

Table A-6. Piping Material Costs

Nominal Pipe Size	Pool-Boiling (1100 psia)		Pressurized Water (2000 psia)	
	Pipe Schedule	Material Cost	Pipe Schedule	Material Cost
1/2 in.	40	$ 0.40	80	$ 0.46
1		0.55		0.65
1-1/2		0.75		1.01
2		0.82		1.17
2-1/2		1.28		1.75
3		1.60		2.24
3-1/2		1.92		2.70
4		2.20	120	4.14
5		3.08		6.07
6	60	5.50		7.90
8		7.20		15.02
10		11.36		22.08
12		15.48		31.04
14		21.14		37.47
16		26.73		47.84
18		33.82	120	59.78
20		40.75	---	---
22		45.00	---	---
24		47.01	---	---

Table A-7. Shop Welding Costs

Size Pipe	Cost/Weld		Size Pipe	Cost/Weld	
	1100 psia Pipe	2000 psia Pipe		1100 psia Pipe	2000 psia Pipe
1/2	15	15	5	40	66
1	17	17	6	56	80
1-1/2	20	20	8	56	112
2	24	24	10	69	145
2-1/2	27	31	12	92	221
3	30	35	14	120	276
3-1/2	33	41	16	150	354
4	35	53	18	196	434

Table A-8. Support Costs

Size of Branch Header (inches)	Approximate Spacing Between Supports (feet)	Concrete		Steel		Total
		Material	Labor	Material	Labor	
1/2	5	$7.00	$7.00	31.35	22.80	68.15
1	7	7.00	7.00	31.35	22.80	68.15
1-1/2	9	7.00	7.00	31.85	22.80	68.65
2	10	7.00	7.00	31.85	22.80	68.65
2-1/2	11	7.00	7.00	32.30	23.75	70.05
3	12	7.00	7.00	32.80	23.75	70.55
3-1/2	13	7.00	7.00	32.80	23.75	70.55
4	14	7.00	7.00	33.25	24.70	71.95
5	16	7.00	7.00	33.75	24.70	72.45
6	17	7.00	7.00	37.05	24.70	75.75
8	19	7.00	7.00	38.50	24.70	77.20
10	22	7.00	7.00	44.85	25.65	84.50
12	23	7.00	7.00	46.75	25.65	86.40
14	25	7.00	7.00	50.75	26.60	91.35
16	26	7.00	7.00	52.45	27.55	94.00
18	28	7.00	7.00	70.30	28.50	112.80
20	29	7.00	7.00	77.00	29.50	120.50
22	31	7.00	7.00	85.00	30.50	129.50
24	32	7.00	7.00	95.00	31.50	140.50

Table A-9. Handling Costs

Size of Pipe to be Handled	Cost/ft.		Size of Pipe to be Handled	Cost/ft.	
	System No. 2 (1100 psia)	System No. 3 (2000 psia)		System No. 2 (1100 psia)	System No. 3 (2000 psia)
1/2 in.	$ 6.25(40)	$ 6.25(80)	5	$ 7.90(40)	$ 8.20(120)
1	6.50(40)	6.50(80)	6	8.10(60)	8.35(120)
1-1/2	6.75(40)	7.00(80)	8	8.25(60)	8.60(120)
2	7.00(40)	7.00(80)	10	8.50(60)	9.00(120)
2-1/2	7.25(40)	7.40(80)	12	8.75(60)	9.50(120)
3	7.40(40)	7.70(80)	14	9.25(60)	10.00(120)
3-1/2	7.60(40)	7.90(80)	16	9.75(60)	10.60(120)
4	7.80(40)	8.00(120)	18	10.60(60)	11.50(120)

Table A-10. Field Weld Cost

Size of Pipe to be Welded	Cost	
	1100 psia	2000 psia
1/2 in.	$ 25.(40)	$ 25.(80)
1	37.(40)	37.(80)
1-1/2	49.(40)	49.(80)
2	57.(40)	57.(80)
2-1/2	34.(40)	35.(80)
3	37.(40)	41.(80)
3-1/2	41.(40)	46.(80)
4	44.(40)	60.(120)
5	53.(40)	79.(120)
6	63.(60)	100.(120)
8	75.(60)	143.(120)
10	94.(60)	198.(120)
12	126.(60)	303.(120)
14	169.(60)	390.(120)
16	223.(60)	498.(120)
18	275.(60)	612.(120)

Table A-11. 2000 psi Pressurized Water Pipe Costs for an 80 ft. Branch Header

Nominal Pipe Diameter (in.)	Straight Pipe Material ($)	Expansion Loop ($)	Middle Shop Weld ($)	Field Welds (2/line) ($)	Handling and Testing ($)	Pipe Supports ($)	Subtotal ($)	Tees or Sockolets (6/line) ($)	Total ($)
1/2	73.60	243.20	30.00	100.00	1236.26	1089.60	2772.66	238.80	3011.46
1	104.00	254.40	34.00	148.00	1322.40	779.20	2643.00	277.62	2920.62
1-1/2	161.60	280.00	40.00	196.00	1440.46	609.60	2727.66	313.62	3041.28
2	187.20	305.60	48.00	228.00	1548.40	548.80	2866.00	129.84	2995.84
2-1/2	280.00	395.20	62.00	140.00	1894.60	508.80	3180.60	129.84	3310.44
3	358.40	499.20	70.00	164.00	1823.36	470.40	3385.36	129.84	3515.20
3-1/2	432.00	592.00	82.00	184.00	1914.96	433.60	3638.56	129.84	3768.40
4	662.40	780.80	106.00	240.00	1984.60	411.20	4186.00	129.84	4315.84
5	971.20	1134.40	132.00	316.00	2146.76	361.60	5061.96	129.84	5191.80
6	1264.00	1510.40	160.00	400.00	2266.20	356.80	5957.40	129.84	6087.24
8	2403.20	2910.40	224.00	572.00	2516.36	324.80	8950.76	129.84	9080.60
10	3532.80	4516.80	290.00	792.00	2804.40	307.20	12243.20	129.84	12373.04
12	4966.40	6796.80	442.00	1212.00	3123.60	300.80	16841.60	129.84	16971.44
14	5995.20	8480.00	552.00	1560.00	3420.00	291.20	20298.40	129.84	20428.24
16	7654.40	11680.00	708.00	1992.00	3805.40	289.60	26129.40	129.84	26259.24
18	9564.80	14880.00	868.00	2448.00	4303.30	321.60	32385.70	129.84	32515.54

Expansion Loops

An expansion U-bend is used approximately every 80 feet in the piping network. The expansion loop is shown in Figure A-6.
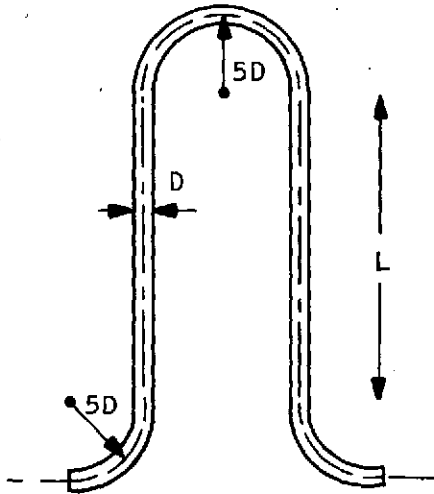

Figure A-6. Expansion Loop

The lateral distance L, required from the branch header, is tabulated in Table A-4 for two operating temperatures.

The cost of an expansion loop is based on a material charge and a bending charge. The material charge is found by multiplying the required length of piping by the material cost per foot. The required length of piping is based on the length, L, and a bending radius of 5 nominal pipe diameters.

$$\text{Length} = 2L + 10D (\pi - 1)$$

The charge for bending the pipe is taken from March 1, 1973 unit price schedules of Southwest Fabricating and Welding Co. These charges are shown in Table A-5.

Costs beyond the table range are extrapolated as needed. The material costs per foot are shown in Table A-6.

Material

The charge for piping material is dependent upon the pipe size and pipe schedule required. The pressure-temperature range, pool-boiling and pressurized water systems were used to determine the pipe schedule required for the cases of Table A-6. These costs are for seamless carbon steel pipe to specification ASTM A-106, Grade B, as of January 1, 1974.

Normally, production runs of carbon steel piping are made in roughly 40-foot lengths. It has been assumed that a shop weld is necessary to bring the length to 80 feet. The price for shop welding is given in Table A-7, as taken from Southwest Fabricating and Welding Co. price schedules.

Pipe Supports

Pipe supports are installed so that branch headers are raised approximately 2 feet above the ground. Since the hot and cold branch headers run next to each other, each support stand can hold both pipe lines (Figure A-7).
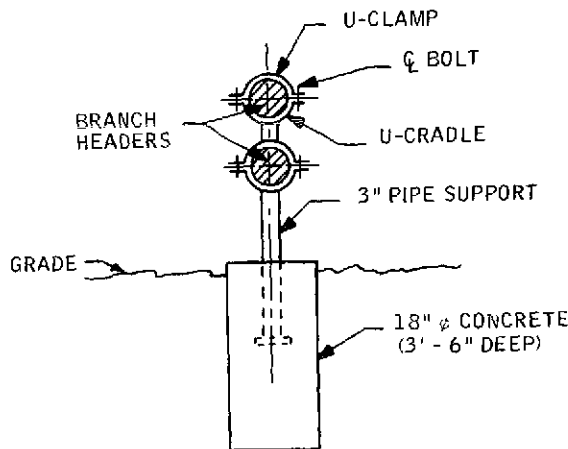

Figure A-7. Pipe Support Concept

The labor and material costs of the supports, along with the spacing between supports, are given in Table A-8 as a function of the size of branch header.

Handling

Handling costs are charged for the labor to move the piping into position and to test completed unit modules. The handling includes the straight pipe and expansion loops lengths. The costs of handling are given in Table A-9 in dollars per foot. The pipe schedule is added parenthetically.

Welds

The cost of field welds as a function of pipe size is given in Table A-10. It is assumed that straight pipe sections are shipped in approximately 80-foot lengths such that welds are required at each end of the section connecting with the expansion loop. When the pipe size changes from one section to the next, an additional weld is charged for the adaptive contraction or expansion pipe. The welds are socket welds for pipe sizes below 2 inches, and butt welds for pipes greater than 2 inches in diameter.

Total Charges Without Connection Pipes

The unit costs of Tables A-4 through A-10 can be used to generate the cost of an 80-foot, installed pipe section. These are shown in Table A-11 for the 2000 psi pressurized-water system concept. The costs of tees or sockolets is added, assuming there are six collectors per 80-foot section. For 1/2-inch connecting pipes, tees will be required for branch headers less than 2 inches. The cost of the tee, shop welded into the branch header line, is estimated below:

| Pipe Diameter	Cost/Tee
1/2 in.	$39.80
1	46.27
1-1/2	52.27

The cost of sockolets is estimated at $21.64 each (includes material, weld and drilled hole), as taken from Southwest Fabricating Co. price schedules.

Table A-9. Handling Costs

Size Of Pipe To Be Handled	Cost/ft.	
	System No. 2 (1100 psia)	System No. 3 (2000 psia)
1/2"	$ 6.25(40)	$ 6.25(80)
1	6.50(40)	6.50(80)
1-1/2	6.75(40)	7.00(80)
2	7.00(40)	7.00(80)
2-1/2	7.25(40)	7.40(80)
3	7.40(40)	7.70(80)
3-1/2	7.60(40)	7.90(80)
4	7.80(40)	8.00(120)
5	7.90(40)	8.20(120)
6	8.10(60)	8.35(120)
8	8.25(60)	8.60(120)
10	8.50(60)	9.00(120)
12	8.75(60)	9.50(120)
14	9.25(60)	10.00(120)
16	9.75(60)	10.60(120)
18	10.50(60)	11.50(120)

Connecting Pipe

The piping which connects the collector to the branch header must be bent in some cases. The material costs of the connecting pipe is found by adding the straight pipe material cost to the cost of bending the pipe. The bending charge is based on a "budgetary" estimate obtained by Black & Veatch for bending 1/2-inch carbon steel, schedule-40 pipe. (See sketch below.)
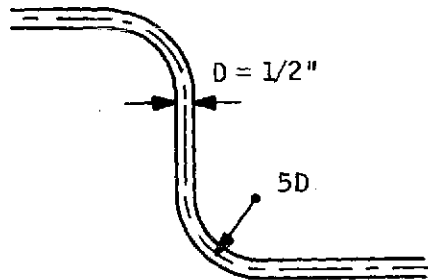
The cost-per-bend estimate is $26.

The length of connecting pipe and the number of bends required is determined by the collector type, orientation and spacing. The following procedure is used to estimate these parameters:

a) **North-south or east-west trough collector:**

From a side view, the piping required to connect the collector to branch header looks like that shown in Figure A-8.

The distance X is determined by the collector spacing as,

$$X = Lc/2-20,$$

where Lc is the length of the spacing rectangle surrounding the collector (Figure A-9).

Since the vertical distance between the branch header and collector is uncertain at this time, it has been estimated at two feet. One bend is needed for each connecting pipe when the connections are over 5 feet from the branch header. The connection is assumed to be made to a shop-fabricated connection joint after the shut-off valve. The connection joint is assumed to be a part of the collector fabrication.

b) **Polar trough collector:**

The polar trough collector is assumed to be mounted at a 33-degree angle to the ground. The piping required connecting pressurized water is the same as for the east-west or north-south mounted trough for one collector. An additional ($40 \cos 33°$) foot of pipe length is required to run under the collector south of the branch header. For the water-steam case, it may be necessary to connect the elevated end of the collector. The necessary pipe length is added and supports and bends are included as required.
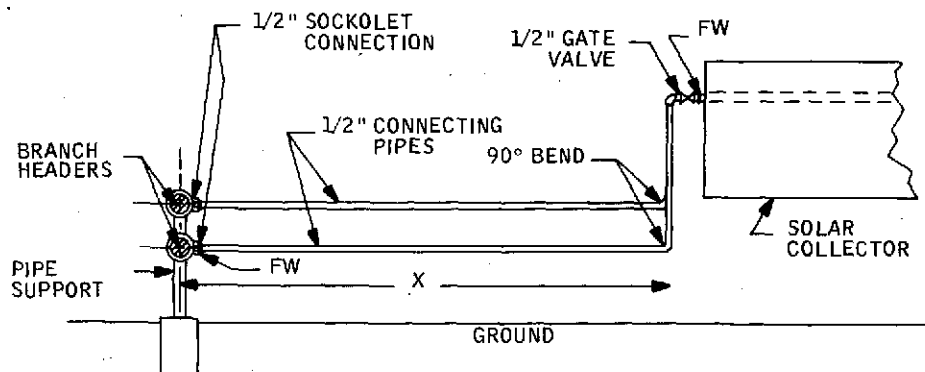
246
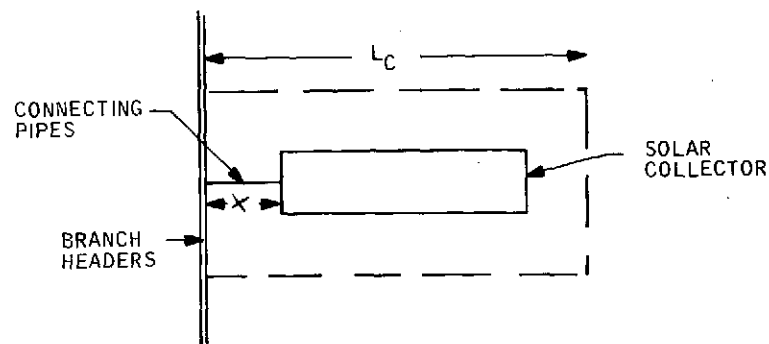
Figure A-8. Piping, Side View

Figure A-9. Determination of Distance X

c) Dish collector

From a side-view, the assumed piping needed to connect the branch header to the dish collector looks like Figure A-10.
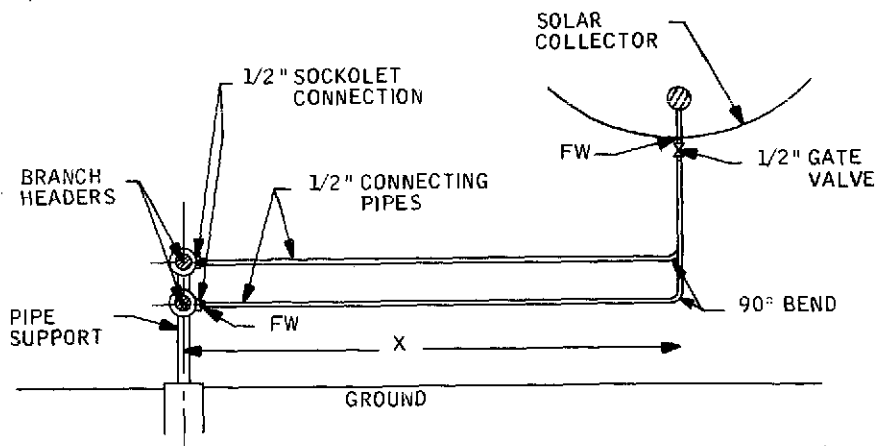

Figure A-10. Dish Collector Piping

The distance X is determined by the collector spacing to be,

$$X = Lc/2,$$

where Lc is defined as before. A vertical pipe run of two feet was again used and one bend per connecting pipe is assumed for connections longer than five feet.

For all collectors, the shut-off valves have been costed at $12 for the 1100 psi water-steam concept, and $72.50 for the 2000 psi pressurized water concept.

SOLAR COLLECTORS

Collector costs are given in Sections VI and X.

APPENDIX B

THERMAL CYCLE CALCULATIONS

The trough or dish collector distributed systems candidates use standard steam turbine-generator power plant equipment. By surveying a number of available units, a method for obtaining reliable turbine-generator/heat rejection system efficiency was developed. For pressurized water system concepts, a method for computing the heat exchanger temperature requirements was formulated. This appendix documents the methods and gives example results for varying turbine inlet conditions and feedwater temperature ratios.

A thermal cycle has a theoretical net heat rate, calculated as follows. From the turbine throttle inlet temperature and pressure, the inlet enthalpy (h_o) and entropy are obtained.

The steam is then assumed to expand isentropically until the condenser pressure is reached. From the condenser pressure and the entropy, the enthalpy of the exhaust steam/water mixture (h_s) is found. The difference between the original enthalpy and this new enthalpy

is the maximum amount of heat which can be extracted in the thermal cycle and theoretically converted to useful work. The entropy and enthalpy of the feed water leaving the condenser are quite different from the turbine exhaust conditions. From the actual temperature and pressure in the condenser, the enthalpy (h_a) of the feed water is found. The difference

between the original inlet enthalpy and this feed water enthalpy is the heat which must be added to the fluid in the cycle. The quotient of the actual heat added divided by the maximum possible heat extracted as work is now multiplied by the conversion factor of 3413 Btu/Kwh. The result is the theoretical heat rate (THR) for the particular thermal cycle.

$$THR = 3413 \frac{h_o - h_a}{h_o - h_s}$$

Efficiency is simply defined as the inverse of the heat rate divided by 3413.

A number of turbines for which the net heat rates are known were compared with their theoretical heat rates. The results are shown in Figure B-1. All of the units surveyed for this figure have a feedwater temperature ratio (FTR) of 0.8.

It can be seen that, except for small units, the ratio of net heat rate to theoretical net heat rate is independent of size. All the points are plotted for valves wide open and a condenser pressure of 2 inches of mercury.

For solar power plants the final feedwater temperature ratio optimal may not be the same as for conventional plants. To provide the capability to vary the feedwater temperature ratio, an analysis of small units which use little or no regenerative feedwater heating was performed. A correlation was found between final feedwater temperature and net turbine-generator heat rate. The feedwater temperature ratio (FTR) is calculated as:

$$FTR = \frac{T_{FF} - T_c}{T_{IN} - T_c}$$

where

T_{FF} = final feedwater temperature, i.e., temperature following last regenerative heater, if any

T_c = saturation temperature at condenser pressure

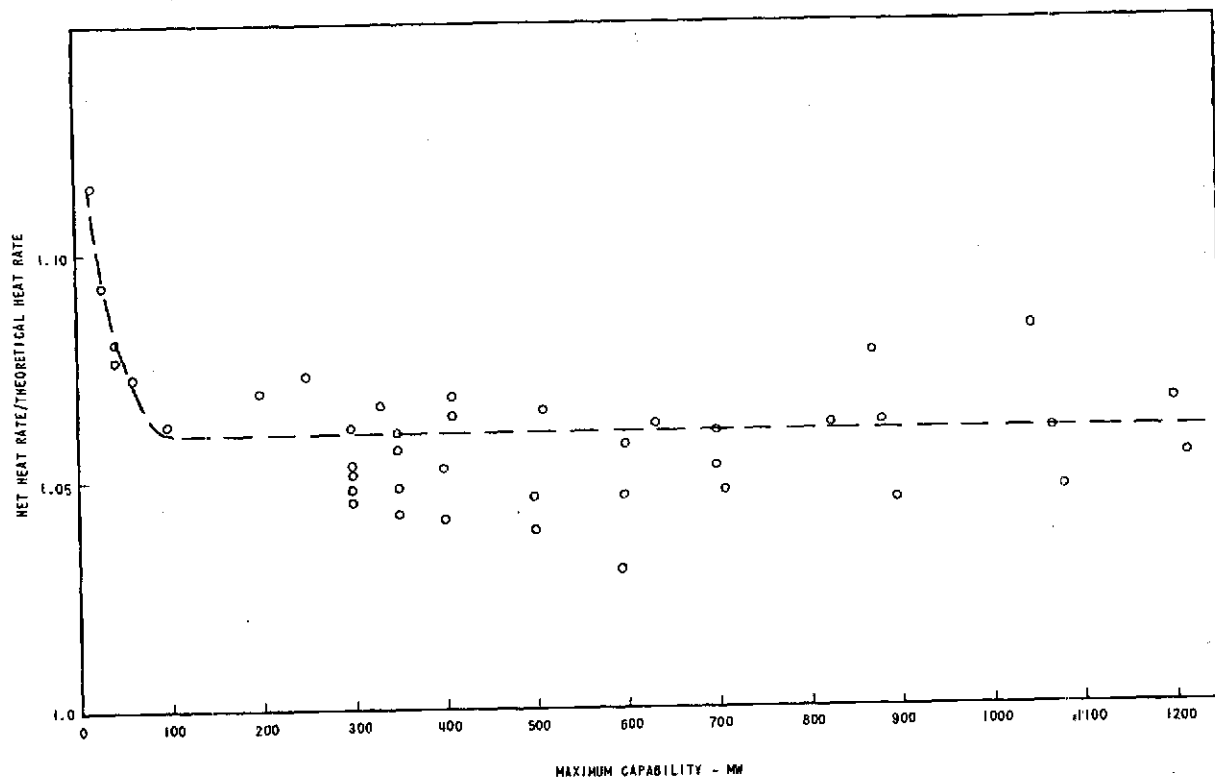T_{IN} = saturation temperature at turbine inlet pressure

Figure B-1. Variation of Net Turbine-Generator Heat Rate
with Unit Size for Conventional Power Plants
with FTR = 0.8

The ratio of net heat rate of theoretical heat rate is plotted versus FTR in Figure B-2. Figure B-2 was developed for turbine inlet conditions of 1000 psia and 500°F. The numbers are probably quite good for any cycle used in the pool boiling or pressurized water system concepts.

To determine the dependency of heat rate upon load and condenser pressure, a number of steam cycles were tabulated. It was found that these variations were highly consistent. The average values are shown in Figure B-3. The curves are normalized to valves wide open and 2 inches of mercury.

It was assumed that the cooling tower would be designed for a 13°F approach at a wet bulb of 76°F. With this assumption, it is possible to calculate the cooling tower approach at other flows and wet bulbs using performance curves prepared by the Marley Company. These other approaches are shown in Figure B-4.

It was assumed that the condenser would be designed for a back pressure of 3.5 inches of mercury at a circulating water temperature of 89°F. With this assumption, the condenser pressure at other flows and water temperatures were found using a condenser analysis program developed by Black & Veatch. These values are shown in Figure B-5.

Since the variation of heat rate with load is known, the throttle flows as a function of load can be calculated. These values were normalized to valves wide open.

The net heat rate can be calculated as follows:

1. Choose a wet bulb and load condition.

2. From Figure B-4, determine the cooling tower approach.

3. The sum of the wet bulb and the approach is the circulating water temperature.

4. From Figure B-5, determine the condenser pressure.

5. From Figure B-3, determine a multiplier.

6. Use Figure B-2 to determine another multiplier based on FTR.

7. For the thermal cycle in question, calculate the theoretical net heat rate as explained in the beginning of this appendix.

8. The desired net heat rate will be the product of the theoretical net heat rate with both multipliers.

As an example of the method, the results for efficiency versus turbine inlet temperature for saturated steam, steam with 50°F superheat, and steam with 350°F superheat are shown in Figures B-6, B-7, and B-8, respectively. The results shown are for valves wide open, a cooling tower approach of 13°F at a wet bulb of 76°F, and a back pressure, of 3.5 inches of mercury.

INLET AND OUTLET TEMPERATURES OF THE HEAT EXCHANGER

The heat exchanger required for the pressurized water system was modeled as the three separate heat exchangers shown in Figure B-9. (For saturated steam at turbine inlet, the superheater is not used.) An iteration scheme was devised to satisfy the first law of thermodynamics across each heat exchanger. The first law equations for each unit are as follows:
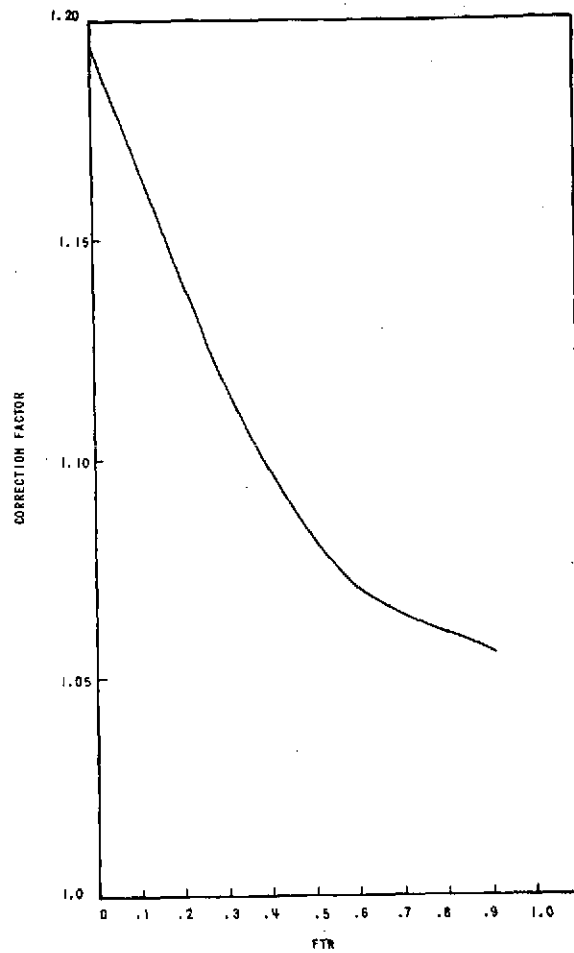
Figure B-2. Variation of Heat Rate Correction Factor with
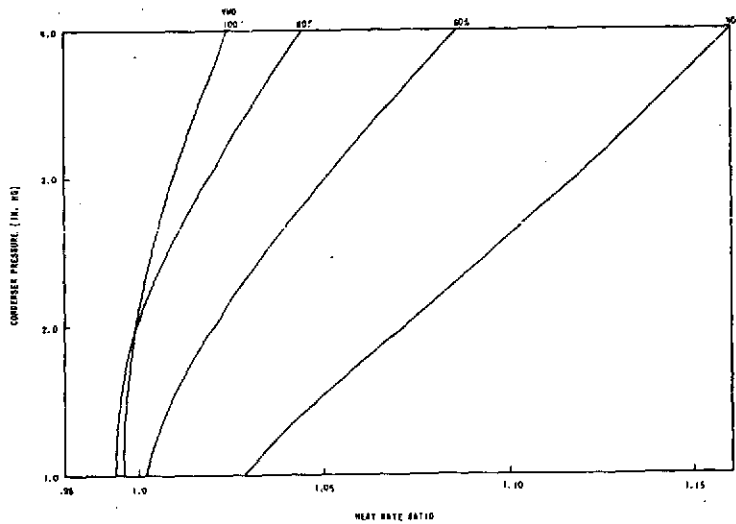Degree of Regenerative Feedwater Heating

Figure B-3. Variation of Heat Rate with Condenser Pressure
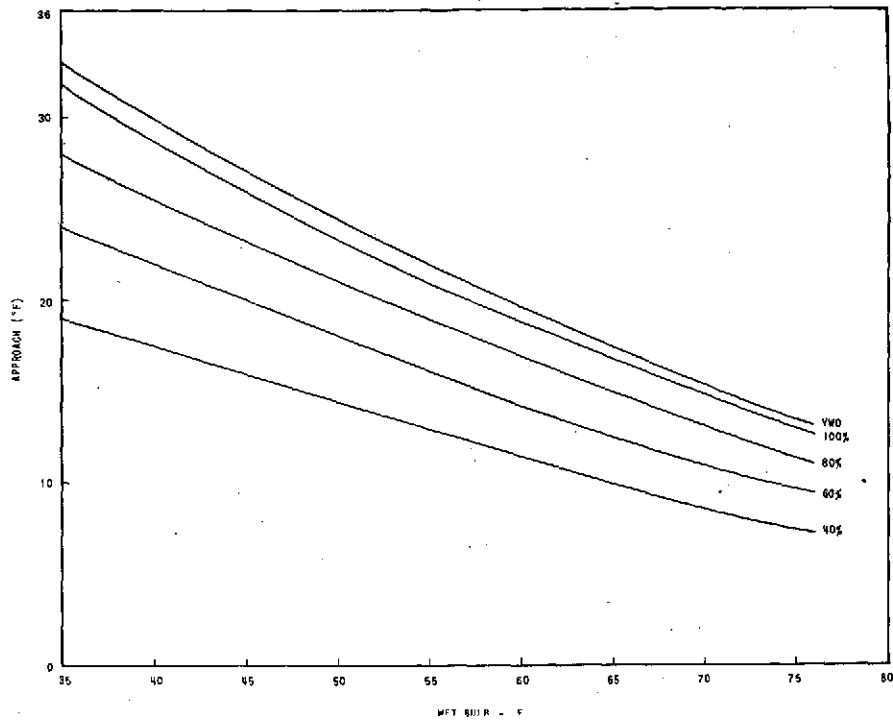for Various Throttle Flows

252

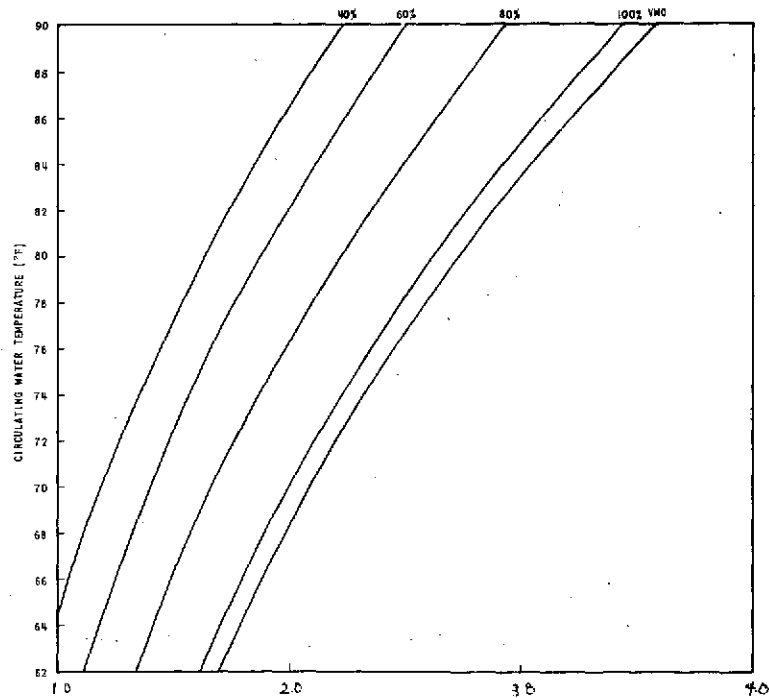Figure B-4. Variation of Cooling Tower with Wet Bulb for
Various Throttle Flows

Figure B-5. Variation of Condenser Pressure with Circulating
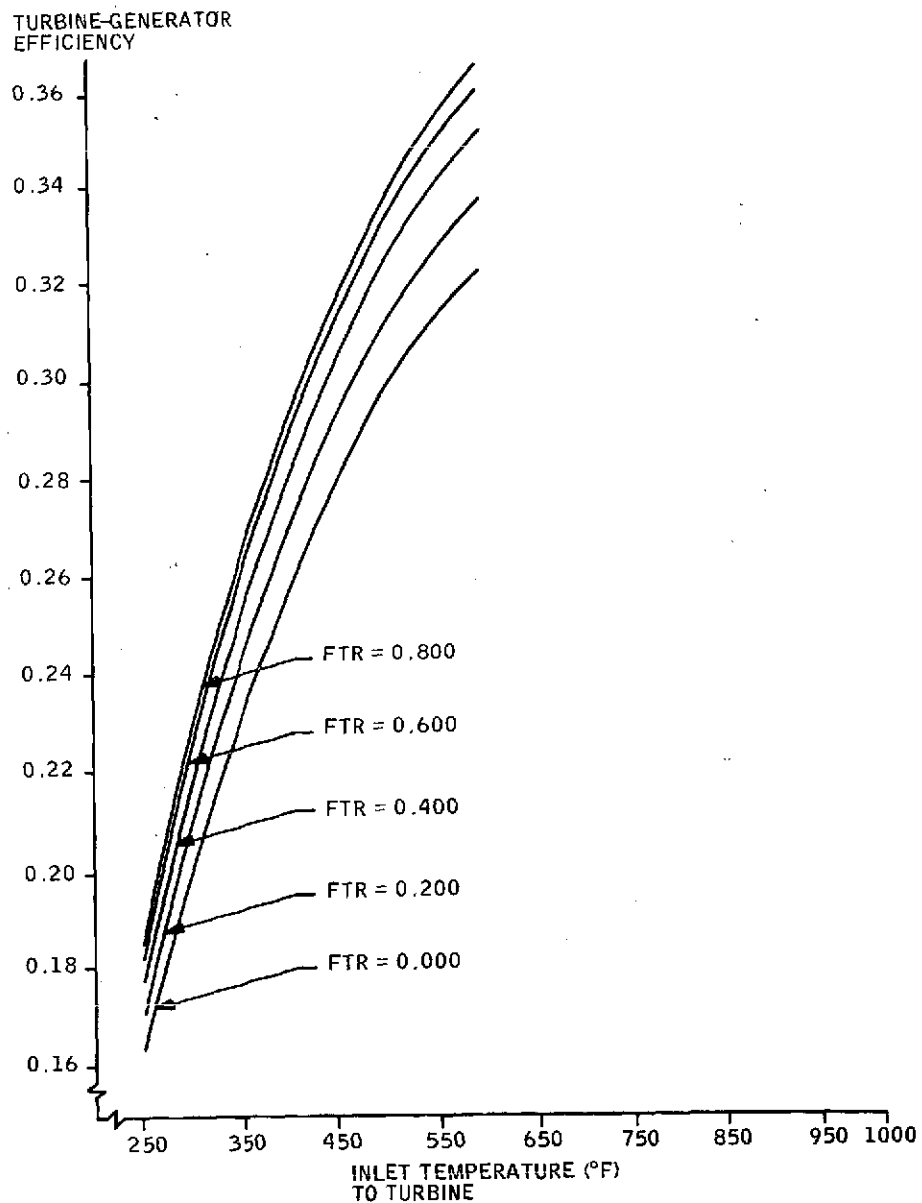Water Temperature for Various Throttle Flows

TURBINE-GENERATOR
EFFICIENCY

0.36

0.34

0.32

0.30

0.28

0.26

0.24   FTR = 0.800

0.22   FTR = 0.600

              FTR = 0.400

0.20   FTR = 0.200

0.18   FTR = 0.000

0.16

250   350   450   550   650   750   850   950 1000
              INLET TEMPERATURE (°F)
              TO TURBINE

Figure B6.   Turbine-Generator Efficiency for Saturated
             Steam Turbine Inlet Conditions
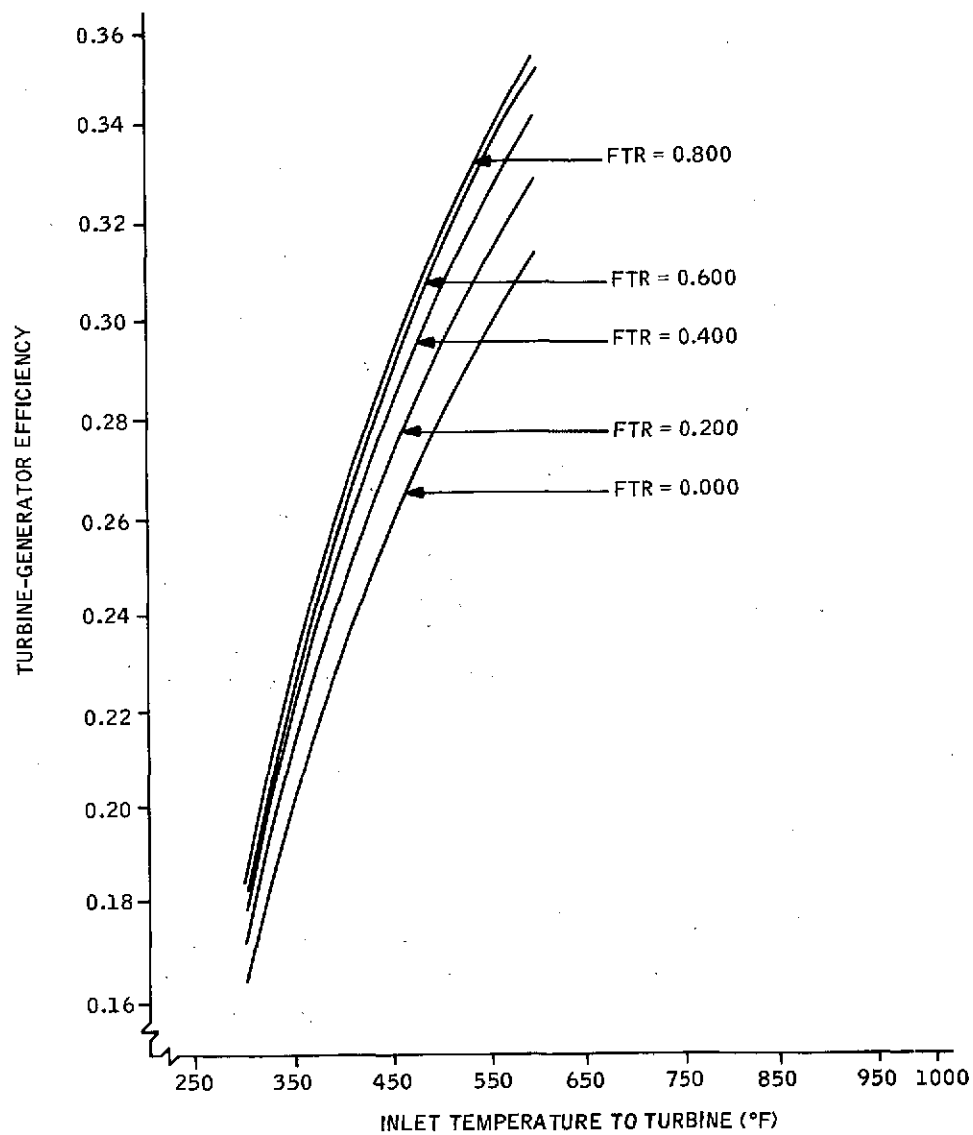
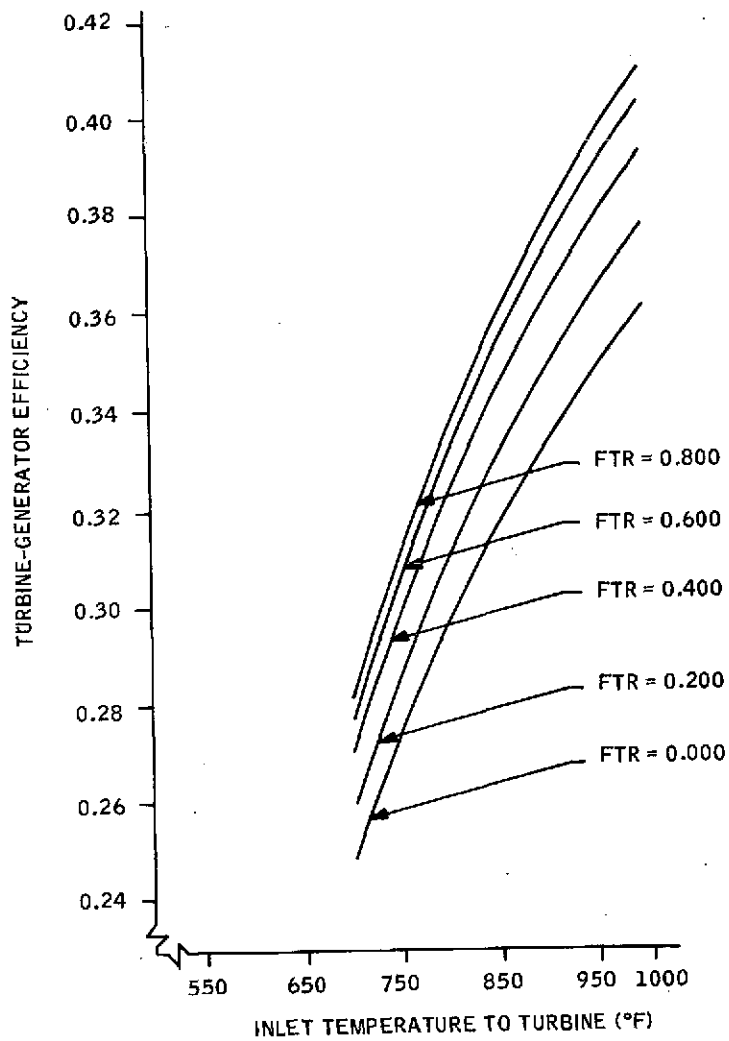Figure B7. Turbine-Generator Efficiency for 50°F Super-
Heated Steam Turbine Inlet Conditions

Figure B8. Turbine-Generator Efficiency for
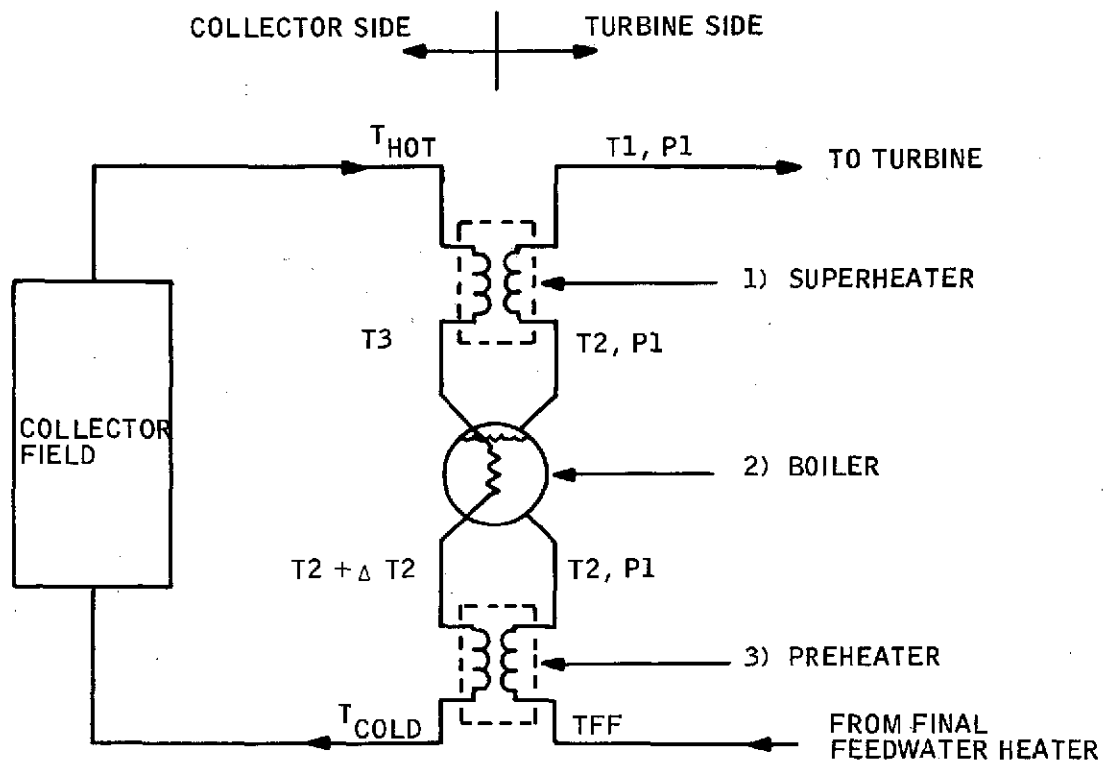350°F of Superheated Steam
Turbine Inlet Conditions

COLLECTOR SIDE   TURBINE SIDE

T_{HOT} T1, P1   TO TURBINE

COLLECTOR
FIELD

T3   T2, P1   1) SUPERHEATER

2) BOILER

$T2 + _\Delta T2$ T2, P1

3) PREHEATER

T_{COLD} TFF   FROM FINAL
                                 FEEDWATER HEATER

Figure B-9. Heat Exchanger Model

Preheater

$$h(T_2 + \Delta T_2) - h(T_{cold}) = \frac{\dot{m}T}{\dot{m}c} [h(T_2) - h(T_{FF})]$$

Boiler

$$h(T_3) - h(T_2 + \Delta T_2) = \frac{\dot{m}T}{\dot{m}c} [h_v(T_2)]$$

Superheater

$$h(T_{hot}) - h(T_3) = \frac{\dot{m}T}{\dot{m}c} [h(T_1) - h(T_2)]$$

where

$\dfrac{\dot{m}T}{\dot{m}c}$ = mass flow ratio of turbine fluid to collector fluid

$h(x)$ = specific enthalpy at x condition

$h_v(x)$ = specific heat of vaporization at x

The heat exchangers were assumed to have no heat losses. Approach (pinch-point) temperatures ΔT_1 and ΔT_2 were used as the driving forces in the superheater and boiler, respectively. As shown in Figure B-10, ΔT_1 minimum was 15°F and minimum ΔT_2 was 20°F.

For a given collector side fluid, turbine side fluid, mass flow ratio, and turbine conditions (i.e., T_1, P_1, and FTR), the heat exchanger inlet and outlet temperatures can be found. Sample results of these calculations are plotted in Figures B-11 through B-13. In each case, the collector fluid is pressurized water at 2000 psia. The heat exchanger inlet and outlet temperatures are plotted for various mass flow ratios as a function of turbine inlet temperatures.

Figure B-11 shows the heat exchanger inlet temperature for a turbine inlet with steam at 50°F superheat. It is noted that the heat exchanger inlet temperature is independent of the feedwater temperature ratio. However, the heat exchanger outlet temperature varies with the FTR. Figures B-12 and B-13 show the outlet temperature of the heat exchanger at feedwater temperature ratios of 0.8 and 0.0.
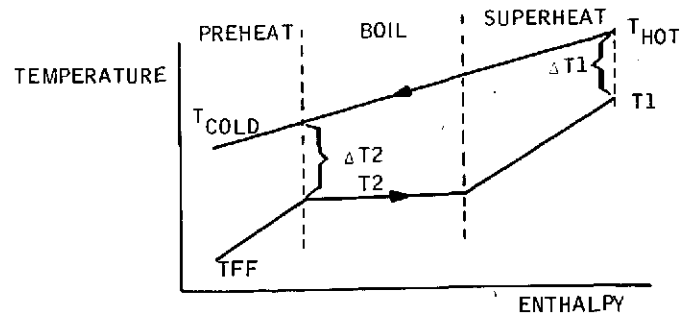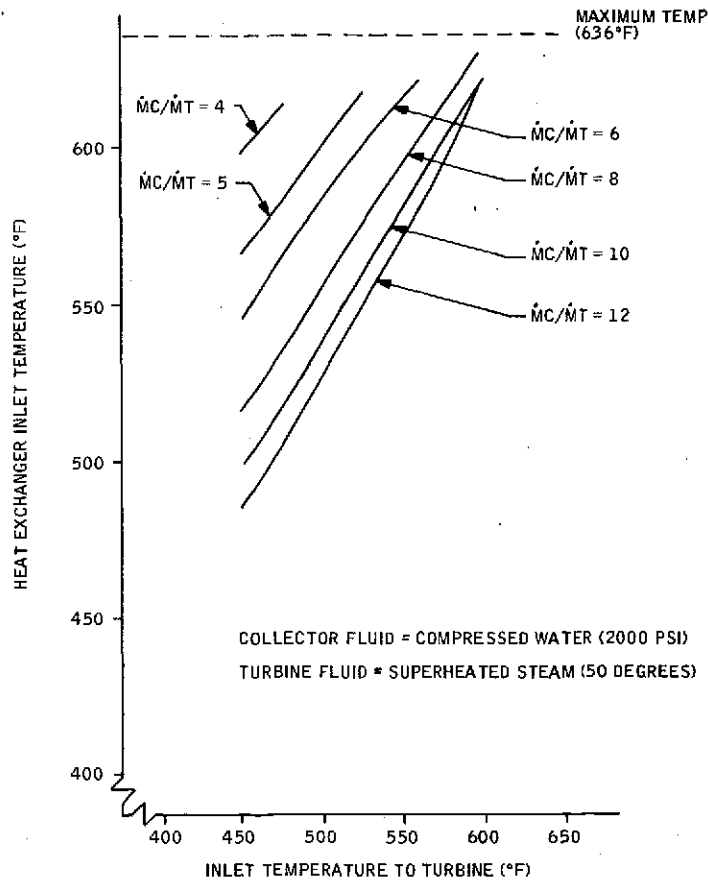
Figure B10. Heat Exchanger Parameters Definitions

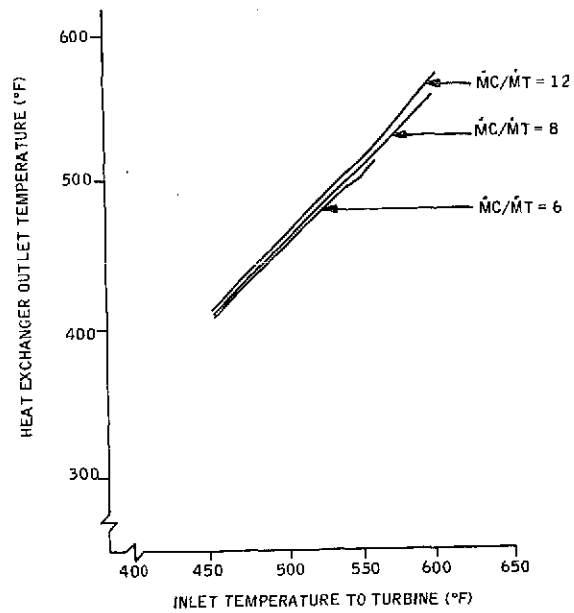Figure B11. Heat Exchanger Inlet Temperature Required
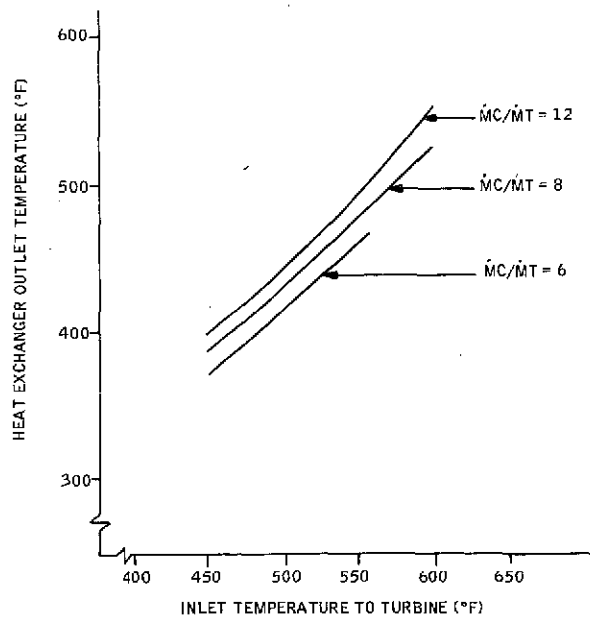
Figure B12. Heat Exchanger Outlet Temperature
for FTR = 0. 8

Figure B13. Heat Exchanger Outlet Temperature
for FTR = 0. 0

260

APPENDIX C

POWER TOWER SIMULATION CODE

A power tower simulation code (Heliak IV) was written to simulate the power tower optical/ thermal performance. This is a presentation of the methodology employed within this code. Basically the premise of the method is that the incident flux on the power tower receiver over the direct solar flux on the heliostat field is equal to the convergent ratio of randomly drawn rays which reach the receiver divided by the total number of rays drawn uniformly over the heliostat field with appropriate scaling of each ray value for reflectance and absorptance losses, etc.

The ray trace flow chart follows the physics of each interaction of the rays as they encounter or miss each surface (see Figure C-1). The first function block in the power tower code flow chart is the uniform draw of ray start points over the collector field. Specifically, points are drawn uniformly over an imaginary surface which covers the field of heliostats called the test plane. If the mirrors were allowed to assume all possible rotational attitudes, they could occupy all points within a sphere centered around the heliostat center. If all such spheres were bounded by planes tangent to the top and bottom of each sphere, the test plane would be the upper plane and the lower plane would be the ground plane. Figure C-2 shows an edge view of this. Once a ray start point is drawn, the trace of the ray from its start point on the test plane to its terminus on the ground plane can be found.

The unit vector $\overline{UR}$ is a unit vector along the ray path from the sun's center to the point on the earth's surface at which the solar plant is located. Variations in the direction of this ray with position on the field are not considered. This amounts to an error of approximately 1 minute of arc per mile of distance from the tower base. The heliostat field is assumed to be a flat plane tangent to the surface of the earth at the tower base. If this were exactly true, there would remain only a very small angular error due to the change in position of the heliostat relative to the earth's orbit plane (about 10^{-6} degrees per mile from the tower base).

Figure C-3 shows that only those heliostats which are "close" or "along" the ray trace from the test plane to the ground plane could be involved in redirecting the ray. It is important to limit the number of "hit tests" (subroutine HITUM) to be numerically performed on each ray to those heliostats which lie along the ray path. Clearly, if all (nominally 10^5) heliostats were tested for a hit for each ray drawn (nominally 10^5) the run time would be prohibitive. A simple algorithm performs the identification of the few (nominally 10^1) heliostats which can interact with the ray.

The identification algorithm (subroutine FINDIT) is based on two facts:

- The spheres of influence of the individual heliostats do not overlap each other.

- The heliostat center locations can be uniquely identified with an ordered pair of integers.

Consider a top view of the test plane with a typical ray path drawn (see Figure C-4). In this example heliostats (3, 2) and (1, 3) are the only possible units which could redirect the ray in question, depending on where the tower is relative to this point in the field.

The identification algorithm uses simple integer arithmetic to find the integer identification code of the closest heliostat to any point (x_p, y_p) on the ray path.
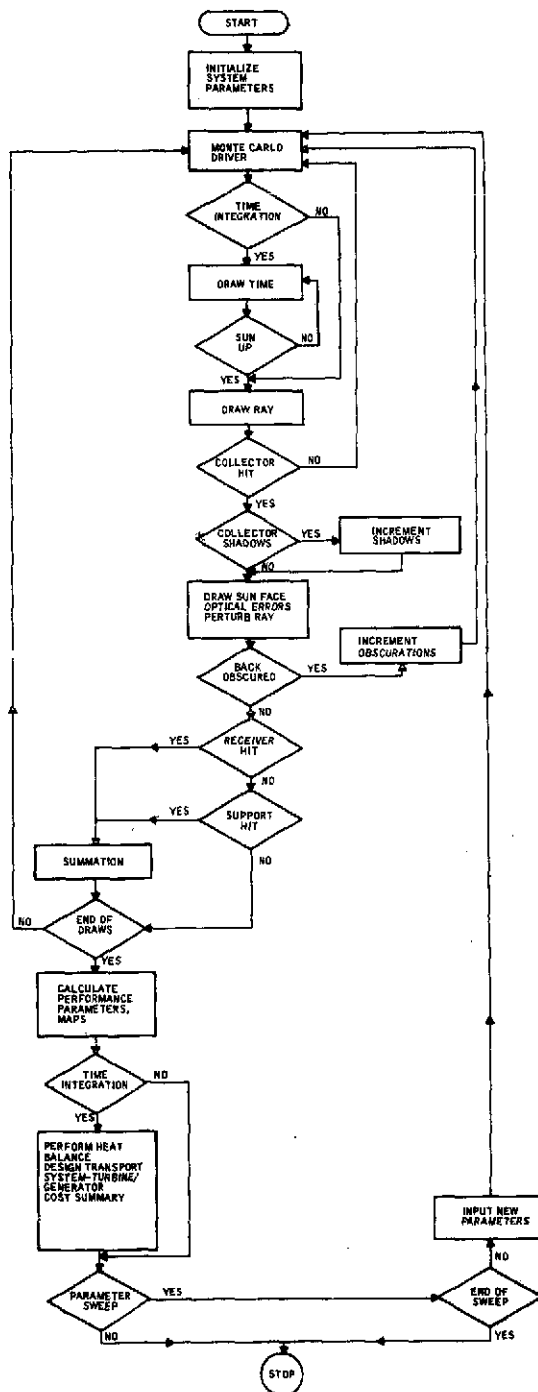
Figure C-1. Power Tower Simulation Code Flow Chart
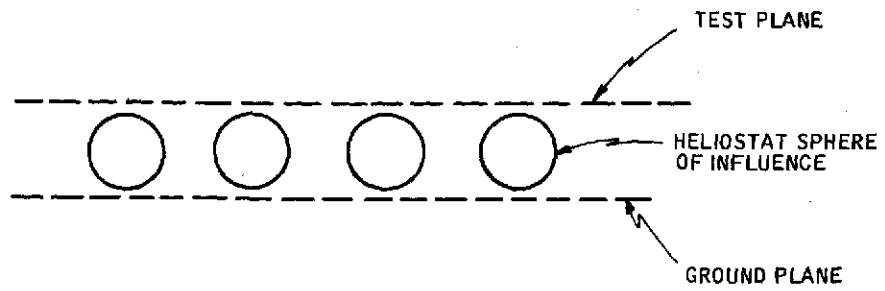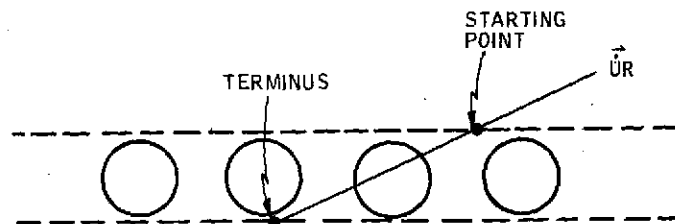
Figure C-2. Edge Path

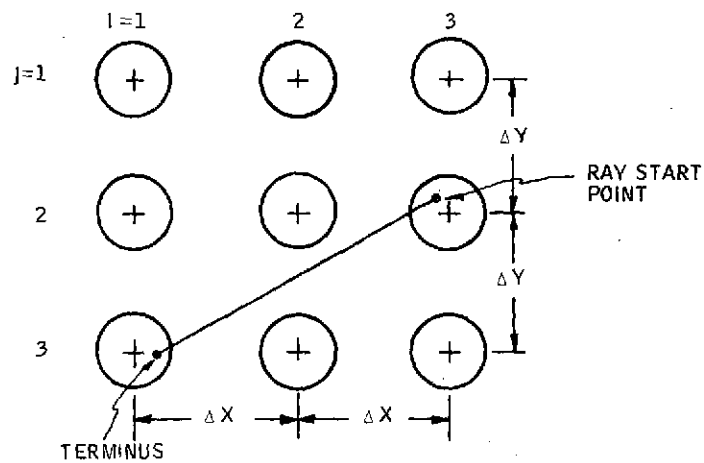Figure C-3. Heliostats Along Ray Trace

Figure C-4. Top View of Ray Path

The method used is to first find the closest heliostat to the ray start point. Then the closest heliostat to the terminus is found. If the closest heliostat to both ends of the line is in fact the same heliostat, then it is the only one that the ray could hit. Figure C-5 shows various examples of this. If the indices of the closest collectors to each end differ by at most one, then there are no collectors between the identified two collectors which could be involved in the redirection of the ray. Thus, only the two identified heliostats need be further considered. Several examples of this are shown in Figure C-6.

Finally, we have the case where the closest heliostats to the end points are different by more than one designation index (as in Figure C-4). In this case, the program simply divides the line segment from the start point to the terminus into many points and then finds the closest heliostat to each of the points. The spacing of the test points along the line is not critical as long as it is less than one heliostat radius. When this test sweep is complete, the code has found a list of one, two or perhaps many different heliostats which could redirect the ray. The requirement that the heliostats cannot overlap guarantees that there are no other heliostats which could redirect the ray. This list of closest adjacent heliostats is in fact more heliostats than could physically be involved with the ray. In Figure C-4, for example, the routine would find (3, 2), (2, 2), (2, 3), and (1, 3).

It would be possible to further reduce the list of heliostats to be tested by using the distance formula to rule out any heliostats which are further than one collector radius from the ray path at its closest point. This was not done in the program because the distance formula requires almost as much computation time to execute as does the hit test itself and would add more complexity to the code.

The next step in the process is to test all the mirrors on the list of possibilities for a reflection of the ray. The HIT test geometry is shown in Figure C-7 where D is the heliostat diameter, (x_p, y_p) are the east and north coordinates of the ray start point, (I, J) are the designation numbers for the heliostat to be tested, and $\vec{UR}$ is the unit vector from the sun center pointing toward the earth at the heliostat field, and $\vec{UMN}$ is the unit normal vector to the (I, J) heliostat with (x_c, y_c, z_c) the coordinate triad of its center of rotation.

$$x_c = I \Delta x \qquad (C-1)$$

$$y_c = J \Delta y \qquad (C-2)$$

$$z_c = D/2 \qquad (C-3)$$

where Δx is the east-west row spacing and Δy is the north-south spacing. The vector from the start point to the hit point on the plane of the heliostat $(\vec{UR})$ is given by:

$$\vec{VR} = \vec{UR} \, L \qquad (C-4)$$

where L is an unknown length.

Recall that any line not parallel to a plane must intersect the plane (not necessarily within the heliostat mirror boundary) at one and only one point. Thus, there will always be a real value of L. We can also write a vector from the ray start point to the center of the heliostat (to be called $\vec{SC}$), which is given by

$$\vec{SC} = \vec{UE} (x_c - x_p) + \vec{UN} (y_c - y_p) + \vec{N} Z_c \qquad (C-5)$$

where $(\vec{UE})$ is a unit vector along the local east direction (positive east), $(\vec{UN})$ is a unit vector along local north (positive north) and $(\vec{N})$ is the unit normal to the earth surface (vertical up positive).
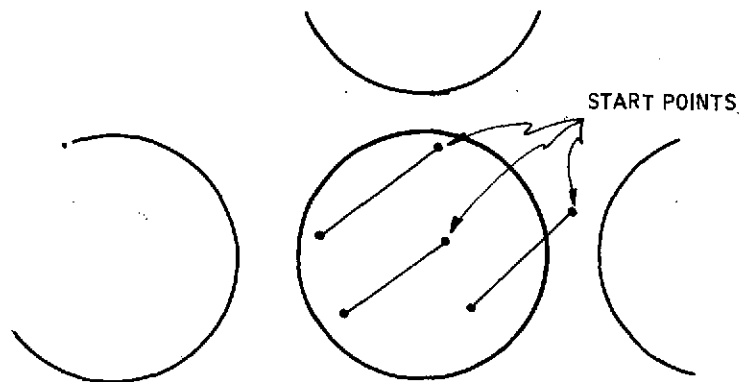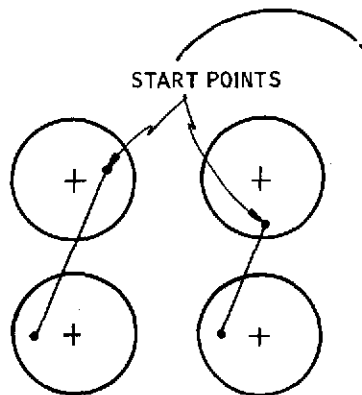
Figure C-5. Various Start Points
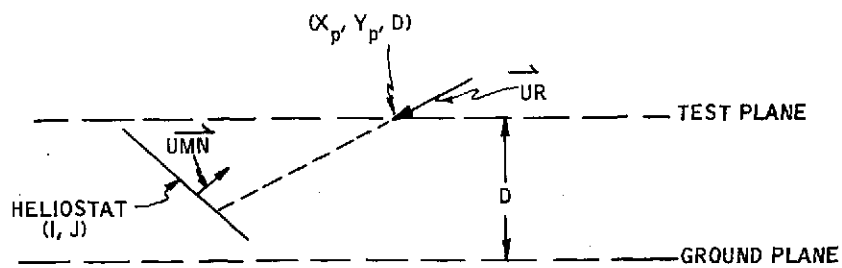

Figure C-6. Two Selected Heliostats

Figure C-7. HIT Test Geometry

Thus, substituting Equations (C-1), (C-2), and (C-3) yields

$$\vec{SC} = \vec{UE}\ (I\,\Delta x - x_p) + \vec{UN}\ (J\,\Delta y - y_p) + (D/2)\vec{N} \qquad (C-6)$$

Since both $\vec{SC}$ and $\vec{UR}$ go from the same point in space to the surface of the plane normal to $\overrightarrow{UMN}$ they must have the same projected length along $\overrightarrow{UMN}$ even though they do not enter the $\overrightarrow{UMN}$ plane at the same point. Thus, we can write the identity

$$\vec{SC} \cdot \overrightarrow{UMN} = \vec{VR} \cdot \overrightarrow{UMN} \qquad (C-7)$$

and from (C-4) we have

$$\vec{SC} \cdot \overrightarrow{UMN} = L\,\vec{UR} \cdot \overrightarrow{UMN} \qquad (C-8)$$

which is a scalar equation for the unknown length L. Now that we know the vector $\vec{VR}$ we can calculate where $\vec{VR}$ touches the plane relative to the heliostat mirror center.

The vector in the heliostat mirror surface plane from the center of the heliostat out to the point where the ray hits the plane ($\vec{RR}$) is given by

$$\vec{RR} = \vec{VR} - \vec{SC}$$
$$= L\,\vec{UR} - \vec{SC} \qquad (C-9)$$

And since the mirrors are circular, the hit test simply involves finding the magnitude of $\vec{RR}$ and comparing it to the heliostat radius. For square or other shapes, a slight modification to the logic test on $\vec{RR}$ is necessary. The order of heliostats tested in this way is from the ray start point to the end point. Thus, the first time a hit is found the ray is redirected. Succeeding heliostats (if any) are also tested and any hits are added to the shadow count.

Notice that Equations C-7 and C-8 require the unit normal ($\overrightarrow{UMN}$) to each heliostat (I, J) tested. The unit normal ($\overrightarrow{UMN}$) is shown in Figure C-8, where $\vec{UT}$ is the unit vector pointing from the heliostat center inwards the tower receiver center (or aim point wherever it is). Figure C-9 shows how a normal vector ($\overrightarrow{MN}$) can be constructed.

Thus,

$$\vec{MN} = \vec{UT} - \vec{UR} \qquad (C-10)$$

The unit normal is simply

$$\overrightarrow{UMN} = (\vec{UT} - \vec{UR})/|\vec{UT} - \vec{UR}| \qquad (C-11)$$

The vector $\vec{UT}$ is found from the non-unit vector ($\vec{T}$) from the heliostat center (x_c, y_c, D/2) to the tower top (0, 0, Th), where Th is the tower height. Thus,

$$\vec{T} = -x_c\,\vec{UE} - y_c\,\vec{UN} + (Th - D/2)\,\vec{N} + \vec{\delta} \qquad (C-12)$$

where $\vec{\delta}$ is a perturbation vector which allows placement of the aim point(s) at other than the tower top receiver center.

The unit vector $\vec{UT}$ then is

$$\vec{UT} = \vec{T}/|\vec{T}| \qquad (C-13)$$

To this point, the analysis has not involved the finite size of the sun or the tracking uncertainties of the heliostats. This simply means that the ray has been traced from its uniform draw start point to the mirror or the ground. Physically this means that we have ignored the finite size of the sun and the tracking errors in the shadow analysis. The finite sun and finite tracking errors tend to "blur" the edges of the mirrors and the edges of the shadows somewhat when taken on average over the whole field.

If at this point in the flow, one of the heliostats on the list of possibilities has in fact tested out to have a hit, we proceed to perturb $\vec{UR}$ and $\vec{UMN}$ for the finite sun size, the tracking errors and the mirror surface slope uncertainty. To begin the perturbation process a ray start point is drawn over the sun's face. The simplest case of this is the assumption that the sun is a "flat" disk of brightness in the sky. The plot of this is shown in Figure C-10. The uniform draw over a disk is simply a uniform draw over the polar coordinate (θ) and a weighted draw over ρ (see Figure C-11).

The weighted draw over ρ comes from the fact that more rays must be drawn in the annulus ρ to $\rho + d\rho$ at large values of ρ than at small values of ρ. Another way to consider this is to plot the sun's energy from 0 out to ρ versus ρ. (See Figure C-12.) The formula for this curve is simply

$$E = E_T \ (\rho/\rho_{max})^2 \qquad (C-14)$$

where E_T is the total energy from the sun's disk and ρ_{max} is the maximum angular extent of the sun.

Thus, if we want to draw uniformly over the area of the disk, we simply draw uniformly over the abscissa (energy axis) of Figure C-12 and Equation (C-14) is inverted to find the ordinate value (ρ) which we want. Thus, if we draw the random number x_1 uniformly from 0 to 1 then the value of ρ for each x_1 is given by the inverse of Equation (C-14) or

$$\rho = \rho_{max} \sqrt{x_1} \qquad (C-15)$$

The (θ) coordinate is found from another (independent) uniform number x_2 drawn from 0 to 1 by

$$\theta = 2\pi \ x_2 \qquad (C-16)$$

If we arbitrarily define two axes in the sun face (UX_1, UX_2) then the rotation angles of $\vec{UR}$ about these axis ($\Delta\theta_1$, $\Delta\theta_2$) are shown in Figure C-13, which are given by

$$\Delta\theta_1 = \rho \sin\theta \qquad (C-17)$$

$$\Delta\theta_2 = \rho \cos\theta \qquad (C-18)$$

Thus, we can perturb $\vec{UR}$ into $\vec{UR}'$ with

$$\vec{UR}' = \frac{(\vec{UR} - Tan\,\Delta\theta_2 \ \vec{UX1} - Tan\,\Delta\theta_1 \ \vec{UX2})}{\sqrt{1 + Tan^2\,\Delta\theta_2 + Tan^2\,\Delta\theta_1}} \qquad (C-19)$$

The three-space drawing from which this can be derived is shown in Figure C-14.

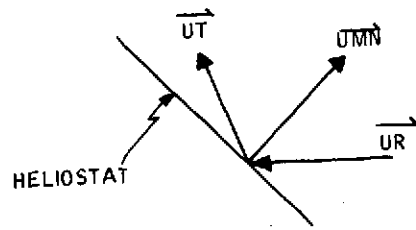Notice that ($\vec{UR}$, $\vec{UX1}$, $\vec{UX2}$) form an orthonormal triad.
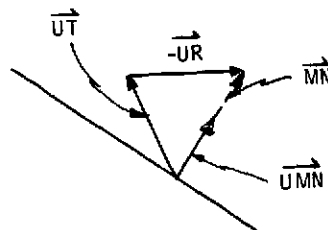
Figure C-8. Unit Normal ($\overrightarrow{UMN}$)
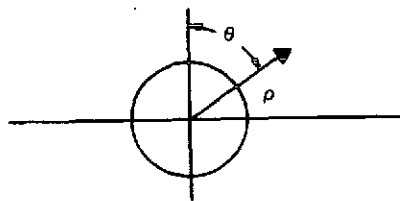

Figure C-9. Normal Vector ($\overrightarrow{MN}$)

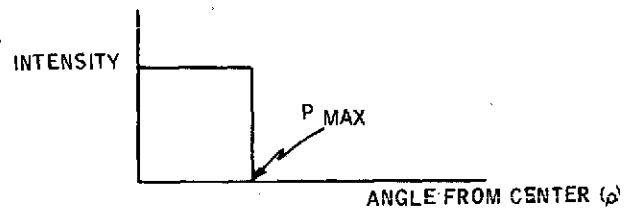Figure C-10. Ray Start Point Plot

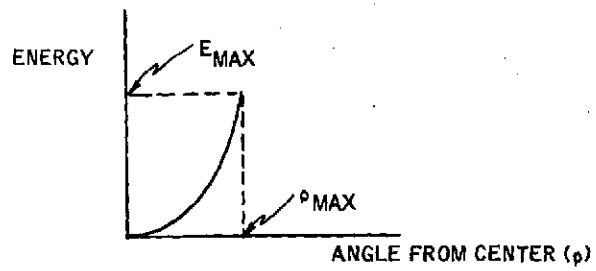Figure C-11. Uniform and Weighted Draw
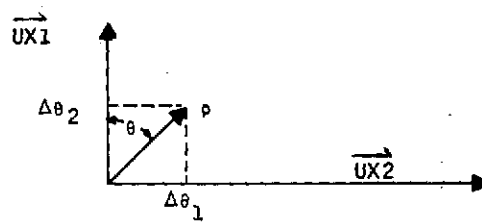
Figure C-12. Energy Plot
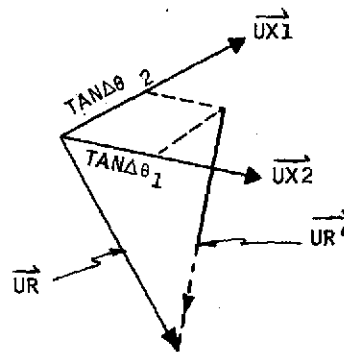

Figure C-13. Rotation Angles

Figure C-14. Three-Space
Drawing

This is all the vector algebra necessary to incorporate the finite sun size into the analysis. The computer code includes a limb-darkening option and an option with limb darkening and scattering outside the geometric sun perimeter.

The process we have outlined here is the same for both of these options except that the weighted draw of ρ is weighted in such a way that the draw is again uniform over the new solar disk energy distribution. This involves plotting brightness versus angular distance from the sun's center and integrating energy as before. Then, the integrated energy curve is curve-fit and the fit function is inverted. This inverse function [analogous to Equation (C-15)] is then the basis for the draw.

The next step in the trace process is to perturb the unit mirror normal $\overrightarrow{UMN}$ for the uncertainties in heliostat tracking. This involves a rotation of $(\overrightarrow{UMN})$ about an axis (the first tracking axis) which is not normal to it. The tracking axes are assumed to be standard gimbal mounts (Figure C-15) with the first axis (attached to earth) vertical $(\vec{N})$ and the second axis perpendicular to $(\vec{N})$ and hence parallel to the ground as it rotates with the heliostat about $(\vec{N})$.

The essential vectors drawn alone are shown in Figure C-16.

We define the plane of $(\vec{N})$ and $(\overrightarrow{UMN})$ and then $(\overrightarrow{UAX})$ is normal to it. We first construct a vector normal to $(\vec{N})$ from $(\vec{N})$ out to the tip of $(\overrightarrow{UMN})$ (non unit), called $(\overrightarrow{NORM})$.

$$\overrightarrow{NORM} = \overrightarrow{UMN} - (\overrightarrow{UMN} \bullet \vec{N}) \vec{N} \qquad (C-20)$$

and

$$\overrightarrow{UAX}_1 = (\vec{N} \times \overrightarrow{UMN})/|(N \times \overrightarrow{UMN})| \qquad (C-21)$$

There is the potential for at most one heliostat in the field for which $(\overrightarrow{UMN})$ is equal to $(\vec{N})$. Such a heliostat must be positioned in exactly the correct place to cause (Equation C-23) to become singular and in millions of rays traced to date this has not happened. Clearly, as $(\overrightarrow{UMN})$ is rotated around $(\vec{N})$ the component of $(\overrightarrow{UMN})$ along $(\vec{N})$ remains unchanged. It is, in fact, only $(\overrightarrow{NORM})$ the component normal to $(\vec{N})$ which rotates. With rotation about $(\vec{N})$ of $\Delta\phi_1$ the $(\overrightarrow{NORM})$ component of $\overrightarrow{UMN}$ is forshortened by a factor of cosine of $\Delta\phi_1$; this component is simply

$$(\overrightarrow{NORM}) \cos \Delta\phi_1$$

The component along $\overrightarrow{UAX}$ is the magnitude of $(\overrightarrow{NORM})$ scaled by $\sin\Delta\phi_1$ or in vector form $|\overrightarrow{NORM}| \sin\Delta\phi_1 \overrightarrow{UAX}$. Thus, the perturbed heliostat normal due to rotation $\Delta\phi_1$ about $\vec{N}(\overrightarrow{UMN})$ is given by

$$\overrightarrow{UMN}_1' = (\overrightarrow{UMN} \cdot \vec{N}) \vec{N} + \overrightarrow{NORM} \cos \Delta\phi_1 + |\overrightarrow{NORM}| \sin \Delta\phi_1 \overrightarrow{UAX} \qquad (C-22)$$

A top view (Figure C-17) of this looking down $\vec{N}$ in which $(\overrightarrow{NORM})$ and $\overrightarrow{UAX}'$) are true lengths may help clarify the derivation of (C-22).

The perturbation of $(\overrightarrow{UAX})$ into $(\overrightarrow{UAX}')$ due to the rotation about $(\vec{N})$ is derived from Figure C-17 also

$$\overrightarrow{UAX}' = \overrightarrow{UAX} \cos \Delta\phi_1 - \overrightarrow{NORM} \sin \Delta\phi |\overrightarrow{NORM}| \qquad (C-23)$$
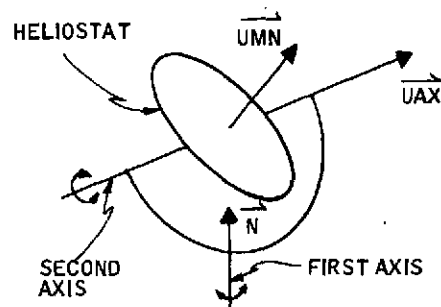
Figure C-15. Tracking Axes
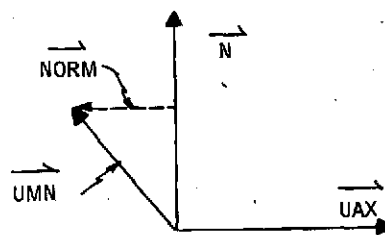
Figure C-16. Essential Vectors
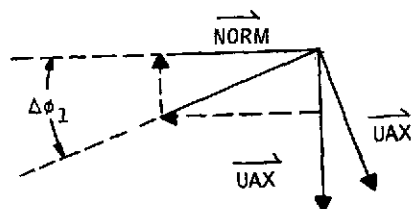
Figure C-17. Top View Looking Down $\vec{N}$

Notice that $\overrightarrow{NORM}/|\overrightarrow{NORM}|$ is simply a unit vector along norm which we have not elected to give a special name. We are now ready to perform the second tracking error rotation which is about $(\overrightarrow{UAX})$ to get $(\overrightarrow{UMN}'')$.

For this next rotation we construct an orthonormal triad $(\vec{N}, \overrightarrow{UAX_1}', \overrightarrow{UAX_2})$ where

$$\overrightarrow{UAX_2} = \overrightarrow{UAX}' \times \overrightarrow{UMN}' \qquad (C-24)$$

This now is a standard coordinate rotation of two perpendicular vectors $(\vec{N}, \overrightarrow{UAX_2})$ about a third perpendicular vector $(\overrightarrow{UAX}')$. This type of rotation can be found in any text and the result is simply

$$\overrightarrow{UMN}'' = [(\overrightarrow{UMN}' \cdot \vec{N}) \cos \Delta\phi_2 + (\overrightarrow{UMN}' \cdot \overrightarrow{UAX_2}) \sin \Delta\phi_2]\vec{N}$$

$$+ [(\overrightarrow{UMN}' \cdot \overrightarrow{UAX_2}) \cos \Delta\phi_2 + (\overrightarrow{UMN}' \cdot \vec{N}) \qquad (C-25)$$

$$\sin \Delta\phi_2] \overrightarrow{UAX_2}$$

where $\Delta\phi_2$ is the error angle of rotation about the second axis. We get $\overrightarrow{UAX_2}$ from

$$\overrightarrow{UAX_2}' = \overrightarrow{UAX_1}' \times \overrightarrow{UMN}'' \qquad (C-26)$$

Notice that $(\overrightarrow{UAX_2}, \overrightarrow{UAX_1}')$ are in the heliostat mirror surface plane before the $\Delta\phi_2$ rotation and that $\overrightarrow{UAX_2}', \overrightarrow{UAX_1}'$) lay in the surface after rotation.

The error angles $(\Delta\phi_1, \Delta\phi_2)$ are drawn at random with a normal distribution (standard error distribution) having a mean and variance specified by the user of the program. If the details of the heliostat drive mechanism become available, any other reasonable distribution of error angles which more nearly matches the reality of the system could be substituted easily for the normal distribution.

The next and final perturbation of the heliostat mirror normal is the angular rotation which represents mirror surface irregularity. The sketch of this perturbation is shown in Figure C-18.

Thus, the final perturbed mirror normal $(\overrightarrow{UMN}''')$ is given by

$$\overrightarrow{UMN}''' = \overrightarrow{UMN}'' \cos \delta_1 + \sin \delta_1 [\overrightarrow{UAX_1}' \cos \delta_2 + \overrightarrow{UAX_2}' \sin \delta_2] \qquad (C-27)$$

where δ_2 is drawn uniformly from 0 to 360 degrees and δ_1 is drawn with a normal distribution having a specified mean and variance. Physically, what this last perturbation means is that the mirror surface normal is locally out of alignment with the average normal by an amount δ_1. The plane in which the δ_1 rotation occurs is equally likely to occur in any direction around the local azimuth. Recall that at this point in the trace we can find the position on the heliostat of the ray being traced from the vector RR. With this we could include a perturbation of the normal which was a function of position on the heliostat surface. Such a position-dependent variation could be a gravity or wind load deflection. If the wind forces and deflections were known only stochastically, this also could be included in the analysis. Also a curvature of the mirror for focussing can be added here.

If the design tradeoff studies should reach the level of trading off structural stiffness to effect cost saving against collector efficiency, it is practical to model these issues with the existing software and involve only minor changes to the perturbation routine.

$$\vec{US}_1 = \vec{UR} - 2(\vec{UR}' \cdot \vec{UMN}'') \vec{UMN}''' \qquad (C-28)$$

To review, $\vec{US}_1$ is the reflected ray which includes the effect of a finite sun size (through $\vec{UR}'$) and an imperfect tracking drive and mirror surface (through $\vec{UMN}'''$).

The next step in the trace is to determine whether or not the ray $(\vec{US}_1)$ passes cleanly out of the mirror field on its way to the receiver or is blocked by an adjacent heliostat.

This process of finding a blockage event involved exactly the same vector algebra and methodology as did the identification and hit testing of all the heliostats which could reflect the incoming ray $(\vec{UR})$. Step one is to find the list of all heliostats which could block the ray on its path to the test plane. The top view of the ray trace from its reflection point on the heliostat out to the test plane is shown in Figure C-19.

In side view, this is shown in Figure C-20.

For purposes of deciding whether or not $(\vec{US}_1)$ is blocked we will ignore the effect of the small error rotations on $(\vec{RR})$ $(\vec{UMN}_1)$ and $(\vec{UMN}_2)$. This is exactly true in the case of perfect optics, and results in translations of the reflection point, and the edges of the heliostats by distances the order of inches while all other pertinent distances (such as the center to center spacing of the heliostats) are of the order of many feet.

The start point of $\vec{US1}$ is at (X_s, Y_s) where:

$$X_s = \Delta X \cdot I1 + \vec{RR} \cdot \vec{UE}$$
$$Y_s = \Delta Y \cdot J1 + \vec{RR} \cdot \vec{UN} \qquad (C-29)$$

The ray $\vec{US1}$ extends a length (L_t) out to the test plane where (L_t) is given by:

$$D/2 = (\vec{RR} + L_t \vec{US1}) \cdot \vec{N} \qquad (C-30)$$

In words, Equation (C-30) means that the distance from the center of the heliostat to the test plane (D/2) is equal to the projection of a vector from the center to the test plane, projected on to the normal to the test plane. Clearly, Equation (C-30) can be solved for (L_t). The location of the point where $\vec{US1}$ crosses the test plane is given by (X_t, Y_t) where

$$X_t = \Delta X \cdot I1 + (\vec{RR} + L_t \vec{US1}) \cdot \vec{UE}$$
$$Y_t = \Delta Y \cdot J1 + (\vec{RR} + L_t \vec{US1}) \cdot \vec{UN} \qquad (C-31)$$

As before all heliostats along the path from the ray start point (X_s, Y_s) to the terminus (X_t, Y_t) are found and the previous logic tests are used to reduce the list to a minimum. The remaining identified heliostats (I2, J2) are then tested to find the position where the $\vec{US1}$ ray crosses the heliostat plane $(\vec{RR2})$. The first vector needed in the test is the vector from the center of heliostat (I1, J1) out to heliostat (I2, J2) called $\vec{VC}$ as in Figure C-21.
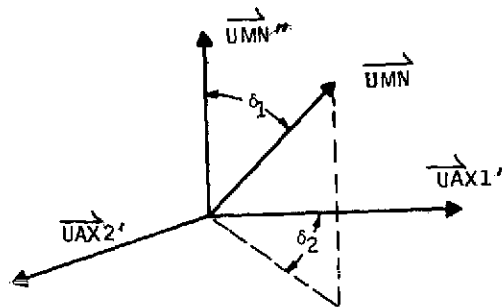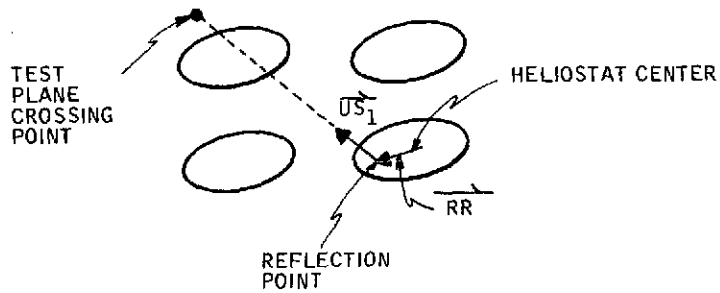
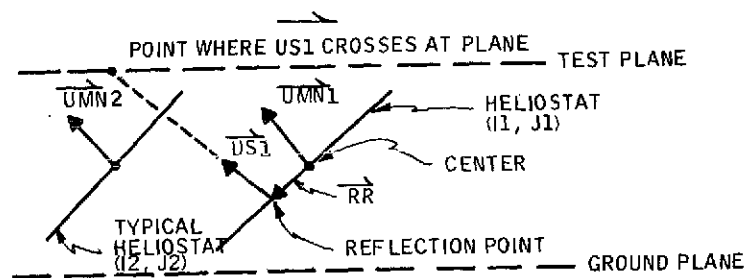Figure C-18. Perturbation Sketch

Figure C-19. Top View, Ray Trace

Figure C-20. Side View, Ray Trace

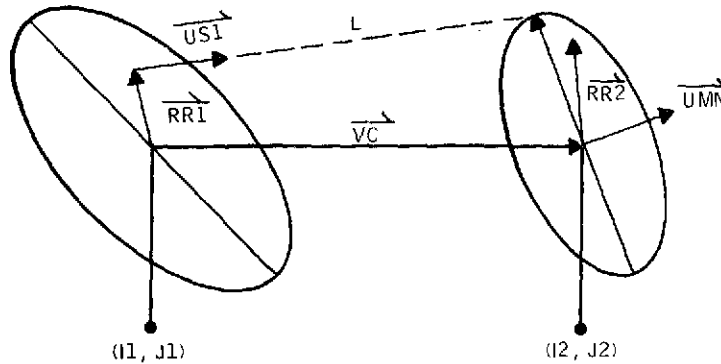Figure C-21. Needed Vector

$$\vec{VC} = \Delta X \ (I2 - I1) \ \vec{UE}$$

$$+ \ \Delta Y \ (J2 - J1) \ \vec{UN}$$

(C-32)

As before, the length (L) of the $\vec{US1}$ ray out to its hit point on the (I2, J2) heliostat plane is given by:

$$(\vec{RR1} + L \ \vec{US1}) \bullet \vec{UMN}_2 = \vec{VC} \bullet \vec{UMN}_2$$

(C-33)

where $\vec{RR1}$ is the vector from the heliostat center to the reflection point on heliostat (I1, J1) and $\vec{UMN}_2$ is the unit normal to heliostat (I2, J2). After solving Equation (C-34) for L we can find $(\vec{RR2})$

$$\vec{RR2} = \vec{US1} \bullet L + \vec{RR1} - \vec{VC}$$

(C-34)

For a circular heliostat the magnitude of $\vec{RR2}$ is compared with the heliostat radius to find out if the (I2, J2) heliostat blocked the ray. If the ray is blocked, the trace ends, the blocked ray count is incremented, and a new ray is drawn. The remainder of the list of candidate blocking heliostats is not checked for multiple blockage. If all the heliostats on the list do not block the ray, it gets cleanly away from the field and the ray is traced on up to the receiver.

The current versions of the code can find the intersection of the ray US1 with any combinations of sphere and cylinder, truncated cone, cruciform and crescent shapes. Each of these routines determines whether or not the ray hit the receiver and if it hit, where on the receiver the hit occurred. If the ray misses, another ray is drawn. If it hits the hit total is incremented. Hits are also sorted out by location on the receiver. That is, the receiver is broken into zones and the number of rays which hit in each zone is used to obtain a flux map of the receiver surface.